ESTIMATING PARTICLE DISPERSAL IN AQUATIC SYSTEMS:
A COMPARISON OF NEW AND CONVENTIONAL TECHNOLOGIES

by

Janelle Marie Hrycik

Submitted in partial fulfilment of the requirements
for the degree of Doctor of Philosophy

at

Dalhousie University
Halifax, Nova Scotia
November 2018

This body of work is dedicated to the memory of my beloved Nana.
I fulfilled my final promise to her and she would be so proud.

Dorothy J. Pawlikowski
15 December 1931 – 01 January 2015

“According to the law of the conservation of energy, not a bit of you is gone; you're just less orderly.”

Aaron Freeman

Table of Contents

List of Tables

List of Figures

Abstract

Dispersal is one of the most important life history strategies involved in species survival and evolution, affecting population dynamics, population genetics, and the spatial scale of population connectivity through the exchange of individuals among geographically separated subpopulations. Aquatic species exchange individuals, and subsequently genes, among subpopulations mainly through early life-stage dispersal; however, the dominant scales of dispersal are still “not known” and the knowledge of how aquatic populations are connected in space and time is thus limited. The extent of early life-stage dispersal is dependent on physical (e.g., advection and diffusion) and biological (e.g., reproduction, behavior, and mortality) processes, and interaction among these physical and biological processes makes distinguishing their separate effects on dispersal challenging. Motivations to study and quantify dispersal and connectivity range from biodiversity conservation to the design of marine reserves and the mitigation of species invasions. Since robust measures of dispersal in aquatic environments are rare, when they are obtained, they must be used to test the assumptions and hypotheses of the numerical models that are often used as the basis of management and conservation decisions. I quantify the dispersal of purely passive particles at the scale of early-stage planktonic organisms in the near-surface upper mixed layer of coastal ocean and lake environments using a new magnetically attractive particle (MAP) and magnetic-collector prototype system that provides a time-integrated estimate of the purely passive component of dispersal from a given source location to a large set of potential sink locations; the biological null model. The quantitative, empirical estimates that the MAPs provide can be used to test other technologies that estimate dispersal, and I qualitatively and quantitatively compare the observed passive particle dispersal estimates to similar estimates derived from hydrodynamic models and concurrently deployed drogued drifters. I illustrated the results in the context of issues surrounding commercially valuable and (or) invasive species, and discussed the limitations of using the various technologies, especially models, to address dispersal and connectivity questions. This thesis has made an advance toward linking the empirical with the theoretical.

List of Abbreviations and Symbols Used

Abbreviations and Symbols	Description	Units
®	registered trademark	
θ	azimuthal coordinates	
A	aperture area; subscript indicates magnetic-collector or grid-cell	cm
β_0	residual drifter velocity in the absence of any wind effect; i.e., the "drain"	
β_1	proportion of wind velocity applied to drifter to achieve observed velocity	
C	concentration of particles	
D	distance	km
esd	equivalent spherical diameter	µm
E	exposition number	
k	number of individual particles	
K_H	horizontal diffusivity	$m^2\ s^{-1}$
K_p	small-scale diffusivity	$m^2\ s^{-1}$
K_V	vertical diffusivity	$m^2\ s^{-1}$
L	distance from source	km
m	grid-cell length	m
MAP	magnetically attractive particle	
n	sample size	
N	particle number estimate; subscript indicates magnetically attractive particle or virtual particle	
N_{eff}	"effective" number of particles available for capture in dispersal domain	
N_{MAPR}	number of magnetically attractive particles released	
N_{VPR}	number of virtual particles released	
p	probability-value statistic	
$p(r,\theta;\ t)$	probability density function; the dispersal kernel	m^{-2}
$P(r \geq L;T)$	probability estimated from the data	

Abbreviations and Symbols	**Description**	**Units**
r	radial coordinates	
r^2	coefficient of determination	
SG	specific gravity	
t	time	d
t_0	time of release	d
T	sampling period	d
T	tidal period	h
u	horizontal velocity	m s^{-1}
u_D	observed drifter velocity	cm s^{-1}
u_t	horizontal tidal current velocity	m s^{-1}
UV	ultraviolet	
v	vertical velocity (**Chapters 2–5**)	m s^{-1}
VP	virtual particle	
w	observed wind velocity (**Chapter 5**)	m s^{-1}
w	vertical velocity (**Chapter 1**)	m s^{-1}
w'	turbulent eddy velocity	m s^{-1}
w_p	rise rate	mm s^{-1}
x	location at time	
z	depth	m
CG	Cape George	
CODE	Coastal Ocean Dynamics Experiment	
CT	Cape Tormentine	
GB	St. George's Bay	
HEC	Huron–Erie Corridor	
MH	Murray Harbour	
MPA	marine protected area	
NB	New Brunswick	
NS	Nova Scotia	
PE	Prince Edward Island	
SH	Shediac	
sGSL	southern Gulf of St. Lawrence	
USA	United States of America	
VHSV	viral haemorrhagic septicemia virus	

Acknowledgements

"If I have seen further, it is by standing upon the shoulders of giants."
Sir Isaac Newton

I owe thanks to many giants…

I will never be able to re-pay my advisor, Dr. Christopher T. Taggart, for his positive influence on my life over the past decade. I have never taken for granted his encouragement, patience, support, and understanding through my countless ups and downs. He believed in my abilities enough for the both of us in the moments I did not, and I am forever indebted to his continued willingness to take a chance on me. He provided every possible opportunity (and then some) for me to succeed. This work would have been unmanageable without him and I am proud to have been his student. Thank you will never be enough.

I thank my Committee Members, Drs. Barry R. Ruddick, Keith R. Thompson, Joël Chassé, and Anna Metaxas. I appreciate their patience over this lengthy commitment and I value the advice and encouragement they provided along the way.

I appreciate the assistance, encouragement, and shared humanity of all of the past and current students and post-docs in the Department of Oceanography, especially those in the Taggart Lab: Sean Brillant, Franziska Broell, Meghan Carr, Kimberley Davies, Delphine Durette-Morin, Matthew Hatcher, Diego Ibarra, Hansen Johnson, Anna Neuheimer, Amy Ryan, Joel Slade, Julie Sperl, and Angelia Vanderlaan. I also acknowledge others whose shared discussions about science and (or) life made an impact: Jean-Pierre Auclair, Jeffrey Barrell, David Bowen, Erin Breen, Michael Brown, Will Burt, Jessica Carrier-Garwood, Rémi Daigle, Laura deGelleke, Katie Hastings, Myriam Lacharité, Michelle Lloyd, Eric Pedersen, Clark Richards, Megan Saunders, Shiliang Shan, Ryan Stanley, and Robin Wilson.

Thank you to Brad Lienhart and Trey Simendinger of MicroPhase Coatings, Inc. for their persistence in helping develop an effective MAP formula. I am grateful for the logistical support provided by J. Mark Hanson, Matthew Hatcher, Water Judge, Mark Merrimen, and the fishing boat captains throughout New Brunswick, Nova Scotia, and Prince Edward Island that made data collection feasible. The analyses in this thesis would not have been possible without the support of many co-op students. From building and deploying collectors to counting particles in thousands of images, it truly was a team effort. Thank you to Anne Benaroya, Miriam Morgan, Katie Kenny-Foeldessy, Robert Lalonde, Karen Devitt, Daniel Pyke, Amy Ryan, and Elizabeth Campbell.

I thank the Department of Oceanography staff, including Sharon Bellefontaine, Lori Lawton, and Amanda Martin. In particular, I express my immense gratitude to Lori for her steadfast assistance throughout every stressful step of preparing, defending, and submitting this thesis. Thank you to Daniel Morrison, who remained a friendly face through nerve-wracking situations and solved any number of technical issues over the years. I am grateful to C.C. Smith for her patience and support in strengthening my quantitative skills, reading through my work, and providing a listening ear as needed.

Thank you to the faculty, staff, teaching assistants, and students in the Biology Department and the College of Sustainability for enriching my experience more than I ever could have imagined. They helped me find my purpose.

Thank you to the past science teachers and mentors who challenged me to believe I could achieve more, especially Dr. Paul Forestell and Mrs. Eunice Reinhold. I recognize how fortunate I have been to learn from such invested instructors throughout every step of my education, and I hope I am able to live up to their example.

Thank you to my parents, Marshall and Sharon Hrycik, for fostering my curiosity about the natural world and love of learning from a young age. I am appreciative to the Hrycik and Pawlikowski families for their continued support in allowing me the freedom to find my own way, especially Jesse Hrycik, Dorothy Pawlikowski, and James Pawlikowski.

Thank you to my best friend, Victoria Martinez, who knows me better than anyone and reminds me of who I am when I often forget. I thank my adopted New England family, especially Cheryl Ball and Tara Duggan. The last couple of years would have been unbearable without them. Thanks to Christopher Demery who provided support throughout the majority of this work. I am grateful to Cathy Goldstein-Mullin, who continues to be my cheerleader, confidant, and voice of reason. Finally, thank you to my pug, Travis. He is the love of my life, the reason I am still here, and the source of so many smiles.

Technological development and study execution was supported by the Natural Sciences and Engineering Research Council (NSERC) Ideas to Innovation Programme, the NSERC Canadian Healthy Oceans Network (CHONe), Fisheries and Oceans Canada Northumberland Strait Research Initiative (NSERI), and in part by the U.S.A. National Science Foundation and by Innovacorp I-3 Technology Funds.

"The crucial lesson was that the scope of things I didn't know wasn't merely vast; it was, for all practical purposes, infinite."

Martin A. Schwartz
The importance of stupidity in scientific research

Chapter 1

Introduction

1.1 Context and Motivation

Organismal movement is one of the most studied, yet least understood, concepts in ecology. The causes of movement are major evolutionary forces that are affected by a plethora of ecological and behavioral phenomena, such as habitat availability and (or) mate choice. Movement consequently results in exposure to varying opportunities and (or) risks. While movement shifts the spatial distribution of individuals, it also has the capacity to transform population, community, and ecosystem dynamics. Organismal movement can be defined in many ways, where the concept of dispersal is considered one of the most important life history strategies involved in species survival and evolution (Wolfenbarger 1975; Shields 1987; Stenseth and Lidicker 1992; Clobert *et al.* 2001; Bowler and Benton 2005; Begon *et al.* 2006; Matthysen 2012; Allen *et al.* 2018).

Early life-stage dispersal influences population abundance and distribution in both terrestrial and aquatic species, is a widespread characteristic that spans taxonomic groups, and is especially exhibited by aquatic vertebrates and invertebrates, terrestrial invertebrates, and aquatic and terrestrial plants. Dispersal affects population dynamics (e.g., the distribution of individuals and ultimately reproduction and recruitment), population genetics (e.g., gene flow), and thus the spatial scale of population connectivity through the exchange of individuals among geographically separated subpopulations (Clobert *et al.* 2001; Kinlan and Gaines 2003; Bowler and Benton 2005; Begon *et al.* 2006; Nathan 2006; Matthysen 2012; Allen *et al.* 2018).

The significance of early life-stage dispersal in explaining the ecology (i.e., abundance and distribution) of aquatic species has been recognized for at least a century (Hjort 1914). Aquatic species exchange individuals, and subsequently genes, among subpopulations mainly through larval dispersal (Scheltema 1986; Metaxas 2001; Kinlan and Gaines 2003; Sale *et al.* 2005; Treml *et al.* 2008; Metaxas and Saunders 2009; Allen *et al.* 2018); however, the dominant scales of dispersal are still “not known” (Pineda *et al.* 2007) and the knowledge of how aquatic populations are connected in space and time is thus limited (Palmer and Strathmann 1981; Franks 1992; Bradbury and Snelgrove 2001; Largier 2003; Siegel *et al.* 2003; Kinlan *et al.* 2005; Byers and Pringle 2006; Cowen *et al.* 2006, 2007; Levin 2006; Edwards *et al.* 2007; Pineda *et al.* 2007; Kool *et al.* 2013; Allen *et al.* 2018; Pineda and Reyns 2018). The extent of early life-stage dispersal is dependent on physical (e.g., advection and diffusion) and biological (e.g., reproduction, behavior, and mortality) processes, and interaction among these physical and biological processes makes distinguishing their effects on dispersal challenging (most authors cited above). As I will further examine, this is a significant problem that lacks a straightforward solution.

Motivations to study and quantify dispersal and connectivity now include the sustainable management of commercially viable and (or) endangered species, the mitigation of the threat of invasive species, the conservation of biodiversity through the design of marine reserves, the prediction of species response to climate change, and the evaluation of the impact of contaminants (Kinlan *et al.* 2005; Cowen *et al.* 2006; Levin 2006; Aiken *et al.* 2007; Becker *et al.* 2007). For example, one of the main factors driving the design and implementation of Marine Protected Areas (MPAs) should be the degree of connectivity among local populations of a species that need protection. With the appropriate data on larval dispersal it should be possible to adjust reserve size, placement, and spacing to achieve specific management objectives (Largier 2003; Palumbi 2003; Shanks *et al.* 2003; Sale *et al.* 2005; Kaplan 2006; Cowen *et al.* 2007; Fogarty and Botsford 2007; Jones *et al.* 2007; Treml *et al.* 2008; Botsford *et al.* 2009; Planes *et al.* 2009; Costello *et al.* 2010; Gaines *et al.* 2010; Green *et al.* 2015; Krueck *et al.* 2017). Further, empirical estimates of dispersal are necessary to guide numerical modeling studies that are often the basis of management and conservation decisions. Robust measurements of dispersal in aquatic environments are rare (e.g., D'Aloia *et al.* 2015), and when they are obtained they must be used to test the assumptions and hypotheses related to such models and to strengthen model capabilities and associated inferences (Thorrold *et al.* 2002; Largier 2003; Siegel *et al.* 2003; Cowen *et al.* 2006; Kaplan 2006; Nathan 2006; Aiken *et al.* 2007; Pineda *et al.* 2007; Werner *et al.* 2007; Cowen and Sponaugle 2009; Metaxas and Saunders 2009; Rasmussen *et al.* 2009; Okubo and Levin 2010; Sponaugle *et al.* 2012; Nickols *et al.* 2015; Almany *et al.* 2017; Krueck *et al.* 2017; Pineda and Reyns 2018).

As the scientific community aims to address gaps in the understanding of dispersal and connectivity, it has become abundantly clear that there is 1) a lack of empirical data and 2) a perhaps unwarranted reliance on models. As a result, existing methods continue to be refined and new approaches continue to be developed. This thesis confronts both 1) and 2) above by obtaining empirical estimates of dispersal in aquatic environments using a new technology and then by comparing such estimates in relation to other conventional technologies that are frequently employed in the study of dispersal.

1.2 Advection and Diffusion

"Dispersal" is a term widely used in the literature, yet it remains loosely defined. Since the study of dispersal uses various approaches among many disciplines, there is debate about what qualifies as dispersal and how it should be defined (Wolfenbarger 1975; Shields 1987; Stenseth and Lidicker 1992; Clobert *et al.* 2001; Weins 2001; Begon *et al.* 2006; Levin 2006; Allen *et al.* 2018). From a physical perspective, Fischer *et al.* (1979, p. 7) define dispersal as the "*scattering of particles or a cloud of contaminants by the combined effects of shear and transverse diffusion*." From a biological perspective, Southwood (1978, p. 327–328) states that dispersal "*covers any movement away from an aggregation or a population…*", while Cowen and Sponaugle (2009, p. 444) specifically describe larval dispersal as "*the intergenerational spread of larvae away from a source to the destination or settlement site at the end of the larval stage*." From my perspective, I view dispersal as movement away from a defined source location through passive and (or) active means (e.g., Begon *et al.* 2006; Levin 2006), and in this thesis, I deal only with the passive component of dispersal. Consequently, dispersal is equivalent to transport as defined below.

It is necessary to first understand the mechanisms underlying dispersal, and this is where the advection-diffusion equation initially provides meaning in an aquatic environment. It is given below, under the assumptions of 1) no variation in the *y*-direction and 2) constant horizontal (*x*) and vertical (*z*) diffusivities, such that:

$$\frac{\partial C}{\partial t} = \underset{\textbf{I}}{-u\frac{\partial C}{\partial x}} \underset{\textbf{II}}{- w\frac{\partial C}{\partial z}} + \underset{\textbf{III}}{K_H\frac{\partial^2 C}{\partial x^2}} + \underset{\textbf{IV}}{K_V\frac{\partial^2 C}{\partial z^2}}\,, \tag{1.1}$$

where *C* is the concentration of particles subject to dispersal, *u* and *w* are the horizontal and vertical water velocities, respectively, and K_H and K_V are the horizontal and vertical diffusivities, respectively. **Terms I** and **II** above relate to advection while **Terms III** and **IV** above relate to diffusion.

In the following Chapters, I will use the word "transport" in a generic sense, consistent with Fischer *et al.* (1979). It will include the effects of advection (**Terms I**, **II**) and diffusion (**Terms III**, **IV**) shown in **Equation 1.1**. Splitting transport into the separate processes of advection and diffusion is generally non-trivial. For example, it is well known that a small amount of vertical diffusion (**Term IV**) occurring in a strongly sheared current (**Term I**) can lead to "shear dispersion" (Fischer *et al.* 1979, Chapter 4; Hannah *et al.* 2006, Appendix B). This effect on transport occurs due to the interaction between **Terms I** and **IV**, and there are no cross-terms that represent these interactions typically included in **Equation 1.1**.

When modeling transport of the early life-stages of organisms (i.e., propagule particles), an important distinction is made between the "passive" nature of such particles and the nature of particles associated with biological phenomena (Franks 1992; Yamazaki 1993; Bradbury and Snelgrove 2001; Metaxas 2001; Levin 2006; Edwards *et al.* 2007; Metaxas and Saunders 2009; Okubo and Levin 2010; Allen *et al.* 2018). "Passive" implies that the characteristics of the particles do not change over time (i.e., essentially inert) and that they move solely due to physical processes (i.e., transport). This is modeled by **Equation 1.1** and it can be referred to as the "biological null model." The concept of transport in **Equation 1.1** can also be extended to cover a wide range of biological processes. Behavior, primarily vertical movement due to swimming and (or) changes in buoyancy, can be modeled by adding a biological component to the advective velocity (u, w) terms. Further, reproduction can be modeled by adding a term of the form RC, where R is a recruitment rate, while mortality can be modeled by subtracting a term of the form MC, where M is a mortality rate. There are many examples in the literature (e.g., Hill 1990; Lynch *et al.* 1998; James *et al.* 2002; Byers and Pringle 2006; Guizien *et al.* 2006; Fiksen *et al.* 2007; North *et al.* 2008; Xue *et al.* 2008; Incze *et al.* 2010; Savina *et al.* 2010; Wolanski and Kingsford 2014) of how this might be achieved in all its biophysical complexity, including the use of other terms not discussed here.

1.3 Scope and Objectives

In this thesis, I focus on the biological null model; i.e., the transport of passive particles. In doing so, I use a combination of theory, hydrodynamic models of varying complexity, and observations. Although I identify the dominant physical processes giving rise to transport, I do not attempt to divide transport among its various contributing physical mechanisms. The overarching argument throughout this thesis is that until the null model can be validated, the veracity of results stemming from the inclusion of biological processes in assessing dispersal remains uncertain.

The goal of this thesis is to empirically quantify the dispersal of purely passive particles at the scale of early-stage planktonic organisms (days to weeks, 1 to 100 km) in the near-surface upper mixed layer of coastal ocean and lake environments using a new technology. To accomplish this goal, I further developed a magnetically attractive particle (MAP) and magnetic-collector prototype technology system (Ruddick and Taggart 2006, 2011) that provides a time-integrated estimate of dispersal from a given source location to a large set of potential sink locations. This technology, conceived by C.T. Taggart and enhanced by B.R. Ruddick and me, provides time-integrated estimates of the purely passive component of dispersal; i.e., the biological null model. I also aim to qualitatively and quantitatively compare observed passive particle dispersal to similar estimates derived from various hydrodynamic models and drogued drifters. Finally, I discuss the results from each study in the context of issues surrounding commercially valuable and (or) invasive species, as well as the potential concerns and implications when using the various technologies to quantify dispersal.

1.4 Thesis Structure

My thesis is divided into six Chapters, including this general Introduction (**Chapter 1**), and three Appendices. In **Chapters 2** through **6**, I address the objectives above. Aside from **Chapter 2**, each Chapter has been designed as a stand-alone manuscript to be submitted for primary publication. The reader is thus forewarned that parts of this

Introduction and subsequent Chapters contain some repetition. In **Chapter 2**, I outline the MAP and magnetic-collector technology system used to measure dispersal in all of the subsequent Chapters. I also explicitly detail how the MAP data are used to estimate dispersal kernels. In **Chapter 3**, I employ the MAP system to empirically estimate dispersal in the coastal ocean of the eastern Northumberland Strait, Prince Edward Island, Canada. The dispersal estimates achieved through the use of the MAP system are compared to similar estimates obtained through simulations derived from a hydrodynamic model. In particular, my results emphasize model sensitivity to variation in the assumed small-scale diffusivity value. In **Chapter 4**, I extend the work in **Chapter 3** to include four additional empirical studies in the Northumberland Strait, where I determine how well the scale of dispersal estimated in **Chapter 3** (a single realization) is representative of the entire region at different locations and times (multiple realizations). I also complete another model comparison with one of these studies as in **Chapter 3**. In **Chapter 5**, I empirically estimate dispersal in a small, shallow lake in the Huron–Erie Great Lakes Corridor using the MAP system and concurrently deployed drogued drifters. In this Chapter, I use the observed spatial patterns of dispersal to create a simple drifter-based Gaussian diffusion model that allows a comparison between empirical and modeled MAP results at corresponding locations, similar to that achieved in **Chapters 3** and **4**. In **Chapter 6**, I synthesize the findings of my research. All Supplementary Figures and Tables corresponding to **Chapters 3**, **4**, and **5** are provided in **Appendices A**, **B**, and **C**, respectively.

At the time of submission, several parts of this thesis have been published and presented at conferences, meetings, and workshops. The majority of **Chapters 2** and **3** are published in Hrycik *et al.* (2013)[1]. I was responsible for the advanced development of the MAP and magnetic-collector technology and all methodologies related to data collection, processing, and analyses, as well as the interpretations and implications of the results. I conducted the majority of the analyses and prepared the manuscript with various contributions from all authors. J. Chassé was responsible for all model simulations (i.e., virtual particles) that I used in the MAP and model comparisons. Additionally, some content in **Chapters 2** and **3** formed the basis of an article[2] that I published in *Current Tides*, the Dalhousie University Department of Oceanography Research Magazine. Various aspects of **Chapters 2** and **3** were presented at the American Society of Limnology and Oceanography Summer Meeting (Sante Fe, New Mexico, USA, 2010). Various aspects of **Chapters 2**, **3**, and **4** were presented at the Conference of Dalhousie Oceanography Graduate Students (Halifax, Nova Scotia, Canada, 2011), the Northumberland Strait Ecosystem Research Initiative Workshop (Moncton, New Brunswick, Canada, 2011), the Canadian Healthy Oceans Network (CHONe) Conference (Montréal, Québec, Canada, 2011), the Department of Fisheries and Oceans Gulf Fisheries Centre (Moncton, New Brunswick, Canada, 2011), the 65th Canadian Conference for Fisheries Research (Moncton, New Brunswick, Canada, 2012), and the Lagrangian Analysis and Prediction of Coastal and Ocean Dynamics (LAPCOD) V Meeting (Miami Beach, Florida, USA, 2012). Various aspects of **Chapters 2**, **3**, **4**, and **5** were presented at the Ocean Sciences Meeting (Honolulu, Hawaii, USA, 2014) and

---

[1] Hrycik, J.M., Chassé, J., Ruddick, B.R., and Taggart, C.T. 2013. Dispersal kernel estimation: A comparison of empirical and modeled particle dispersion in a coastal marine system. *Estuarine, Coastal, and Shelf Science* **133**, 11-22. doi: 10.1016/j.ecss.2013.06.023

[2] Hrycik, J.M. 2013. MAP-ing where things go: New technology to measure dispersal in the coastal ocean. *Current Tides* **1**, 8-11.

the Canadian Meteorological and Oceanographic Society (CMOS) Congress (Halifax, Nova Scotia, Canada 2018).

Chapter 2

The magnetically attractive particle (MAP) and magnetic-collector technology system

Empirically measuring aquatic dispersal and estimating dispersal kernels

The reader is advised that portions of this Chapter are included in subsequent Chapters and is published in:

Hrycik, J.M., Chassé, J., Ruddick, B.R., and Taggart, C.T. 2013. Dispersal kernel estimation: A comparison of empirical and modeled particle dispersion in a coastal marine system. *Estuarine, Coastal and Shelf Science* **133**, 11-22. doi: 10.1016/j.ecss.2013.06.023

2.1 Introduction

In any fluid system, scientists are interested in answering the following questions:

1. Where do "things" (e.g., particles) come from?
2. **Where do they go?**
3. How are they mixed?
4. **What are the time and space scales?**
5. **How do we model it?**
6. **Can we validate the models?**

Some of the most frequently employed technologies to answer these questions include the use of conventional drifters, dye, and numerical models; however, there are well-known limitations associated with each of these methods. Lagrangian drifters can become costly if in large numbers and must be continuously monitored (tracked) over the study period. When a study is complete, recovery can also become expensive, and costs increase with the scale of drifter dispersal. Most importantly, they do not behave at a particle (i.e., egg or larval) scale and are thus unsuitable for tracing particles. While dye can be traced in the near-field, it quickly becomes too dilute to measure with increasing space and time scales. It is virtually impossible to survey the dispersal field in all places and at all times, and attempting to do so also increases the costs with the scale of the dispersal field; this is especially true with the use of expensive monitoring equipment and ship survey time that requires thousands of dollars per day in large, open systems. As is the case with drifters, dye is inappropriate for tracing particles since it is dissolved in the water column and therefore disperses differently than particles. Numerical models are extensively used in a dispersal and connectivity context and are often the basis of management and conservation decisions; however, some model parameters are unknown, assumed, or poorly (empirically) estimated. From a particle-tracing perspective, they are rarely tested and (or) validated in a particle-tracing mode (Hitchcock and Cowen 2007; Lumpkin and Pazos 2007; Olson 2007; Pineda *et al.* 2007; Rossby 2007; Werner *et al.* 2007; Ruddick and Taggart 2011; Putnam and He 2013; Pineda and Reyns 2018). To surmount some of these challenges, I use a new technology – magnetically attractive particles (MAPs) – to address **Questions 2** and **4** through **6** above throughout the remainder of this thesis.

2.2 Magnetically attractive particles (MAPs) and magnetic-collector arrays

The MAPs are composed of hollow glass (SiO_2) microspheres that provide buoyancy, magnetite (Fe_3O_4) that provides magnetic attraction and mass, and a food-safe epoxy resin that acts as a binding agent. The particles are ideally designed to be spherical, in the 100 to 500 μm equivalent spherical diameter (esd) size range (see example in **Fig. 2.1**), and with a specific gravity (SG) of 1.00 for freshwater-applications or a SG designed to match *in situ* surface layer density (nominally 1.02) for marine-applications.

The MAPs were manufactured under contract by MicroPhase Coatings, Inc. (Garner, North Carolina, USA) in batches of 5 to 10 kg with specifications of 1) an average rise rate of less than 4 mm s^{-1} in water with a SG of 1.00, 2) size-sorted within the 200 to 500 μm esd size range, and 3) a target density such that no more than 10% of MAPs float in water with a SG of 1.00 and no more than 10% of MAPs sink out of the surface layer in water with a SG of 1.02. This design allows the MAPs to mimic passive propagules suspended in the near-surface mixed layer of a given density (**Fig. 2.2**). When manufactured with color additives (i.e., dyes or pigments), the MAPs can be used in multiple-release tracer studies (e.g., **Chapter 5**). Each batch of MAPs underwent extensive quality control testing in the laboratory to determine magnetic attraction, rise rate, and density and size distributions before deemed acceptable for use in a field study. If it was discovered during quality control testing that a given batch of MAPs did not conform to the target density specifications detailed above, the batch underwent treatment to remove those that sunk out of the surface layer in water with the desired density (see **Table 2.1**). Remaining MAPs were then oven-dried prior to release in the field.

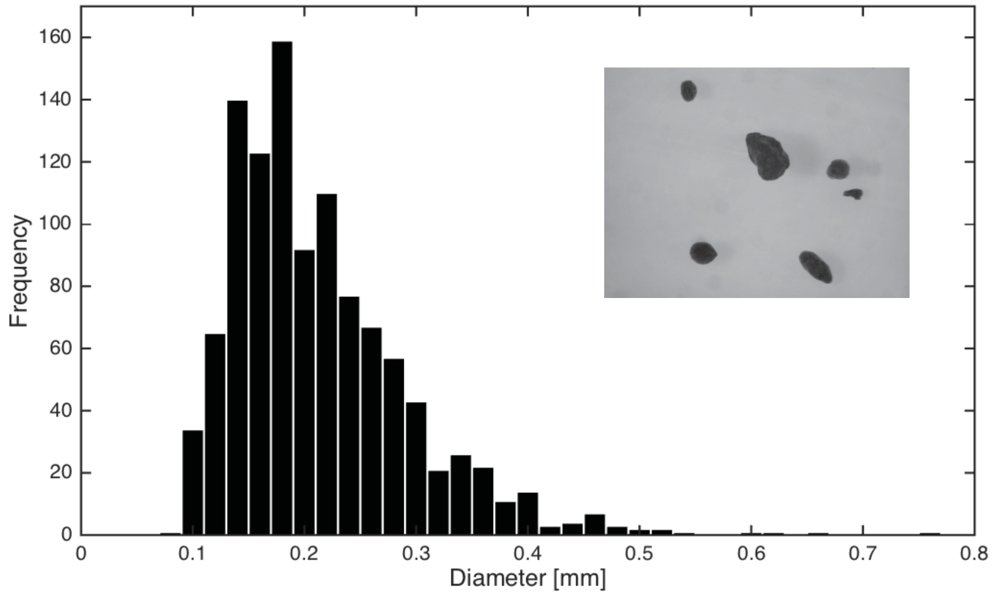

Figure 2.1 Size frequency histogram distribution of a haphazardly selected subsample (*n* = 1090) of magnetically attractive particles (MAPs) released within Murray Harbour during the particle tracing study detailed in **Chapter 3**. The inset provides a plan-view image of MAPs drawn from the size distribution.

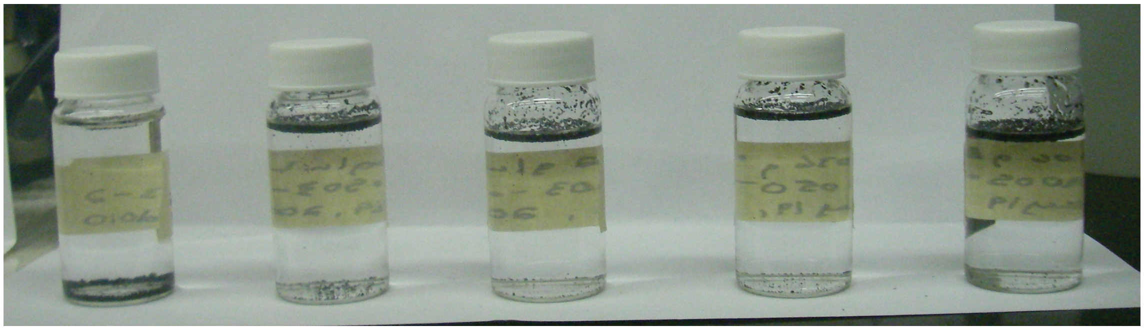

Figure 2.2 Illustration of one batch of magnetically attractive particles (MAPs) undergoing density distribution quality control testing in waters (left to right) with a SG of 1.00, 1.01, 1.02, 1.036, and 1.06 after 5 d. This batch had a target SG of 1.02 and was later released during the 2010 studies detailed in **Chapter 4**.

Table 2.1 Summary of magnetically attractive particle (MAP) batches used throughout this thesis, indicating the batch numbers with treatment ("x" if applicable; as detailed in text), the field study where that batch was released, the number of collectors both deployed and recovered (parentheses) in that field study, and the corresponding thesis Chapter.

MAP Batch	Treatment	Field Study	Collectors	**Chapter**
20090311	N/A	Cape Tormentine	40 (33)	**4**
20090311-floaters	x	Murray Harbour	46 (40)	**3**
20100503-1	N/A	Shediac	58 (56)	**4**
20100503-2	N/A	Shediac	58 (56)	**4**
20100514-1	N/A	Shediac	58 (56)	**4**
20100514-2	N/A	St. George's Bay	70 (69)	**4**
20100514-3	N/A	St. George's Bay	70 (69)	**4**
20100514-4	N/A	Cape George	60 (60)	**4**
20100514-5	N/A	Cape George	60 (60)	**4**
20090625-G	N/A	Lake St. Clair	30 (20)	**5**
20090625-Y	N/A	Lake St. Clair	30 (20)	**5**

All batches used in this thesis were sent for toxicity assay and assessment where each MAP formulation was evaluated among rainbow trout (*Oncorhynchus mykiss*) gill, liver, and spleen cell lines for any potential effects on cell viability. Across an 80-fold range of MAP exposure dose and up to four days post-exposure, MAPs did not induce any significant morphological changes or adverse toxicological effects on any cell line (Lee 2010). Additionally, MAPs were released only when environmentally sound permitting by governing agencies was obtained. In the field preceding release, all batches were treated with dilute Triton® X-100, a non-ionic surfactant that prevented MAP clumping once they were mixed in water of *in situ* density. It should be noted that all MAPs eventually degrade to their silica and magnetite components.

The MAPs are one component of a system (Ruddick and Taggart 2006, 2011) that, when coupled with a moored magnetic-collector array, allows the direct measurement of particle transport within the array domain. The magnetic-collectors are passive samplers designed to float near the surface and vane into the current such that any MAP suspended in the near-surface layer that flows through a collector will be captured (**Fig. 2.3**). Flume studies demonstrated a greater than 90% probability of MAP capture when passing through a collector at flow speeds less than 0.8 to 1.0 m s^{-1} (Benaroya 2012). The rectangular collector tube is nominally 35 cm long with a square aperture in which the leading end is fitted with strong rare-earth magnets encased within plastic tubes. The collectors used in these studies were composed of two superimposed tubes, one near-surface and one below surface, each fitted with four magnet tubes and each tube containing two magnets (**Fig. 2.3**). The total aperture area was 86.45 cm^2. The polar

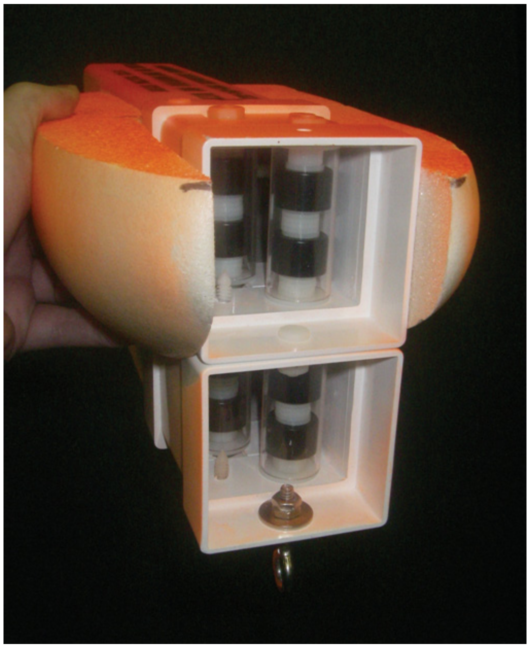

Figure 2.3 Leading-end aperture image of a magnetic-collector designed to capture near-surface and sub-surface magnetically attractive particles (MAPs). Rare-earth magnets within their encasement tubes are located within the aperture, floatation nacelles are attached to the upper tube, and the mooring attachment is located on the lower tube.

orientation of the magnets within and between the two tubes was designed to maximize the magnetic field for particle capture. In all studies, the moored collector arrays were designed according to deployment and recovery logistics. In **Chapters 3** and **4**, the collector arrays were additionally informed by using expected winds for the time of year within the hydrodynamic model running in virtual particle tracing mode (as detailed in **Chapter 3**). Collectors were deployed prior to the start of a study and following a point-source release of MAPs and their transport over a given period, the magnetic-collectors were recovered and the particles captured by the magnets were enumerated.

Upon retrieval, each magnet tube was removed from each collector and stripped of captured MAPs that were then placed in a counting cell and imaged from above (e.g., **Fig. 2.1 inset**). In **Chapter 5**, the counting cells were imaged under ultraviolet (UV) light to 1) separate the pigmented MAPs from the abundant biological matter that coated the magnet tubes, and 2) distinguish the two different pigmented MAPs from each other. The total area (mm^2) of MAPs in each calibrated image was measured using SigmaScan Pro (Version 5.0). In **Chapters 4** and **5**, MAP estimates are reported as the total area (mm^2) of particles captured by each collector. In **Chapter 3**, the imaged-area (mm^2) of MAPs captured by each collector was converted to a particle number estimate (N_{MAP}) by dividing the imaged-area by the area of a single MAP, assuming the median diameter of the batch used in that study. For simplicity in **Section 2.3** below, N is used as a proxy for MAP area.

The advantage of this system lies in its ability to time-integrate the transport of MAPs through the magnetic-collector array over various time (days to weeks) and space (1 to 100 km) scales, and thus the capacity to measure long-range dispersal. When large numbers (order 10^9) are used, the MAPs function as passive particle tracers, where the release point represents a source location and the magnetic-collector array represents sink locations within the potential dispersal domain. In summary, the system makes use of billions of particle drifters that can be used to estimate dispersal parameters (**Chapters 3**, **4**, and **5**) and to make direct comparisons with similar virtual particle (VP) dispersal estimates provided by both a simple drifter-based Gaussian diffusion model (**Chapter 5**) and a 3D prognostic hydrodynamic modeling system (**Chapters 3** and **4**).

2.3 Estimating dispersal kernels

Considering the magnetic-collectors as "nets" that capture passing particles, the observed number (*N*) of MAPs at a location (*x*) of a given magnetic-collector can each be considered generically as

$$N = A \int_{t_0}^{t_0+T} C(x,t) \cdot u(x,t) \cdot \mathrm{d}t, \tag{2.1}$$

where A is the aperture area of a collector at x, C is the concentration of MAPs at x, u is the horizontal flow velocity through a collector at x, t_0 is the time of release, and T is the integration period (the post-release collection duration).

While **Equation 2.1** expresses the MAP captures at each spatial (magnetic-collector) location, the observations can be used to obtain a probability density function that can be considered an estimate of the dispersal kernel. The resulting estimates are equivalent to sampling the two-dimensional dispersal kernel at a finite number of locations over a given sampling period T and its associated environmental conditions. There may be variability associated with, for example, the tidal cycles and (or) variable winds, and replicate releases or a long-term steady release would be required to obtain an ensemble and (or) a time-averaged dispersal kernel.

Although dispersal is typically two-dimensional, heterogeneous, and anisotropic (Gawarkiewicz *et al.* 2007), preliminary analyses indicated that N_{MAP} was primarily a function of in-water distance L between the source and the collector locations, allowing the estimation of a greatly simplified single-variable dispersal kernel (e.g., Gerrodette 1981). In this thesis, the estimates of the observed number (N) of MAPs are presented in a semi-log manner ($\log_e N$ as a function of L) and consistent with the linear relation $\log_e N = b - aL$. The linear relation is equivalent to an exponential function, $n(L) = e^b \cdot e^{-aL}$, where n represents the observed number of MAPs at distance L, with an e-folding scale of a^{-1}. In the following Chapters, the e-folding scale is simply the length scale where $n(L)$ decreases by a factor of e.

I define the dispersal kernel $p(r,\theta;\ t)$ as the probability density function describing the spatial distribution of particles relative to a source location (e.g., Clark *et al.* 1998; Nathan *et al.* 2008). For the sake of definitiveness, $p(r,\theta;\ t)$ is the probability density function (units m^{-2}) of a particle that is released at $r = 0$, $t = 0$ at any position (r,θ) and later time t, where r and θ are the radial and azimuthal coordinates, respectively, in the two-dimensional horizontal plane. I wish to estimate the dispersal kernel p from the observation of MAP integrated capture numbers that are approximated as $n(L) = e^{b} \cdot e^{-aL}$. If I consider p to be a radially symmetric function, and ignore the subtlety that the domain may include land, then I can take the in-water distance L as equivalent to radius. I denote $P(r \geq L;T)$ as the probability that a particle is located at a distance L or greater from the release point at time T, so that

$$P(r \geq L; T) = \int_{L}^{\infty} r\,\mathrm{d}r \int_{0}^{2\pi} \mathrm{d}\theta\, p(r, \theta; T), \tag{2.2}$$

where P on the left is the probability that I can estimate using the data and p on the right is the probability density function (i.e., the dispersal kernel) that I want to determine. I assume a radially symmetric distribution and that I can estimate the left hand side of **Equation 2.2** functionally by

$$P(L) \equiv P(r \geq L; T) \approx \frac{n(L)}{N_{eff}}, \tag{2.3}$$

where $n(L)$ is the regression formula for the fit to N_{MAP} that is $n(L) = e^{b} \cdot e^{-aL}$ and N_{eff} is the “effective” number of MAPs in the dispersal domain and is essentially unknown; however, I can rearrange **Equation 2.3** to

$$P(L) = \left(\frac{e^{b}}{N_{eff}}\right) e^{-aL}, \tag{2.4}$$

where the rational coefficient is a constant. I require that $P(L = 0) = 1$, which is the same as $P(r \geq 0;T) = 1$; i.e., the probability of a particle being somewhere is equal to 1, and thus

$$\left(\frac{e^{b}}{N_{eff}}\right) = 1. \tag{2.5}$$

I use **Equation 2.5** as opposed to the regression coefficient b and the actual number of MAPs (N_{MAPR}) released because N_{MAPR} is not necessarily the number of MAPs available for capture within the dispersal domain. Thus, I have

$$P(L) \equiv P(r \ \geq L; T) \approx \ e^{-aL}. \tag{2.6}$$

Substituting **Equation 2.6** into **Equation 2.2** yields

$$e^{-aL} \ = \int_{L}^{\infty} r \, \mathrm{d}r \int_{0}^{2\pi} \mathrm{d}\theta \, p(r, \theta; T), \tag{2.7}$$

and as I am assuming p is radially symmetric, then $p(r,\theta;\ T) = p(r;\ T)$, and **Equation 2.7** becomes

$$e^{-aL} \ = \ 2\pi \int_{L}^{\infty} r \, p(r; T) \, \mathrm{d}r, \tag{2.8}$$

Taking the derivative of both sides of **Equation 2.8** with respect to L gives

$$\frac{\mathrm{d}}{\mathrm{d}L}(e^{-aL}) = \ 2\pi \ \frac{\mathrm{d}}{\mathrm{d}L} (\int_{L}^{\infty} r \, p \, (r; T) \, \mathrm{d}r). \tag{2.9}$$

and

$$-ae^{-aL} = 2\pi\big(-L \, p(L; T)\big). \tag{2.10}$$

Solving **Equation 2.10** for p and multiplying both sides by $2\pi L$ gives an observational estimate of the dispersal kernel:

$$2\pi L \, p(L; T) = \ ae^{-aL}. \tag{2.11}$$

Fitting to an exponential function and normalizing in this manner has three advantages: first, the simple form with a single parameter (a) is conceptually and analytically useful while retaining accuracy; second, the paucity of observations in the large-distance "tail" of the distribution does not significantly affect the estimation of the dispersal kernel; and third, the analytic function allows estimation of expected results for locations that were not experimentally sampled. Note that the method above can be applied to any function of in-water distance, not just an exponential.

In the following Chapters I plot $2\pi L \cdot p(L)$ rather than $p(L)$ because the probability of dispersal from the source ($L = 0$) to all distances within a specific distance D is given by $\int_0^D 2\pi L\, p(L)\, \mathrm{d}L$, where the quantity $2\pi L\ p(L)$ is also known as the "dispersal distance kernel" – the probability density function of distance traveled from the source, regardless of direction (Nathan 2006; Nathan *et al.* 2008; Nathan *et al.* 2012). The dispersal kernel has an implicit dependence on time T; i.e., it represents an estimate arising from the environmental conditions present during the study period, and will depend on the timing and duration of the experiment.

2.4 Advantages of the MAP and magnetic-collector technology system

The MAP and magnetic-collector technology system overcomes many of the issues associated with conventional tracing technologies while providing a direct quantitative measure of dispersal. MAPs are relatively inexpensive, do not degrade easily, and can be designed to a specified density, shape, and size. Mixtures from different release-sources can be identified (e.g., **Chapter 5**), and MAPs can be collected at large spatial scales and over long time periods using the simple magnetic-collector technology. A single MAP experiment in a given area has proven to be valuable in testing the Lagrangian predictive capabilities of a model (e.g., **Chapters 3** and **4**), and the model can subsequently be improved and used with greater confidence to conduct complementary dispersal studies.

This system is capable of addressing a plethora of issues, including the dispersal of invasive species, eggs, and larvae, as well as the dispersal of propagules in aquaculture and at deep-sea vents. Besides these biological motives, there is also potential for the MAPs to mimic sediment transport (e.g., Benaroya 2012) and the tracing of contaminants, effluent, and (or) river plumes, in addition to sewer, storm-water, floc, produced water (e.g., Ruddick and Taggart 2011), and erosion tracing. The following Chapters utilize the MAP and magnetic-collector technology system to empirically examine dispersal in the context of just a few of the issues mentioned above.

Chapter 3

A comparison of empirical and modeled particle dispersal in a coastal marine system

Dispersal in the eastern Northumberland Strait, Canada

The reader is advised that the majority of this Chapter is published in:

Hrycik, J.M., Chassé, J., Ruddick, B.R., and Taggart, C.T. 2013. Dispersal kernel estimation: a comparison of empirical and modeled particle dispersion in a coastal marine system. *Estuarine, Coastal and Shelf Science* **133**, 11-22. doi: 10.1016/j.ecss.2013.06.023

3.1 Introduction

Early life-stage dispersal influences recruitment in both terrestrial and aquatic species, is a widespread characteristic that spans taxonomic groups, and is especially exhibited by aquatic vertebrates and invertebrates, terrestrial invertebrates, and aquatic and terrestrial plants. It is a fundamental process that contributes to variation in the abundance and distribution of a species (Clobert *et al.* 2001; Kinlan and Gaines 2003; Bowler and Benton 2005; Begon *et al.* 2006; Nathan 2006; Mattysen 2012; Allen *et al.* 2018). Biological dispersal refers to the spread of individuals away from a source location through passive and (or) active means (e.g., Begon *et al.* 2006; Levin 2006), where the passive component is especially important within a fluid such as air or water. Dispersal affects population dynamics (e.g., the distribution of individuals and ultimately reproduction and recruitment), population genetics (e.g., gene flow), and thus the spatial scale of population connectivity through the exchange of individuals among geographically separated subpopulations (Clobert *et al.* 2001; Kinlan and Gaines 2003; Bowler and Benton 2005; Begon *et al.* 2006; Nathan 2006; Matthysen 2012; Allen *et al.* 2018). Dispersal is often defined in terms of the dispersal kernel, the function that describes the probability of a particle or propagule moving from some source location to all other locations (Clark *et al.* 1998; Siegel *et al.* 2003; Nathan 2006; Cowen *et al.* 2007; Gawarkiewicz *et al.* 2007; Nathan *et al.* 2008; Nathan *et al.* 2012).

The significance of dispersal in explaining the ecology (i.e., abundance and distribution) of marine species has been recognized for at least a century (Hjort 1914). Marine species exchange individuals, and subsequently genes, among subpopulations mainly through larval dispersal (Scheltema 1986; Metaxas 2001; Kinlan and Gaines 2003; Sale *et al.* 2005; Treml *et al.* 2008; Metaxas and Saunders 2009; Allen *et al.* 2018); however, the dominant scales of dispersal in the ocean are still “not known” (Pineda *et al.* 2007) and thus the knowledge of how marine populations are connected in space and time is thus limited (Palmer and Strathmann 1981; Franks 1992; Bradbury and Snelgrove 2001; Largier 2003; Siegel *et al.* 2003; Kinlan *et al.* 2005; Byers and Pringle 2006; Cowen *et al.* 2006; 2007; Levin 2006; Edwards *et al.* 2007; Pineda *et al.* 2007; Kool *et al.* 2013; Pineda and Reyns 2018). The extent of early life-stage dispersal is dependent on physical (e.g., advection and diffusion) and biological (e.g., reproduction, behavior, and mortality) processes, and interactions among these physical and biological processes makes distinguishing their effects on dispersal challenging (most authors cited above).

Motivations to study and quantify dispersal and connectivity now include the sustainable management of commercially valuable and (or) endangered species, the mitigation of threats of invasive species, the conservation of biodiversity through the design of marine reserves, the prediction of species response to climate change, and the evaluation of the impact of contaminants (Kinlan *et al.* 2005; Cowen *et al.* 2006; Levin 2006; Aiken *et al.* 2007; Becker *et al.* 2007). For example, one of the main factors driving the design and implementation of Marine Protected Areas (MPAs) should be the degree of connectivity among local populations of a species that need protection. With appropriate data on larval dispersal it should be possible to adjust reserve size, placement, and spacing to achieve specific management objectives (Largier 2003; Palumbi 2003; Shanks *et al.* 2003; Sale *et al.* 2005; Kaplan 2006; Cowen *et al.* 2007; Fogarty and Botsford 2007; Jones *et al.* 2007; Treml *et al.* 2008; Botsford et al. 2009; Planes *et al.* 2009; Costello et al. 2010; Gaines *et al.* 2010; Green *et al.* 2015; Krueck *et al.* 2017). Further, empirical estimates of dispersal are necessary to guide numerical modeling studies that are often the basis of management and conservation decisions. Robust measurements of dispersal in the marine environment are rare (e.g., D'Aloia *et al.* 2015), and when they are obtained they must be used to test the assumptions and hypotheses related to such models and to strengthen model capabilities and associated inferences (Thorrold *et al.* 2002; Largier 2003; Siegel *et al.* 2003; Cowen *et al.* 2006; Kaplan 2006; Nathan 2006; Aiken *et al.* 2007; Pineda *et al.* 2007; Werner *et al.* 2007; Cowen and Sponaugle 2009; Metaxas and

Saunders 2009; Rasmussen *et al.* 2009; Okubo and Levin 2010; Sponaugle *et al.* 2012; Nickols *et al.* 2015; Almany *et al.* 2017; Krueck *et al.* 2017; Pineda and Reyns 2018).

In this Chapter I provide a direct measure of particle dispersal in the Northumberland Strait region of the southern Gulf of St. Lawrence and make a direct comparison to dispersal estimates provided by hydrodynamic modeling of the same region. I do so through the use of an advanced technology system that can address and overcome many of the issues associated with conventional tracing technologies (e.g., drifters, dye, and numerical models) frequently employed in the study of dispersal (**Chapter 2**; Ruddick and Taggart 2006, 2011). The system uses magnetically attractive particles (MAPs) and a moored magnetic-collector array that allows me to quantify the passive component of the dispersal kernel in the near-surface mixed layer at the scale of dispersing early-stage planktonic organisms (days to weeks, 1 to 100 km), thereby providing the biological null model of larval dispersal. The weak buoyancy and slow rise rate designed in the MAPs provide important properties that allow them to mimic weakly buoyant, passive propagules. Further, as the passive component of connectivity is driven by advective and diffusive processes, knowledge of the dispersal kernel allows the degree of passive connectivity in space and time to be readily estimated for a defined region.

Given the ubiquitous use of dispersal and connectivity estimates that are based on numerical models, it is exceptionally important to compare the MAP results with similar results provided by an existing high-resolution hydrodynamic model designed for the study area that computes Lagrangian trajectories. In addition to achieving a direct model comparison, assessment, and possible improvement, I perform sensitivity tests related to the variation of a key but generally not well-quantified parameter; small-scale diffusivity. Environmental conditions during MAP experiments vary in an uncontrolled manner such that there will always be unanswered questions about dispersal in conditions different from those present for any given experiment. The advantage of comparing MAP results with model results, under the same conditions, is that the model predictions can be extrapolated to determine the effects of different environmental conditions (e.g., winds, tidal cycle) on dispersal estimates. Only when this is achieved can the biological influences (e.g., behavior, mortality) on dispersal be confidently incorporated and assessed when using such models.

3.2 Methods

3.2.1 Study site

This particle dispersal study was conducted in the eastern Northumberland Strait (**Fig. 3.1**) in August 2009. The Strait is nominally 20 to 30 km wide, 30 to 40 m deep at mid-channel, and separates eastern New Brunswick (NB) and Nova Scotia (NS) from Prince Edward Island (PE). Residual flow through the Strait is normally west to east with a net flow of the order kilometers per day (Lauzier 1965). Particles (detailed in **Chapter 2** and briefly summarized below) were released inside Murray Harbour, PE and the particle collector array (also detailed in **Chapter 2** and briefly summarized below) was deployed from inside the Harbour and out into the eastern Strait; a region that is dynamic and tidally-active and where currents can reach 1.5 m s^{-1}, particularly along the Murray Head

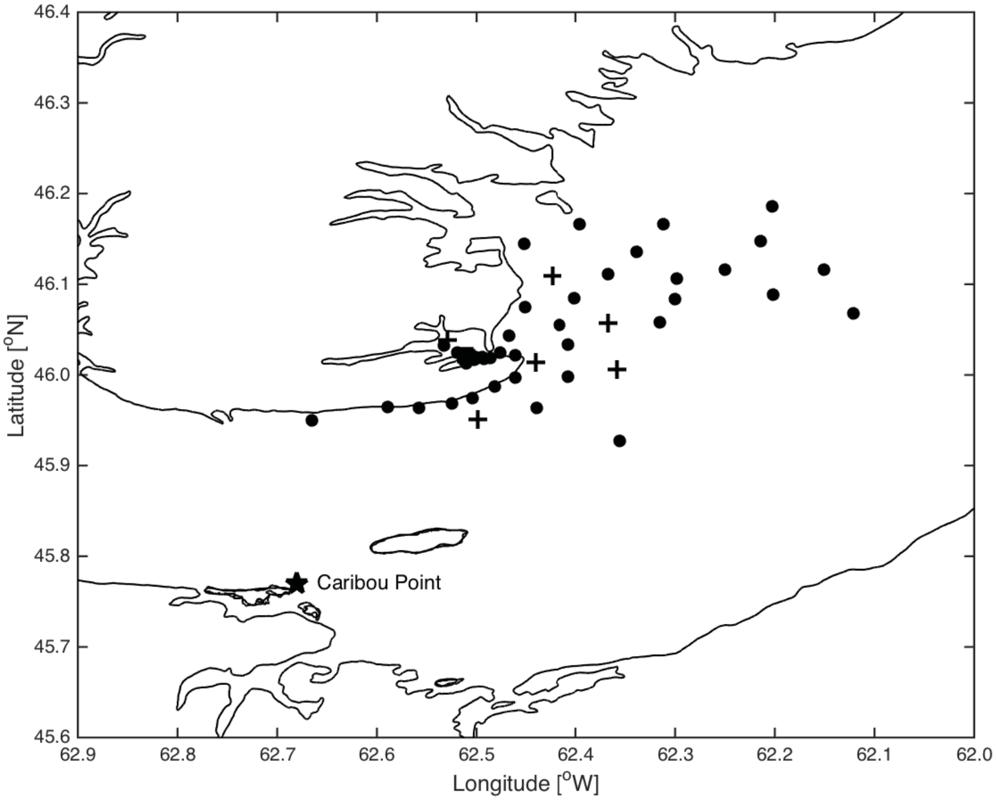

Figure 3.1 Coastline chart of the eastern Northumberland Strait between Prince Edward Island and Nova Scotia illustrating the locations of recovered (filled circles) and unrecovered (crosses) collectors. The dense group of collectors within Murray Harbour also represents the MAP source location. The location of Caribou Point, where wind speed and direction were recorded, is indicated with a star.

peninsula. There were variable winds during the study, including the passage of Hurricane Bill through the region two days post-release. **Figure A.1** illustrates the cyclonic expression of Hurricane Bill and the evolution of the wind-driven surface-drift velocity that was estimated as three percent of the wind velocity (Csanady 1982). Wind speed and direction were recorded hourly at Caribou Point, NS (Environment and Climate Change Canada, Historical Data Archive), on the south side of the Strait (see **Fig. 3.1**). Detailed variations in the wind field velocity components (u, v) over the deployment period are provided in **Figure A.2**.

3.2.2 Summary of the MAP and magnetic-collector array technology system

*The reader is advised that a more detailed description of the MAP and magnetic-collector array technology system is provided in **Chapter 2**.*

The MAPs are composed of hollow glass (SiO_2) microspheres that provide buoyancy, magnetite (Fe_3O_4) that provides magnetic attraction and mass, and a food-safe epoxy resin that acts as a binding agent. The particles are ideally designed to be spherical, in the 100 to 500 μm equivalent spherical diameter (esd) size range, and with a specific gravity (SG) designed to match *in situ* surface layer density; a nominal specific gravity (SG) of 1.02 for marine-applications. In this study, the MAPs had a median esd of 195 μm and a geometric mean esd of 200 μm (**Fig. A.3**), a nominal SG of 1.02, and an average rise rate of 1 to 4 mm s^{-1} in water with a SG of 1.02. The MAPs are one component of a system (**Chapter 2**; Ruddick and Taggart 2006, 2011) that, when coupled with a moored magnetic-collector array, allows the direct measurement of particle dispersal within the array domain. The magnetic-collectors are passive samplers designed to float near the surface and vane into the current such that any MAP suspended in the near-surface layer that flows through a collector will be captured (**Fig. 2.3**). Collectors were deployed prior to the start of the study and following a point-source release of MAPs and their dispersal over a given period, the magnetic-collectors were recovered and the particles captured by the magnets were enumerated. This system essentially makes use of billions of particle drifters that can be used to estimate dispersal parameters and to make direct comparisons with similar virtual particle (VP) dispersal estimates provided by models.

3.2.3 Hydrodynamic modeling

I used a 3D prognostic hydrodynamic modeling system (Saucier and Chassé 2000; Chassé and Miller 2010) that incorporates a large-scale 4 km nominal-mesh model covering the entire Gulf of St. Lawrence region with a nested 200 x 200 m mesh model that envelops most of the Northumberland Strait (**Fig. A.4**). The low- and high-resolution models employ the same physics, though the time-stepping of the 4 km model is 5 minutes and that of the 200 m model is 30 seconds. The generic code of the model contains a Mellor-Yamada Level II Turbulence closure scheme, a free surface, and semi-implicit solution techniques. There are 32 depth layers (*z*-levels) in the 4 km model while the 200 m model is limited to 8 *z*-levels (due to the generally shallow depth of the Northumberland Strait) with a surface-layer thickness of 2 m. This hydrostatic model is forced by bulk-formula heat flux, density, tides (five primary constituents input at the boundaries of the 4 km model), observed winds (NOAA-CIRES Climate Diagnostics Center, NCEP), and observed runoff from the St. Lawrence River measured at Québec

City, as well as runoff from other rivers based on monthly climatology interpolated to the model time step. Temperature and salinity are initialized at the beginning of a simulation and are free to evolve with time under forcing. The model calculates horizontal eddy viscosities (K_H) using the parameterization of Smagorinsky (1963); i.e., it is dependent on mesh size and on calculated horizontal velocity shear. The calculated values are then used in the momentum and advection-diffusion equations. Thus, the calculated horizontal viscosities are not constant in time and a lower bound of 50 $m^2 s^{-1}$ is applied to the momentum equations to ensure the numerical stability of the model.

3.2.4 MAP dispersal

Approximately 30 kg ($\sim 7.4 \times 10^9$) of MAPs were released in the surface layer (0 to 0.5 m) at a distance of 0.25 km from the nearest shore in the main channel (6 m depth) of Murray Harbour over a 6 h period, centered 3 h either side of the local flood tide maximum at 10:48 h ADST on 21 August 2009. Subsamples of MAPs suspended in water of *in situ* density were monitored over the study (dispersal) period and the proportion that sunk out of what would have been the surface layer was accounted for in estimating the total number released. Magnetic-collectors had previously been deployed inside the Harbour and over a domain of ~700 km^2 located near the eastern entrance to the Northumberland Strait (**Fig. 3.1**). The moored collector array was designed according to deployment and recovery logistics and by using expected winds for the time of year when the hydrodynamic model was running in VP tracing mode (see below). A total of 46 collectors were deployed and 40 were recovered after a period of 5 to 7 d post-release. Upon retrieval, each magnet tube was removed from each collector and stripped of captured MAPs that were then placed in a counting cell and imaged from above. The total area (mm^2) of MAPs in each calibrated image was measured using SigmaScan Pro (Version 5.0). The imaged-area (mm^2) of MAPs captured by each collector was converted to a particle number estimate (N_{MAP}) by dividing the imaged-area by the area of a single MAP, assuming the median diameter of 195 μm (above).

3.2.5 VP dispersal

Estimating the dispersal of virtual particles (VPs) in the hydrodynamic model consisted of a point-source release of 1.92×10^5 VPs uniformly distributed throughout the 2 m surface layer in the same location in Murray Harbour, on the same date, and over the same 6 h release period as the MAP release. Corresponding model simulation results at 5, 6, and 7 d periods post-release were examined to match the same post-release periods associated with the magnetic-collector retrievals. The model accommodates neither "beaching" nor vertical rise nor sink of VPs. A small-scale diffusivity (K_p), achieved by a random walk of VPs, was employed to mimic the horizontal stirring processes that occur on scales smaller than the 200 m grid-scale model is able to resolve. I used constant K_p values of 0, 2, 5, and 25 $m^2 s^{-1}$ among several simulations, as well as minimum values of 50 and 80 $m^2 s^{-1}$, based on the Smagorinsky (1963) formulations that provide high eddy viscosity values only in areas of very high horizontal shear. Thus, K_p rarely rises above the minimum K_H of 50 $m^2 s^{-1}$ used in solving the momentum equations. The model estimated the total number (N) of VPs drifting through each grid-cell by calculating an exposition number (E) for each grid-cell (i,j) over the post-release study period (5, 6, or 7 d). The sum of the number of individual (k) VPs passing through a cell was multiplied by the distance that each VP moved (Δm) over a time-step and was normalized by cell length (m) according to

$$E_{ij} = \sum_{k=1}^{Nij} \frac{\Delta m_k}{m} \tag{3.1}$$

3.2.6 MAP and VP comparisons

Considering the collectors and model grid-cells as "nets" that capture passing particles, the observed number (N) of MAPs or VPs at a location (x) of a given magnetic-collector and its corresponding grid-cell can each be considered generically as

$$N = A \int_{t_0}^{t_0+T} C(x,t) \cdot u(x,t) \cdot \mathrm{d}t, \tag{3.2}$$

where A is the aperture area of a collector or grid cell at x, C is the concentration of MAPs or VPs at x, u is the horizontal flow velocity through a collector or grid-cell at x, t_0 is the time of release, and T is the integration period (the post-release collection duration).

Following the net analogy, a magnetic-collector acts like a small stationary net that vanes into the flow with an aperture dimension of 13.3 x 6.5 cm and a model grid-cell as a similar net with a surface-layer grid-cell aperture dimension of 2 x 200 m. To compare the MAP collector results (N_{MAP}) with the model exposition results, E_{ij} was converted to number to account for the differences in the two measurements (number versus exposition; magnetic-collector aperture versus grid-cell aperture). Accordingly, virtual particle number (N_{VP}) from exposition in each grid-cell, E_{ij}, associated with each collector location was calculated as

$$N_{VP} = E_{ij} \cdot \frac{A_{coll}}{A_{cell}} \cdot \frac{N_{MAPR}}{N_{VPR}}, \tag{3.3}$$

where A_{coll} is the magnetic-collector aperture area, A_{cell} is the grid-cell aperture area, N_{MAPR} is the number of MAPs released at the point source in Murray Harbour, and N_{VPR} is the number of VPs released at the same location in the model. Each collector-specific N_{VP} estimate was based on the average N_{VP} of that collector-specific grid-cell N_{VP} and the eight surrounding grid-cell N_{VP} values. With the proportionality constants in **Equation 3.3**, the MAP estimates from the magnetic-collector system allow a direct comparison with the VP estimates from the model as they are essentially measuring the same thing – the time integral of particles passing through a location over time.

As none of the N_{MAP} and N_{VP} estimates were consistent with a normal distribution, they were logarithmically transformed to obtain distributions more consistent with normality for regression purposes. All uncertainties are presented as 95% confidence intervals.

3.2.7 Estimating dispersal kernels

While **Equation 3.2** expresses the MAP or VP captures at each spatial (magnetic-collector or grid-cell) location, the observations can be used to obtain a probability density function that can be considered an estimate of the dispersal kernel. The resulting estimates are equivalent to sampling the two-dimensional dispersal kernel at a finite number of locations over a given sampling period T and its associated environmental conditions. There may be variability associated with, for example, the tidal cycles and (or) variable winds, and replicate releases or a long-term steady release (or multiple model simulations) would be required to obtain an ensemble and (or) a time-averaged dispersal kernel.

Although dispersal is typically two-dimensional, heterogeneous, and anisotropic (Gawarkiewicz *et al.* 2007), preliminary analyses indicated that both N_{MAP} and N_{VP} were primarily a function of in-water distance L between the source and the collector (or grid-cell) locations, allowing estimation of a greatly simplified single-variable dispersal kernel (e.g., Gerrodette 1981). The estimates of the observed number (N) of MAPs or VPs are presented here in a semi-log manner ($\log_e N$ as a function of L) and consistent with the linear relation $\log_e N = b - aL$. The linear relation is equivalent to an exponential function, $n(L) = e^b \cdot e^{-aL}$, where n represents the observed number of MAPs or VPs at distance L, with an e-folding scale of a^{-1}. In this case the e-folding scale is simply the length scale where $n(L)$ decreases by a factor of e.

I define the dispersal kernel $p(r,\theta;\ t)$ as the probability density function describing the spatial distribution of particles (i.e., MAPs or VPs) originating at a source location (e.g., Clark *et al.* 1998; Nathan *et al.* 2008). For the sake of definitiveness, $p(r,\theta;\ t)$ is the probability density function (units m^{-2}) of a particle that is released at $r = 0$, $t = 0$ at any position (r,θ) and later time t, where r and θ are the radial and azimuthal coordinates, respectively, in the two-dimensional horizontal plane. I wish to estimate the dispersal kernel p from the observation of MAP or VP integrated capture numbers that are approximated as $n(L) = e^b \cdot e^{-aL}$. If I consider p to be a radially symmetric function, and ignore the subtlety that the domain includes land, then I can take the in-water distance L

as equivalent to radius. I denote $P(r \geq L;T)$ as the probability that a particle is located at a distance L or greater from the release point at time T, so that

$$P(r \geq L;T) = \int_{L}^{\infty} r\,\mathrm{d}r \int_{0}^{2\pi} \mathrm{d}\theta\, p(r,\theta;T), \tag{3.4}$$

where P on the left is the probability that I can estimate using the data and p on the right is the probability density function (i.e., the dispersal kernel) that I want to determine. I assume a radially symmetric distribution and that I can estimate the left hand side of **Equation 3.4** functionally by

$$P(L) \equiv P(r \geq L;T) \approx \frac{n(L)}{N_{eff}}, \tag{3.5}$$

where $n(L)$ is the regression formula for the fit to N_{MAP} or N_{VP} that is $n(L) = e^{b} \cdot e^{-aL}$ and N_{eff} is the "effective" number of MAPs or VPs in the dispersal domain and, particularly for MAPs, is essentially unknown (addressed further below in Discussion); however I can rearrange **Equation 3.5** to

$$P(L) = \left(\frac{e^{b}}{N_{eff}}\right) e^{-aL}, \tag{3.6}$$

where the rational coefficient is a constant. I require that $P(L = 0) = 1$, which is the same as $P(r \geq 0;T) = 1$; i.e., the probability of a particle being somewhere is equal to 1, and thus

$$\left(\frac{e^{b}}{N_{eff}}\right) = 1. \tag{3.7}$$

I use **Equation 3.7** as opposed to the regression coefficient b and the actual number of MAPs (N_{MAPR}) or VPs (N_{VPR}) released because N_{MAPR} is not necessarily the number of MAPs available for capture within the dispersal domain. Thus, I have

$$P(L) \equiv P(r \geq L; T) \approx e^{-aL}. \tag{3.8}$$

Substituting **Equation 3.8** into **Equation 3.4** yields

$$e^{-aL} = \int_{L}^{\infty} r \, \mathrm{d}r \int_{0}^{2\pi} \mathrm{d}\theta \, p(r, \theta; T), \tag{3.9}$$

and as I am assuming *p* is radially symmetric, then $p(r,\theta;\ T) = p(r;\ T)$, and **Equation 3.9** becomes

$$e^{-aL} = 2\pi \int_{L}^{\infty} r \, p(r; T) \, \mathrm{d}r. \tag{3.10}$$

Taking the derivative of both sides of **Equation 3.10** with respect to *L* gives

$$\frac{\mathrm{d}}{\mathrm{d}L}\left(e^{-aL}\right) = 2\pi \frac{\mathrm{d}}{\mathrm{d}L}\left(\int_{L}^{\infty} r \, p\,(r; T) \, \mathrm{d}r\right), \tag{3.11}$$

and

$$-ae^{-aL} = 2\pi\left(-L \, p(L; T)\right). \tag{3.12}$$

Solving **Equation 3.12** for *p* and multiplying both sides by $2\pi L$ gives an observational estimate of the dispersal kernel:

$$2\pi L \, p(L; T) = ae^{-aL}. \tag{3.13}$$

Fitting an exponential function and normalizing in this manner has three advantages: first, the simple form with a single parameter (*a*) is conceptually and analytically useful while retaining accuracy; second, the paucity of observations in the large-distance “tail” of the distribution does not significantly affect the estimation of the dispersal kernel; and third, the analytic function allows estimation of expected results for locations that were not experimentally sampled. Note that the method above can be applied to any function of in-water distance, not just an exponential.

In the results below I plot $2\pi L\cdot p(L)$ rather than $p(L)$ because the probability of dispersal from the source ($L = 0$) to all distances within a specific distance D is given by $\int_0^D 2\pi L\, p(L)\, \mathrm{d}L$, where the quantity $2\pi L\ p(L)$ is also known as the "dispersal distance kernel" – the probability density function of distance traveled from the source, regardless of direction (Nathan 2006; Nathan *et al.* 2008; Nathan *et al.* 2012). The dispersal kernel has an implicit dependence on time T; i.e., it represents an estimate arising from the environmental conditions present during the study period, and will depend on the timing and duration of the experiment.

3.3 Results

3.3.1 MAP dispersal

MAPs were captured by each of the 40 magnetic-collectors that were recovered 5 to 7 days post-release; i.e., there were no zero returns, though 6 collectors were not recovered (**Fig. 3.2**). The spatial distribution of the missing collectors did not appear systematic and I assumed that the missing data did not compromise my analyses and interpretation thereof. The majority of MAPs among collectors were concentrated near the source location within Murray Harbour. Beyond the Harbour, the particle concentrations among fewer MAPs were collected toward the northeast with increasing distance from the source location. In the following comparisons of MAPs and VPs, the reader is reminded that the modeled estimates of VPs can potentially span a much larger domain that extends beyond

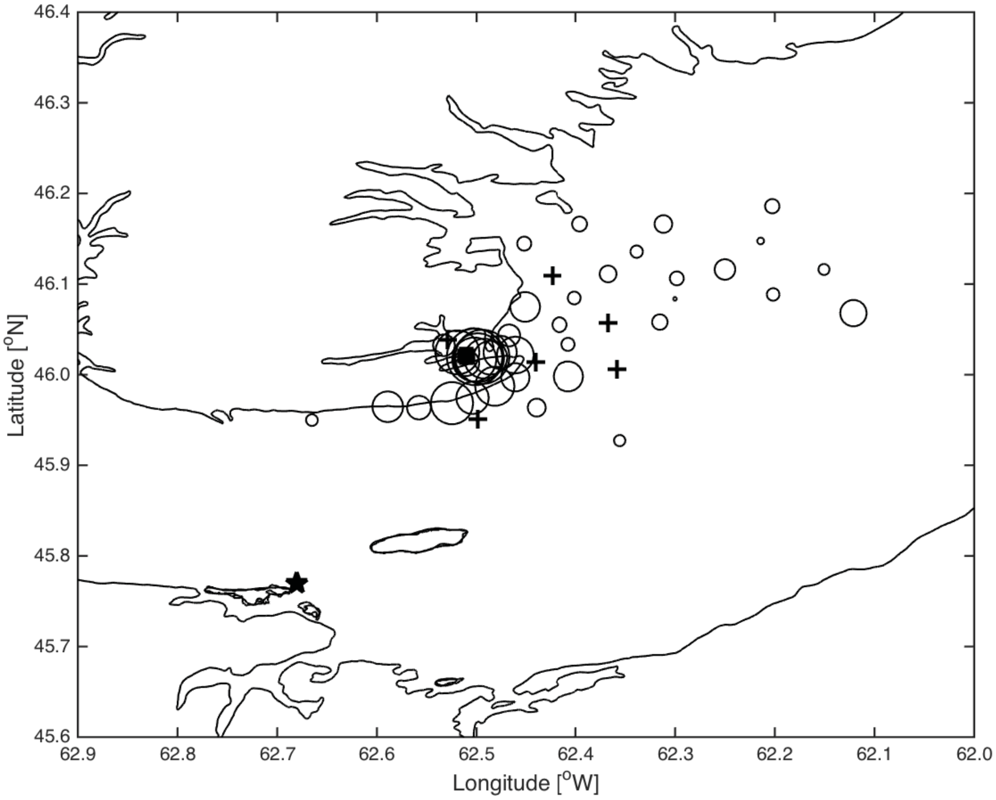

Figure 3.2 Coastline chart of the eastern Northumberland Strait between Prince Edward Island and Nova Scotia illustrating the location-specific relative number (linearly expanding-area circles with maximum 2,450 in Murray Harbour; square) of MAPs captured among the recovered collectors, where the locations of collectors not recovered are denoted by crosses. The location of weather station Caribou Point, where wind speed and direction were recorded, is indicated with a star.

that defined by the magnetic-collector array.

3.3.2 VP dispersal

Modeled VP positions at discrete same-phase times over several tidal cycles, up to approximately 2.5 days post-release, using various K_p values (**Fig. 3.3**), reflected several aspects of the observed MAP concentration distribution illustrated in **Figure 3.2**, particularly along the Murray Head peninsula. I selected the K_p values shown to first illustrate streakiness from just tidal influences (0 $m^2 s^{-1}$), a value that is typically used among modelers (2 $m^2 s^{-1}$), as well as a value large enough such that VPs encompass the entire collector array (80 $m^2 s^{-1}$). With no small-scale diffusion (K_p = 0 $m^2 s^{-1}$), the "streaky" nature of the VP field was apparent as it evolved with the tide, transporting the particles south and west along the peninsula (T), then folding and reversing north-eastward but further offshore (+2 tidal cycles), and then essentially repeating the tidal evolution (+4 tidal cycles), as well as reflecting particle advection with the tidal residual to the northeast. When K_p was increased to 2 $m^2 s^{-1}$, over the same tidal evolution, the VPs became more dispersed to the south and northeast of Murray Head peninsula. Where previously the streaks began to fold and reverse, the increased K_p produced a more dispersed field with relatively large concentrations aligned with the residual current. Using a minimum K_p of 80 $m^2 s^{-1}$, the resultant dispersive effect was more apparent over the same tidal evolution, though now with VPs being dispersed further from the localized concentration.

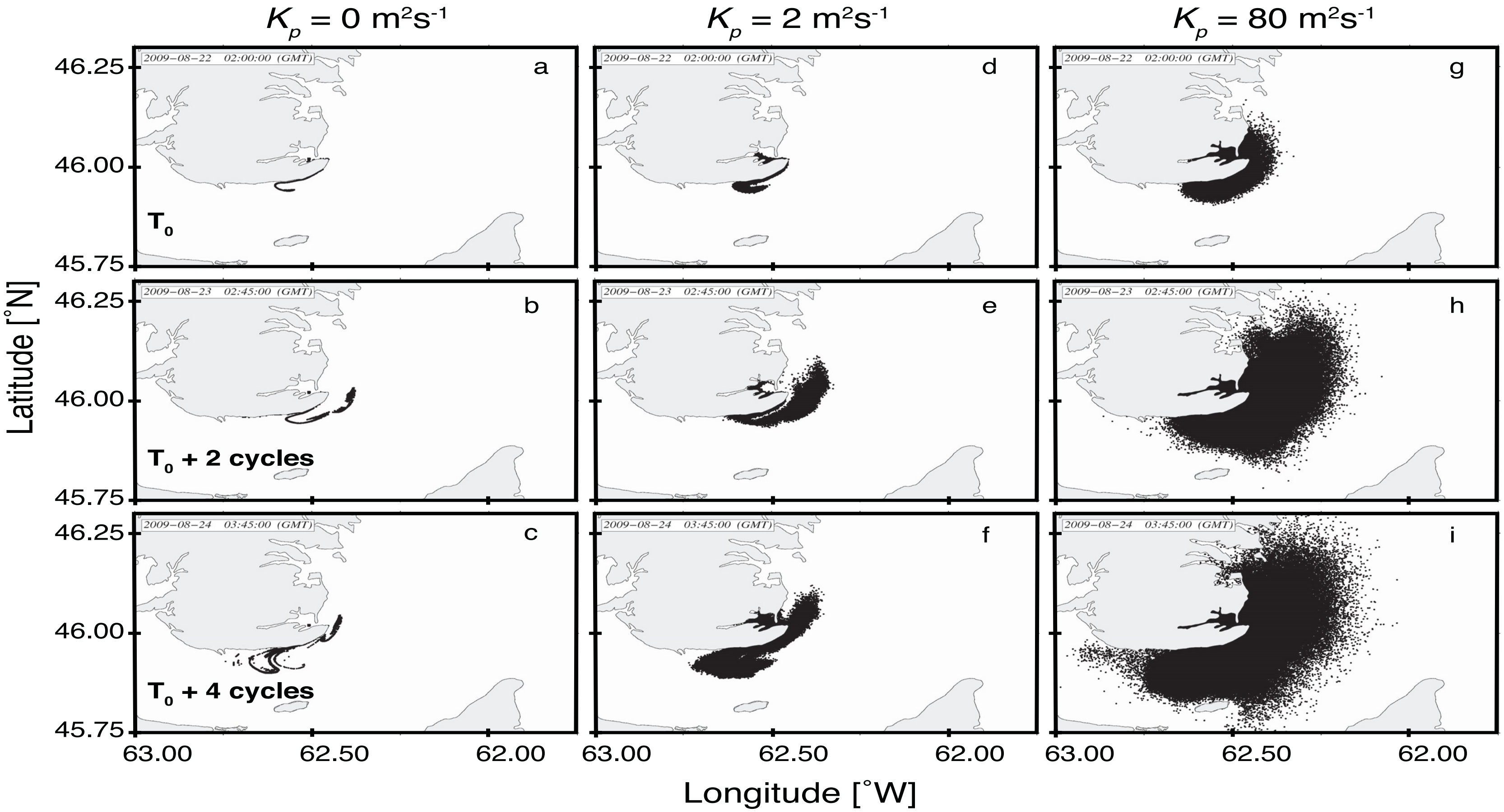

Figure 3.3 Coastline charts of the eastern Northumberland Strait illustrating examples of the near common-phase M2 tidal cycle evolution (ordinate charts) of modeled VP dispersal from the source in Murray Harbour as augmented by the random walk small-scale diffusivities (K_p, abscissa charts) of 0 $m^2 s^{-1}$ (a-c), constant 2 $m^2 s^{-1}$ (d-f), and minimum 80 $m^2 s^{-1}$ (g-i). Discrete times on the abscissa charts evolve from T = 13.5 h post-release to two (T + 24.8 h) and four (T + 49.8 h) subsequent tidal cycles.

The VP exposition number estimates (**Fig. 3.4**), based on a constant K_p of 25 $m^2\ s^{-1}$, reflected various aspects of the observed MAP capture number estimates among collectors (**Fig. 3.2**). The rationale for choosing a K_p value of 25 $m^2\ s^{-1}$ is detailed below. A visual comparison of **Figures 3.2**, **3.3**, and **3.4** indicates that the model VP field effectively reflected the general features of the observed MAP field. Within the confines of the collector array, the model tended to show low exposition numbers of VPs in areas where the magnetic-collectors captured low numbers of MAPs (typically offshore), as well as high exposition numbers of VPs in areas where the collectors captured high numbers of MAPs (in Murray Harbour and along the Murray Head peninsula). VP exposition number estimates, based on the other constant and minimum K_p values, illustrated patterns similar to those addressed above, except that the VP dispersal fields did not encompass the entirety of the MAP dispersal field at constant K_p values of 2 and 5 $m^2\ s^{-1}$ (**Figs. A.5**, **A.6**). At minimum K_p values of 50 and 80 $m^2\ s^{-1}$, the VP fields filled the entire model domain, at least to the north and east (**Figs. A.7**, **A.8**).

3.3.3 MAP and VP comparisons

The relation between N_{VP} and N_{MAP}, based on a constant K_p of 25 $m^2\ s^{-1}$ (**Fig. 3.5**), indicated a significant ($p < 0.001$) and generally linear ($r^2 = 0.49$) relation, though the confidence interval around the expected number of particles estimated by the model (N_{VP}) in relation to the observed (N_{MAP}) was large. Notably, the slope (1.00 ± 0.33) indicates

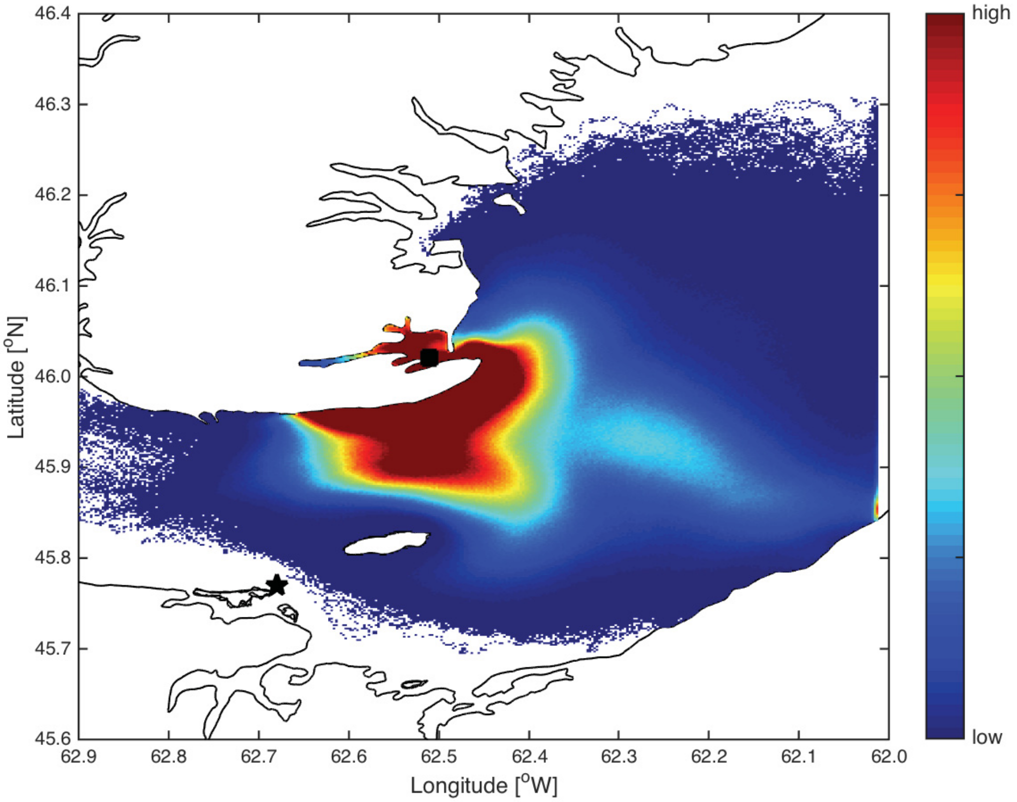

Figure 3.4 Coastline chart of the eastern Northumberland Strait and scale bar illustrating the exposition number (E_{ij}; low to high) of VPs (released in Murray Harbour; black square) within each 200 m^2 grid cell across the model domain as of 09:00 h on 28 August 2009 and based on a constant K_p of 25 $m^2 s^{-1}$. VPs cannot move beyond the right-hand boundary of the 200 m resolution model domain that parallels 62°W longitude. The location of weather station Caribou Point, where wind speed and direction were recorded, is indicated with a star.

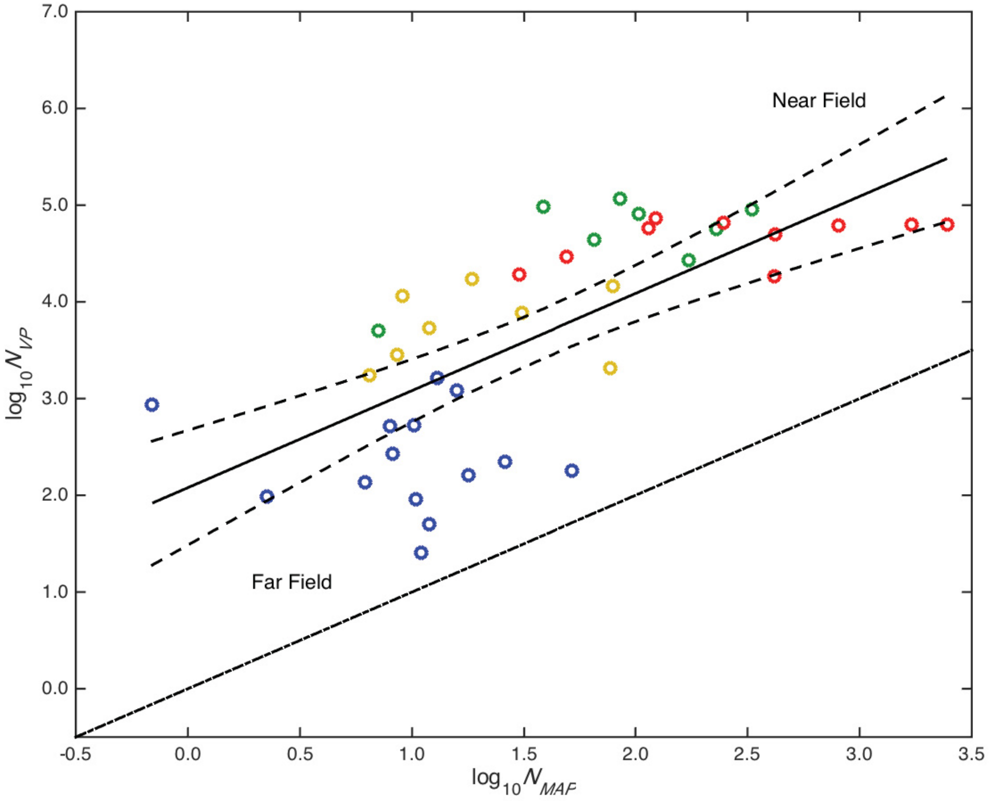

Figure 3.5 Log-log relation of N_{VP} as a function of N_{MAP} where N_{VP} modeling used a constant K_p of 25 $m^2\,s^{-1}$. The regression model [$\log_{10}N_{VP} = 2.08 + 1.00 \log_{10}N_{MAP}$; $r^2 = 0.49$; $p < 0.001$] is illustrated by a solid line with the 95% confidence interval around the model (dashed lines) fitted to the estimates nominally classified as near- to far-field distances from the source inside Murray Harbour (red), along the coast of the peninsula (green), in nearshore open waters (yellow), and offshore open waters (blue). The 1:1 relation is illustrated as a dashed-dotted line.

that the relative dilution between MAPs and VPs tends to be proportional, while the intercept (2.08 ± 0.59) indicates that the model predictions exceeded the MAP captures by two orders of magnitude. In addition, N_{VP} tended to over-estimate N_{MAP} as the collector locations progressed from the near-field inside Murray Harbour to along the coast and nearshore open water, and progressively under-estimated into the far-field offshore open water. This pattern was apparent among all relations between N_{VP} and N_{MAP} based on the other K_p values (**Figs. A.9–A.12**), despite the fact that the slopes of the relations were sensitive to the K_p values used in the model simulations (**Fig. 3.6**; **Table A.1**). At small K_p values, the slopes were greater than 1 (1.66 ± 0.62 at $K_p = 2$ m^2 s^{-1} and 1.44 ± 0.53 at $K_p = 5$ m^2 s^{-1}), and at higher K_p values, the slopes were less than 1 (0.81 ± 0.25 at $K_p = 50$ m^2 s^{-1} and 0.69 ± 0.20 at $K_p = 80$ m^2 s^{-1}). Based on the 95% confidence intervals around the slope estimates at each of the various K_p values used, it appears that on average, the appropriate K_p for modeling this system over the study period lies somewhere around a constant 25 m^2 s^{-1} that is bracketed by a constant 5 m^2 s^{-1} and a minimum 50 m^2 s^{-1} K_p.

3.3.4 Estimating dispersal kernels

The number of MAPs captured by the magnetic-collectors decreased exponentially with in-water distance L from the source location (**Fig. 3.7a**). The resultant dispersal kernel for the purely passive particles provided an estimated *e*-folding scale of 7.15 km with lower and upper 95% confidence limits of 5.19 and 11.44 km, respectively (**Fig. 3.7b**).

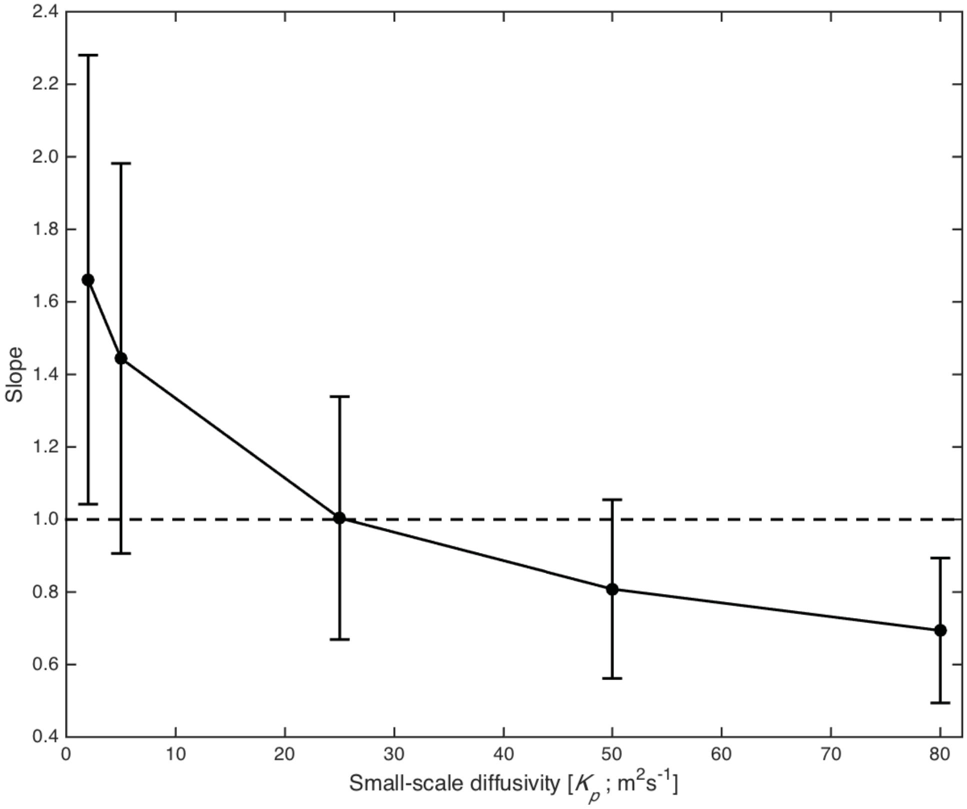

Figure 3.6 Slopes of the log-log regressions of N_{VP} on N_{MAP} (e.g., **Fig. 3.5**) as a function of constant (2, 5, and 25 m^2 s^{-1}) and minimum (50 and 80 m^2 s^{-1}) K_p values used in N_{VP} modeling, each with their associated 95% confidence intervals. The dashed line illustrates the 1:1 proportional change (i.e., slope = 1).

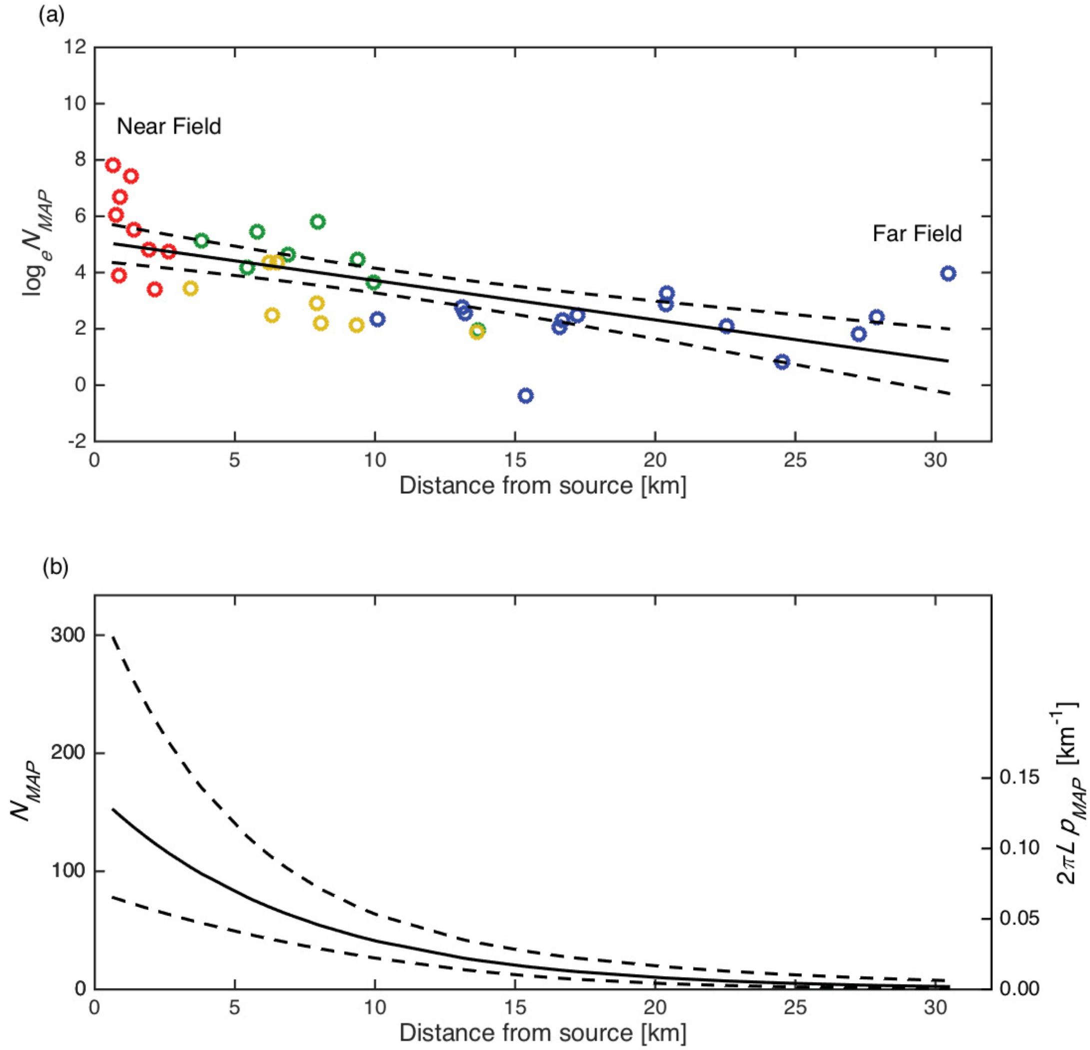

Figure 3.7 Log-linear (a) and exponential decay (b) of N_{MAP} as a function of distance L (km) from the source location. The regression model [$\log_e N_{MAP} = 5.12 - 0.14\ L$; $r^2 = 0.43$; $p < 0.001$] in (a) is illustrated by a solid line with the upper and lower 95% confidence limits around the model (dashed lines) fitted to the N_{MAP} estimates nominally classified as near- to far-field distances from the source inside Murray Harbour (red), along the coast of the peninsula (green), in nearshore open waters (yellow), and in offshore open waters (blue). The exponential decay [$N_{MAP} = 1.67 \times 10^2\ e^{-0.14\,L}$] in (b) is illustrated by a solid line with the upper and lower 95% confidence limits (dashed lines). The exponential decay (solid line) can be interpreted as $2\pi L\ p_{MAP}$ (right ordinate) with an e-folding scale of 7.15 km that has upper and lower 95% confidence limits of 11.44 and 5.19 km.

The uncertainties associated with the decrease in N_{MAP} at small L are large and may be related to a relatively rapid and constant proportional decay near the source location within Murray Harbour, followed by a slower and proportionally constant decay thereafter (**Fig. 3.7a**). The 95% confidence intervals around $2\pi L\ p_{MAP}(L)$ (not shown) were smaller than those around N_{MAP} since p_{map} is obtained from a derivative of N_{MAP} and is affected only by uncertainty in the slope a, whereas both the slope and intercept, and their respective uncertainties, affect N_{MAP}. Since the uncertainties associated with the intercept ($L = 0$) were large (± 0.70; approximately an order of magnitude), $N_{MAP}(L)$ was not well estimated within the Harbour. Evidence for this is demonstrated by assessing the decrease in N_{MAP} as a function of L for the collectors located only within the Harbour, wherein the slope was estimated at -1.21 ± 1.41 (**Fig. A.13a**), relative to -0.14 ± 0.05 (**Fig. 3.7a**) with all collectors included.

The number of VPs estimated among the model simulations also decreased exponentially with L for each of the K_p values used (**Figs. 3.8a**, **A.14a–A.17a**; **Table A.2**), and thus were in general agreement with the decrease in MAPs (**Fig. 3.7a**). As K_p increased, the *e*-folding scales for each of the VP dispersal kernel estimates also increased (**Fig. 3.9**), with the model again exhibiting sensitivity to K_p, as in **Figure 3.6**. When taking the 95% confidence intervals into account, I can conclude that an appropriate K_p for modeling this system, on average, over the study period, lies somewhere between the minimum K_p values of 50 and 80 $m^2\ s^{-1}$, which is greater than is indicated when using the N_{MAP} and N_{VP} comparison above (**Fig. 3.6**). The N_{VP} regression on L from the model simulation using a minimum K_p of 80 $m^2\ s^{-1}$ (**Fig. 3.8a**) provided an *e*-folding scale estimate of

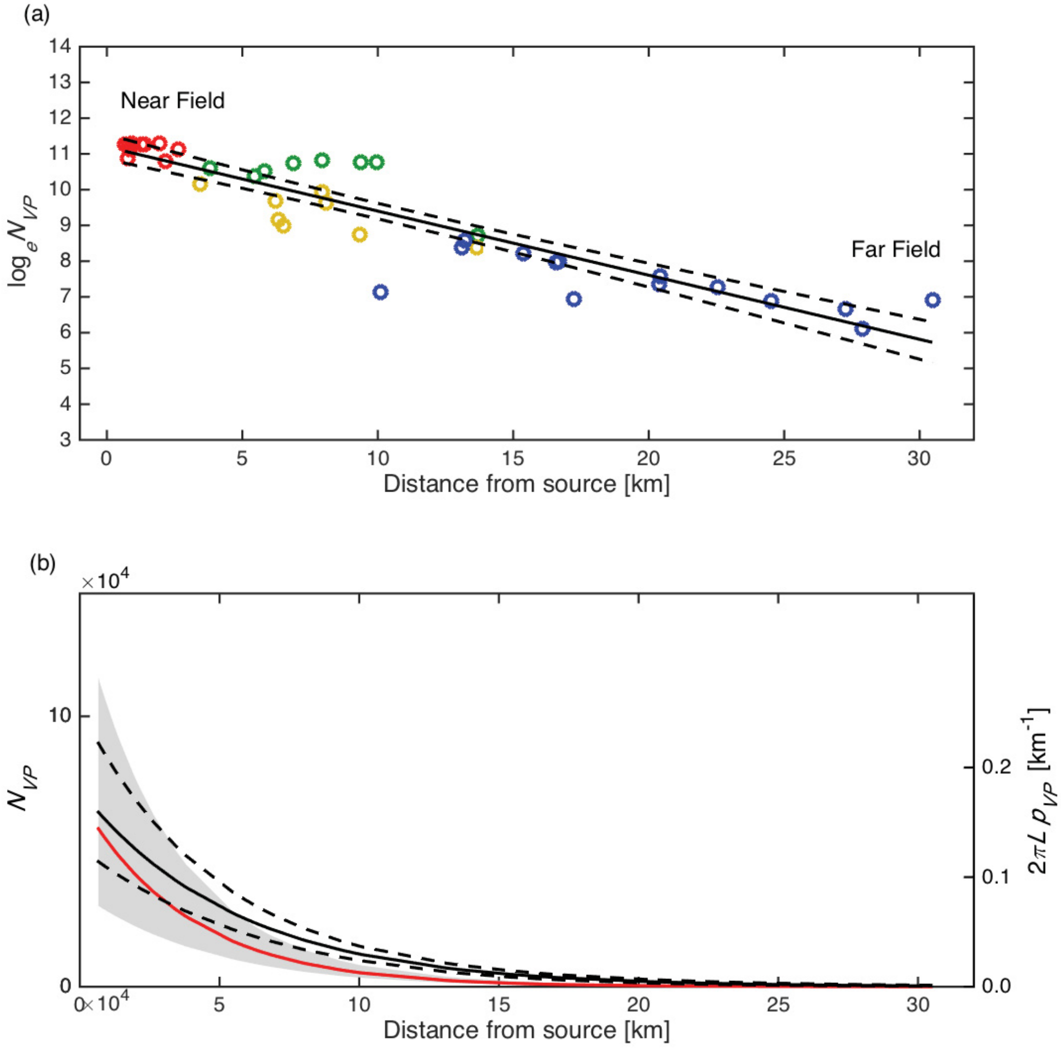

Figure 3.8 Log-linear (a) and exponential decay (b) of N_{VP} as a function of distance L (km) from the source location and based on a minimum K_p of 80 m^2 s^{-1}. The regression model [$\log_e N_{VP} = 11.19 - 0.18\ L$; $r^2 = 0.84$; $p < 0.001$] in (a) is illustrated by a solid line with the upper and lower 95% confidence limits around the model (dashed lines) fitted to the N_{VP} estimates nominally classified as near- to far-field distances from the source inside Murray Harbour (red), along the coast of the peninsula (green), in nearshore open waters (yellow), and in offshore open waters (blue). The exponential decay [$N_{VP} = 7.27 \times 10^4\ e^{-0.18\ L}$] in (b) is illustrated by a solid black line with the upper and lower 95% confidence limits (dashed lines). The exponential decay (solid black line) can be interpreted as $2\pi L\ p_{VP}$ (right ordinate) with an e-folding scale of 5.57 km that has upper and lower 95% confidence limits of 6.52 and 4.87 km. The exponential decay [$N_{VP} = 9.64 \times 10^4\ e^{-0.26\ L}$] based on a constant K_p of 25 m^2 s^{-1} is illustrated by the solid red line with the upper and lower 95% confidence limits (shaded). When interpreted as $2\pi L\ p_{VP}$, the e-folding scale is 3.86 km with upper and lower 95% confidence limits of 4.85 and 3.21 km.

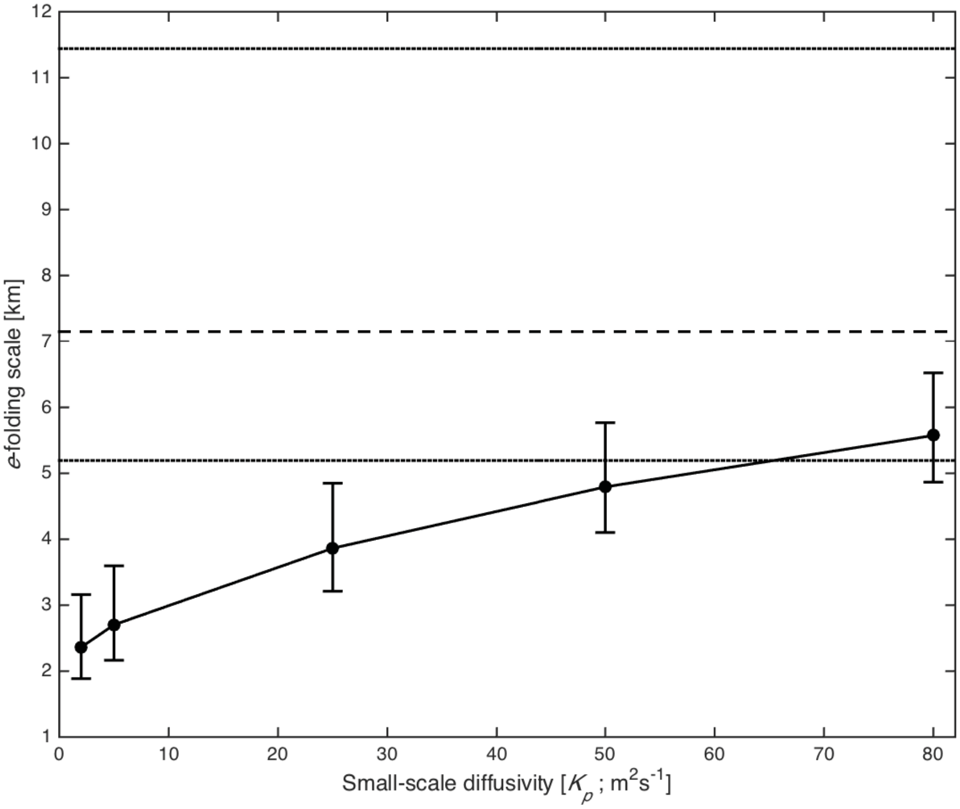

Figure 3.9 Change in *e*-folding scales of the N_{VP} exponential decay relations (e.g., **Fig. 3.8**) as a function of constant (2, 5, and 25 m^2 s^{-1}) and minimum (50 and 80 m^2 s^{-1}) K_p values with their associated upper and lower 95% confidence limits. The estimated MAP *e*-folding scale (e.g., **Fig. 3.7**) of the observed dispersal kernel (dashed line) is shown for comparison with the upper and lower 95% confidence limits (dotted lines).

5.57 km with upper and lower 95% confidence limits of 6.52 and 4.87 km, respectively, which was comparable to the *e*-folding scale estimate of 3.86 km with upper and lower 95% confidence limits of 4.85 and 3.21 km, respectively, when using a constant K_p of 25 $m^2\ s^{-1}$ (**Figs. 3.8b**, **A.16**).

In summary, the largest difference in the *e*-folding scales lie in the "tails" of the dispersal kernels, which is apparent when comparing that derived from a constant K_p of 25 $m^2\ s^{-1}$ with that derived using a minimum K_p of 80 $m^2\ s^{-1}$ (**Figure 3.8b**). Each of the exponential decay relations associated with the *e*-folding scales derived using the other K_p values (**Fig. 3.9**) are provided in **Figures A.14–A.17**. Again, the reader is reminded that the 95% confidence intervals shown in **Figure 3.8b** are associated with the exponential function, N_{VP}, and not with the probability density function, $2\pi L\ p_{VP}(L)$.

3.4 Discussion

3.4.1 MAP and VP comparisons

The spatial distributions of the MAP capture number estimates and the VP exposition number estimates generally agree well (**Figs. 3.2**, **3.3**, and **3.4**) and indicate that the model predictions generally reflect the Lagrangian particle displacements measured using the MAP collectors. The general correspondence between the observed particle collections and the Lagrangian predictions from the model should allow similar model predictions to be made using different environmental conditions, such as variations in the wind field, and (or) release location(s) within the model domain.

In my initial MAP and VP number comparisons (e.g., **Fig. 3.5**), I focused primarily on the slope of the relation because my aim was to determine the same relative dilution between the observed and modeled estimates (i.e., slope = 1) by varying the small-scale diffusivity coefficient (K_p) in the model. A strong MAP-VP agreement would be reflected in a linear relationship with a slope of 1.00, and thus examining the relation is the first-order test of the observed particle number distribution (N_{MAP}) and the expected particle number distribution provided by the model (N_{VP}).

In doing so, I demonstrated a sensitivity that the model exhibits to a varying K_p. I achieved a slope of 1 by using a constant K_p of 25 $m^2 s^{-1}$ (**Fig. 3.6**), though I make no inference that this value of K_p is the "best" value for modeling this system; this is addressed further below concerning my estimation of the dispersal kernels. A detailed comparison of the MAP and VP dilution rates revealed subtle differences in the slope that appeared to be a function of K_p. My results indicate that the "true" K_p is varying over space and time as illustrated by the seemingly systematic deviations from the regression models as the estimates progress from the near- to the far-field. If there were no or small deviations, I could conclude that I have identified the "true" K_p for this system and study period. As this is not the case, a constant value of 25 $m^2 s^{-1}$ over the entire 7-day study appears to best represent a space and time average of the small-scale diffusivity, though the 95% confidence intervals require a conservative conclusion that K_p is varying in space and time somewhere between 5 and 50 $m^2 s^{-1}$, considerably higher than the typical value of K_p first employed in the model. I thus suggest that using a typical 2 $m^2 s^{-1}$ value for modeling similar physical environments is inadequate. Nevertheless, by examining model results among K_p values in comparison with the MAP estimates, I have provided a practical means of calibrating such models and (or) systems, as well as a means of potentially improving the models.

While a slope of 1.00 is achieved for the model simulation comparison using a constant K_p of 25 $m^2 s^{-1}$ (**Fig. 3.5**), the model over-estimates the MAP numbers by approximately two orders of magnitude, and does so at all values of K_p used, no matter the slope (**Table A.1**). These elevations can be explained by a number of factors that may be dependent on how the MAPs and the magnetic-collectors behave in the field and (or) on how the model performs in practice.

It is possible that there are MAP losses from the surface layer over time due to sinking and (or) beaching, processes that are not included in the model. It is also possible that the MAPs are so neutrally buoyant that they are vertically mixed throughout the water column, at least to depths greater than 2 m, by tidally- or wind-induced turbulence, and are thus not uniformly available for capture by the magnetic-collectors located the surface; i.e., the surface layer becomes increasingly diluted by losses to deeper layers, a process that is also not included in the model. Either or both possibilities could explain why the decay in N_{MAP} estimates in the Harbour (near-field) is particularly rapid relative to the far-field in relation to N_{VP} estimates (**Fig. 3.5**).

Unresolved issues in the model, some alluded to above, may also help explain the elevations. Although the model resolution (200 m^2) is respectable for an ocean model, it does not appropriately resolve Murray Harbour due to the size of the Harbour domain and the presence of numerous small islands relative to the grid-cell size and the number of open-water grid-cells. Such a limitation in resolution likely explains why the N_{VP} estimates in the Harbour (near-field) are near constant relative to the far-field where the decay is more rapid than that observed by the N_{MAP} estimates (**Fig. 3.5**). In addition, the model does not capture some events well, such as Hurricane Bill, because the wind field forcing is not highly resolved due to the nature of the wind-field data used for forcing. Finally, as demonstrated above, the sensitivity of the small-scale diffusivity applied to the VPs in the model may contribute to the slope elevations. The sensitivity can be rationalized, but not fully explained, by considering mechanisms such as shear dispersion by tidal currents that would be experienced by the MAPs but are not simulated by the model. This sensitivity is addressed below.

3.4.2 Streakiness, shear dispersion, and model sensitivity to K_p

A physical mechanism that explains the dependence of the model predictions on K_p is illustrated in **Figure 3.3**, which shows the cumulative effect of Lagrangian tidal advection, the dominant stirring mechanism in the region and thus the model. It is clear that dispersal is stronger along the shore to the south and west of Murray Harbour and weaker to the north and the east. It is apparent that the VPs disperse in a complex pattern with numerous streaks that effectively double in number with each tidal cycle, partially due to the continuous release of the VPs over 6 hours. Increasing K_p from 0 to 2 $m^2 s^{-1}$ and to a minimum of 80 $m^2 s^{-1}$ causes diffusion to fill the gaps between the streaks while retaining a similar overall shape and location of the VP distribution. In theory, an advection-diffusion process could be best-fitted (or approximated) using a diffusion-only model, but this is not what has been simulated here, as the distributional shape of the diffusing VPs (K_p = 2 m^2 s^{-1} and K_p = 80 m^2 s^{-1}) retain traits of the advection-only experiment (K_p = 0 m^2 s^{-1}). A diffusion-only model would demonstrate that an exceedingly high K_p value would be necessary to achieve any meaningful far-field relation with the observed N_{MAP} estimates; i.e., only when the appropriate advective and diffusive processes are employed do the empirical and modeled results begin to conform (Lynch *et al.* 1998; Largier 2003; Siegel *et al.* 2003; Levin 2006; Gawarkiewicz *et al.* 2007; Werner *et al.* 2007; Xue *et al.* 2008; Botsford *et al.* 2009; Sponaugle *et al.* 2012; Putnam and He 2013; Wolanski and Kingsford 2014).

The streakiness observed in **Figure 3.3** is similar to what I have visually observed in preliminary field trials using the MAPs. It is also similar to that argued by Garrett (1983) and observed by Ledwell *et al.* (1988) for isopycnal stirring in the deep-ocean thermocline, caused in our case by lateral stirring in the tidal currents (Ridderinkhof and Zimmerman 1992). Tracer streaks are repeatedly multiplied by the stretching and folding action that is an essential part of "chaotic stirring" (Aref 1984; Zimmerman 1986; Ottino 1990). The processes involved in forming the streaks and the diffusion among them are likely responsible for the sensitivity in the model predictions to K_p; thus, the comparisons between N_{MAP} and N_{VP} serve to help constrain the appropriate small-scale diffusivity in the model.

The details of mixing behavior depend on the transverse streak spacing (L ~ 1 to 5 km), the tidal period (T = 12.42 h), and the small-scale diffusivity (K_p). I thus expect model sensitivity to the small-scale diffusivity will occur as long as particles diffuse a distance less than L in T, corresponding to a diffusivity of $\frac{L^2}{T} \approx 20$ to 500 $m^2 s^{-1}$ and not dissimilar to the estimates employed in our model simulations (**Fig. 3.6**). Diffusivities smaller than the above allow streakiness to persist and diffusivities larger than the above will "smooth" over the streaks and reduce the sensitivity.

How can agreement between the modeled VP and the observed MAP number estimates be affected by a model diffusivity enhanced beyond the nominal value of 2 $m^2 s^{-1}$? One possibility that is known to occur physically, but that is not explicitly included in the model, is shear dispersion that arises from a combination of vertical mixing and vertically sheared currents. The physical characteristics of the MAPs include weak positive buoyancy, with a rise rate (w_p) of 1 to 4 mm s^{-1}. Zimmerman (1986) gives the velocity of turbulent eddies (w') as approximately 5 x 10^{-3} u_t, where u_t is the horizontal tidal current velocity. It follows that if u_t is equal to 0.5 m s^{-1}, then w' would be approximately 2.5 mm s^{-1}, comparable to the rise rate of the MAPs. It is therefore likely that the tidal currents in the Northumberland Strait generate sufficiently strong turbulence to mix the MAPs within the water column, and if so mixed, the MAPs would experience shear dispersion, while in the model, the VPs are constrained to the upper z-layer (0 to 2 m). Zimmerman (1986) reviews models and observations for the tidal vertical shear contribution to dispersal and shows that the equivalent (effective) corresponding horizontal diffusion coefficient is typically in the range of 10 to 25 $m^2 s^{-1}$, with a strong spatial dependence related to depth and tidal current variation. I have shown above that this is sufficient to cause lateral diffusion among streaks within a tidal period. In summary, the slow rise rate that is characteristic of the MAPs could allow them to be vertically mixed in the water column by tidally generated turbulence, and they would thus be dispersed by vertical shear. The VPs are constrained to remain in the modeled surface layer and are unaffected by shear dispersion. While I have demonstrated reasonable agreement between N_{MAP} and N_{VP}, it is improved by imposing a small-scale diffusivity in the model large enough to simulate constant and spatially uniform shear dispersion.

3.4.3 Estimating dispersal kernels

I have demonstrated the ability of a new, empirical method to directly estimate the passive component of a particle dispersal kernel in a coastal marine system. As the null model of propagule dispersal, the physical connectivity estimates can be applied, in the geographic area in question, to any passive planktonic organism in the surface mixed layer. In this study, I estimated that the MAP-based dispersal kernel has an *e*-folding scale of 7.15 km, and this is approximately twice the width of Murray Harbour and the same size as its length. This scaling argument implies that there is considerable potential for retention in the Harbour that may favor local endemic populations and (or) invasive species that find their way into the Harbour via shipping or other vectors. For example, if the dispersal kernel is defined as $p(L) = (2\pi L)^{-1} ae^{-aL}$ (i.e., **Equation 3.13**), when a^{-1} is approximately 0.85 km, similar to the estimated *e*-folding scale of the dispersal kernel within Murray Harbour (i.e., **Fig. A.13**), then the probability of passive retention within a distance D and over time T is $\int_0^D 2\pi L\, p(L)dL = \int_0^D ae^{-aL}\, dL = 1 - e^{aD}$. Assuming that D is equal to 7 km for the length of the Harbour, the probability of retention is 0.9973. It should be noted that this estimate does not address directed swimming and (or) mortality, and (or) subtleties associated with directional dispersal and (or) irregular coastline. Similar arguments imply that exported propagule concentrations diminish rapidly over relatively short length scales. In another example, concentrations would fall to $\frac{1}{e^4}$ = 1.80% of the original number at a distance of 28 km from the source (i.e., four *e*-folding scales of 7.15 km), and to $\frac{1}{e^6}$ = 0.20% of the original number at a distance of 42 km from the source (i.e., six *e*-folding scales of 7.15 km), thus limiting dispersal and hence connectivity over large distances.

I have also shown that $p_{MAP}(L)$ is not well estimated within the Harbour (**Fig. A.13**) if the near-field estimates are used along with the far-field estimates in determining the dispersal kernel, since the *e*-folding scale within the Harbour is much lower at approximately 0.85 km. Thus, concentrations in the Harbour decrease far more rapidly with distance relative to outside the Harbour, thereby further limiting dispersal and connectivity. These empirical estimates of dispersal can provide context in the dispersal of a local problematic invasive species. Retention of the invasive vase tunicate (*Ciona intestinalis*) within Prince Edward Island estuaries and harbors is known to negatively impact the local bivalve aquaculture industry, and larval dispersal ability has implications to the management of both the industry and the invasion (Carver *et al.* 2003; Locke *et al.* 2007; Ramsay *et al.* 2008; Daigle and Herbinger 2009; Lutz-Collins *et al.* 2009; Ramsay *et al.* 2009; Kanary *et al.* 2011; Fitridge *et al.* 2012; Collin *et al.* 2013). Thus, I conclude that estimating dispersal kernels in coastal environments requires very careful consideration of semi-enclosed and nearshore waters separately from open-ocean waters as the consequences may be considerable.

Although linear regression models (e.g., **Figs. 3.7**, **3.8**) have the advantage of a simplified single-parameter dispersal kernel that represents the observations reasonably, although not perfectly well, any experimental observations of MAP captures can be similarly used to yield the probability of spatial transfer from source (i.e., release) to sink (i.e., collector) locations, giving direct observations of the physical component of the dispersal kernel. In complex physical geometries, with non-uniform flows and anisotropic and non-uniform dispersal, the dispersal kernel could take virtually any (one- or two-dimensional) form, and could reasonably be expected to depend on sink location; i.e., as a two-dimensional function. In light of this, it is quite remarkable that given the complexity of Murray Harbour and the eastern Northumberland Strait, a region of anisotropic and non-uniform dispersal confounded by complex shoreline geometry, that a simple exponential function gives a reasonable representation of the dispersal probability with a single parameter; the *e*-folding scale. It is additionally surprising and gratifying that the dispersal kernel estimated using the numerical model is correspondingly simple, and that the residual variability (deviations from the linear fit) are similar in both the model and observations.

The magnetic-collectors sample a single realization of the probability density function, as illustrated above (**Figs. 3.2** and **3.4**), to within a normalization factor required to give an integrated probability of one. The magnetic-collector array design in our study demonstrated remarkable efficacy in that the bulk of the distribution appears to have been sampled with sufficient detail to capture the structure, and yet with sufficiently smooth results that oversampling was not apparent. The smooth results are likely associated with the time-integration estimate that the collectors provide – any streaks of MAPs that occur at intermediate stages of dispersal are swept through collectors, and the collectors thus yield MAP numbers that are not sensitive to their precise locations. The collectors sampled a single dispersal realization under specific environmental conditions, and result in a sampling uncertainty that is difficult to quantify without knowledge of the two-dimensional dispersal kernel. Additionally, having collectors at a finite number of locations in the far-field, where probabilities are small and areas are large, makes computation of the appropriate kernel difficult. For these reasons, I chose to present my dispersal kernels in one-dimension. Further, p_{MAP} and p_{VP} are primarily a function of in-water distance L so that available observations are more parsimonious for estimating a one-dimensional dispersal kernel than a two-dimensional one. I suggest that the simplified one-dimensional dispersal kernel may not be unique to the chosen source location and (or) environmental conditions, but may be representative of the entire Northumberland Strait region where similar tidal and residual currents are present. **Chapter 4** details the analyses of four additional MAP studies in this region that allow me to test this hypothesis.

As in the MAP and VP comparisons above (**Fig. 3.6**), the VP *e*-folding scales also exhibit sensitivity to the small-scale diffusivity value (**Fig. 3.9**). To approach the MAP *e*-folding scale estimate, the modeled K_p had to be raised to at least a minimum value of 50 $m^2 s^{-1}$.

This reflects my inference above that there may not be one "best" value of K_p when modeling this system. Further, I determined that nearly the entire exponential decay relation (including the 95% confidence limits) for a constant K_p of 25 $m^2 s^{-1}$ envelops that for a minimum K_p of 80 $m^2 s^{-1}$ (**Fig. 3.8b**). The majority of the difference between the two lies in the "tails" of the dispersal kernels, implying that the far-field is important for estimating connectivity when using dispersal kernels. For example, the likelihood of survival and establishment of a larva may fall within one *e*-folding scale distance, say less than 5 km, using either kernel estimate (e.g., **Fig 3.8b**), but potential establishment lies beyond that scale distance in the far-field "tails" where the p_{VP} estimates diverge. Dispersal rates, particularly those of invasive species, are extremely sensitive to the "tail" of the dispersal kernel. It is often within the "tail" that modeling dispersal becomes problematic (Kot *et al.* 1996; Clark *et al.* 1998; Higgins and Richardson 1999; Bullock and Clarke 2000; Cain *et al.* 2000; Cowen *et al.* 2000; Bossenbroek *et al.* 2001; Nathan *et al.* 2003; Shanks et al. 2003; Nathan 2005; Trakhtenbrot *et al.* 2005; Klein *et al.* 2006; Dyer 2007; Skarpaas and Shea 2007; Nathan *et al.* 2008; Okubo and Levin 2010; Gillespie *et al.* 2012; Putman and He 2013; Simpson *et al.* 2014; García and Borda-de-Água 2017; Jordano 2017). I note that when using any value of K_p in the model, the MAPs have a greater *e*-folding scale than the VP estimates provide (**Fig. 3.9**). When sub-grid dispersal is employed, others have found that it not only achieves a more realistic model (e.g., Döös *et al.* 2011), but that models exhibit sensitivity to this parameter when using values similar to those in my study (e.g., Xue *et al.* 2008). This suggests, along with my results, that many hydrodynamic models may be too spatially conservative in their dispersal predictions (e.g., Okubo and Levin 2010). Sub-grid-scale parameterizations are not well understood and thus not well modeled, and this is a key area in need of improvement when using numerical models (Werner *et al.* 2007).

Many numerical hydrodynamic models are frequently used as a central tool in MPA planning, invasive species mitigation efforts, the prediction of ecosystem response to changing environmental conditions, source-sink estimation (connectivity), and the dispersal and impact of contaminants. Accordingly, spatially conservative estimates of dispersal, and thus connectivity, may have serious implications and (or) consequences for extant or planned management and conservation. The life-history characteristics of a species in question, or the source and (or) volatility of a contaminant, will need to be examined in the context of the physical connectivity when making management and conservation decisions. Using such models as first approximations can be highly informative for initial planning purposes and for urgent mitigation responses; however, I argue that when dispersal is a core feature of an issue, such models should not be used to dictate planning and response until they can be tested for planning and response purposes, and not only the purpose for which they (the models) were originally designed. I suggest that dispersal and model assessment is examined here in a new, strongly Lagrangian manner, and that the MAPs can achieve a quantitative, empirical estimate of the dispersal kernel that has never before been accomplished.

Chapter 4

Scales of dispersal in the Northumberland Strait

Is a single realization representative of the entire system?

4.1 Introduction

The coastal waters of the Southern Gulf of St. Lawrence (sGSL), encompassing the Northumberland Strait, support economically and socially important commercial fisheries, including the multi-million dollar American lobster (*Homarus americanus*) fishery. The sGSL also supports nearshore crab, fish, groundfish, and shellfish fisheries, as well as an active bivalve aquaculture industry (Hanson *et al.* 2014). The dynamics, connectivity, and persistence of the populations that support these fisheries are fundamentally regulated by dispersal during planktonic (egg or larvae) early life-stages (Metaxas 2001; Kinlan and Gaines 2003; Sale *et al.* 2005; Levin 2006). Quantifying dispersal is thus a critical step when assessing, monitoring, and sustainably managing these populations and, as well, in predicting how they will respond to challenges such as climate change, overfishing, and the potential impact of non-indigenous species that may thrive in the sGSL, such as the invasive vase tunicate (*Ciona intestinalis*; Carver *et al.* 2003; Locke *et al.* 2007; Ramsay *et al.* 2008; Daigle and Herbinger 2009; Lutz-Collins *et al.* 2009; Ramsay *et al.* 2009; Kanary *et al.* 2011; Fitridge *et al.* 2012; Collin *et al.* 2013) and the European green crab (*Carcinus maenas*; Cohen *et al.* 1995; Grosholz and Ruiz

1996; Audet *et al.* 2003; Roman 2006; Klassen and Locke 2007; Therriault *et al.* 2008; Compton *et al.* 2010; Haarr and Rochette 2012; Cosham *et al.* 2016).

Biological dispersal refers to the spread of individuals away from a source location through passive and (or) active means (e.g., Begon *et al.* 2006; Levin 2006), where the passive component is especially important within a fluid such as air or water. Dispersal affects population dynamics (e.g., the distribution of individuals and ultimately reproduction and recruitment), population genetics (e.g., gene flow), and thus the spatial scale of population connectivity through the exchange of individuals among geographically separated subpopulations (Clobert *et al.* 2001; Kinlan and Gaines 2003; Bowler and Benton 2005; Begon *et al.* 2006; Nathan 2006; Matthysen 2012; Allen *et al.* 2018). Dispersal is often defined in terms of the dispersal kernel, the function that describes the probability of a particle or propagule moving from some source location to all other locations (Clark *et al.* 1998; Siegel *et al.* 2003; Nathan 2006; Cowen *et al.* 2007; Gawarkiewicz *et al.* 2007; Nathan *et al.* 2008; Nathan *et al.* 2012; Hrycik *et al.* 2013).

The scales of marine dispersal are empirically difficult to measure (Thorrold *et al.* 2002; Largier 2003; Siegel *et al.* 2003; Kinlan *et al.* 2005; Cowen *et al.* 2006; Levin 2006; Pineda *et al.* 2007; Werner *et al.* 2007; Metaxas and Saunders 2009; Kool *et al.* 2013; Pineda and Reyns 2018) and a more realistic quantification of the spatial patterns of dispersal is required to address the extant and future management questions raised in the Northumberland Strait and the sGSL. Further, management decisions are often based on modeling studies, and these models can be tested and possibly improved with empirical estimates of dispersal (Thorrold *et al.* 2002; Largier 2003; Siegel *et al.* 2003; Cowen *et al.* 2006; Nathan 2006; Aiken *et al.* 2007; Pineda *et al.* 2007; Werner *et al.* 2007; Cowen and Sponaugle 2009; Rasmussen *et al.* 2009; Okubo and Levin 2010; Sponaugle *et al.* 2012; Hrycik *et al.* 2013; Nickols *et al.* 2015; Almany *et al.* 2017; Krueck *et al.* 2017; Pineda and Reyns 2018). Since ecosystem structure and function within the sGSL is currently in a state of rapid change (Savenkoff *et al.* 2007; Benoît and Swain 2008; Bundy *et al.* 2009; Hanson *et al.* 2014), it is especially vital to obtain direct measures of dispersal that can be incorporated into these models to predict and mitigate other probable changes that can ecologically and economically impact the region. Once a model is validated, model predictions can then be extrapolated to determine the effects of varying environmental conditions (e.g., winds, tidal cycle), as well as to confidently incorporate biological influences (e.g., behavior, mortality) on dispersal.

In this Chapter I provide direct measures of particle dispersal in the Northumberland Strait region of the southern Gulf of St. Lawrence using a proven advanced technology system of magnetically attractive particles (MAPs) and magnetic-collector arrays (**Chapters 2** and **3**; Ruddick and Taggart 2006, 2011; Hrycik *et al.* 2013). This system overcomes many of the issues associated with conventional tracing technologies (e.g., drifters, dye, and numerical models) frequently employed in the study of dispersal (**Chapter 2**, Ruddick and Taggart 2006, 2011). It allows me to quantify the passive component of the dispersal kernel in the near-surface mixed layer at the scale of dispersing early-stage planktonic organisms (days to weeks, 1 to 100 km). Such data provide the biological null model of larval dispersal. The weak buoyancy and slow rise rate designed in the MAPs provide important properties that allow them to mimic weakly buoyant, passive propagules. Further, as advective and diffusive processes drive the passive component of connectivity, knowledge of the dispersal kernel allows the degree of passive connectivity in space and time to be readily estimated for a defined region (e.g., **Chapter 3**; Hrycik *et al.* 2013).

Environmental conditions during MAP experiments vary in an uncontrolled manner such that there will always be unanswered questions about dispersal in conditions different from those present for any given experiment. In **Chapter 3**, I suggested that the simplified one-dimensional dispersal kernel may not be unique to the release location in Murray Harbour and (or) the environmental conditions present during that study, but may be representative of the entire Northumberland Strait region where similar tidal and residual currents exist. The additional four studies analyzed in this Chapter will allow me to determine how well the scale of dispersal estimated in **Chapter 3** (i.e., a single realization) is representative of the entire region at different locations and times (i.e., multiple realizations). Using the same hydrodynamic model as in **Chapter 3**, I also repeat the MAP and VP comparison for another location and time in the Northumberland Strait to assess the model's veracity. The results presented here are applicable to the management of the local fisheries, industry, and species invasions, as the potential population-level distributions of the species in question are dependent on the dispersal of individual eggs and (or) larvae in planktonic early-life stages.

4.2 Methods

4.2.1 Study site

In addition to the Murray Harbour (MH; see **Fig. 4.1**) study detailed in **Chapter 3**, three particle dispersal studies were conducted in the Northumberland Strait off the coasts of Shediac (SH), Cape Tormentine (CT), and Cape George (CG), as well as one study within St. George's Bay (GB; **Fig. 4.1**). The Strait is nominally 20 to 30 km wide, 30 to 40 m deep at mid-channel, and separates eastern New Brunswick (NB) and Nova Scotia (NS) from Prince Edward Island (PE). Residual flow through the Strait is normally west to east with a net flow of the order kilometers per day (Lauzier 1965). St. George's Bay, located at the eastern end of the Strait, is surrounded by mainland Nova Scotia but is open to the Strait and the Gulf of St. Lawrence to the north. The Bay has an approximate area of 900 km^2 with an average depth of 24 m and a maximum depth of 40 m at the mouth. It is without strong oceanographic features and exhibits a residence time of approximately one month (Petrie and Drinkwater 1978; Harding *et al.* 1982; Drinkwater 1989). Particles (detailed in **Chapter 2** and briefly summarized below) were separately released at each of the nearshore locations illustrated in **Fig. 4.1** after the respective particle collector arrays (also detailed in **Chapter 2** and briefly summarized below) were deployed. It should be noted that while some of the collector arrays among the Northumberland Strait studies overlapped in space, they never coincided in time. There were variable winds during each of the studies examined here. Wind speed and direction were recorded hourly at Summerside, PE, on the northwestern side of the Strait, and at Caribou Point, NS (Environment and Climate Change Canada, Historical Data Archive), on the south side of the Strait (**Fig. 4.1**). Detailed variations in the wind field velocity

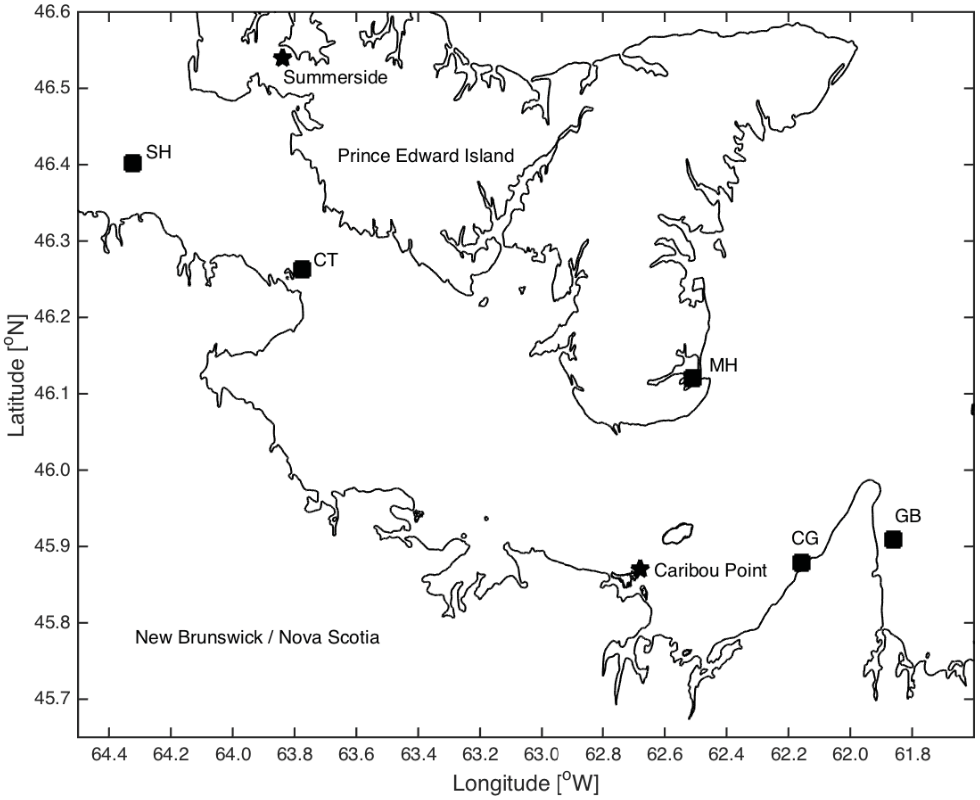

Figure 4.1 Coastline chart of the Northumberland Strait between Prince Edward Island and New Brunswick / Nova Scotia illustrating the MAP source locations (squares) at Shediac (SH), Cape Tormentine (CT), Murray Harbour (MH), Cape George (CG), and St. George's Bay (GB). The locations of Summerside and Caribou Point, where wind speed and direction were recorded, are indicated with stars.

components (u, v) over each deployment period were examined (**Figs. B.1–B.4**) using the data provided by the closest station (i.e., Summerside or Caribou Point; **Fig. 4.1**) respective to the given MAP release.

4.2.2 Magnetically attractive particle (MAP) deployment, dispersal, and analyses

4.2.2.1 Summary of the MAP and magnetic-collector array technology system

The reader is advised that a more detailed description of the MAP and magnetic-collector array technology system is provided in ***Chapter 2****.*

The MAPs are composed of hollow glass (SiO_2) microspheres that provide buoyancy, magnetite (Fe_3O_4) that provides magnetic attraction and mass, and a food-safe epoxy resin that acts as a binding agent. The particles are ideally designed to be spherical, in the 100 to 500 μm equivalent spherical diameter (esd) size range, and with a specific gravity (SG) designed to match *in situ* surface layer density; a nominal specific gravity (SG) of 1.02 for marine-applications. In the four studies detailed in this Chapter, the MAPs had median and geometric mean equivalent spherical diameters (esd) as summarized in **Table 4.1** (see **Figs. B.5–B.8**), a nominal specific gravity (SG) of 1.02, and an average rise rate of 1 to 4 mm s^{-1} in water with a SG of 1.02. The MAPs are one component of a system (**Chapter 2**; Ruddick and Taggart 2006, 2011) that, when coupled with a moored magnetic-collector array, allows the direct measurement of particle dispersal within the array domain. The magnetic-collectors are passive samplers designed to float near the surface and vane into the current such that any MAP suspended in the near-surface layer that flows through a collector will be captured (**Fig. 2.3**).

Table 4.1 Summary of the median and geometric mean equivalent spherical diameters (esd; µm) of MAPs released in each of the Northumberland Strait studies, including Shediac (SH), Cape Tormentine (CT), Murray Harbour (MH), Cape George (CG), and St. George's Bay (GB).

Study	Median esd (µm)	Geometric mean esd (µm)
SH	312	311
CT / MH	195	200
CG	361	362
GB	336	336

Collectors were deployed prior to the start of each study and following a point-source release of MAPs and their dispersal over a given period, the magnetic-collectors were recovered and the particles captured by the magnets were enumerated. This system essentially makes use of billions of particle drifters that can be used to estimate dispersal parameters and to make direct comparisons with similar virtual particle (VP) dispersal estimates provided by models.

4.2.2.2 MAP dispersal

There were four separate particle dispersal studies:

1. MAPs were released in the surface layer (0 to 0.5 m) off the coast of Shediac (SH), New Brunswick (at 46.30°N, 64.32°W; **Fig. 4.1**) over a 6 h period; 3 h either side of the local flood tide maximum at 11:15 h ADST on 28 June 2010. A total of 58 collectors were deployed and 56 were recovered after a period of 7 to 9 d post-release. Wind data during this study were obtained from Summerside, PE.
2. MAPs were released in the surface layer (0 to 0.5 m) off the coast of Cape Tormentine (CT), New Brunswick (at 46.16°N, 63.77°W; **Fig. 4.1**) over a 12 h period beginning at 07:30 h ADST on 27 June 2009. A total of 40 collectors were deployed and 33 were recovered after a period of 7 to 9 d post-release. Wind data during this study were also obtained from Summerside, PE.
3. MAPs were released in the surface layer (0 to 0.5 m) off the coast west of Cape George, Nova Scotia (at 45.78°N, 62.16°W; **Fig. 4.1**) over a 6 h period; 3 h either side of the local flood tide maximum at 17:30 h ADST on 21 August 2010. A total of 60

collectors were deployed and 60 were recovered after a period of 6 to 7 d post-release. Wind data during this study were obtained from Caribou Point, NS.

4. MAPs were released in the surface layer (0 to 0.5 m) off the western coast of St. George's Bay, Nova Scotia (at 45.81^{o}N, 61.86^{o}W; **Fig. 4.1**) over a 1 h period beginning at 17:55 h ADST on 30 July 2010. A total of 70 collectors were deployed and 69 were recovered after a period of 7 to 10 d post-release. Wind data during this study were also obtained from Caribou Point, NS.

For each study, subsamples of MAPs suspended in water of *in situ* density were monitored over the study (dispersal) period to estimate the proportion that would sink out from the surface layer. Magnetic-collectors had previously been deployed prior to each MAP study, with spatial coverage designed according to deployment and recovery logistics and, except for the GB study, by using expected winds for the time of the year within the hydrodynamic model running in VP tracing mode (see below and **Chapter 3**). Upon retrieval, captured MAPs were removed from each collector and imaged from above, with the total area (mm^2) of MAPs in each calibrated image measured using SigmaScan Pro (Version 5.0). In this Chapter, the numbers of MAPs collected are quantified as total area (mm^2) of particles captured by each collector.

4.2.2.3 Estimating dispersal kernels

*The reader is advised that a more detailed description of using the MAP data to estimate dispersal kernels is provided in **Chapter 2**.*

I define the dispersal kernel as the probability density function describing the spatial distribution of particles relative to a source location (e.g., Clark *et al.* 1998; Nathan *et al.* 2008). Observational estimates of the one-dimensional dispersal kernels were calculated for each study according to **Equation 2.11** in **Chapter 2**, $2\pi L\, p(L;T) = ae^{-aL}$, where the number (area) of particles at time T is primarily a function of in-water distance L between the source and the collector locations. This simple probability density function (p) with a single parameter (a) is derived in **Chapter 2**, and results in an e-folding scale of a^{-1}. The e-folding scale is simply the length scale where the number (area) of particles at distance L decreases by a factor of e. The resulting estimates are unique to the given sampling period T and its associated environmental conditions; variability related to, for example, the tidal cycles and (or) wind events can not be considered without replicate releases or a long-term steady release. Since this Chapter examines multiple MAP studies in the same geographical region, I am able to examine the effects of source location, time, and (or) changing environmental conditions among the dispersal kernel estimates.

4.2.3 Hydrodynamic modeling, virtual particle (VP) dispersal, and resulting MAP and VP comparisons

4.2.3.1 Summary of hydrodynamic modeling

*The reader is advised that a more detailed description of the hydrodynamic modeling system is provided in **Chapter 3**.*

I used a 3D prognostic hydrodynamic modeling system (Saucier and Chassé 2000; Chassé and Miller 2010) that incorporates a large-scale 4 km nominal-mesh model covering the entire Gulf of St. Lawrence region with a nested 200 x 200 m mesh model that envelops most of the Northumberland Strait (**Fig. A.4**). The low- and high-resolution models employ the same physics, though the time-stepping of the 4 km model is 5 minutes and that of the 200 m model is 30 seconds. While there are 32 *z*-layers in the 4 km model, the generally shallow depth of the Northumberland Strait limits the 200 m model to 8 *z*-levels; there is a surface-layer thickness of 2 m. As detailed in **Chapter 3**, the model is forced by bulk-formula heat flux, density, tides, observed winds, and observed runoff from the St. Lawrence River measured at Québec City, as well as runoff from other rivers based on monthly climatology interpolated to the model time step. Temperature and salinity are initialized at the beginning of a simulation and are free to evolve with time under forcing. Using the parameterization of Smagorinsky (1963), the model calculates horizontal eddy viscosities (K_H) that are then used in the momentum and advection-diffusion equations; a lower bound of 50 $m^2 s^{-1}$ ensures the numerical stability of the model.

4.2.2.2 Summary of VP dispersal

The reader is advised that a more detailed description of modeling VP dispersal is provided in ***Chapter 3****.*

Given that a MAP and VP comparison was conducted for only one (CT) of the four (SH, CT, CG, GB) studies examined in this Chapter, it follows that VP dispersal was estimated only for the CT study. Accordingly, the hydrodynamic model emulated a point-source release of 3.04 x 10^5 VPs in the same location off the coast of Cape Tormentine, on the same date, and over the same 12 h period as the MAP release. VPs were uniformly distributed throughout the 2 m surface layer. Corresponding model simulation results at 7, 8, and 9 d periods post-release were examined to match the same post-release periods associated with magnetic-collector retrievals. The model accommodates neither "beaching" nor vertical rise nor sink of VPs. A small-scale diffusivity (K_p), achieved by a random walk of VPs, was used to mimic the horizontal stirring processes that occur on sub-grid scales. Based on the K_p sensitivity results in **Chapter 3**, I employed a constant K_p value of 25 $m^2 s^{-1}$. The model estimated the total number (N) of VPs drifting through each grid-cell by calculating an exposition number (E) for each grid-cell (i,j) over the post-release study period (7, 8, or 9 d) according to **Equation 3.1** in **Chapter 3**.

4.2.3.3 Summary of MAP and VP comparisons

The reader is advised that a more detailed description of the MAP and VP comparison is provided in ***Chapter 3****.*

Since a MAP and VP comparison was already completed for one of the studies (MH) in the eastern Strait (**Chapter 3**), the CT study was chosen for an additional comparison due to its location in the interior Strait. There was not a way of estimating the absolute observed number (N) of MAPs captured at each magnetic-collector location as in **Chapter 3**, so the MAP particle area (mm^2) estimates were normalized to obtain proxy MAP number (N) estimates. Dividing the particle area captured in each collector by the maximum particle area captured among collectors resulted in a normalized MAP number estimate between 0 and 1 that allows me to make a direct number versus number comparison with the VP results consistent with that in **Chapter 3**. The exposition numbers (E_{ij}) for each grid-cell were converted to VP number (N) estimates by applying the proportionality constants from **Equation 3.3** in **Chapter 3**. Each collector-specific

N_{VP} estimate was again based on the average N_{VP} of that collector-specific grid-cell N_{VP} and the eight surrounding grid-cell N_{VP} values.

As none of the N_{MAP} and N_{VP} estimates were consistent with a normal distribution, they were logarithmically transformed to obtain distributions more consistent with normality for regression purposes. All uncertainties are presented as 95% confidence intervals.

4.3 Results

4.3.1 MAP dispersal

There were four separate particle dispersal studies:

1. In the Shediac (SH) study, MAPs were captured by 55 of the 56 magnetic-collectors that were recovered 7 to 9 days post-release; i.e., there was one zero return and two collectors were not recovered. The majority of MAPs among collectors were concentrated along and near the New Brunswick coast northwest and southeast of the source location, with elevated concentrations also to the north and northeast on the Prince Edward Island side of the Strait. In general, MAP concentrations did not decrease with increasing distance from the source location as expected (**Fig. 4.2**).
2. In the Cape Tormentine (CT) study, MAPs were captured by each of the 33 magnetic-collectors that were recovered 7 to 9 days post-release; i.e., there were no zero returns, though seven collectors were not recovered. The majority of MAPs captured among collectors were concentrated northwest of the source location and northeast along the coast of Prince Edward Island. In general, as in the SH study, MAP concentrations did not decrease with increasing distance from the source location (**Fig. 4.3**).

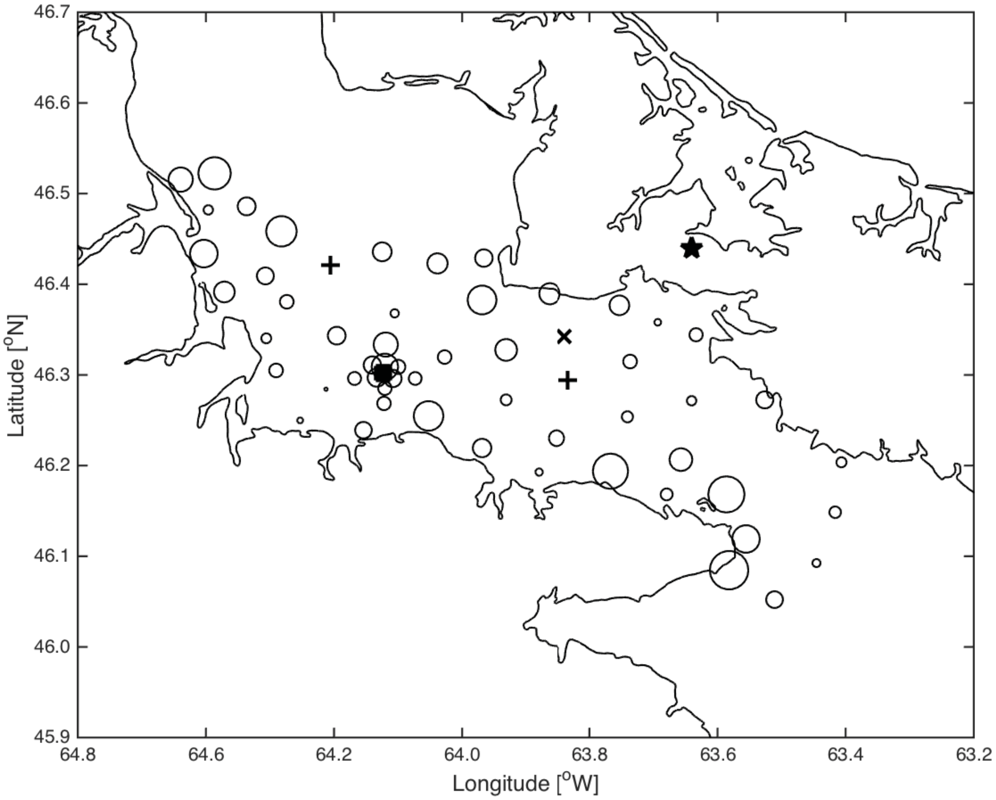

Figure 4.2 Coastline chart of the Northumberland Strait between Prince Edward Island and New Brunswick / Nova Scotia illustrating the location-specific relative number (linearly expanding-area circles) of MAPs captured among the recovered collectors. MAPs were released off the coast of Shediac (SH; square). An “x” denotes the locations of empty recovered collectors (i.e., zero returns) while the locations of collectors not recovered are denoted by crosses. The location of weather station Summerside, where wind speed and direction were recorded, is indicated with a star.

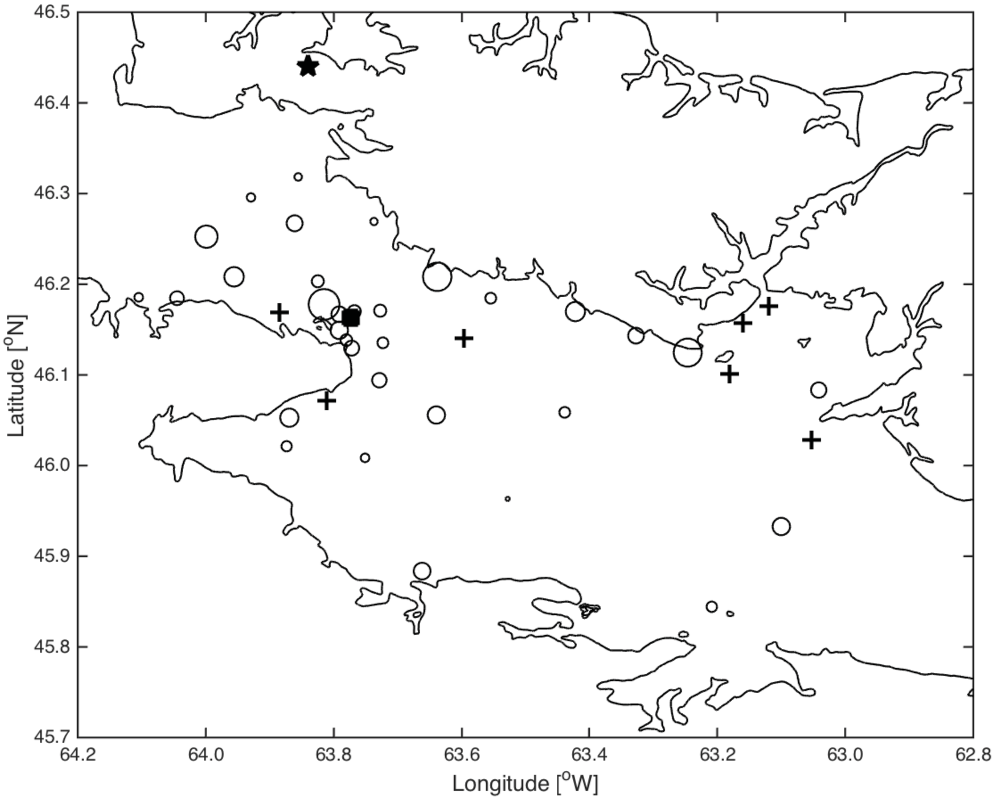

Figure 4.3 Coastline chart of the Northumberland Strait between Prince Edward Island and New Brunswick / Nova Scotia illustrating the location-specific relative number (linearly expanding-area circles) of MAPs captured among the recovered collectors. MAPs were released off the coast of Cape Tormentine (CT; square). The MAP locations of collectors not recovered are denoted by crosses. The location of weather station Summerside, where wind speed and direction were recorded, is indicated with a star.

3. In the Cape George (CG) study, MAPs were captured by 43 of the 60 magnetic-collectors that were recovered 6 to 7 days post-release; i.e., there were 17 zero returns and all collectors were recovered. The majority of MAPs among collectors were concentrated near the source location along the coast west of Cape George; however, concentrations were also elevated throughout the eastern Strait, northwest and northeast of the source location. Small concentrations of MAPs were also captured in a few of the collectors located within St. George's Bay. As in the MH study (**Chapter 3**), generally, though not systematically, fewer MAPs were captured with increasing distance from the source location (**Fig. 4.4**).

4. In the St. George's Bay (GB) study, MAPs were captured by 20 of the 69 magnetic-collectors that were recovered 7 to 10 days post-release; i.e., there were 49 zero returns and 1 collector was not recovered. The majority of MAPs among collectors were concentrated along the western and southern margins of St. George's Bay, although there were a small number of collectors with elevated concentrations both within the Bay and in the eastern Strait outside of the Bay. As in the MH (**Chapter 3)** and CG studies, generally, though not systematically, fewer MAPs were captured with increasing distance from the source location (**Fig. 4.5**).

In the SH and CT studies, I assumed that the spatial distribution of the missing collectors did not compromise the data analyses and my interpretation thereof. In the following comparison of MAPs and VPs in the CT study, the reader is reminded that the modeled estimates of VPs can potentially span a much larger domain that extends beyond that defined by the magnetic-collector array.

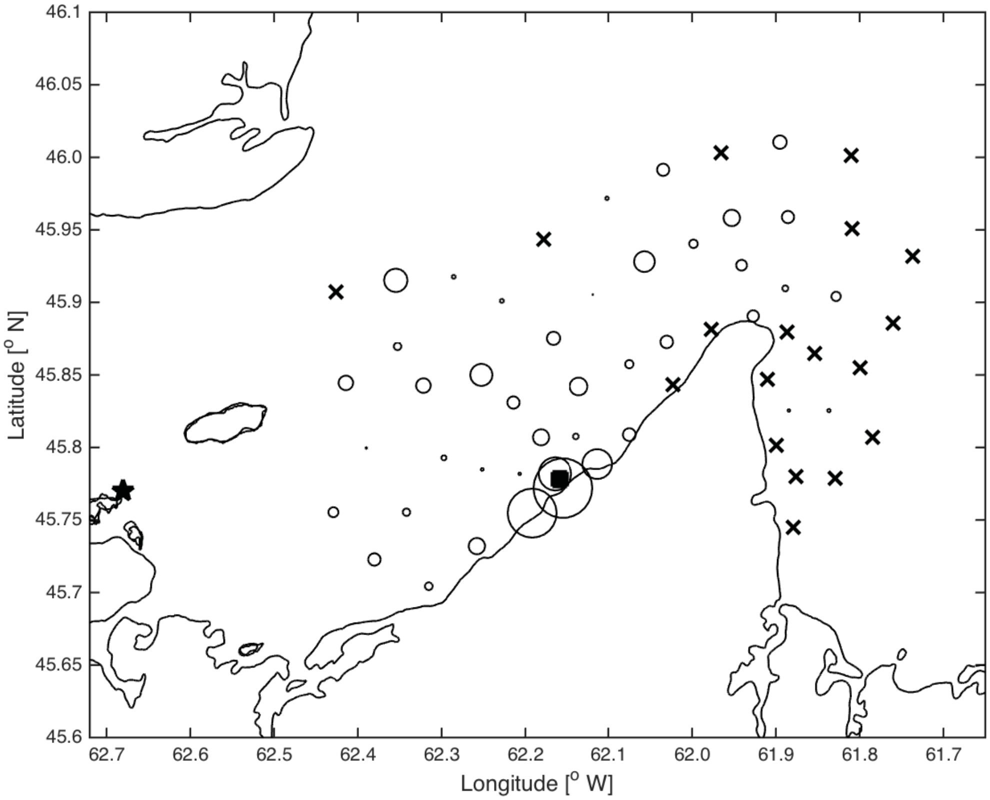

Figure 4.4 Coastline chart of the eastern Northumberland Strait between Prince Edward Island and Nova Scotia illustrating the location-specific relative number (linearly expanding-area circles) of MAPs captured among the recovered collectors. MAPs were released off the coast west of Cape George (CG; square). An "x" denotes the locations of empty recovered collectors (i.e., zero returns). The location of weather station Caribou Point, where wind speed and direction were recorded, is indicated with a star.

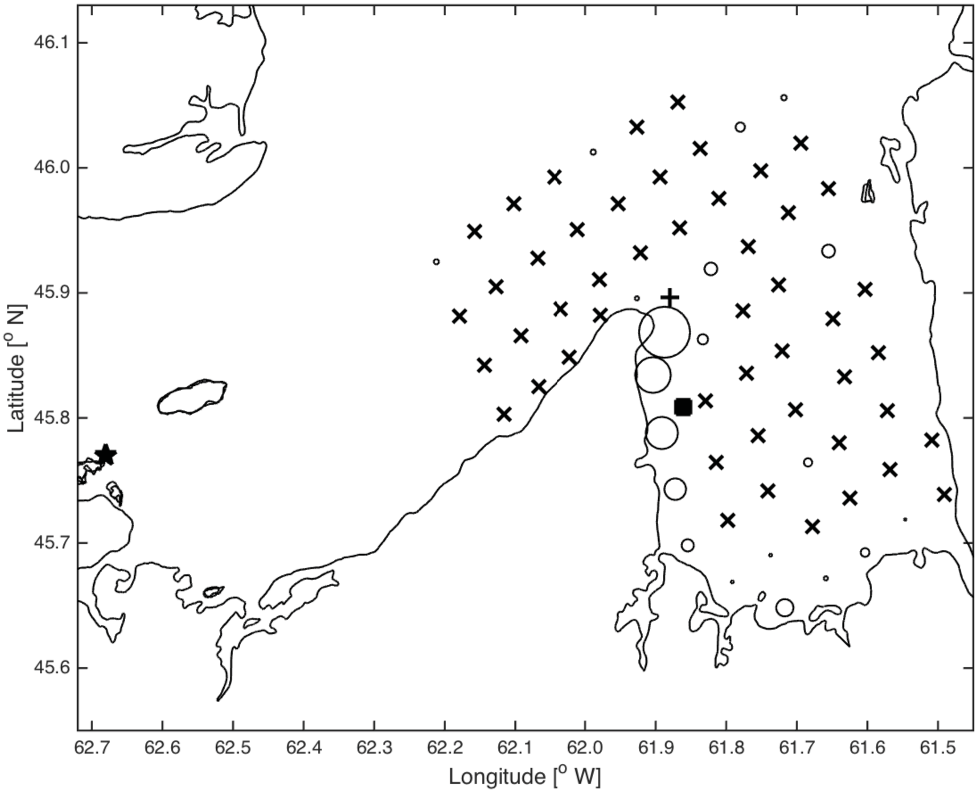

Figure 4.5 Coastline chart of the eastern Northumberland Strait between Prince Edward Island and Nova Scotia illustrating the location-specific relative number (linearly expanding-area circles) of MAPs captured among the recovered collectors. MAPs were released within St. George's Bay (GB; square). An "x" denotes the locations of empty recovered collectors (i.e., zero returns). The location of weather station Caribou Point, where wind speed and direction were recorded, is indicated with a star.

4.3.2 Estimating dispersal kernels

The four studies interestingly resulted in two different types of dispersal kernels. The number of MAPs captured by the magnetic-collectors in both the Shediac (SH) and Cape Tormentine (CT) studies remained approximately constant with in-water distance *L* from the respective source locations (**Figs. 4.6a**, **4.7a**). The resultant dispersal kernel for the MAPs released in the SH study provided an estimated *e*-folding scale of 344.83 km (**Fig. 4.6b**), while the dispersal kernel for the MAPs released in the CT study resulted in an estimated *e*-folding scale of 1.00 x 10^4 km (**Fig. 4.7b**). In both studies, the calculated uncertainties rendered the *e*-folding scale estimates were meaningless. I did not observe an exponential decay of MAPs with increasing distance from the source location in either study. Instead, the MAPs dispersed throughout the entire collector domain at all scales, essentially resulting in an infinite dispersal kernel; this is likely related to their dispersal through the restricted passage of the Northumberland Strait combined with tidal and wind influences (addressed further below in Discussion). Alternatively, the number of MAPs captured by the magnetic-collectors in both the Cape George (CG) and St. George's Bay (GB) studies decreased exponentially with in-water distance *L* from the respective source locations (**Figs. 4.8a**, **4.9a**), as was expected and also observed in the MH study (**Chapter 3**; see **Fig. 3.7**). The resultant dispersal kernel for the MAPs released in the CG study provided an estimated *e*-folding scale of 8.09 km with lower and upper 95% confidence limits of 5.68 and 14.03 km, respectively (**Fig. 4.8b**). The dispersal kernel for the MAPs released in the GB study resulted in a comparable *e*-folding scale estimate of 13.44 km with lower and upper 95% confidence limits of 7.32 and 81.30 km, respectively (**Fig. 4.9b**). It should be noted that the CG and GB estimates are also similar to the *e*-folding

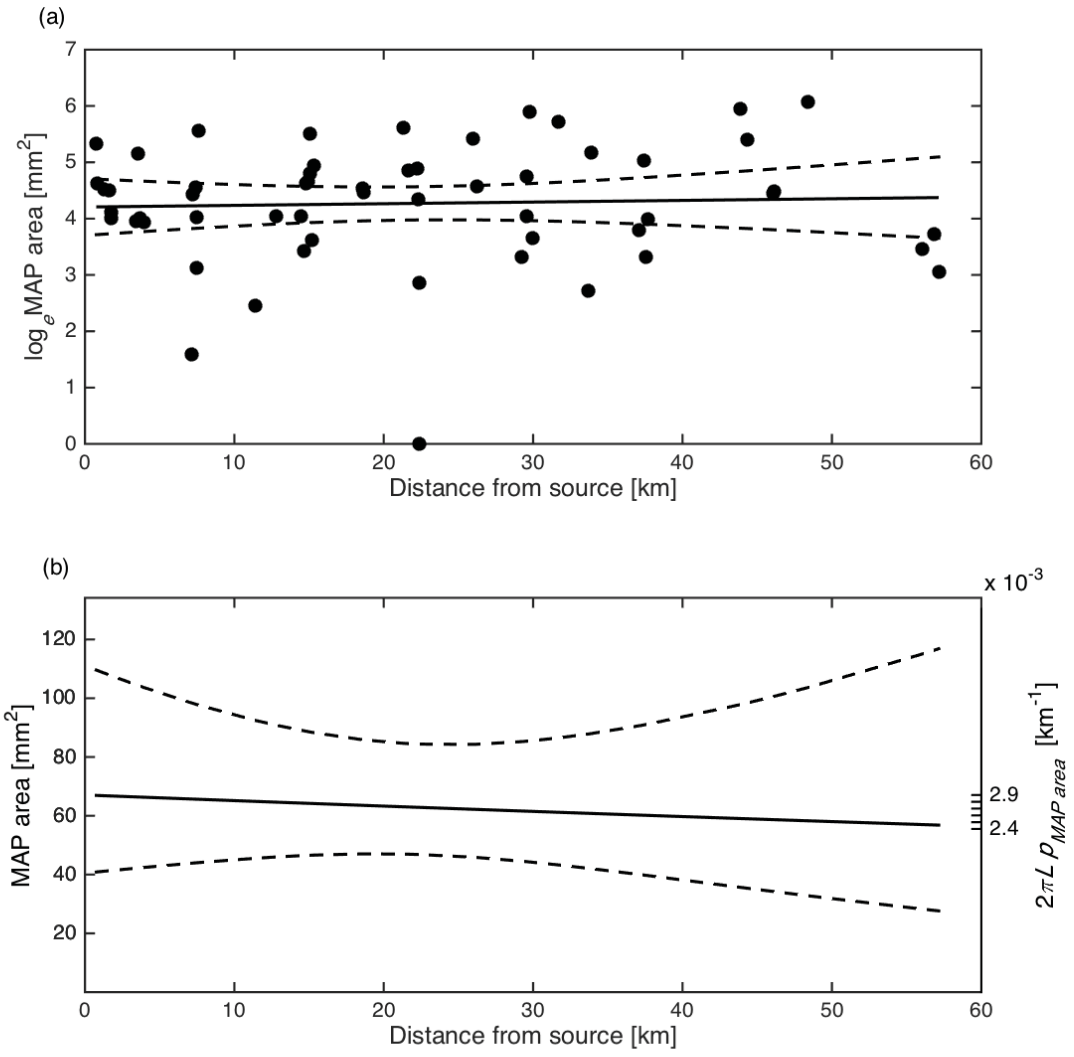

Figure 4.6 Log-linear (a) and exponential decay (b) of MAP area (mm^2) as a function of distance L (km) from the source location off the coast of Shediac (SH). The regression model [log$_e$MAP area = 4.21 – 2.9 x 10^{-3} L; r^2 = 1.80 x 10^{-3}; p = 0.75] in (a) is illustrated by a solid line with the upper and lower 95% confidence limits around the model (dashed lines) fitted to the MAP area estimates. The exponential decay [MAP area = 6.74 x 10^1 $e^{-2.9 \times 10^{-3} L}$] in (b) is illustrated by a solid line with the upper and lower 95% confidence limits (dashed lines). The exponential decay (solid line) can be interpreted as $2\pi L\ p_{MAP}$ (right ordinate) with an e-folding scale of 344.83 km that has meaninglessly large upper and lower 95% confidence limits (dashed lines).

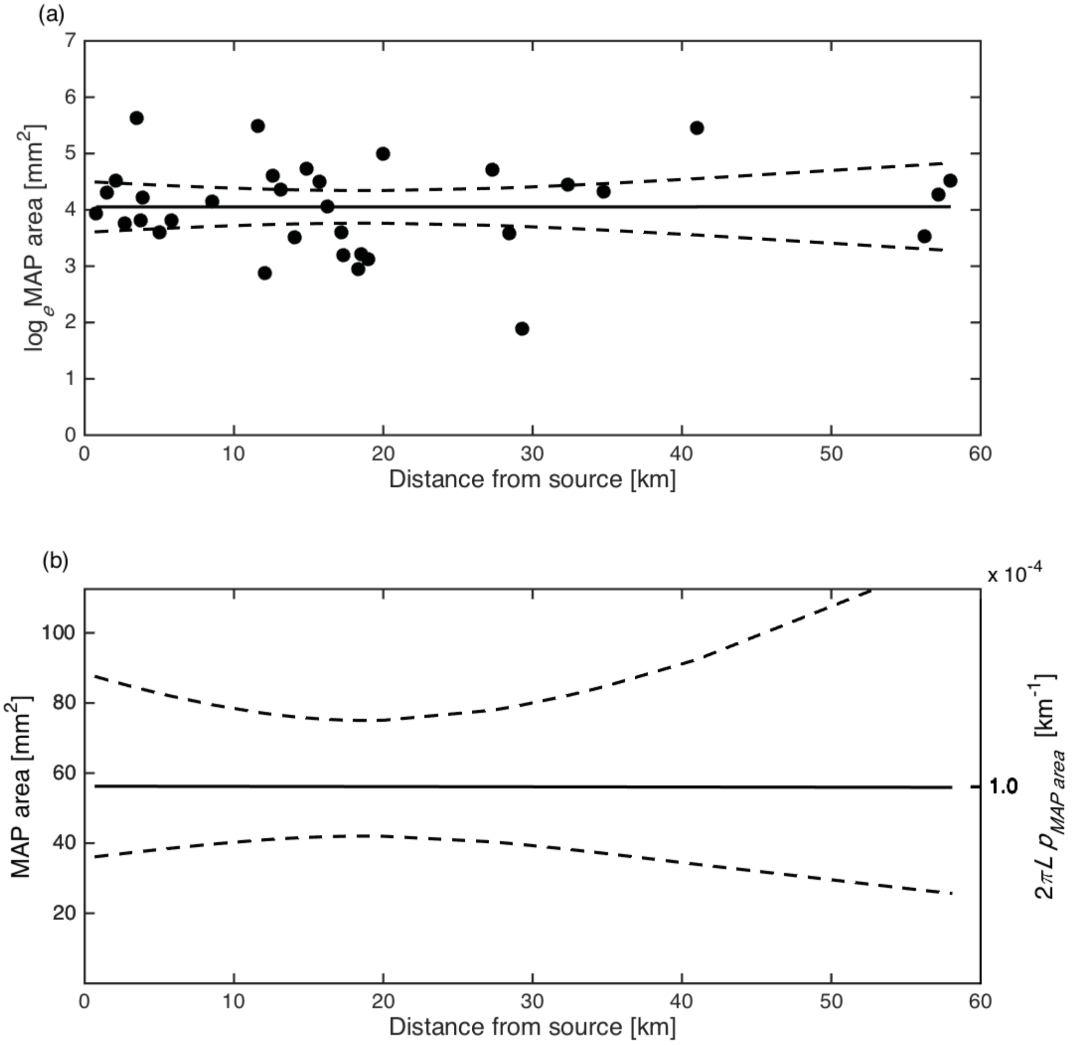

Figure 4.7 Log-linear (a) and exponential decay (b) of MAP area (mm^2) as a function of distance L (km) from source location off the coast of Cape Tormentine (CT). The regression model [$\log_e$MAP area $= 4.03 - 1.00 \times 10^{-4} L$; $r^2 = 3.19 \times 10^{-6}$; $p = 0.99$] in (a) is illustrated by a solid line with the upper and lower 95% confidence limits around the model (dashed lines) fitted to the MAP area estimates. The exponential decay [MAP area $= 5.63 \times 10^1 e^{-1.00 \times 10\text{-}4\, L}$] in (b) is illustrated by a solid line with the upper and lower 95% confidence limits (dashed lines). The exponential decay (solid line) can be interpreted as $2\pi L\, p_{MAP}$ (right ordinate) with an e-folding scale of 1.00×10^4 km that has meaninglessly large upper and lower 95% confidence limits (dashed lines).

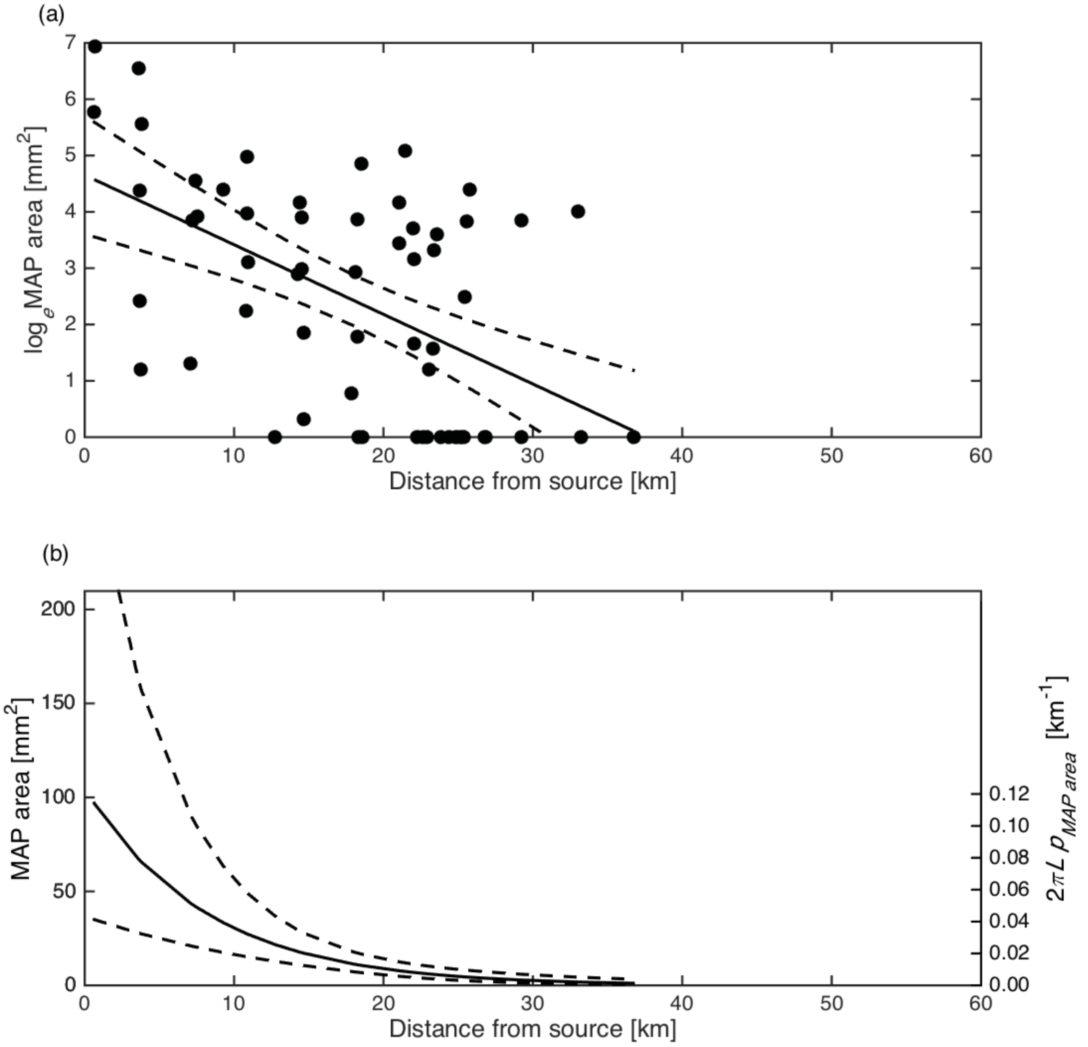

Figure 4.8 Log-linear (a) and exponential decay (b) of MAP area (mm^2) as a function of distance L (km) from the source location west of Cape George (CG). The regression model [log$_e$MAP area = 4.65 – 0.12 L; $r^2 = 0.28$; $p < 0.001$] in (a) is illustrated by a solid line with the upper and lower 95% confidence limits around the model (dashed lines) fitted to the MAP area estimates. The exponential decay [MAP area = $1.05 \times 10^2\, e^{-0.12L}$] in (b) is illustrated by a solid line with the upper and lower 95% confidence limits (dashed lines). The exponential decay (solid line) can be interpreted as $2\pi L\ p_{MAP}$ (right ordinate) with an e-folding scale of 8.09 km that has upper and lower 95% confidence limits of 14.03 and 5.68 km.

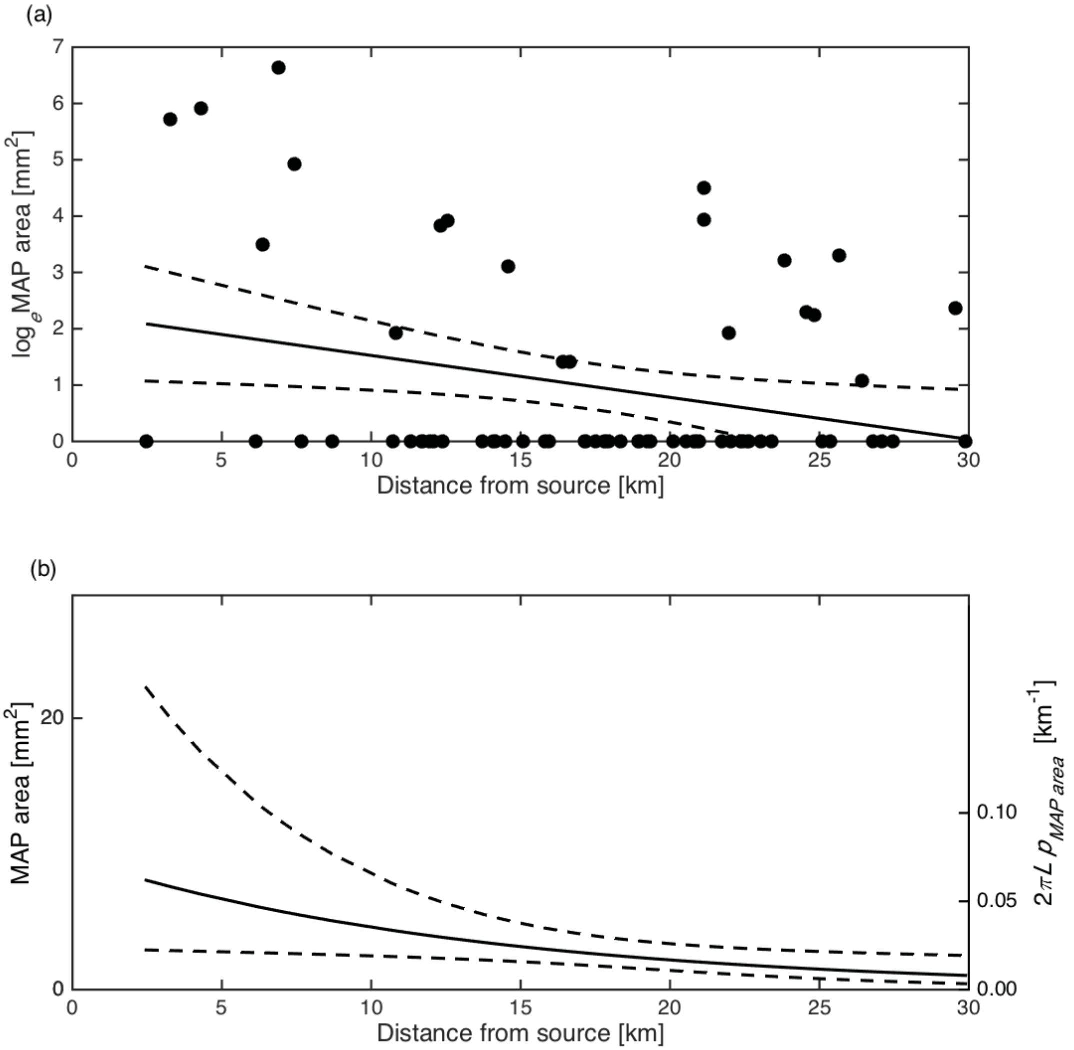

Figure 4.9 Log-linear (a) and exponential decay (b) of MAP area (mm^2) as a function of distance L (km) from the source location in St. George's Bay (GB). The regression model [$\log_e$MAP area = 2.27 – 7.44 x 10^{-2} L; r^2 = 7.85 x 10^{-2}; p = 1.97 x 10^{-2}] in (a) is illustrated by a solid line with the upper and lower 95% confidence limits around the model (dashed lines) fitted to the MAP area estimates. The exponential decay [MAP area = 9.69 $e^{-7.44 \text{ x } 10^{-2} L}$] in (b) is illustrated by a solid line with the upper and lower 95% confidence limits (dashed lines). The exponential decay (solid line) can be interpreted as $2\pi L\, p_{MAP}$ (right ordinate) with an e-folding scale of 13.44 km that has upper and lower 95% confidence limits of 81.30 and 7.32 km.

scale (5.19–11.44 km) that was observed in the MH study in **Chapter 3** (**Fig. 3.7b**).

As in **Chapter 3**, the reader is reminded that the 95% confidence intervals shown in **Figures 4.6b–4.9b** are associated with the exponential function, MAP area, and not with the probability density function, $2\pi L\ p_{MAP\ area}(L)$. The 95% confidence intervals around $2\pi L\ p_{MAP\ area}(L)$ (not shown) were smaller than those around MAP area since $p_{MAP\ area}$ is affected only by uncertainty in the slope *a*, whereas both the slope and intercept, and their respective uncertainties, affect MAP area.

4.3.3 VP dispersal and resulting MAP and VP comparisons

4.3.3.1 VP dispersal

The VP exposition number estimates for the CT study (**Fig. 4.10**), based on a constant K_p of 25 $m^2\ s^{-1}$, reflected some aspects of the observed MAP capture number estimates among collectors (**Figs. 4.3**, **4.10**). I chose this K_p value due to my result in **Chapter 3** that a constant value of 25 $m^2\ s^{-1}$ over the entire study period appears to best represent a space and time average of the small-scale diffusivity (addressed further below in Discussion). When overlaying the MAP results on the VP results in **Figure 4.10**, a visual comparison indicates that the model effectively reflected the general features of the observed MAP field both near the source and up the Strait to the northwest, but it did not capture the MAP field down the Strait to the southeast. Within the confines of the collector array, the model tended to show high exposition numbers of VPs in areas northwest of the source where the magnetic-collectors captured high numbers of MAPs; however, MAPs were transported down the Strait much further than VPs in the model. It

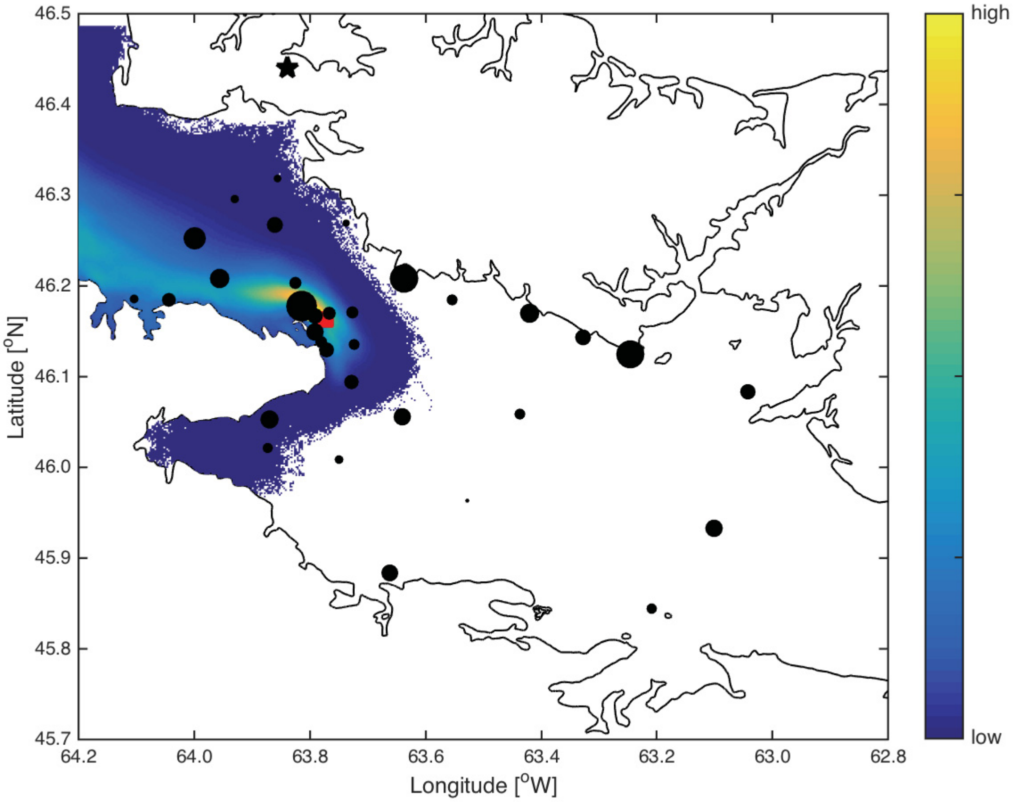

Figure 4.10 Coastline chart of the Northumberland Strait between Prince Edward Island and New Brunswick / Nova Scotia and scale bar illustrating the exposition number (E_{ij}; low to high) of VPs (released off the coast of Cape Tormentine; red square) within each 200 m^2 grid cell across the model domain as of 08:15 h on 06 July 2009 and based on a constant K_p of 25 m^2 s^{-1}. The location-specific relative numbers of MAPs captured among the recovered collectors are shown in black (linearly expanding-area circles). The location of weather station Summerside, where wind speed and direction were recorded, is indicated with a star.

is again important to note that I can not compare MAP and VP results in the locations where I did not deploy collectors (i.e., up the Strait northwest of the collector array).

4.3.3.2 MAP and VP comparisons

Based on a constant K_p of 25 m^2 s^{-1}, there was no significant relationship between N_{VP} and N_{MAP} when all corresponding collector and grid-cell locations were included (**Fig. 4.11**), and thus no justification for completing a regression. This is not surprising given the model results in **Figure 4.10** where so many of the collector-specific grid-cells estimated zero VPs. To achieve an appropriate N_{VP} and N_{MAP} comparison at equivalent locations where there are both VP and MAP data, I removed from the relation all points that represented empty model grid-cells. This essentially constrains my analyses to the left hand side of **Figure 4.10**, and thus to smaller space and time scales (i.e., dispersal in the near-field over the beginning of the study). While there is some improvement, it is not significant (**Fig. 4.12**). Using the constrained data, I also calculated a dispersal kernel for the near-field. In this limited dataset, the number of VPs estimated by the model decreased exponentially with distance from the source L. With a constant K_p of 25 m^2 s^{-1}, the N_{VP} regression on L (**Fig. 4.13a**) provided an *e*-folding scale estimate of 3.90 km with upper and lower 95% confidence limits of 31.35 and 2.08 km, respectively (**Fig. 4.13b).** This contradicts the MAP results where concentration remained approximately constant with increasing distance from the source L (**Fig. 4.7**), even when only viewing results in the near-field. Again, the reader is reminded that the 95% confidence intervals shown in **Figure 4.13b** are associated with the exponential function, N_{VP}, and not with the probability density function, $2\pi L\, p_{VP}(L)$.

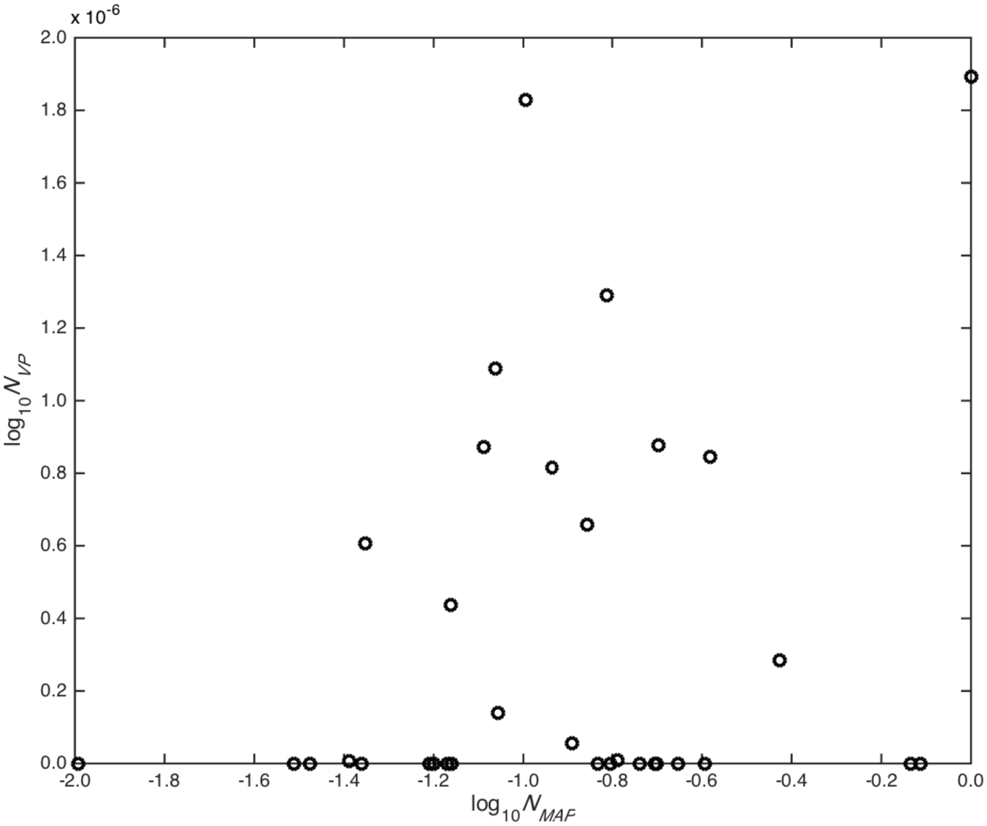

Figure 4.11 Log-log relation of N_{VP} as a function of N_{MAP} where N_{VP} modeling used a constant K_p of 25 m^2 s^{-1}. When all collector-specific grid-cell locations are considered, there is no relationship.

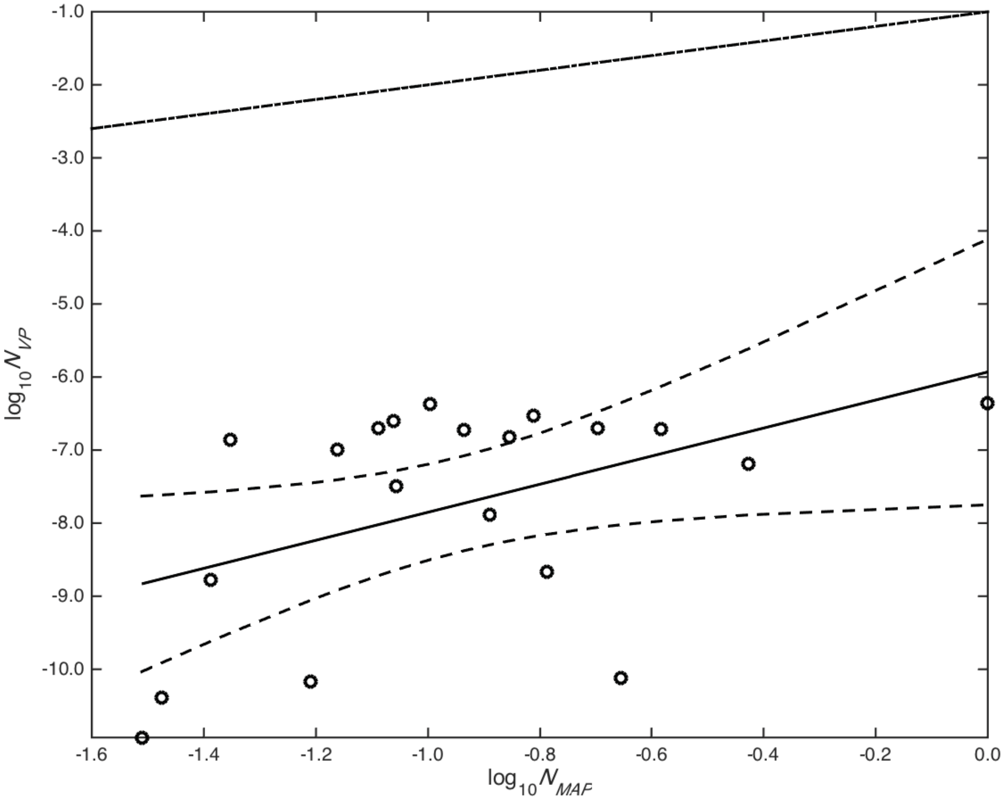

Figure 4.12 Log-log relation of N_{VP} as a function of N_{MAP} where N_{VP} modeling used a constant K_p of 25 m^2 s^{-1} and all points that represented empty model grid-cells were removed. The regression model [$\log_{10}N_{VP} = -4.93 + 1.92 \log_{10}N_{MAP}$; $r^2 = 2.19 \times 10^{-1}$; $p = 3.73 \times 10^{-2}$] is illustrated by a solid line with the 95% confidence interval around the model (dashed lines) fitted to the estimates. The 1:1 relation is illustrated as a dashed-dotted line.

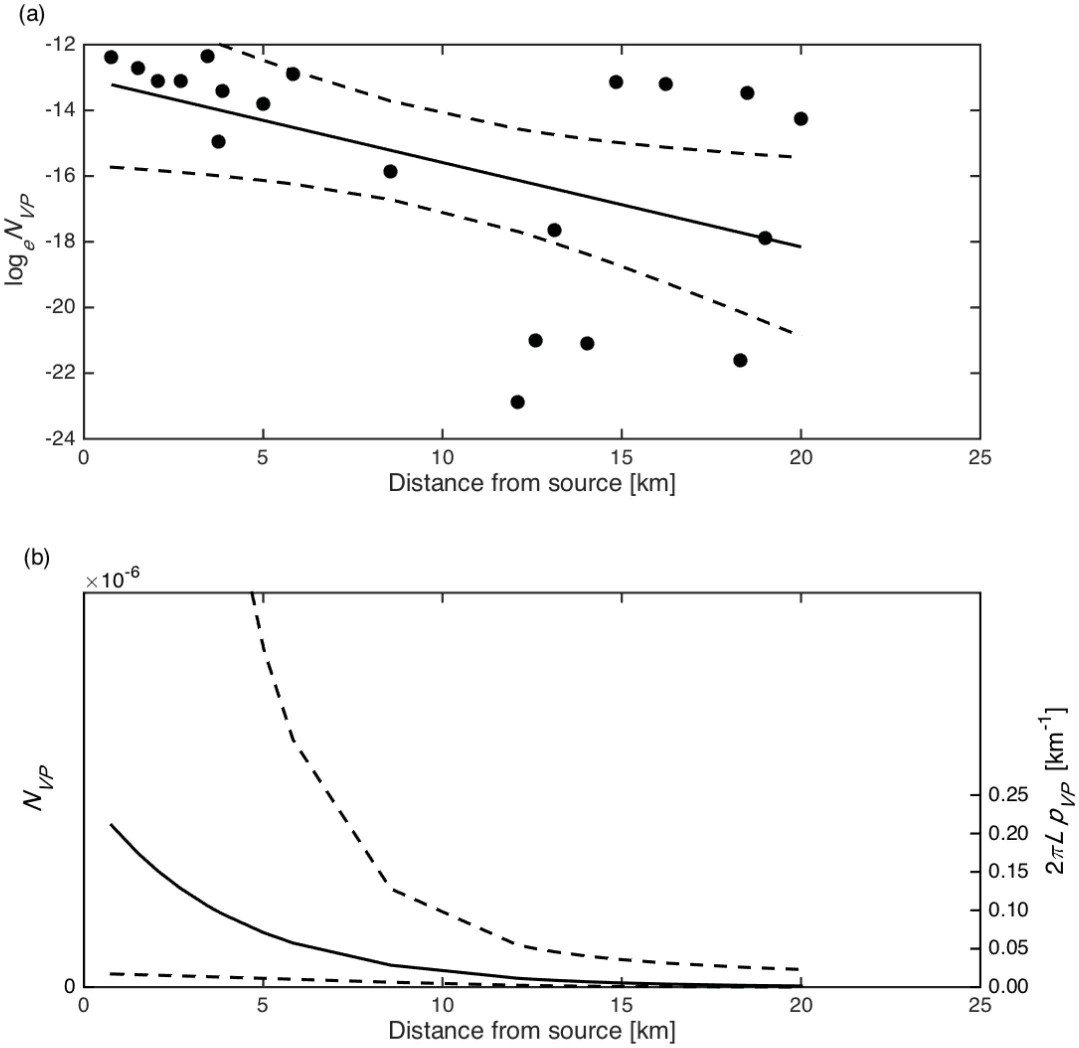

Figure 4.13 Log-linear (a) and exponential decay (b) of N_{VP} as a function of distance L (km) from the source location off the coast of Cape Tormentine (CT). The regression model [$\log_e N_{VP}$ = -13.02 – 2.57 x 10^{-1} L; r^2 = 2.42 x 10^{-1}; p = 2.75 x 10^{-2}] in (a) is illustrated by a solid line with the upper and lower 95% confidence limits around the model (dashed lines) fitted to the N_{VP} estimates. The exponential decay [N_{VP} = 2.22 x10^{-6} $e^{-2.57 \text{ x } 10\text{-}1\ L}$] in (b) is illustrated by a solid line with the upper and lower 95% confidence limits (dashed lines). The exponential decay (solid line) can be interpreted as $2\pi L\ p_{VP}$ (right ordinate) with an e-folding scale of 3.90 km that has upper and lower 95% confidence limits of 31.35 and 2.08 km.

4.4 Discussion

4.4.1 Estimating dispersal kernels

I have again demonstrated the ability of the MAP and magnetic-collector system to empirically estimate the passive component of a particle dispersal kernel in the coastal ocean of the Northumberland Strait. Interestingly, I observed two different types of dispersal kernel estimates that require separate examination and interpretation. In the SH and CT studies, I obtained infinite dispersal kernel estimates with extremely large uncertainties (**Figs. 4.6**, **4.7**). This is not what I expected and not what I observed in the MH study in **Chapter 3**. An infinite dispersal kernel symbolizes mixing throughout the entire domain at all scales, and the dispersed MAP fields with no zero returns shown in **Figures 4.2** and **4.3** corroborate this argument. In these two studies, the dispersal kernel estimates are of little value as MAPs disperse throughout the entire Strait over the respective study periods. It should be noted that there are likely decays in the SH and CT dispersal kernels as shown in the MH, CG, and GB studies; however, it would only be observed at a much longer time scale.

The infinite dispersal kernels observed in these two studies are likely related to particle dispersal through the narrow passage of the interior Northumberland Strait. The strong surface tidal currents in this constricted portion of the Strait (Lauzier 1965; Lu *et al.* 2001; Saucier *et al.* 2003; Chasse and Miller 2010; Hrycik *et al.* 2013), combined with the wind influences on the residual flow from west to east (see **Figs. B.1**, **B.2**), created the MAP fields observed in both the SH and CT studies. Residual surface non-tidal drift from the mainland to Prince Edward Island, observed in both studies, is known to be one of the features of the spring and summer seasons within the Northumberland Strait, as first observed by Lauzier (1965) with drift bottle experiments. Similar patterns were observed in the wind field velocity components (*u*, *v*) and wind speed during both studies. Throughout the first half of both studies, winds were mostly blowing up the Strait; however, during the second half of both studies, winds were blowing across the Strait (**Figs. B.1**, **B.2**). These patterns are reflected in the observed MAP fields, where particles dispersed from the mainland to the coast along Prince Edward Island as the residual current transported particles from west to east.

As in **Chapter 3,** the physical connectivity estimates can be applied to any passive planktonic organism in the surface waters of this region, and the results I obtained in the interior Strait have serious implications to propagule dispersal. According to my results, any passive egg or larva in the surface layer will disperse everywhere within the Strait in approximately one week. This is especially concerning for invasive species that rely on early life-stage dispersal and may thrive in the sGSL, such as the invasive vase tunicate (*Ciona intestinalis*; Carver *et al.* 2003; Locke *et al.* 2007; Ramsay *et al.* 2008; Daigle and Herbinger 2009; Lutz-Collins *et al.* 2009; Ramsay *et al.* 2009; Kanary *et al.* 2011; Fitridge *et al.* 2012; Collin *et al.* 2013) and the European green crab (*Carcinus maenas*; Cohen *et al.* 1995; Grosholz and Ruiz 1996; Audet *et al.* 2003; Roman 2006; Klassen and Locke 2007; Therriault *et al.* 2008; Compton *et al.* 2010; Haarr and Rochette 2012; Cosham *et al.* 2016). Since I already discussed the vase tunicate invasion in **Chapter 3**, as an illustrative example, I will focus here on the European green crab, a highly adaptable, opportunistic, and successful invader that likely has not reached its full invasion potential (Roman 2006; Compton *et al.* 2010). The sGSL contains abundant coastal and estuarine habitat and exhibits warm summer temperatures that provide ideal conditions for the further establishment and success of the European green crab outside its current range (most authors cited above). Once a source population is established, as one currently is within the sGSL, oceanographic transport mechanisms are the main vector for coastal larval dispersal (Jamieson *et al.* 1998; Hidalgo *et al.* 2005; Roman 2006). As such, it is important to empirically estimate the potential scales of dispersal from the present distribution, and use these data to test the biophysical models that currently predict the rate of expansion and spatial implications of further invasions. With this information, an appropriate contingency plan can be implemented to contain further spread of this species. As the European green crab interacts with its environment, there is the risk of cascading impacts on habitat structure, trophic interactions, and biodiversity. Along with the threatened integrity of coastal ecosystems, there is also the likelihood of economic consequences to the local fisheries and industry. Based on the impacts of green crab elsewhere owing to their extensive global invasion history, there is cause for great concern of dispersal to additional waters throughout the Gulf of St. Lawrence and potentially to other coastal waters along the Atlantic coast of Nova Scotia (Roman 2006; Klassen and Locke 2007; Therriault et al. 2008).

The second type of dispersal kernel I observed in the CG and GB studies (**Figs. 4.8**, **4.9**) was similar to the result I obtained in the MH study (**Chapter 3**; **Figs. 3.7**). The number of MAPs in all three studies exponentially decreased with distance from the source location *L* (**Figs. 3.7a**, **4.8a**, **4.9a**). Further, when taking the 95% confidence limits into account, all three estimates are comparable. The dispersal kernel estimates in the MH (7.15 km; see **Fig. 3.7b**) and CG (8.09 km; see **Fig. 4.8b**) studies were essentially identical and I thus conclude that there is a generic dispersal kernel that is applicable to the eastern Northumberland Strait. As in MH, I also see a more rapid decay in N_{MAP} estimates in the near-field of the CG study; this is likely due to the same MAP issues as discussed in **Chapter 3** and below. The CG results appear to be highly reflective of the observed variable winds during the study (**Fig. B.3**). MAPs were first transported in high concentrations toward shore near the source, followed by dispersal into the eastern Strait to the north and northwest during a period of strong southerly winds and then back to the east, resulting in small MAP concentrations near the mouth of St. George's Bay and inside the Bay.

While the dispersal kernel result from the GB study (**Fig. 4.9**) is comparable to the results from the studies in the eastern Strait (**Figs. 3.7**, **4.8**), there are some key differences, as the MAP release occurred within the Bay. The abundance of zero returns (i.e., empty recovered collectors) indicates that the MAPs dispersed in a streaky manner once transported away from the western margin of the Bay. There were collectors with MAPs captured in the central and eastern Bay, as well as outside the Bay in the eastern Strait (**Fig. 4.5**). Recirculation of surface layer water within the Bay is a possibility when the Bay is highly stratified during the summer months (Petrie and Drinkwater 1978). Water, and any MAPs within it, leaving the Bay on the western side and moving east could re-enter the Bay on the eastern side. This is a possible explanation for the elevated MAP concentrations observed in the eastern Bay. Petrie and Drinkwater (1978) documented a persistent anti-cyclonic eddy in the mean surface circulation that would act as a retention mechanism for particles within the Bay; however, recent observations (Lesperance *et al.* 2011a,b) have shown that the circulation in the Bay is more variable, shifting between anti-cyclonic and cyclonic patterns due to wind influences. Wind serves to modulate the interaction between the Bay and the Northumberland Strait, so it follows that if even the anti-cyclonic eddy is present and closed, water could still be exchanged between the Bay and the Strait through tidal- or wind-driven currents. There is especially the potential for a large exchange of water under strong wind conditions (Harding *et al.* 1982). I observed a large number of MAPs being transported toward the mouth of the Bay and then some dispersing out into the eastern Strait. This is reflective of the observed winds blowing mostly to the north and northeast during this study (**Fig. B.4**), and Drinkwater (1989) did find that the Bay's residual circulation can be altered for weeks after wind events. Further, with interacting physical and biological mechanisms, it is easy to see how spatial heterogeneity, or "patchiness" (e.g., Franks 1992; Yamazaki 1993; Natunewicz *et al.* 2001; Martin 2003; Thackeray *et al.* 2004; Daigle *et al.* 2016) of distributions can form and (or) persist within the Bay. Planktonic early-life stages experience very different hydrodynamic conditions despite relatively small distances between spawning sites within the Bay (Daigle *et al.* 2016), and as a result, the wind-driven circulation dominates transport, with larval behavior playing a relatively minor role in this Bay and similar physical environments (Taggart and Leggett 1987; Hudon and Fradette 1993; Werner *et al.* 1997; Natunewicz *et al.* 2001; Thackeray *et al.* 2004; Petrone *et al.* 2005; Tilburg *et al.* 2006; Savina *et al.* 2010; Daigle *et al.* 2016)

In summary, my earlier suggestion that the simplified one-dimensional dispersal kernel may be representative of the entire Northumberland Strait region is not true. While I observe a generic dispersal kernel in the eastern Strait, it does not accurately represent the dynamics of the interior Strait. A dispersal kernel estimate in the interior Strait is of little value, since I have shown that any particles or propagules in the surface layer would disperse throughout the entire Strait in a matter of days. The varying dispersal kernel estimates in this system again suggest, as in **Chapter 3**, that semi-enclosed and nearshore waters must be considered separately from open ocean waters (e.g., Nickols *et al*. 2012).

4.4.2 MAP and VP comparisons

With the same method of MAP and VP comparison as in the MH study (**Chapter 3**), I have shown that the spatial distributions of the MAP capture number estimates and the VP exposition number estimates in the CT study only agree well in the near-field (**Fig. 4.10**). This indicates that the model predications generally reflect the Lagrangian particle displacements measured using the MAP collectors near the source location and at shorter space and time scales, but that the model cannot adequately emulate the MAP results in the far-field as time evolves. This is why a VP dispersal kernel can only be estimated in the near-field (**Fig. 4.13**) at collector-specific grid-cell locations where there are both MAP and VP data. The divorce of MAP and VP results in the far-field is due to some unresolved issue in the model and (or) in how the modeled results are used; for example, in its inability to accurately represent the observed winds and (or) in the inclusion of wind-induced shear within the surface layer. As stated in **Chapter 3**, the wind field forcing is not highly resolved due to the nature of the wind data used for forcing. As a result, the model does not capture the advective component of dispersal properly in the CT study, which explains why the VPs did not disperse as far east as the MAPs. It is conceivable that advective forces are large and important in systems with strong, coherent, alongshore flows (e.g., Werner *et al.* 1997; Kaplan 2006; Aiken *et al.* 2007;

Hoyer *et al.* 2015). While the MAP and VP results do not agree as well as in the MH study, I see the same time-related discrepancies corresponding to the near- and far-field in both studies. In MH and CT, I observed high concentrations of MAPs in the near-field, close to the respective source locations and along the coast, with lower concentrations in the far-field. The far-field effect is clear when visually comparing the low concentrations of VPs throughout the eastern Strait in the MH study (i.e., the blue in **Fig. 3.4**) and the low concentrations of VPs in what would be considered the far-field in the CT study (i.e., the blue in **Fig. 4.10**).

It stands to reason that the discrepancy in the far-field may also be due to a poorly chosen K_p value in the model. As mentioned above, I chose a constant K_p value of 25 m^2 s^{-1} due to my result in **Chapter 3** that this value over the entire study period appears to best represent a space and time average of the small-scale diffusivity; however, there is no "best" K_p value when modeling this system and the true K_p is varying in space and time. If a larger K_p value were employed in the model, how would this change VP dispersal? As observed in the exposition number results at varying small-scale diffusivities in **Chapter 3** (**Figs. 3.4**, **A.5–A.8**), the overall shape of the highly concentrated VP patch remains intact with increasing K_p. The most notable change as the K_p value increases exists in the far-field, specifically in the distance that the VPs disperse within the domain – the higher the value of K_p, the more dispersed the far-field becomes (i.e., the entire domain is blue in **Fig. A.7**, indicating that there are low concentrations of VPs everywhere in the far-field). Therefore, if I used a higher K_p value in the CT study, I would expect the far-field to extend beyond the range shown at a constant K_p value of 25 m^2 s^{-1} (**Fig. 4.10**). While a higher K_p value may cause the VPs to disperse further down the Strait, it is unlikely that they would advect as far east as I captured MAPs. While increasing the K_p value from a constant of 25 m^2 s^{-1} (**Fig. 3.4**) to a minimum of 80 m^2 s^{-1} (**Fig. A.7**) results in a more dispersed VP field, changes to the extent of its range are minimal. Without appropriate wind influences in the model, the advective component of dispersal within the Strait cannot be obtained. Given these arguments, I believe the choice to use a constant K_p of 25 m^2 s^{-1} is adequate here.

As I have shown in **Chapter 3**, dispersal rates are especially sensitive to the "tail" of the dispersal kernel and it is often within this "tail" that modeling dispersal becomes problematic (Kot *et al.* 1996; Clark *et al.* 1998; Higgins and Richardson 1999; Bullock and Clarke 2000; Cain *et al.* 2000; Cowen *et al.* 2000; Bossenbroek *et al.* 2001; Nathan *et al.* 2003; Shanks et al. 2003; Nathan 2005; Trakhtenbrot *et al.* 2005; Klein *et al.* 2006; Dyer 2007; Skarpaas and Shea 2007; Nathan *et al.* 2008; Okubo and Levin 2010; Gillespie *et al.* 2012; Putman and He 2013; Simpson *et al.* 2014; García and Borda-de-Água 2017; Jordano 2017). While the MAP dispersal kernel in the CT study did not exhibit a "tail" as that in the MH study, the MAP and VP comparison results show that modeling the far-field is an issue. There is no relationship in the number versus number comparison when all collector-specific grid-cells were included (**Fig. 4.11**) and only a non-significant improvement when empty grid-cell locations were removed (**Fig. 4.12**). This raises a huge concern when using such a model to predict the long-range dispersal of propagules in the near-surface mixed layer. Spatially conservative dispersal estimates can have significant consequences in the management of any species (e.g., **Chapter 3**; Okubo and Levin 2010; Hrycik *et al.* 2013), but are substantial for invasive species. When considering the European green crab example discussed above, it would be extremely difficult to mitigate any future impact of its expansion if individuals dispersed much further than predicted. The life-history characteristics of the green crab also act to enhance long-distance natural dispersal (Roman 2006; Therriault *et al.* 2008), so the potential implications in this case could be severe.

Long-distance dispersal is also influenced by sporadic events, and single wind episodes and (or) storms can extend the reach of dispersal in the far-field. Further, it has been found that when dispersal contains both short- and long-distance components, it is the long-distance (far-field) dispersal of just a few individuals that governs the invasion speed, even though long-distance dispersal events are rare (e.g., Goldwasser *et al.* 1994; Kot *et al.* 1996; Clark *et al.* 1998; Neubert and Caswell 2000; Shigesada and Kawasaki 2002; Okubo and Levin 2010; Hoyer *et al.* 2015). The disproportionate influence of long-distance dispersal on the range and rate of geographic spread makes measuring and modeling dispersal even more challenging, as far-field dispersal patterns may vary on a case-by-case basis. As already seen in **Chapter 3**, events may not be well modeled due to the nature of the wind field data used for forcing.

MAP behavior in the field is also a concern, as it was in **Chapter 3**. As detailed in the MH study, it is possible that there are MAP losses from the surface layer over time due to sinking and (or) beaching. It is also possible that the physical characteristics of the MAPs cause them to experience shear dispersion, as discussed in detail in **Chapter 3**. The MAPs released in the CT study were from the same batch as those released in the MH study (see **Table 2.1**), so it is likely that they behave similarly and are thus affected by the same regional processes. Given the potential of MAP behavior, it was an initial concern that the lack of decay with increasing distance from the source in the CT study was a "fluke;" however, this concern was alleviated after examining the results of the SH study. The results from these two studies in the interior Northumberland Strait are similar despite using different batches of MAPs and occurring in different years.

The coastal waters of the Northumberland Strait and the sGSL are rapidly changing, with predator-prey interactions in flux and invasive species successfully colonizing at an unprecedented rate (Savenkoff *et al.* 2007; Benoît and Swain 2008; Bundy *et al.* 2009; Hanson *et al.* 2014). It is unknown how these changes and others such as climate change may impact ecosystem structure and function, as well as the fisheries and industry that ultimately depend on the various species in this region. For example, the sGSL American lobster population is currently at a high and increasing level that supports the highly lucrative nearshore fishery in this region (Comeau and Hanson 2018); however, this positive outlook can change if environmental conditions become less favorable. With American lobster in this region there remain uncertainties related to the contemporary carrying capacity of the population and the potential effects of climate change on habitat suitability – factors that may play a role in the fluctuations of landings. Sustainable management strategies must continue to adapt, and with so many unpredictable variables, it is vital to both quantify dispersal and to understand the assumptions and limitations of the models that use dispersal in attempts to predict future ecological and economic impacts.

Chapter 5

Combining technologies to quantify dispersal in Lake St. Clair

The synergistic power of MAPs, drifters, and models

5.1 Introduction

The North American Laurentian Great Lakes represent the world's largest freshwater resource, containing approximately eighteen percent of the Earth's surface fresh water (Bolsenga and Herdendorf 1993; Waples *et al.* 2008). The Lakes drain into the Atlantic Ocean through the St. Lawrence River and, as a result, humans have relied on the Lakes as a major transportation route for thousands of years (Kelly 2007; Waples *et al.* 2008). The five large Lakes – Superior, Michigan, Huron, Erie, and Ontario – are joined as one body of freshwater by numerous small lakes, rivers, and tributaries. These are collectively known as the Great Lakes "connecting channels" and are a vital component of the Great Lakes system, providing additional habitat for phytoplankton, invertebrates, and vertebrates across several life-stages (Vanderploeg *et al.* 2002; Boase *et al.* 2014; Bennion and Manny 2014; Henning *et al.* 2014; Hondorp *et al.* 2014; McDonald *et al.* 2014; Roseman *et al.* 2014; Sullivan and Stepien 2014).

One of these connecting channels, the Huron–Erie Corridor (HEC), joins Lakes Huron and Erie and includes the St. Clair–Detroit River ecosystem, encompassing southern

Lake Huron, the St. Clair River, Lake St. Clair, the Detroit River, and western Lake Erie (Bolsenga and Herdendorf 1993; Bennion and Manny 2014; Roseman *et al.* 2014, Sullivan and Stepian 2014). The St. Clair River enters Lake St. Clair via the largest freshwater delta in the world, and the abundant coastal wetlands along the shores of the HEC are among the most productive habitats in the Great Lakes system (Herdendorf *et al.* 1986; Francis *et al.* 2014; Henning *et al.* 2014; Hondorp *et al.* 2014; Roseman *et al.* 2014; Sullivan and Stepien 2014). It follows that the HEC is home to both native (e.g., lake sturgeon; Auer 1996; Auer and Baker 2002; Manny and Kennedy 2002; Nichols *et al.* 2003; Holtgren and Auer 2004; Peterson *et al.* 2007; Mandrak and Cudmore 2010; Bouckaert *et al.* 2014; Welsh *et al.* 2017) and introduced and invasive species (e.g., Asian carp; Herborg *et al.* 2007; Buck *et al.* 2010; Cooke *et al.* 2010; Mandrak and Cudmore 2010; Stockstad 2010; Murphy and Jackson 2013; Cuddington *et al.* 2014; Wittmann *et al.* 2014; Embke *et al.* 2016), and is also heavily developed for industrial, commercial, residential, and recreational uses (Herdendorf *et al.* 1986; Griffiths 1991; Kelly 2007). There has been particular concern with regional transoceanic commercial shipping traffic acting as an important mechanism in the continued establishment of invasive species due to ballast-water release, despite the current regulations for ballast-water management in both Canada and the USA that aim to reduce propagule pressure at the initial introductory stage (Ricciardi and Rasmussen 1998; Ricciardi and MacIsaac 2000; MacIsaac *et al.* 2002; Colautti *et al.* 2003; Grigorovich *et al.* 2003; Drake and Lodge 2004; Holeck *et al.* 2004; Bailey *et al.* 2005; Duggan *et al.* 2005; Colautti *et al.* 2006; Ricciardi 2006; Costello *et al.* 2007; Gray *et al.* 2007; Simberloff 2009; Rup *et al.* 2010; Bailey *et al.* 2011; Briski *et al.* 2012; DiBacco *et al.* 2012; Bailey 2015; MacIsaac *et al.* 2015). As a shared international resource, the HEC faces growing issues concerning habitat alteration, degradation, and fragmentation, as well as overfishing, loss of habitat and biodiversity, introductions of non-indigenous species (most authors cited above; Dextrase and Mandrak 2006; Atkinson and Domske 2015; Smith *et al.* 2015), and the spread of pathogens (e.g., viral haemorrhagic septicemia virus, VHSV; Groocock *et al.* 2007; Pham 2009; Bain *et al.* 2010; VHSV Expert Panel and Working Group 2010; Faisal and Winters 2011; Faisal *et al.* 2012; Pham *et al.* 2012; Wagner *et al.* 2014; Escobar *et al.* 2017), and pollutants (e.g., microplastics; Zbyszewski and Corcoran 2011; Eriksen *et al.* 2013; Wagner *et al.* 2014; Zbyszewski *et al.* 2014; Driedger *et al.* 2015; Dris *et al.* 2015; Eerkes-Medrano *et al.* 2017; Hoffman and Hittinger 2017; Horton *et al.* 2017; Dean *et al.* 2018).

Biological dispersal refers to the spread of individuals away from a source location through passive and (or) active means (e.g., Begon *et al.* 2006; Levin 2006), where the passive component is especially important within a fluid such as air or water. Dispersal affects population dynamics (e.g., the distribution of individuals and ultimately reproduction and recruitment), population genetics (e.g., gene flow), and thus the spatial scale of population connectivity through the exchange of individuals among geographically separated subpopulations (Clobert *et al.* 2001; Kinlan and Gaines 2003; Bowler and Benton 2005; Begon *et al.* 2006; Nathan 2006; Matthysen 2012; Allen *et al.* 2018). Dispersal is often defined in terms of the dispersal kernel, the function that describes the probability of a particle or propagule moving from some source location to all other locations (Clark *et al.* 1998; Siegel *et al.* 2003; Nathan 2006; Cowen *et al.* 2007;

Gawarkiewicz *et al.* 2007; Nathan *et al.* 2008; Nathan *et al.* 2012; Hrycik *et al.* 2013). The scales of aquatic dispersal are empirically difficult to measure (Thorrold *et al.* 2002; Largier 2003; Siegel *et al.* 2003; Kinlan *et al.* 2005; Cowen *et al.* 2006; Levin 2006; Pineda *et al.* 2007; Werner *et al.* 2007; Metaxas and Saunders 2009; Kool *et al.* 2013; Pineda and Reyns 2018), and addressing the issues mentioned above (e.g., transport of pathogens, pollutants, and propagules) requires insight into the local spatial patterns of dispersal that can be gained by quantifying the dispersal kernel (Ricciardi and Rasmussen 1998; MacIsaac *et al.* 2004). This more profound understanding of dispersal is required to develop wide-ranging strategies that address the numerous conservation and management questions raised within the Great Lakes system (Arim *et al.* 2006; DeVanna Fussell *et al.* 2016).

In this Chapter I provide a direct measure of particle dispersal in Lake St. Clair using a proven advanced technology system of magnetically attractive particles (MAPs) and a magnetic-collector array (**Chapters 2–4**; Ruddick and Taggart 2006, 2011; Hrycik *et al.* 2013). This system overcomes many of the issues associated with conventional tracing technologies (e.g., drifters, dye, and numerical models) frequently employed in the study of dispersal (**Chapter 2**; Ruddick and Taggart 2006; 2011). It allows me to quantify the passive component of the dispersal kernel in the near-surface mixed layer at the scale of dispersing early-stage planktonic organisms (days to weeks, 1 to 100 km). Such data provide the biological null model of larval dispersal. The weak buoyancy and slow rise rate of the MAPs are important properties that allow them to mimic weakly buoyant, passive particles. Further, as advective and diffusive processes drive the passive component of connectivity, knowledge of the dispersal kernel allows the degree of passive connectivity in space and time to be readily estimated for a defined region (e.g., **Chapters 3** and **4**; Hrycik *et al.* 2013).

I also have the unique opportunity in this study to explain the MAP dispersal results in relation to the movement of concurrently deployed conventional drogued drifters across the Lake. I can then use the observed spatial patterns of dispersal to create a simple drifter-based Gaussian diffusion model, driven by winds and validated using a set of observed drifter trajectories. This allows a MAP and VP comparison at corresponding locations, similar to that achieved in **Chapters 3** and **4**. In particular, this study illustrates the synergistic power of using multiple measures of dispersal to tease apart a more complete picture over the study period that could not be achieved with only one measure. The results presented here are applicable to a number of pertinent issues in the HEC, including the dispersal and connectivity of both native and non-indigenous species, as well as pollutants such as mircoplastics.

5.2 Methods

5.2.1 Study site

The particle and drifter dispersal study was conducted in July 2009 in Lake St. Clair (**Fig. 5.1**). Various features of the Lake and its connecting channels are described by Quinn (1992), Herdendorf *et al.* (1986), Schwab *et al.* (1989), Lang and Fontaine (1990), Bolsenga and Herdendorf (1993), Holtschlag and Koschik (2002), Rao and Schwab (2007), Anderson *et al.* (2010), and Anderson and Schwab (2011). In brief, the Lake is

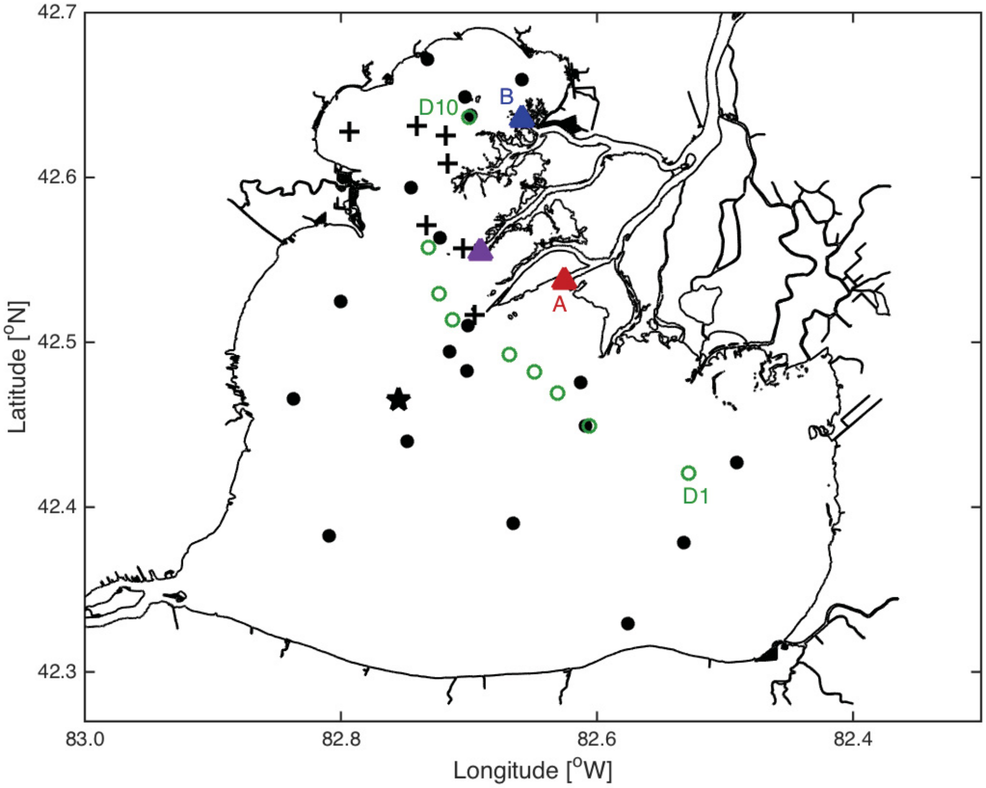

Figure 5.1 Coastline chart of Lake St. Clair illustrating the locations of recovered (black filled circles) and unrecovered (black crosses) collectors and drifter deployments (green open circles). MAP source locations are denoted by triangles, where the northern triangle (blue) represents the B-source, the southern triangle (red) represents the A-source, and the intermediate triangle (purple) represents the hypothetical averaged A+B source. Note that there were also unrecovered collectors at all three MAP source locations. The location of Station LSCM4, where wind speed and direction were recorded, is indicated with a star.

heart-shaped, small, and shallow, with a surface area of approximately 1100 km^2, a volume of approximately 3.8 km^3, and an average depth of approximately 3.5 m. The Lake is located in the center of the HEC and forms part of the international water border between Canada and the USA. The only shipping channel to the upper Great Lakes runs through the HEC and the channel is routinely dredged from Lake Huron to Lake Erie, increasing the maximum natural depth (6.4 m) of Lake St. Clair to approximately 8.0 m along the channel. Thermal stratification is rare and ephemeral due to the combination of shallow depth and high, wind-driven wave energy interacting through the water column with the bathymetry and shoreline. The average hydraulic retention time in the Lake is approximately 7 to 9 days; however, wind-driven circulation can influence the residence time of water entering from each of the channels and tributaries that flow into the Lake along the northern margin.

Water transport through the Lake is described by most of the authors cited above and is summarized as follows. Lake St. Clair is hydraulically linked to Lake Huron via the St. Clair River to the north and to Lake Erie via the Detroit River to the south, and variations in water level and flow between sections of the HEC are thus interdependent. Outflow from the three upper Great Lakes – Superior, Michigan, and Huron, with a combined volume of approximately 20,700 km^3 – is carried by the St. Clair River into Lake St. Clair through five channels integral to the delta. These channels and their respective contributions to the St. Clair River total an average transport of 5000 to 5700 m^3 s^{-1} into the Lake by the North (34%), Middle (21%), South (19%), and Bassett Channels (5%), and the St. Clair Cutoff (21%). There are also three major rivers, the Sydenham, Thames, and Clinton Rivers, that increase the discharge into the Lake by 120 to 150 m^3 s^{-1}. Outflow is carried to Lake Erie by the Detroit River. Flow from the five delta channels through the Lake and into the Detroit River is driven by a natural decrease in elevation from Lake Huron to Lake Erie and by wind stress on the Lake.

Color-coded particles (detailed in **Chapter 2** and briefly summarized below) were separately released where the North and South Channels enter Lake St. Clair (**Fig. 5.1**) after the particle collectors (also detailed in **Chapter 2** and briefly summarized below) were deployed throughout the Lake (**Fig. 5.1**). Drogued drifters (detailed below) were concurrently released along the central southeast to northwest axis of the Lake (**Fig. 5.1**). The physical features (i.e., depth, shape, size, and surrounding flat topography) of Lake St. Clair make it predisposed to wind effects from all directions, and there are interactions among the hydraulically-forced and the wind-induced currents in different regions of the Lake that may change with varying wind conditions (Schwab *et al.* 1989; Holtschlag and Koschick 2002; Anderson *et al.* 2010; Anderson and Schwab 2011). The direction from which the wind blows over the Great Lakes region is typically southwest to west; however, day-to-day fluctuations occur (Rao and Schwab 2007) and there were variable winds during my study. Wind speed and direction were recorded hourly at Station LSCM4 in Lake St. Clair (National Oceanic and Atmospheric Administration, National Buoy Center), located near the center of the Lake on the northwest side of the shipping channel (**Fig. 5.1**).

5.2.2 Magnetically attractive particle (MAP) deployment, dispersal, and analyses

5.2.2.1 Summary of the MAP and magnetic-collector array technology system

The reader is advised that a more detailed description of the MAP and magnetic-collector array technology system is provided in ***Chapter 2****.*

The MAPs are composed of hollow glass (SiO_2) microspheres that provide buoyancy, magnetite (Fe_3O_4) that provides magnetic attraction and mass, and a food-safe epoxy resin that acts as a binding agent. The particles are ideally designed to be spherical, in the 100 to 500 μm equivalent spherical diameter (esd) size range, and with a specific gravity (SG) designed to match *in situ* surface layer density; a nominal specific gravity (SG) of 1.00 for freshwater-applications. In this study, the MAPs had a median esd of 371 μm and a geometric mean esd of 370 μm (**Fig. C.1**), a nominal SG of 1.00, and an average rise rate of 1 to 4 mm s^{-1} in water with a SG of 1.00. They were manufactured with one of two color pigments (A, B) to distinguish between the two source locations. The size distributions of the colored MAPs separately (A, B) were representative of that of the two colors combined (A+B). The MAPs are one component of a system (**Chapter 2**; Ruddick and Taggart 2006, 2011) that, when coupled with a moored magnetic-collector array, allows the direct measurement of particle dispersal within the array domain. The magnetic-collectors are passive samplers designed to float near the surface and vane into the current such that any MAP suspended in the near-surface layer that flows through a collector will be captured (**Fig. 2.3**). Collectors were deployed prior to the start of the study and following a point-source release of MAPs and their dispersal over a given period, they were recovered and the particles captured by the magnets were enumerated. This system essentially makes use of billions of particle drifters that can be used to estimate dispersal parameters and to make direct comparisons with similar dispersal estimates provided by conventional drogued drifters and models.

5.2.2.2 MAP dispersal

The A-MAPs were released in the surface layer (0–0.5 m) across the width of the South Channel where it enters the Lake over a 3-minute period at 11:26 h EDST on 17 July 2009 (**Fig. 5.1**). The B-MAPs were released in the surface layer (0–0.5 m) across the width of the North Channel where it enters the Lake over a 5-minute period at 13:05 h EDST on 17 July 2009 (**Fig. 5.1**). Subsamples of both A- and B-MAPs suspended in water of *in situ* density were monitored over the study (dispersal) period to estimate the proportion that would sink out from the surface layer. Magnetic-collectors had previously been deployed throughout the Lake, with spatial coverage constructed by deployment and recovery logistics. A total of 30 collectors were deployed and 20 were recovered after a period of 5 to 6 d post-release. Upon retrieval, captured MAPs were removed from each collector and imaged from above under UV light (see **Chapter 2**), with the total area (mm^2) of MAPs in each calibrated image measured using SigmaScan Pro (Version 5.0). In this Chapter, the numbers of MAPs collected are quantified as total area (mm^2) of particles captured by each collector.

Since the A- and B-MAPs employed in this study were produced using pigments, I attempted to differentiate captured MAPs based on the source location; however, inherent manufacturing difficulties prevented a confident differentiation of A from B. Therefore, any categorizations of A- versus B-MAPs in this Chapter are subjective, uncertain, and based on comparisons between individual MAPs from a given captured particle image to known A- and B-MAPs from a standard sample image. Given the separate observed spatial patterns (see **Figs. C.3, C.4**), I believe this subjective differentiation is reasonable, yet I still caution the reader to carefully examine the individual A- and B-MAP results. Due to this uncertainty, A- and B-MAPs were combined to obtain a total A+B MAP capture estimate for each collector.

5.2.2.3 Estimating dispersal kernels

The reader is advised that a more detailed description of using the MAP data to estimate dispersal kernels is provided in ***Chapter 2****.*

I define the MAP dispersal kernel as the probability density function describing the spatial concentration distribution of particles relative to a source location (e.g., Clark *et al. 1998*; Nathan *et al.* 2008). Observational estimates of the one-dimensional dispersal kernels were calculated according to **Equation 2.11** in **Chapter 2**, $2\pi L\, p(L;T) = ae^{-aL}$, where the number (area) of particles at time T is primarily a function of in-water distance L between the source and the collector locations. This simple probability density function (p) with a single parameter (a) is derived in **Chapter 2**, and results in an *e*-folding scale of a^{-1}. The *e*-folding scale is simply the length scale where the number (area) of particles at distance L decreases by a factor of e. The resulting estimates are unique to the given sampling period T and its associated environmental conditions; variability related to, for example, wind events, cannot be considered without replicate releases or a long-term steady release; this is addressed further in **Chapter 4**. As the MAPs were released from two locations in this study, dispersal kernel estimates were calculated using multiple sources. A dispersal kernel for A-MAPs was estimated using the A-source location where the South Channel enters the Lake, while a dispersal kernel for B-MAPs was estimated using the B-source location where the North Channel enters the Lake. These results are interpreted with caution due to the subjective nature of A and B differentiation described above, and therefore a dispersal kernel for A+B MAPs was calculated in two ways. First, the A and B source locations were averaged to create a hypothetical source location where the Middle Channel enters the Lake, and L for each collector location was measured using this assumed location. The resultant dispersal kernel for A+B MAPs is again interpreted with caution since the estimates of L in this case are not true in-water distances. Second, a dispersal kernel was calculated using a combination of the A- and B-MAP data from their respective source locations (i.e., two points for every collector location) to achieve an estimate of the A+B MAP dispersal kernel using true in-water distances; this is the dispersal kernel estimate I focus on here.

5.2.3 Drogued drifter deployment, movement, and analyses

5.2.3.1 Summary of drogued drifters

I used satellite-tracked, surface-drogued, Lagrangian drifters, similar to the common X-shaped Davis design used in the USA Coastal Ocean Dynamics Experiment (CODE; Davis, 1985). Each inexpensive, lightweight drifter consisted of a 50-cm vertical tubular hull with four drag-producing vanes extending 38-cm radially from the hull over most of its length. All drifters were outfitted with a low-profile, self-contained Comtech Mobile Trackpack[3] (dimensions 13.5 x 6.9 x 2.1 cm) mounted at the top of the hull that reported

---

[3] http://sofex.comtechmobile.com/sens.html

GPS position approximately every 30 minutes; the time-lapse between sequential positions was variable. Approximately 10-cm of the hull containing the Trackpack remained just above the surface in an effort to reduce wind effects on each drifter. The drifters were hand-deployed and retrieved and the trajectory of each drifter was examined at the end of the dispersal period (5 to 6 d).

5.2.3.2 Drifter movement

Ten drifters (D1 to D10) were sequentially released in the Lake along a central southeast to northwest transect over a 2 h 45 m period beginning at 10:00 h EDST on 17 July 2009 (**Fig. 5.1**). A total of seven drifters and their time and location data were recovered after the 6 d post-release period. Two drifters (D1, D2) beached less than half-way through the dispersal period on the southeast shore of the Lake and one drifter (D6) was lost; these drifters are not included in the analyses below.

5.2.3.3 Drifter and wind analyses

I define the drifter study period as the time from first drifter deployment to last drifter retrieval (**Fig. 5.2**). Location data for each drifter within this period were linearly interpolated to 15-m time intervals that were common to each drifter for later comparative analyses among drifters and with the observed winds, though the length of the time-series varied among drifters (see **Fig. 5.6**). Detailed variations in the u and v velocity components for each drifter over the deployment period were derived from drifter direction and speed (**Figs. C.9–C.17**), and scatterplot matrices for both u and v were used to illustrate the relations between the wind and drifter estimates and all possible pairs of drifter estimates (**Figs. 5.8**, **5.9**; addressed further below). To consider the *u* and *v* components together, complex regressions (*u* + i*v*) for each drifter were computed to obtain the off-set between drifters and the complex regression with the wind (i.e., optimal scale and rotation; **Table C.1**). Additionally, linear regression was used to assess drifter speed estimates as a function of wind speed estimates (**Table C.2**). In addition to the short D1 and D2 series, I also excluded the D8 series from the average speed calculation due to its anomalous speed increases when the drifter became entrained in the strong flow upon entering the dredged channel near the Detroit River at the end of the study period.

The wind data recorded at Station LSCM4 were interpolated to 15-m time intervals to align with the drifter series over the same study period. As with the drifter data, detailed variations in the wind field velocity components (*u*, *v*) over the deployment period were examined (**Fig. C.8**), and scatterplot matrices for both *u* and *v* were used to illustrate the relations between the wind and drifter estimates (**Figs. 5.8**, **5.9**). The complex and linear regression for each drifter, as a function of the wind, was performed as detailed above (**Tables C.1**, **C.2**). To further examine coherence among the wind and drifter data series, *u* and *v* components and the complex regressions (*u* + i*v*) of the wind and drifters D5 and D10 were examined for autocorrelation, both with and without the trend removed (**Figs. C.18–C.22**). D5 and D10 were chosen as representative drifter data series due to their proximity, respectively, to the A- and B-MAP source locations and for later use in a simple Gaussian dispersal model (addressed in further detail below). Cross-correlation functions were calculated on the de-trended complex regression data series to assess lags in both D5 and D10 with the wind (**Figs. C.18e–C.19e**).

Following the analyses of the wind-drifter relations, I used a simple complex regression model of slab flow to ascertain how well the variations in wind velocity accounted for the observed variation in drifter velocities (trajectories). Each predicted drifter trajectory was computed as

$$u_D = \beta_0 + \beta_1 w + error, \tag{5.1}$$

where u_D is the observed drifter velocity, β_0 is the residual drifter velocity in the absence of any wind effect (i.e., the "drain"; addressed further below), β_1 is the proportion of wind velocity applied to the drifter to achieve the observed velocity, and w is the observed wind velocity. Setting $\beta_0 = 0$ and integrating this equation yields the predicted drifter trajectory that was then compared to the observed trajectory. When setting $\beta_1 = 0$ (i.e., ignoring the wind effect), I was able to examine the net displacement of each drifter due to the residual "drain" of water from the system that is independent of wind influences (**Table C.3**). Coherence between the observed and predicted trajectories for D5 and D10 were examined with cross-correlation functions as above (**Fig. C.23**).

5.2.4 Simple dispersal model and resulting MAP and VP comparisons

5.2.4.1 Simple Gaussian dispersal model and VP dispersal

The drifter data do not in themselves provide dispersal kernel estimates that can be directly compared with the MAP dispersal kernel estimates, as was possible in the MAP and VP comparisons completed in **Chapters 3** and **4**. To achieve a comparison at corresponding locations, I thus used both the MAP and drifter spatial patterns of dispersal to create a simple Gaussian dispersal model that diffused virtual particles (VPs) while advecting them along observed drifter trajectories. The slab movement of water was modeled separately using two observed drifter trajectories – that of D5, the drifter deployed closest to the A-MAP source location and that of D10, the drifter deployed closest to the B-MAP source location. The modeled dispersal period (t_0–t_1) was defined as the common period for both D5 and D10, and this also accommodated variability in the timing of the A- and B-MAP releases and magnetic-collector and drifter recovery; a summary of all deployment and recovery time periods is provided in **Figure 5.2**. To account for the shoreline and bathymetry, the starting location of each modeled drifter trajectory was virtually "moved" to the mid-point between the corresponding MAP source location and the actual drifter deployment locations (see **Fig. 5.1**). Since the starting locations of the modeled trajectories are further away from land than the true MAP source locations, the VPs are already diffused when the model simulation begins. As a result, I am not modeling a point source release.

For each modeled drifter trajectory, a diffuse Gaussian distribution of VPs was released at the mid-point described above and allowed to diffuse over the model period while advecting along the drifter trajectory. At the end of each simulation, the relative concentration of VPs was calculated using **Terms III** and **IV** of **Equation 1.1** in **Chapter 1**. In this simple model, the small-scale diffusivity coefficient in the *x*- and *y*-directions are equal and I assume a slab response to the observed winds; the model thus corresponds to an evolving "diffusion kernel" that moves with the flow. To obtain a similar measure for later comparison with the observed A+B MAP data, the relative

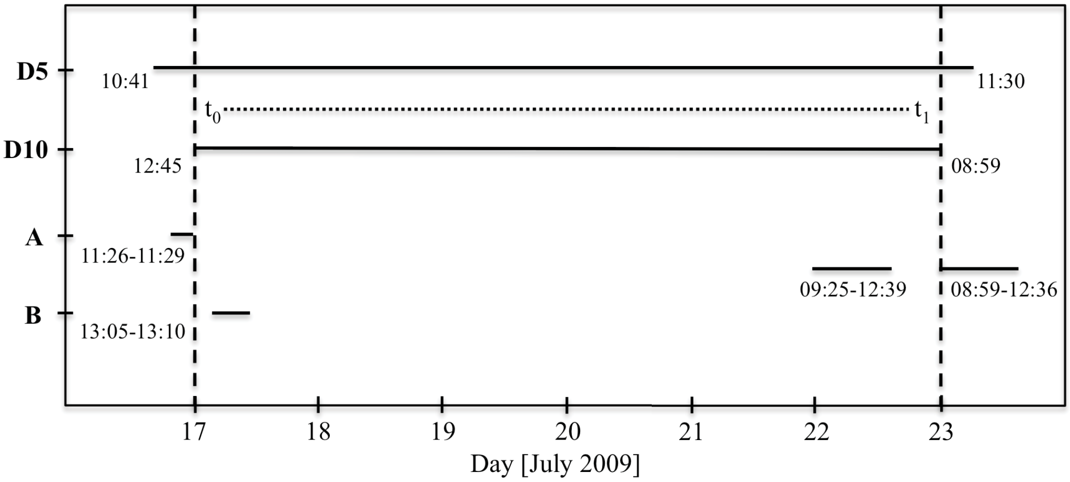

Figure 5.2 Diagram denoting the deployment and recovery time periods of D5, D10, A-MAPs, and B-MAPs (solid lines). The modeled dispersal period (t_0–t_1; dotted line) from 13:00 h EDST on 17 July 2009 through 09:00 h EDST on 23 July 2009 encompasses the common period for both D5 and D10, and also accommodates variability in the timing of the A- and B-MAP releases and magnetic-collector and drifter recovery.

concentration of VPs from both D5 and D10 trajectory simulations were combined. Small-scale diffusivity (K_p) sensitivity tests similar to those achieved in **Chapter 3** were conducted by repeating the model simulations at constant K_p values of 2, 5, 25, 50, and 80 $m^2 s^{-1}$.

5.2.4.2 MAP and VP comparisons

A Box-Cox transformation (**Fig. C.2**) was applied to the A+B MAP data to approximate normality for use in optimal interpolation of the limited *in situ* MAP data to locations where no magnetic-collectors were deployed. When interpolating the data, I used a smoothing length scale of 0.05 degrees in both the *x*- and *y*-directions. The empirical field of relative MAP concentration that results can then be qualitatively compared to the modeled field of relative VP concentration near corresponding magnetic-collector and grid-cell locations. I achieve this direct comparison by scaling the modeled VP concentrations based on the observed MAP concentrations and then examining the empirical field with respect to the scaled modeled field.

5.3 Results

5.3.1 MAP dispersal

MAPs were captured by 19 of the 20 magnetic-collectors that were recovered 5 to 6 days post-release; i.e., there was one zero return and ten collectors were not recovered (**Fig. 5.3**). The ten missing collectors were mostly from the northwest quadrant of the Lake and were either destroyed or stolen due to the abundance of recreational boaters. Since the study domain is small and collectors were deployed throughout the entire Lake, I

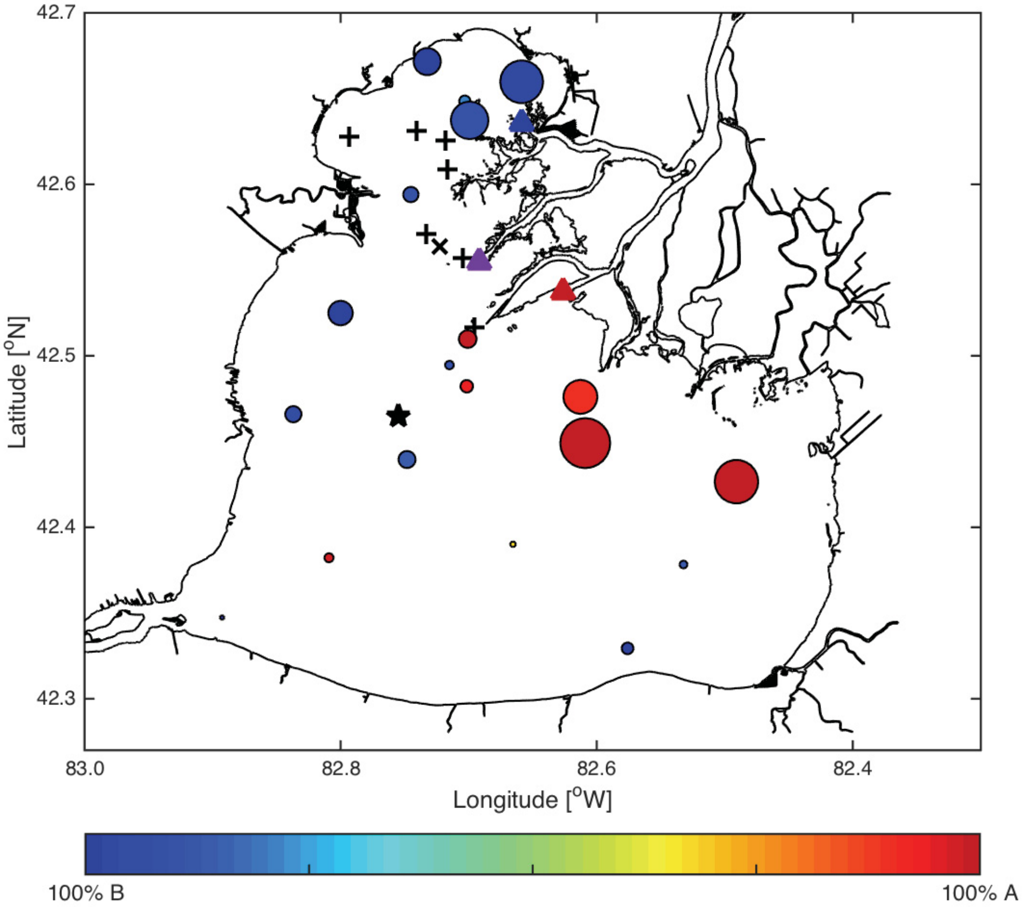

Figure 5.3 Coastline chart of Lake St. Clair illustrating the location-specific relative number (linearly expanding-area circles) of A+B MAPs captured among the recovered collectors, where the color scale bar corresponds to the proportion of A- versus B-MAPs at each collector. MAP source locations are denoted by triangles, where the northern triangle (blue) represents the B-source, the southern triangle (red) represents the A-source, and the intermediate triangle (purple) represents the hypothetical averaged A+B source. An "x" denotes the locations of empty recovered collectors (i.e., zero returns) while crosses denote the locations of collectors not recovered. Note that there were also unrecovered collectors at all three MAP source locations. The location of Station LSCM4, where wind speed and direction were recorded, is indicated with a star.

assumed that the spatial distribution of the missing collectors did not compromise the data analyses and my interpretation thereof. Based on the subjective categorization described above, the majority of A-MAPs among collectors were concentrated in the northeastern margin of the Lake, south and southeast of the A-MAP source location (**Figs. 5.3**, **C.3**). The majority of B-MAPs among collectors were concentrated in the northwestern margin of the Lake, closest to the B-MAP source location (**Figs. 5.3**, **C.4**). As in the MH, CG, and GB studies (**Chapters 3** and **4**), generally, though not systematically, fewer MAPs were captured with increasing distance from the respective source locations.

5.3.2 Estimating dispersal kernels

The number of both A- and B-MAPs captured by the collectors decreased exponentially with in-water distance L from the respective source locations (**Figs. C.5a–C.7a**). The resultant dispersal kernel for the A-MAPs released from the A-source location provided an estimated *e*-folding scale of 7.08 km with lower and upper 95% confidence limits of 3.58 and 322.58 km, respectively (**Fig. C.5b**), while that for B-MAPs originating from the B-source location resulted in a comparable *e*-folding scale of 14.16 km with decreased lower and upper 95% confidence limits of 6.37 and 63.29 km, respectively (**Fig. C.6b**). The exponential decay of B-MAPs with increasing distance from the source yielded a shallower curve than that of A-MAPs, likely related to the differences in bathymetry and shoreline proximity near the two source locations. The B-source location near the northwest margin of the Lake was relatively more sheltered, thus reducing the wind fetch effect relative to the A-MAP source location. Since the absolute differentiation of A- and B-MAPs was subjective, the respective A- and B-MAP dispersal kernel estimates are interpreted with caution and the A+B MAP dispersal kernel estimates were examined in the following two ways.

When using the hypothetical averaged source location as the source (see **Fig. 5.3**), the resultant A+B dispersal kernel provided an estimated *e*-folding scale of 11.34 km with lower and upper 95% confidence limits of 5.47 and 156.25 km, respectively (**Fig. C.7b**). This estimate is again interpreted with caution because a) the distances from the hypothetical source location do not represent true in-water distances and b) the zero datum from the empty (i.e., zero return) collector is not included in the regression model (**Fig. C.7a**). As a result, I then calculated a dispersal kernel using a combination of the A- and B-MAP data from their respective source locations. With two data points for every collector location, this provided an A+B dispersal kernel that used true in-water distances and included the empty (i.e., zero return) collector in the regression model (**Fig. 5.4a**). The resulting *e*-folding scale estimate was 11.45 km with lower and upper 95% confidence limits of 6.37 and 56.82 km, respectively (**Fig. 5.4b**), and represents the most robust estimate of the MAP dispersal kernel in this study. The "best" representation for the entire Lake lies somewhere in **Figure 5.5**, where the exponential decay of MAP area with increasing distance from the source for both A- and B-MAPs are shown on the same axes; however, the *e*-folding scale for the northern margin of the Lake is likely closer to that of the B- MAPs (**Fig. C.6**), while the *e*-folding scale for the southern margin of the Lake is likely closer to that of the A-MAPs (**Fig. C.5**).

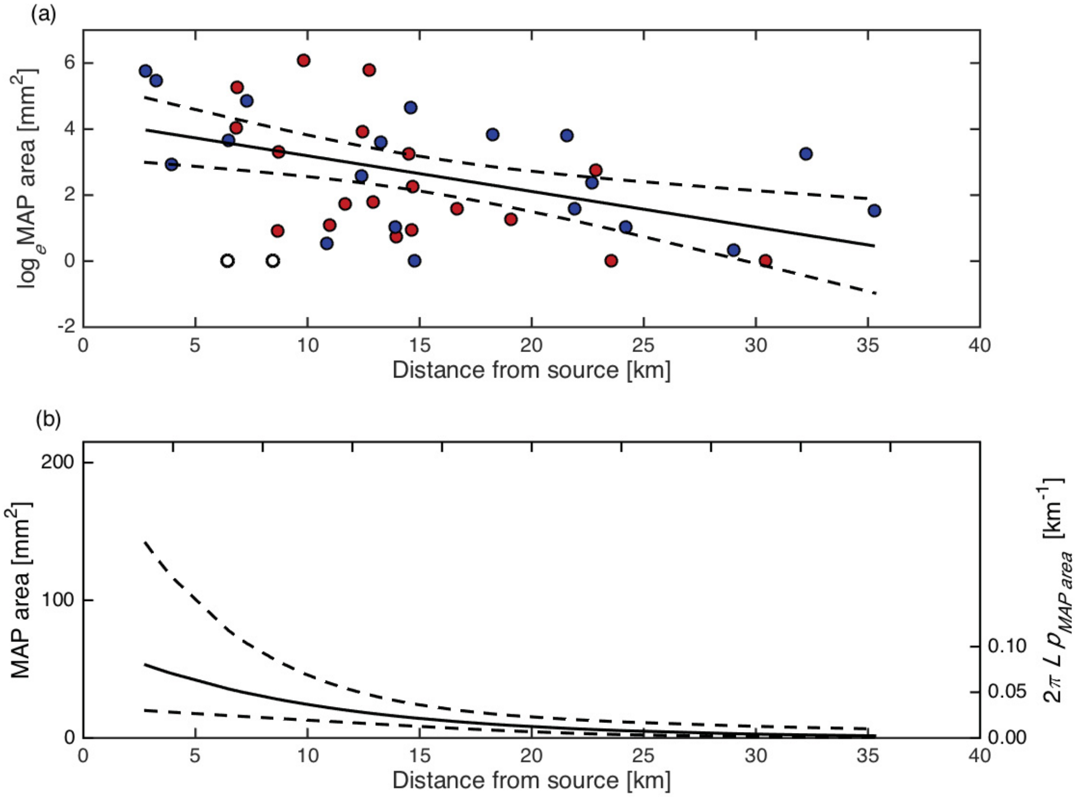

Figure 5.4 Log-linear (a) and exponential decay (b) of A+B MAP area (mm^2) as a function of distance L (km) from the respective A- and B-source locations, with A shown in red and B shown in blue. The regression model [$\log_e$MAP area = 3.79 – 0.09L; r^2 = 0.14; p = 0.02] in (a) is illustrated by a solid line with the upper and lower 95% confidence limits around the model (dashed lines) fitted to the MAP area estimates. The points associated with the empty recovered collector (i.e., zero returns) are shown with no color. The exponential decay [MAP area = $4.43 \times 10^1 e^{-0.09\,L}$] in (b) is illustrated by a solid line with the upper and lower 95% confidence limits (dashed lines). The exponential decay (solid line) can be interpreted as $2\pi L\ p_{MAP}$ (right ordinate) with an e-folding scale of 11.45 km that has upper and lower 95% confidence limits of 56.82 and 6.37 km.

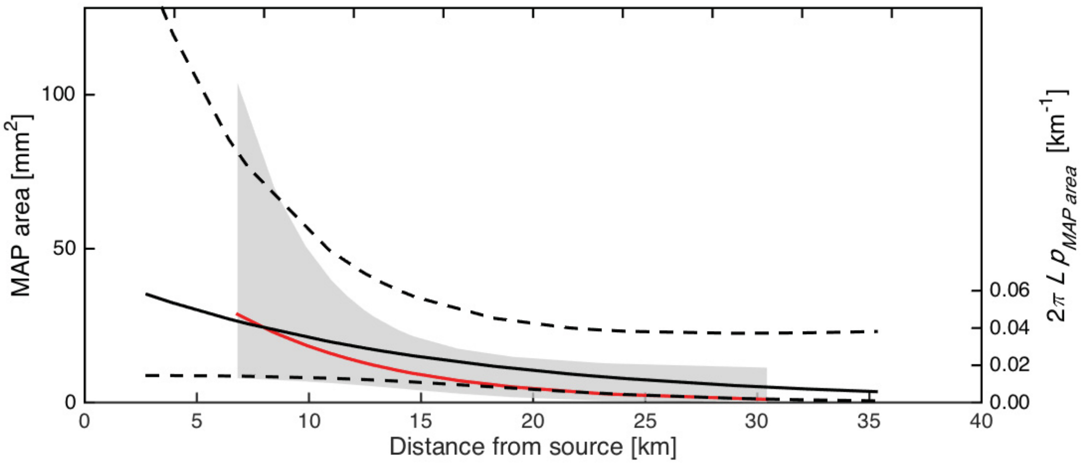

Figure 5.5 Exponential decay of A- and B-MAP area (mm^2) as a function of distance L (km) from the respective A- and B-source locations. The exponential decay of A-MAPs [MAP area = $7.52 \times 10^1 e^{-0.14L}$] is illustrated by a solid black line with the upper and lower 95% confidence limits (dashed lines). The exponential decay (solid black line) can be interpreted as $2\pi L\ p_{MAP}$ (right ordinate) with an e-folding scale of 7.08 km that has upper and lower 95% confidence limits of 322.58 and 3.58 km (see **Fig. C.5**). The exponential decay [MAP area = $4.29 \times 10^1 e^{-0.07L}$] of B-MAPs is illustrated by the solid red line with the upper and lower 95% confidence limits (shaded). When interpreted as $2\pi L\ p_{MAP}$, the e-folding scale is 14.16 km with upper and lower 95% confidence limits of 63.29 and 6.37 km (see **Fig. C.6**).

As in **Chapters 3** and **4**, the reader is reminded that the 95% confidence intervals shown in **Figures 5.4b**, **5.5**, and **C.5b–C.7b** are associated with the exponential function, MAP area, and not with the probability density function, $2\pi L\, p_{MAP\ area}(L)$. The 95% confidence intervals around $2\pi L\, p_{MAP\ area}(L)$ (not shown) were smaller than those around MAP area since $p_{MAP\ area}$ is affected only by uncertainty in the slope a, whereas both the slope and intercept, and their respective uncertainties, affect MAP area.

5.3.3 Drifter movement

Time and location data were retrieved from nine of the ten drifters deployed in the Lake; one drifter (D6) malfunctioned and provided no data. D1 and D2 beached on the eastern margin of the Lake less than half-way through the dispersal period (see **Fig. 5.6**) and were not included in further analyses. Overall, patterns among drifter movement throughout this study are highly coherent (**Fig. 5.6**). The change in direction observed in every drifter after approximately two days is well explained by a change in the prevailing wind direction (**Fig. C.8**; addressed further below). Drifter movement reflected various aspects of the observed MAP capture estimates among collectors (**Fig. 5.3**), and a visual comparison of **Figures 5.3** and **5.6** indicates that the drifters mirror the general features of the MAP field in the eastern half of the Lake especially well.

5.3.4 Drifter and wind analyses

Drifter movement was clearly a function of wind speed and direction (**Figs. 5.7**, **5.8**, **5.9**). Detailed variations in the wind and drifter field velocity components (u, v) components are provided in **Figures C.8–C.17** and are summarized in **Figure 5.7**, where coherence

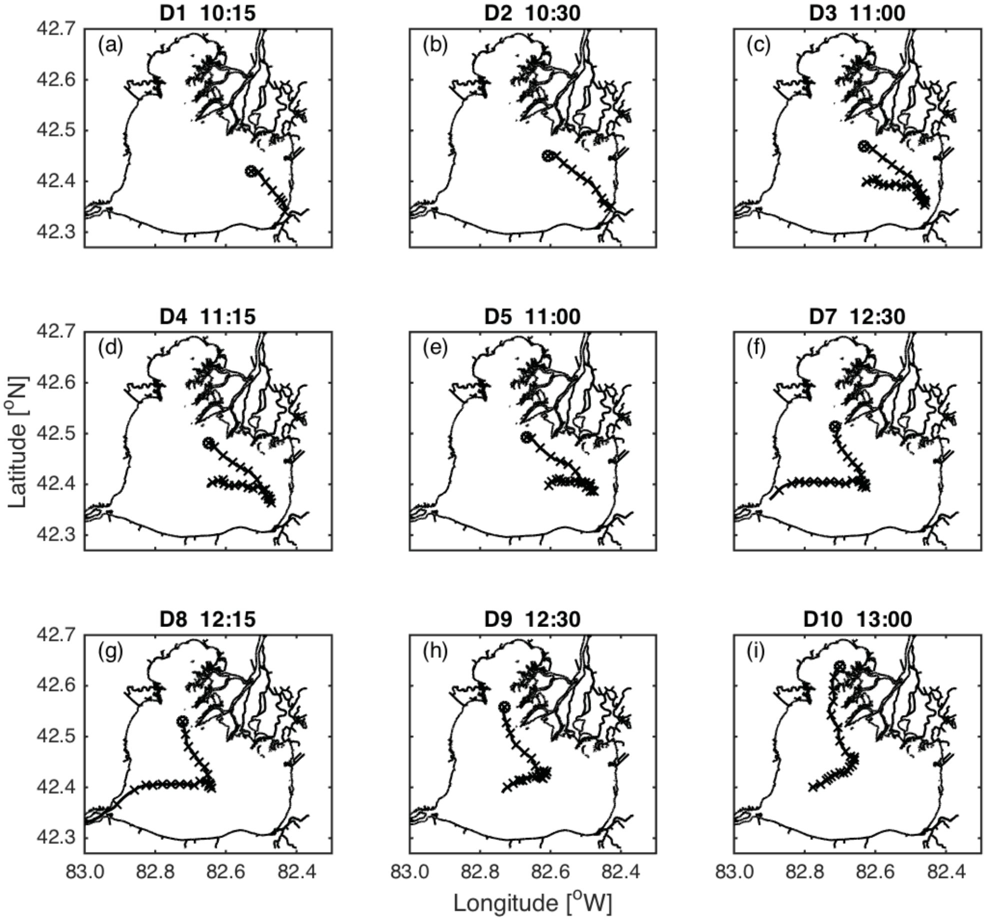

Figure 5.6 Coastline charts of Lake St. Clair illustrating (a–i) observed drifter (D1–D10) movement during the July 2009 particle tracing study. Drifter deployment locations are denoted with open circles and deployment times on 17 July 2009 are indicated above the respective subplots in EDST. Drifter positions are interpolated to a 15-m resolution and 6-h intervals are shown with an "x."

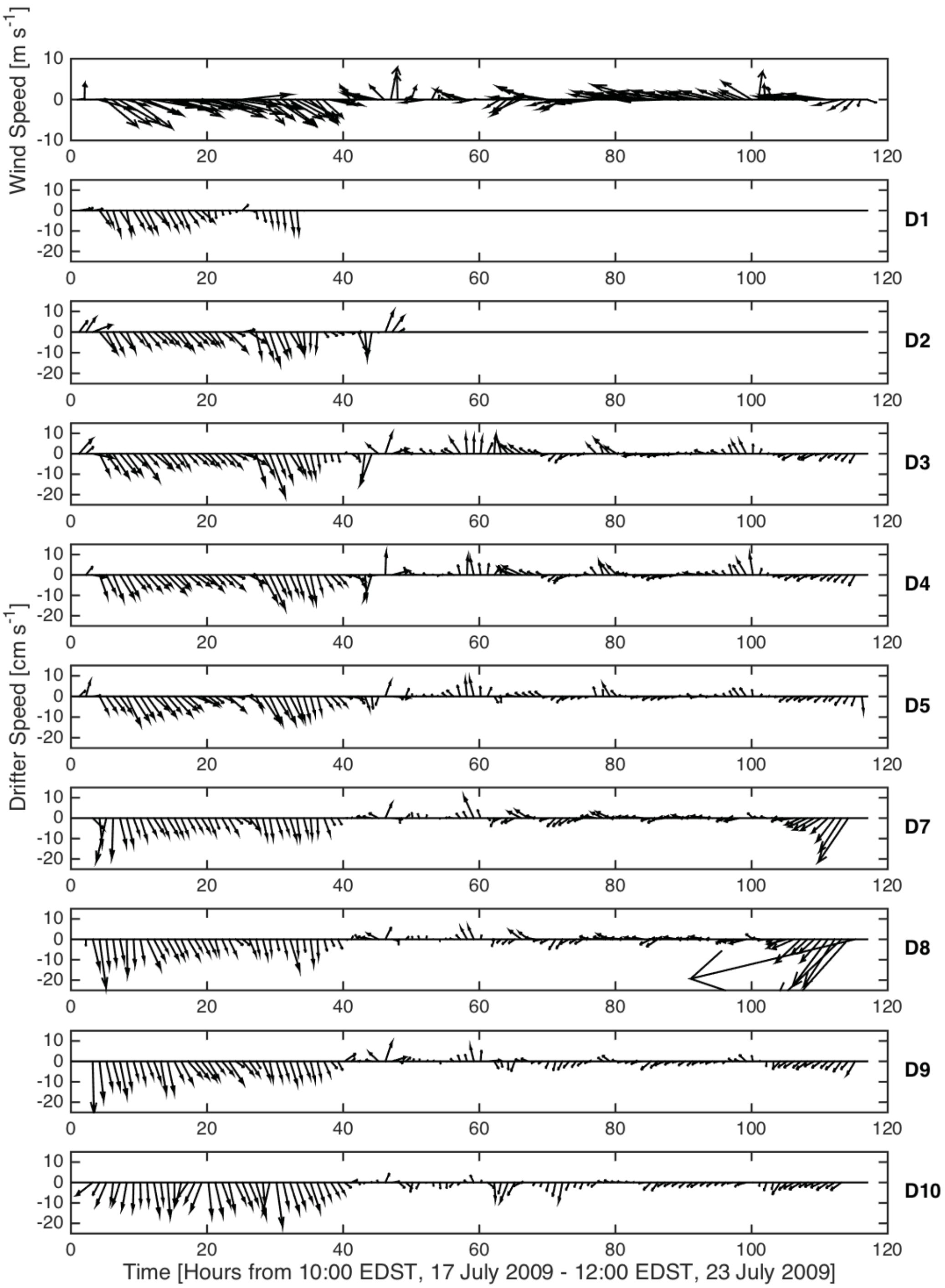

Figure 5.7 Wind speed (m s^{-1}), recorded at Station LSCM4, and drifter speed (cm s^{-1}) among all drifters (D1–D10) during the July 2009 Lake St. Clair particle tracing study, where the lengths of the arrows are proportional to speed. Arrows are depicted at a 1.25-h resolution.

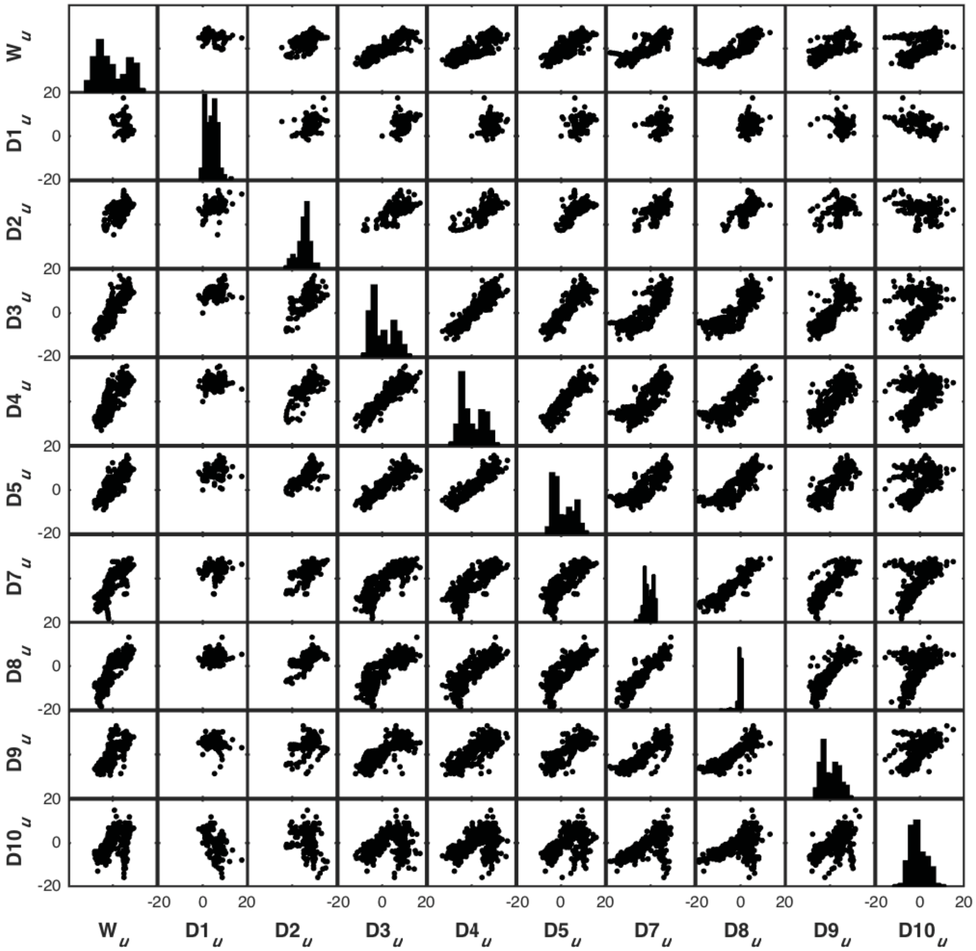

Figure 5.8 Scatterplot matrix showing the relations between wind (W; m s^{-1}) and drifter (D1–D10; cm s^{-1}) *u* estimates and all possible pairs of drifter *u* estimates, where the diagonal shows the frequency distribution of *u* for each variable centered around zero. The bimodality in most histograms relates to the wind reversal from +*u* to –*u*. Note the conventional units of cm s^{-1} for drifters and m s^{-1} for wind; however, common units of cm s^{-1} are used in the corresponding table. The coefficients of determination (r^2) associated with the complex regressions $u + iv$ for all possible pairings depicted in this Figure are provided in **Table C.1**.

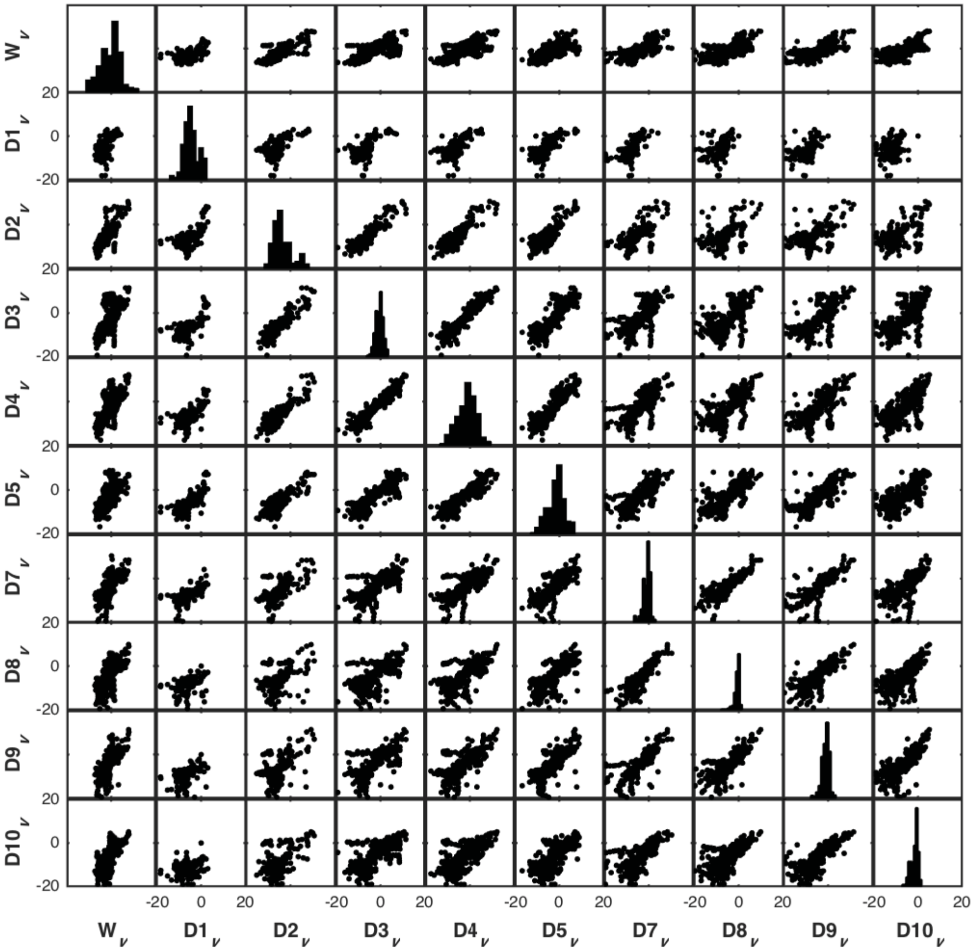

Figure 5.9 Scatterplot matrix showing the relations between wind (W; m s^{-1}) and drifter (D1–D10; cm s^{-1}) *v* estimates and all possible pairs of drifter *v* estimates, where the diagonal shows the frequency distribution of *v* for each variable centered around zero. Note the conventional units of cm s^{-1} for drifters and m s^{-1} for wind; however, common units of cm s^{-1} are used in the corresponding table. The coefficients of determination (r^2) associated with the complex regressions $u + iv$ for all possible pairings depicted in this Figure are provided in **Table C.1**.

among drifters is evident. D8, and to a lesser extent D7, experienced anomalous speed increases toward the end of the study period (see **Fig. 5.7**) when the influence of the underlying circulation due to the dredged channel began to exceed the wind effect and thus carried the drifter toward the Detroit River.

The relations between the *u* and *v* components of the wind and each drifter are visualized in **Figures 5.8** and **5.9**. It can be seen in both the *u* (**Fig. 5.8**) and *v* (**Fig. 5.9**) components that most of the drifters (D3–D10) were behaving as in slab flow in response to the variations in the wind throughout most of the study period. This is supported by the positive coefficients of determination (r^2) obtained from the complex regressions between the wind and each drifter $u + iv$ estimate and all possible pairs of drifter $u + iv$ estimates (see **Table C.1**). It should be noted that the bimodality in most histograms along the diagonal in **Figure 5.8** was related to wind reversal during the study period in the east–west direction from $+u$ to $-u$ (see **Figs. C.8a, C.11a–C.17a**). Wind and drifter speed estimates were also examined (**Fig. 5.10**), and the parameters for the linear regressions of drifter speed as a function of wind speed (i.e., the first row of **Figure 5.10**) are summarized in **Table C.2**. The average slopes among these regressions (i.e., the first row of **Table C.2**) provide the appropriate percentage to use when estimating wind-driven surface-drift from the wind over this study period. When excluding D1, D2, and D8 due to their anomalies, I calculated this percentage as 1.11% ± 1.41% of the wind velocity, less than the standard three percent often used in coastal ocean systems (**Chapter 3**; Csanady, 1982).

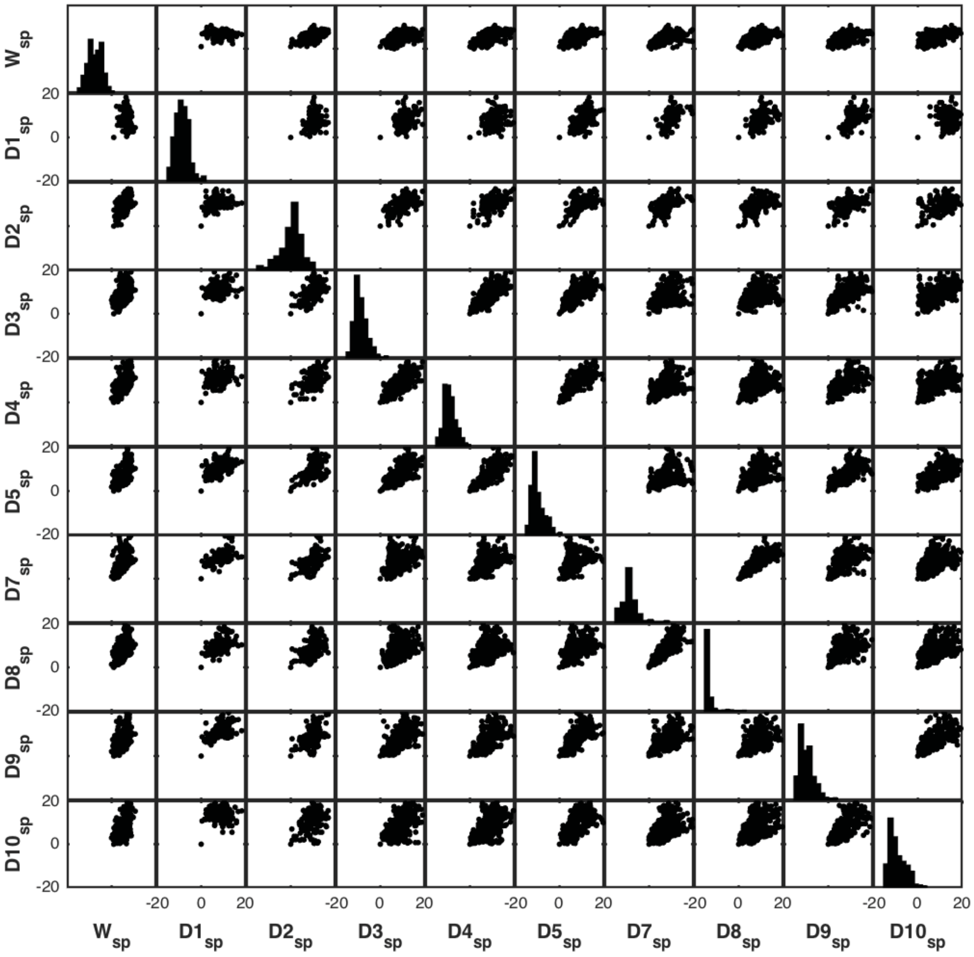

Figure 5.10 Scatterplot matrix showing the relations between wind (W; m s^{-1}) and drifter (D1–D10; cm s^{-1}) speed estimates and all possible pairs of drifter speed estimates, where the diagonal shows the frequency distribution of speed for each variable centered around zero. Note the conventional units of cm s^{-1} for drifters and m s^{-1} for wind; however, common units of cm s^{-1} are used in the corresponding table. Regression parameters for the scatterplots in the first row only are provided in **Table C.2**.

When examining the autocorrelation of the complex regressions between the wind and both D5 and D10, the de-correlation time scale decreased when using the de-trended data (**Figs. C.18**, **C.19**). This is to be expected; however, I also found that there are different de-correlation scales that apply to the *u* and *v* components. In every case, the *u* component de-correlates more slowly than the *v* component (**Figs. C.20–C.22**). The other drifters (not shown) were consistent with these results, verifying that all drifters in this study responded almost immediately to variability in the wind.

It follows that the wind velocities predicted the observed drifter velocities (i.e., trajectories) well when using a simple regression model. Observed and predicted drifter movements due to surface-layer wind-drift are shown in **Figure 5.11**, and the cross-correlograms confirm that the observed and predicted drifter trajectories are coherent (see **Fig. C.23** for D5 and D10, as examples). Setting the wind effect to zero in the complex regression model allows me to examine the net displacement of each drifter in the Lake due to the residual flow (i.e., the "drain") over the length of the data record (**Fig. 5.11**) or over a given time interval (**Fig. 5.12**). The parameters used to estimate the predicted drifter trajectories from the observed trajectories, and thus the contribution of the residual "drain," are provided in **Table C.3**; the optimal wind scale ranged from 0.98 x 10^{-2} to 1.34 x 10^{-2} and the optimal wind rotation ranged from -36.21 to -4.01.

5.3.5 Simple dispersal model and resulting MAP and VP comparisons

The simple drifter-based Gaussian diffusion model, using similar small-scale diffusivity (K_p) values to those in **Chapter 3**, reflected several aspects of the observed MAP field

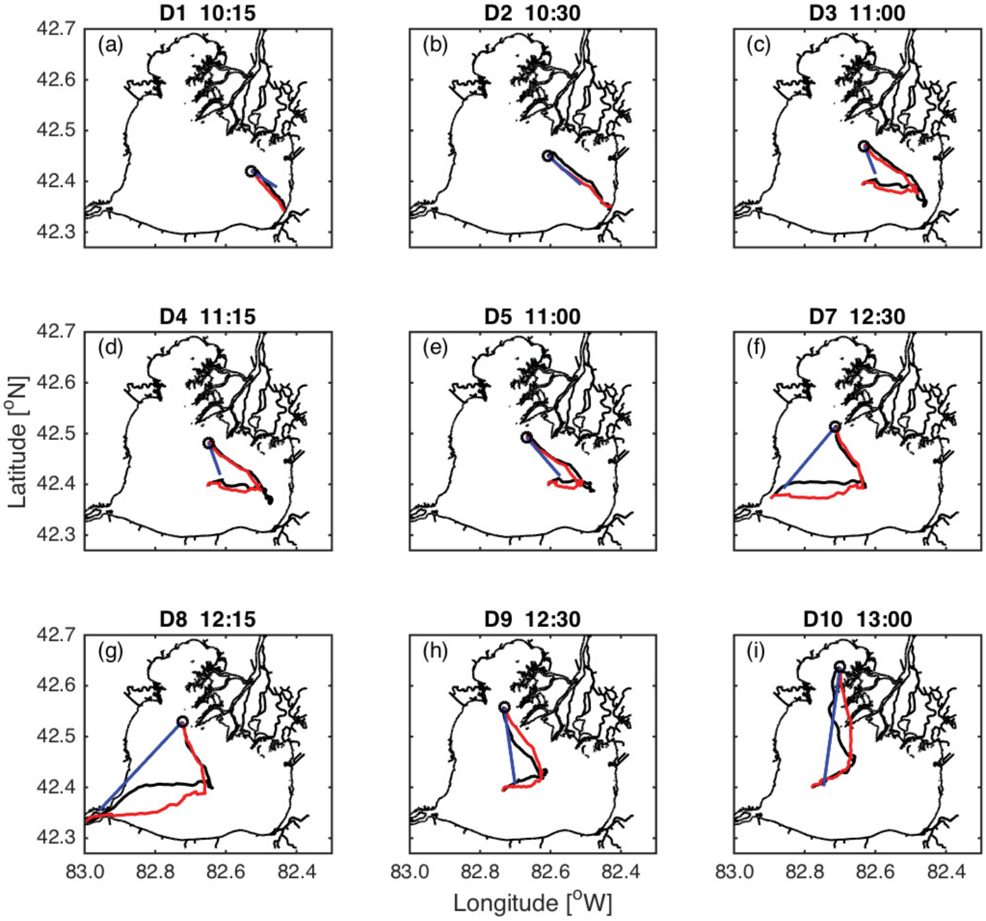

Figure 5.11 Coastline charts of Lake St. Clair illustrating (a–i) observed (black) drifter (D1–D10) movement, predicted (red) drifter movement due to surface-layer wind drift, and drifter net displacement (blue) due to the residual flow in the absence of any wind effect (i.e., the "drain") during the July 2009 particle tracing study. Drifter deployment locations are denoted with open circles and deployment times on 17 July 2009 are indicated above the respective subplots in EDST. Drifter positions are interpolated to a 15-m resolution.

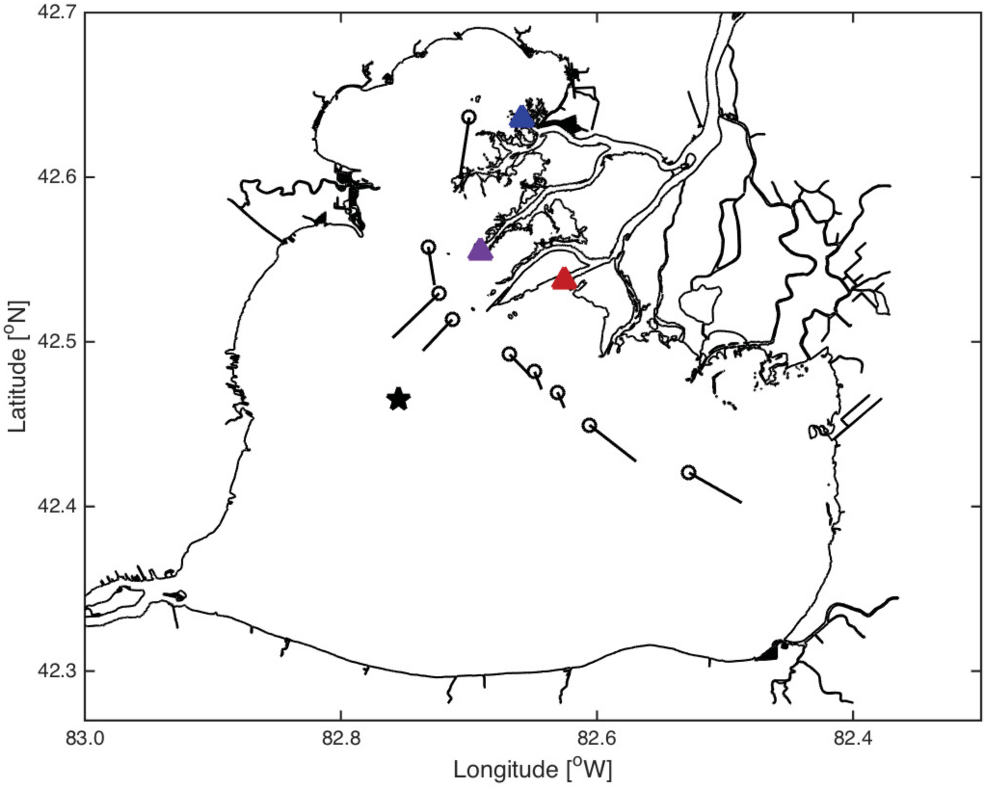

Figure 5.12 Coastline chart of Lake St. Clair illustrating drifter net displacement (km) over 24 hours of the July 2009 particle tracing study due to the residual flow in the absence of any wind effect; i.e., the “drain.” Drifter deployment locations are denoted with open black circles. MAP source locations are denoted by triangles, where the northern triangle (blue) represents the B-source, the southern triangle (red) represents the A-source, and the intermediate triangle (purple) represents the hypothetical averaged A+B source. The location of Station LSCM4, where wind speed and direction were recorded, is indicated with a star.

distribution illustrated in **Figures 5.3** and **5.13**, particularly in the eastern half of the Lake. The smoothing length scale of 0.05 degrees in both the *x*- and *y*-directions produced a minimum relative MAP concentration of 0.0, a maximum relative MAP concentration of 7.3, and a standard deviation of 0.46 (**Fig. 5.13**). The gradient near the source locations, especially that near the B-source location, is not well resolved due to the ten missing collectors that were concentrated in that region of the Lake. The location-specific MAP area estimates among recovered collectors and the resulting contours are provided in **Figures C.24** and **C.25**, respectively. In the following MAP and VP comparisons, the reader is again reminded that the modeled estimates of VPs can potentially span a much larger domain that extends beyond that defined by the magnetic-collector array and, as such, MAP and VP comparisons can only be confidently compared near the collector locations.

A visual comparison of **Figures 5.13** and **5.14** indicates that the model effectively reflected the general features of the observed MAP field when using a constant K_p of 50 m^2 s^{-1}. Within the confines of the collector array, the model tended to show relatively low concentrations of VPs in areas where the magnetic-collectors captured low concentrations of MAPs, typically further from the source locations, except in the northwestern portion of the Lake near the B-source location. The model also obtained high concentrations of VPs in areas where the collectors captured high concentrations of MAPs, in the northwest and southeastern portions of the Lake. VP concentration estimates, based on the other K_p values, illustrated patterns similar to those addressed above, but the VP dispersal fields did not encompass the entirety of the MAP dispersal

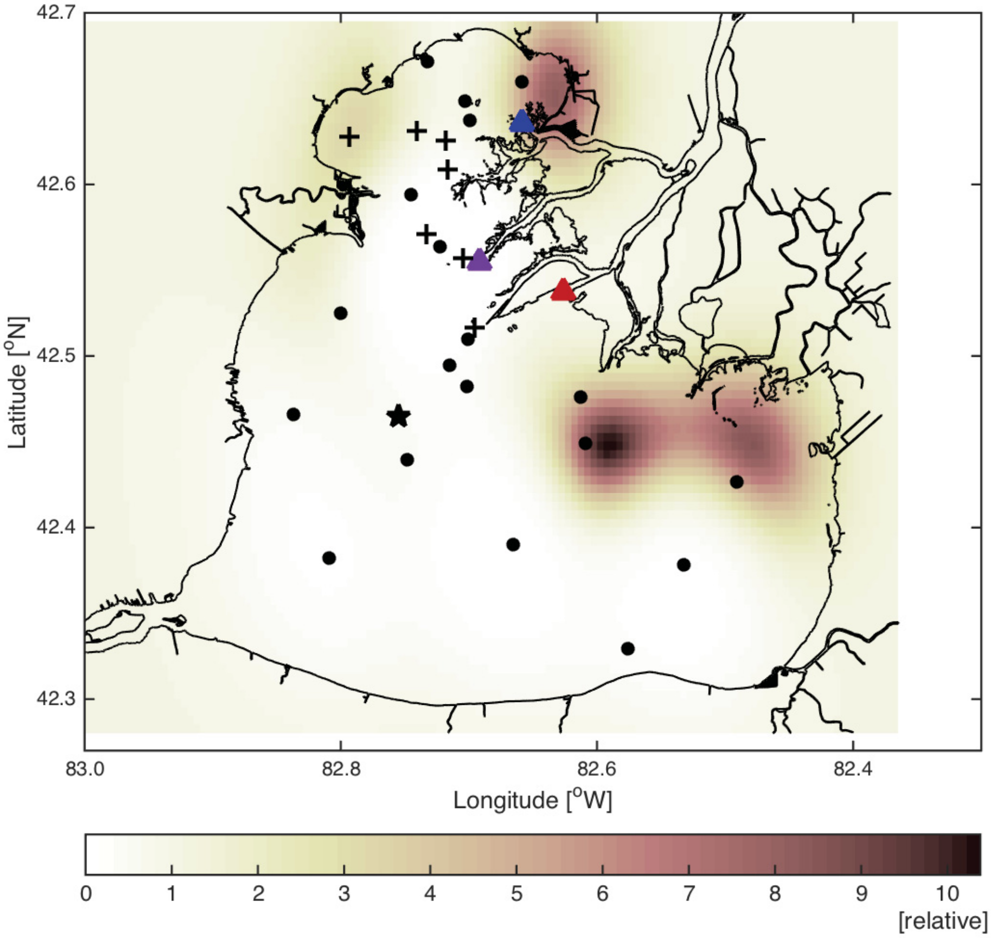

Figure 5.13 Coastline chart of Lake St. Clair and scale bar illustrating the relative number of A+B captured MAPs, with recovered collector locations denoted by filled black circles. MAP source locations are denoted by triangles, where the northern triangle (blue) represents the B-source, the southern triangle (red) represents the A-source, and the intermediate triangle (purple) represents the hypothetical averaged A+B source. The location of Station LSCM4, where wind speed and direction were recorded, is indicated with a star.

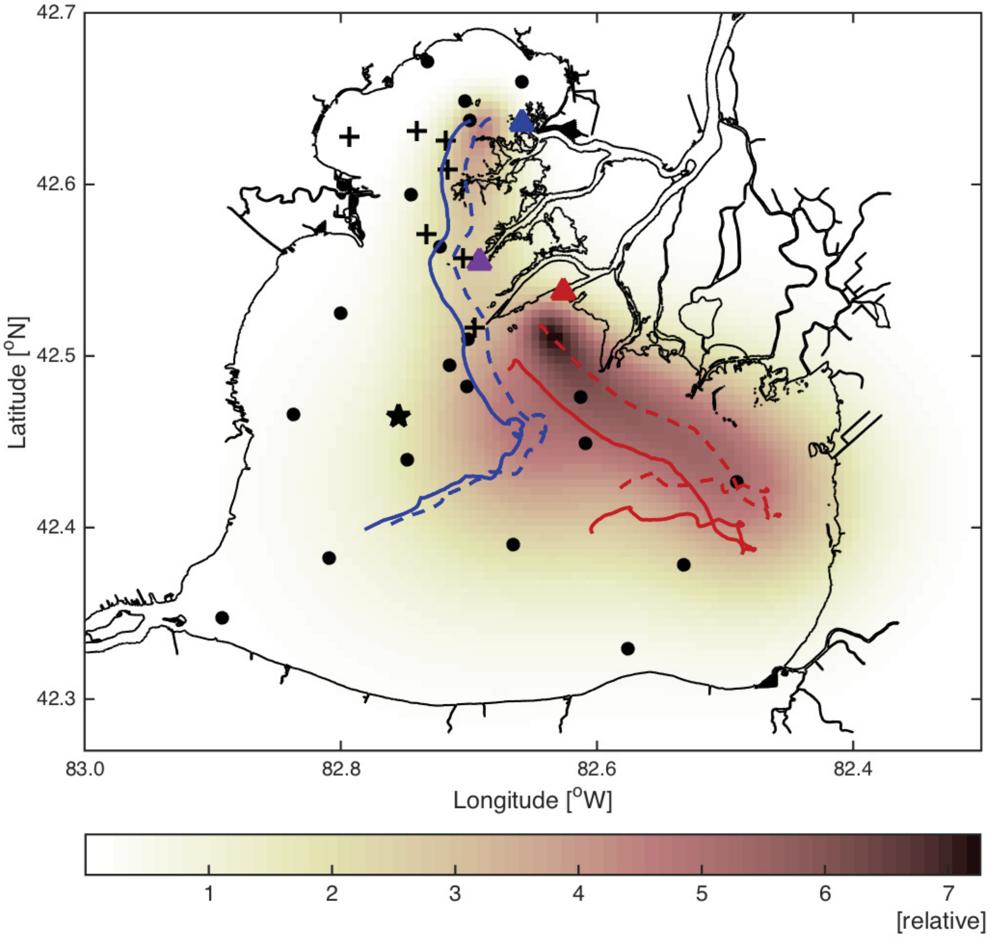

Figure 5.14 Coastline chart of Lake St. Clair and scale bar illustrating the relative number of VPs at each grid cell across the model domain as of 09:00 h EDST on 23 July 2009, and based on a small-scale diffusivity (K_p) constant of 50 $m^2\ s^{-1}$. Note that a scaling factor was applied so that the modeled and empirical results are directly comparable. The observed drifter trajectories are shown with solid lines (D5 red; D10 blue) and the modeled drifter trajectories are shown with dashed lines (D5 red; D10 blue). Black filled circles denote recovered collector locations. MAP source locations are denoted by triangles, where the northern triangle (blue) represents the B-source, the southern triangle (red) represents the A-source, and the intermediate triangle (purple) represents the hypothetical averaged A+B source. The location of Station LSCM4, where wind speed and direction were recorded, is indicated with a star. VPs cannot move beyond the coastline.

field at any K_p value that was examined (**Figs. C.26–C.29**). At low K_p values (2 m^2 s^{-1} and 5 m^2 s^{-1}), the VPs remain along the modeled drifter trajectories (**Figs. C.26**, **C.27**). When K_p was increased from 25 m^2 s^{-1} to 50 m^2 s^{-1} and to 80 m^2 s^{-1}, the VP field was more dispersed with relatively large concentrations in regions where I obtained relatively large MAP concentrations (**Figs. 5.3**, **5.13, C.28, C.29**); however, the VPs still did not reach the collector locations furthest from the source locations. In summary, as also evident in **Chapters 3** and **4**, the largest differences in the MAP and VP dispersal estimates exist in the far-field.

5.4 Discussion

5.4.1 Estimating dispersal kernels

I have again demonstrated the ability of the MAP and magnetic-collector system to empirically estimate the passive component of a particle dispersal kernel, but in a small, shallow freshwater lake system. As in **Chapters 3** and **4**, the physical connectivity estimates can be applied to any passive planktonic organism and (or) particulate resident in the surface waters of this region, and the results I obtained in the Lake have implications to the dispersal of both native and invasive species, as well as pollutants such as microplastics. I estimated that the A+B MAP dispersal kernel has an *e*-folding scale of 11.45 km (**Fig. 5.4**), and this is approximately one-quarter of the Lake's length and (or) width. As examined in **Chapter 3**, the probability of passive retention within a distance D and over time T is $\int_0^D 2\pi L\ p(L)dL = \int_0^D ae^{-aL}\,dL = 1 - e^{aD}$. Assuming that D is equal to 40 km for the length and (or) width of the Lake, when a^{-1} is equal to the estimated dispersal kernel of 11.45 km, I estimate the probability of passive retention to be 1.00. As the period of my study was 5 to 6 days, this is consistent with the average 7- to 9-d residence time of water in Lake St. Clair. The residence time of the Lake can actually vary from 2 to 30 days, depending on wind direction, circulation patterns, and the seasonal variation in the amount of water flowing out of Lake Huron (Quinn 1992, Herdendorf *et al.* 1986, Schwab *et al.* 1989, Lang and Fontaine 1990, Bolsenga and Herdendorf 1993, Holtschlag and Koschik 2002, Rao and Schwab 2007, Anderson *et al.* 2010, Anderson and Schwab 2011). For example, if water flows directly through the dredged shipping channel, water remains in the Lake for the minimum of 2 days. If my study had exceeded 7 to 9 days, it is likely that MAPs would have entered the Detroit River at the southern end of Lake St. Clair; however, I have shown that concentrations would fall to $\frac{1}{e^4}$ = 1.80% of the original number at a distance of 46 km from the source (i.e., four *e*-folding scales of 11.45 km), which covers the entire north-south length of the Lake. This suggests that propagule or particulate concentrations that enter Lake St. Clair diminish rapidly over relatively short length scales, limiting dispersal and hence connectivity over the length of the Lake.

The subjective categorization of A- and B-MAPs from their respective source locations suggests that a single dispersal kernel estimate may not apply to the entire Lake. As I concluded in **Chapters 3** and **4**, the dispersal kernel likely varies in space and time. This postulation is supported in the Lake because of the different *e*-folding scale estimates I obtained based on the separate A- (7.08 km; **Fig. C.5**) and B- (14.16 km; **Fig. C.6**) MAP source locations. The B-MAP release in the northwestern margin of the Lake produced a shallower exponential decay curve as distance from the source increased (**Figs. 5.5**, **C.6**).

In this more sheltered region of the Lake, there is likely a reduced wind effect and an increased shoreline influence that impacts the ease of dispersal and thus increases the residence time. In summary, a space- and time-varying dispersal kernel in this study supports the conclusions in **Chapters 3** and **4** that estimating dispersal kernels requires consideration of semi-enclosed and nearshore waters separately from open waters.

These empirical estimates of dispersal can provide an illustrative context for some of the current and developing issues in the HEC with both environmental and socio-economic consequences. Even though the Lake is highly diffusive, I have shown above that dispersal and connectivity are limited over the length of Lake St. Clair. When considering non-indigenous species, this suggests that the main constraint to potential establishment and invasion success is propagule pressure, which is based on propagule numbers, sizes, and spatial and temporal patterns of arrival (Ricciardi and Rasmussen 1998; Ricciardi and MacIsaac 2000; MacIsaac *et al.* 2002; Colautti *et al.* 2003; Grigorovich *et al.* 2003; Drake and Lodge 2004; Holeck *et al.* 2004; Bailey *et al.* 2005; Duggan *et al.* 2005; Lockwood *et al.* 2005; Colautti *et al.* 2006; Ricciardi 2006; Costello *et al.* 2007; Gray *et al.* 2007; Simberloff 2009; Rup *et al.* 2010; Bailey *et al.* 2011; Briski *et al.* 2012; DiBacco *et al.* 2012; Bailey 2015; MacIsaac *et al.* 2015). Minimum concentrations necessary for successful establishment, settlement, and subsequent aggregation are unknown, and this becomes further complicated by unknown spatial scales of dispersal in the HEC (Grigorovich *et al.* 2003; MacIsaac *et al.* 2004; Ricciardi 2006; Gray *et al.* 2007; Wells *et al.* 2011). The HEC accounts for a disproportionately high percentage of invasion success due to ballast-water discharge (Grigorovich *et al.*

2003; Ricciardi 2006; Dopazo *et al.* 2008; Sieracki *et al.* 2014a). Given the shallow, warm waters of Lake St. Clair that provide high habitat suitability, the management of ballast-mediated transport due to transoceanic commercial shipping is especially important at ports upstream in the St. Clair River. While advection and mixing in the St. Clair River may typically prevent invasion success in planktonic populations (e.g., Sun *et al.* 2013), the wind-driven dynamics in this region mean that infrequent events can heavily influence species distributions (e.g., Thackeray *et al.* 2004; **Chapters 3** and **4**; addressed further below). While propagule concentrations fall to a small fraction of their initial level after dispersal throughout the Lake (above), there are still a minimal number of individuals transported to the far-field. In the case of invasive species, as discussed in detail in **Chapter 4**, small numbers can lead to further range expansion since it is the long-distance (far-field) dispersal of just a few individuals that govern the invasion speed (e.g., Goldwasser *et al.* 1994; Kot *et al.* 1996; Clark *et al.* 1998; Neubert and Caswell 2000; Shigesada and Kawasaki 2002; Okubo and Levin 2010; Hoyer *et al.* 2015). Further, since Lake St. Clair is so small and shallow, wind events would easily increase the potential far-field dispersal.

Lake St. Clair contains the majority of the coastal wetlands in the Great Lakes system, and this diverse habitat provides spawning grounds for over 65 fish species (Herdendorf *et al.* 1986), including broadcast spawners like the threatened endemic lake sturgeon (*Acipenser fulvescens*; Auer 1996; Auer and Baker 2002; Manny and Kennedy 2002; Nichols *et al.* 2003; Holtgren and Auer 2004; Peterson *et al.* 2007; Mandrak and Cudmore 2010; Bouckaert *et al.* 2014; Welsh *et al.* 2017) and multiple species of introduced Asian carp (Herborg *et al.* 2007; Buck *et al.* 2010; Cooke *et al.* 2010; Mandrak and Cudmore 2010; Stockstad 2010; Murphy and Jackson 2013; Cuddington *et al.* 2014; Wittmann *et al.* 2014; Embke *et al.* 2016). These fishes have early life-stages that are well emulated by the MAPs. Both the restoration and conservation efforts for lake sturgeon populations in the spawning grounds of the lower St. Clair River and the identification of dispersal pathways to mitigate further range expansion of Asian carp in the Great Lakes basin require quantifying the extent of larval drift. It is not until the potential spatial scales of dispersal are known that targeted management strategies will be successful and the effects of compounding factors such as climate change, habitat degradation, and overfishing on these populations can be examined thoroughly.

I focus here on the recent and increasing concern in the Laurentian Great Lakes regarding the spread of pollutants, especially microplastic (<5 mm, although the definition varies and is inconsistent among studies) particles (Zbyszewski and Corcoran 2011; Eriksen *et al.* 2013; Wagner *et al.* 2014; Zbyszewski *et al.* 2014; Driedger *et al.* 2015; Dris *et al.* 2015; Eerkes-Medrano *et al.* 2017; Hoffman and Hittinger 2017; Horton *et al.* 2017; Dean *et al.* 2018). High abundances of microplastic particles have been found in the surface waters of the Great Lakes and are linked to both fragments derived from the breakdown of macroplastics and to microbeads found in consumer products such as facial cleansers and toothpastes (Eriksen *et al.* 2013); however, the distribution and dispersal of these particles is largely unknown, and robust sampling of microplastics in aquatic environments has proven to be challenging (Cole *et al.* 2011; Zbyszewski *et al.* 2014; Dris *et al.* 2015; Rocha-Santos and Duarte 2015; Twiss 2016; Avio *et al.* 2017; Eerkes-

Medrano *et al.* 2017; Horton *et al.* 2017; Dean *et al.* 2018). The watersheds surrounding the Great Lakes are heavily developed and densely populated, with the Lakes providing more than 40 million residents with access to drinking and industrial water, food, hydro-electric supplies, recreation, and transportation. Lake St. Clair, in particular, is one of the most utilized regions in the Great Lakes system (Kelly 2007).

There has been considerable recent global interest regarding the potential human health impacts of microplastic pollution, resulting in extensive media coverage and the creation of legislation to lessen the abundant use of plastics in consumer products. My study shows that with a local release microplastic particles would be present in every part of the Lake within one week. Further, contaminants can attach to microplastic particles and bio-accumulate when swallowed by fish. When a fish is then caught and eaten, it becomes a potential carrier of pollutants further up the food chain (Derraik 2002; Cole *et al.* 2011; Zbyszewki and Corcoran 2011; Eriksen *et al.* 2013; Driedger *et al.* 2015). Microplastic debris may also serve as a vector to transport non-indigenous species and (or) pathogens that enter the system via ballast-water discharge and (or) through migratory fish (Pham 2009; Cole *et al.* 2011; Pham *et al.* 2012; Sieracki *et al.* 2014a,b; Wagner *et al.* 2014; Driedger *et al.* 2015; Avio *et al.* 2017; Eerkes-Medrano *et al.* 2017). For example, the process of range expansion of the invasive viral haemorrhagic septicemia virus (VHSV) in the Great Lakes basin is unknown (Groocock *et al.* 2007; Bain *et al.* 2010; VHSV Expert Panel and Working Group 2010; Faisal and Winters 2011; Faisal *et al.* 2012; Escobar *et al.* 2017), and this highly dispersive virus may be able to use inanimate objects such as microplastic debris to propagate among fish populations (Pham 2009; Pham *et al.* 2012; Wagner *et al.* 2014). In addition to the socio-economic and health impacts that microplastic particles introduce, microplastics in the Great Lakes system have the ability to intensify this issue in marine systems since the Great Lakes flow into the St. Lawrence River and ultimately to the North Atlantic Ocean; the Lakes thus represent a potential upstream source of plastic pollution into the North Atlantic Gyre (Eriksen *et al.* 2013; Wagner *et al.* 2014; Eerkes-Medrano *et al.* 2017). Addressing any of the concerns above regarding microplastic pollution requires insight into the spatial patterns of dispersal that an empirical dispersal kernel can provide.

5.4.2 Drifter and wind analyses

The coherence among drifters in my study (**Fig. 5.7**) shows that the near-surface water in Lake St. Clair was mainly moving as a slab, with the majority of motion explained by variability in the observed wind speed and direction. This strong wind influence is not surprising given the shape, size, and depth of the Lake, and implies that advection is dominant relative to diffusion in this system. As discussed in previous Chapters, this means that single wind events can greatly impact propagule and (or) particulate dispersal and distribution (e.g., Thackeray *et al.* 2004), as sensitivity to the wind is much greater than sensitivity to the small-scale diffusivity. Drifter movement is the combination of residual flow and dispersal affected by fluctuations in the wind. While the change in direction of the drifters after approximately two days is well explained by the change in the observed wind direction (**Fig. C.8**), it does not explain why both the MAPs and drifters dispersed as far as the entrance of the Detroit River. Ignoring the wind effect in a simple regression model (**Equation 5.1**) allowed me to examine the residual flow (i.e., the “drain”; **Figs. 5.11**, **5.12**). It is clear that Lake St. Clair is an advective flow-through system (Quinn 1992, Herdendorf *et al.* 1986, Schwab *et al.* 1989, Lang and Fontaine 1990, Bolsenga and Herdendorf 1993, Holtschlag and Koschik 2002, Rao and Schwab 2007, Anderson *et al.* 2010, Anderson and Schwab 2011), with drifters becoming entrained in the dredged navigation channel and flowing into the Detroit River in the absence of wind (blue in **Fig. 5.11**). As evident with D7 and D8 (**Fig. 5.11**), drifter release location, with respect to the inflow and dredged navigation channel, has a large effect on a) whether a given drifter reaches the Detroit River and b) how long it can take to arrive there. It is recognized that there may be significant differences between sections of the Lake due to the formation of either hydraulically-driven (western) or wind-induced (eastern) zones (Schwab *et al.* 1989; Holtschlag and Koschick 2002; Anderson *et al.* 2010; Anderson and Schwab 2011). The relationship between hydraulically-driven currents and wind-induced circulation throughout the HEC is key to understanding hydrodynamics in the Lake and how specific wind conditions may change this relationship, temporarily restructure flow in the Lake, and influence scales of dispersal.

5.4.3 MAP and VP comparisons

The MAP spatial distribution field estimates are time-integrated, but the drifters combined with the simple Gaussian dispersal model allow time as a variable to be considered. The model allowed me to examine, within the drifter domain, how the MAP field evolved from the two point sources (A, B) and explains how and why the observed distribution field of MAPs emerged at the end of the study period (**Figs. 5.13**, **C.24–C.25**). Interestingly, the model demonstrated that the sum total of particles in a given collector are captured at different times throughout the study. **Figure 5.15** illustrates that a collector can receive the majority of its particles at the beginning of the study (e.g., Collector 11), at the end of the study (e.g., Collector 13), or at multiple times during the study (e.g., Collector 15). The MAP data provide a snap-shot of a time-integrated state at the end of a given dispersal period; however, the novelty and significance of interpreting the MAPs in conjunction with drifters in this simple model demonstrates how the time-integrated state at a given location actually developed over space and time. It is important to remember that the MAP (**Fig. 5.13**, **C.24**, **C.25**) and VP (**Fig. 5.14**, **C.26–C.29**) fields can only be confidently compared at the magnetic-collector locations near observed drifter trajectories because the data resulting from the optimal interpolation is subjective where there are no "true" data points.

As in **Chapter 3**, I demonstrated a sensitivity that the model exhibits to a varying small-scale diffusivity (K_p). My results again indicate that there is no "best" modeled value and the "true" K_p is likely varying in space and time. At constant K_p values equal to or greater than 50 $m^2 s^{-1}$ (**Figs. 5.14**, **C.29**), the resultant VP field is basically uniform, while there are large consequences to the changes in K_p at values less than 50 $m^2 s^{-1}$ (**Figs. C.26–C.28**). At lower K_p values, a small change can cause a large impact to the outcome of dispersal. This is evident when comparing how the VPs remain along the modeled drifter trajectories at constant K_p values of 2 $m^2 s^{-1}$ and 5 $m^2 s^{-1}$ (**Figs. C.26**, **C.27**) to how the VP field becomes progressively more smoothed at constant K_p values of 25 $m^2 s^{-1}$ and above (**Figs. 5.14**, **C.28**, **C.29**). As K_p increases, the majority of the differences between model simulations lie in the far-field, again implying that the far-field, and thus the "tail"

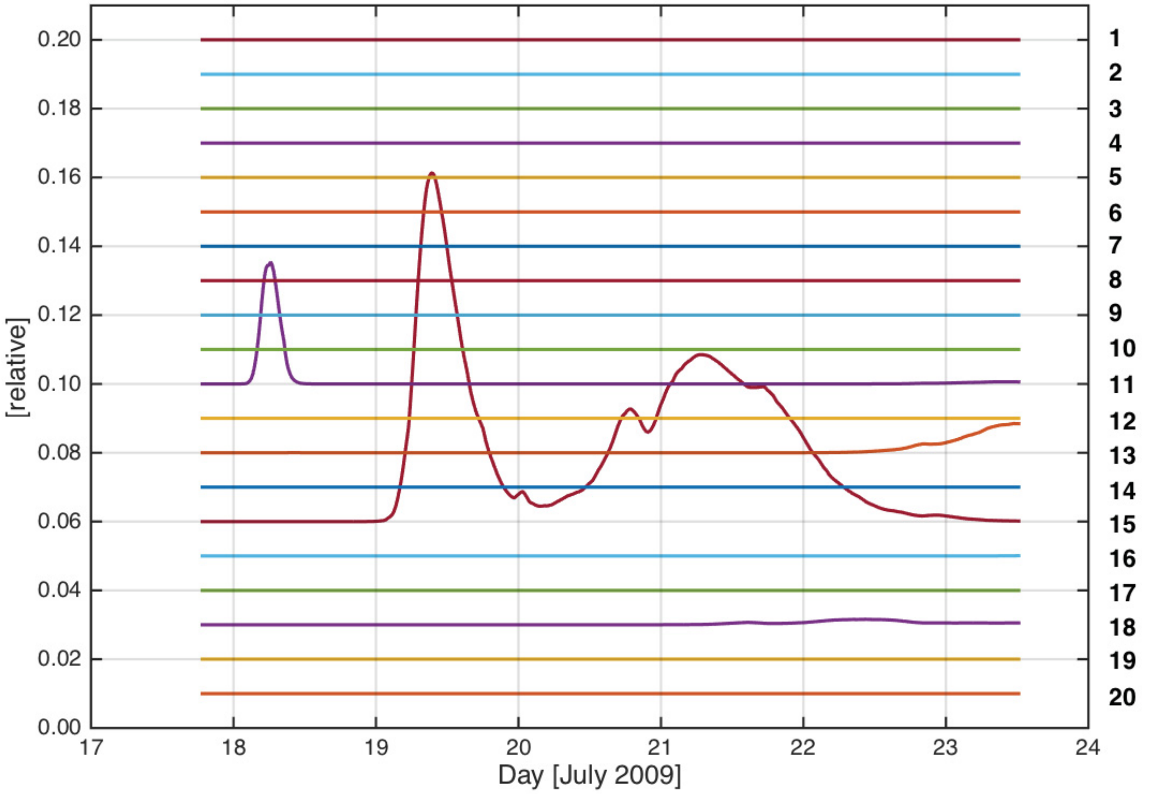

Figure 5.15 Example time series of relative MAP concentrations in each recovered collector (colored lines, 1–20 on right ordinate) over the modeled dispersal period from 13:00 h EDST on 17 July 2009 through 09:00 h EDST on 23 July 2009.

of the dispersal kernel, are important when estimating connectivity. As previously stated in **Chapters 3** and **4**, dispersal rates are extremely sensitive to the "tail" of the dispersal kernel, and it is often within this "tail" that modeling dispersal becomes problematic (Kot *et al.* 1996; Clark *et al.* 1998; Higgins and Richardson 1999; Bullock and Clarke 2000; Cain *et al.* 2000; Cowen *et al.* 2000; Bossenbroek *et al.* 2001; Nathan *et al.* 2003; Shanks et al. 2003; Nathan 2005; Trakhtenbrot *et al.* 2005; Klein *et al.* 2006; Dyer 2007; Skarpaas and Shea 2007; Nathan *et al.* 2008; Okubo and Levin 2010; Gillespie *et al.* 2012; Putman and He 2013; Simpson *et al.* 2014; García and Borda-de-Água 2017; Jordano 2017). Both the high-resolution hydrodynamic modeling system employed in **Chapters 3** and **4** and the simple Gaussian diffusion model used here exhibit difficulties reflecting the far-field MAP observations, indicating once more that modeled long-distance dispersal predictions may be too spatially conservative (e.g., **Chapter 3**; Okubo and Levin 2010; Hrycik *et al.* 2013). This is especially true in Lake St. Clair where single wind events have such a profound impact on the outcome of long-distance dispersal, as modeling infrequent events is particularly challenging.

In summary, this study demonstrated the power of using the empirical dispersal estimates provided by the MAPs and conventional drogued drifters in combination, with the simple Gaussian diffusion model affording new information that could not be achieved with only one measure of dispersal.

Chapter 6

Conclusions

The current state of dispersal and connectivity research demonstrates both a lack of empirical data and a perhaps unwarranted reliance on models. This thesis aimed to address both of these issues. Given my objectives, I successfully quantified the dispersal of purely passive particles at the scale of early-stage planktonic organisms in the near-surface upper mixed layer of coastal ocean (**Chapters 3** and **4**) and lake (**Chapter 5**) environments using a new technology. To do so, I further developed a magnetically attractive particle (MAP) and magnetic-collector prototype technology system (**Chapter 2**; Ruddick and Taggart 2006, 2011) that provides a time-integrated estimate of the purely passive component of dispersal from a given source location to a large set of potential sink locations; the biological null model. The empirical estimates of dispersal (**Chapters 3**, **4**, and **5**) are undoubtedly the most novel contribution of this thesis, proving that long-distance dispersal can be more easily measured in the field at varying space- and time-scales; however, I discovered that dispersal kernel estimates are not always applicable based on the dynamics of the system (**Chapter 4**). The quantitative, empirical estimates that the MAPs provide can also be used to test other technologies that estimate dispersal. I qualitatively and quantitatively compared the observed passive particle dispersal estimates to similar estimates derived from hydrodynamic models (**Chapters 3**, **4** and **5**) and drogued drifters (**Chapter 5**). Finally, I interpreted the results from each study in the context of issues surrounding commercially valuable and (or) invasive species (**Chapters 3**, **4** and **5**), and addressed the potential concerns and implications when using the various technologies to quantify dispersal (**Chapters 2–5**).

The results presented here share common themes among Chapters that form the major findings of this thesis. I have shown that there appear to be parameter-value issues with some models, and that small-scale diffusivity (K_p) is important and likely varying in space and time (**Chapters 3**, **4**, and **5**). With no "best" value to employ, modeling becomes even more challenging. When using models in a predictive context, it is wise to remember that the proper use of models comes from recognition of their limitations. Past conditions do not necessarily dictate what to expect in the future, and when models are used for conservation and management purposes, they must first be tested and validated in a dispersal and connectivity context (e.g., **Chapters 3** and **4**). The passive component of dispersal that the null model provides represents the fundamental constraints on all of the coupled biophysical outcomes. As such, until the null model is validated, the veracity of results stemming from the inclusion of biological processes in assessing dispersal remains uncertain. Many factors beyond science influence management decisions, and scientists should strive for model credibility based on empirical data to strengthen their predictions and suggestions that ultimately need to be weighed against socio-economic pressures. I have additionally shown that semi-enclosed water masses need to be treated differently than open-ocean water masses when considering dispersal, as the far-field (i.e., the "tail" of the dispersal kernel) determines the potential long-distance dispersal (**Chapters 3**, **4**, and **5**). My analyses show that models can struggle to capture the far-field effect, and spatially conservative estimates of dispersal based on these models can have significant consequences in the management of any species, and can be especially severe in the case of invasive species (e.g., **Chapters 3**, **4**, and **5**). Finally, I demonstrated the synergistic power of using multiple measures of dispersal together to obtain new information that could not be achieved with only one measure (**Chapter 5**).

When employing a new technology to address a well-established problem, the first goal is to determine whether the desired measurement is even possible. Can an aquatic dispersal kernel be quantified using the MAP and magnetic-collector prototype technology system? The studies I present here show that it is not only possible, but replicable. Now that the MAP and magnetic-collector system has proven to be effective in the near-surface upper mixed layer, it can be applied in other contexts to answer remaining dispersal questions. For example, it is conceivable that magnetic-collectors can be deployed at multiple depths throughout the water column to capture any potential vertical distribution of MAPs during a given study. A larger magnetic-collector array designed in this way would address some of the issues both inherent in the MAPs and in their application to particles affected by biological phenomena. The primary concern with MAP production and quality control is in their resulting density distribution, and collectors at varying depths will capture MAPs that sink out of the upper mixed layer. Additionally, the ability to capture MAPs at multiple depths allows comparison with active organisms that may alter their depth via swimming and (or) buoyancy changes. In this case, thanks to the biological null model obtained with the MAPs, the complex issue of biophysical dispersal can be separated into its biological and physical components.

One of the major challenges I encountered when studying dispersal is an inconsistent and varied use of language. Since dispersal is studied using various approaches among many disciplines, there is no consistent definition of “dispersal.” The use of the word “dispersal” in the literature is extensive; however, it is not well defined each time it is used. As a result, dispersal estimates that do exist are not easily comparable. The scientific community should develop a common working language across disciplines, including both terrestrial and aquatic researchers in this discussion.

This thesis provides a proof of concept of a simple technological system that achieves an empirical measure of an aquatic dispersal kernel at a relatively low cost and allows a direct comparison to modeled predictions. As such, it has made an advance toward linking the empirical with the theoretical.

Literature Cited

Aiken, C.M., Navarrete, S.A., Castillo, M.I., and Castilla, J.C. 2007. Along-shore larval dispersal kernels in a numerical ocean model of the central Chilean coast. *Marine Ecology Progress Series* **339**, 13-24. doi: 10.3354/meps339013

Allen, R.M., Metaxas, A., and Snelgrove, P.V.R. 2018. Applying movement ecology to marine animals with complex life cycles. *Annual Review of Marine Science* **10**, 19-42. doi: 10.1146/annurev-marine-121916-063134

Almany, G.R., Planes, S., Thorrold, S.R., Berumen, M.L., Bode, M., Saenz-Agudelo, P., Bonin, M.C., Frisch, A.J., Harrison, H.B., Messmer, V., Nanninga, G.B., Priest, M.A., Srinivasan, M., Sinclair-Taylor, T., Williamson, D.H., and Jones, G.P. 2017. Larval fish dispersal in a coral-reef seascape. *Nature Ecology & Evolution* **1**, 0148. doi: 10.1038/s41559-017-0148

Anderson, E.J., Schwab, D.J., and Lang, G.A. 2010. Real-time hydraulic and hydrodynamic model of the St. Clair River, Lake St. Clair, Detroit River system. *Journal of Hydraulic Engineering* **136.8**, 507-518. doi: 10.1061/(ASCE)HY.1943-7900.0000203

Anderson, E.J. and Schwab, D.J. 2011. Relationships between wind-driven and hydraulic flow in Lake St. Clair and the St. Clair River Delta. *Journal of Great Lakes Research* **37.1**, 147-158. doi: 10.1016/j.jglr.2010.11.007

Aref, H. 1984. Stirring by chaotic advection. *Journal of Fluid Mechanics* **143**, 1-21. doi: 10.1017/S0022112084001233

Arim, M., Abades, S.R, Neill, P.E., Lima, M., and Marquet, P.A. 2006. Spread dynamics of invasive species. *Proceedings of the National Academy of Sciences of the United States of America* **103.2**, 374-378. doi: 10.1073/pnas.0504272102

Atkinson, J.F. and Domske, H.M. 2015. Great Lakes under stress: Invasive species as agents of ecosystem change. *Lessons in Conservation* **5**, 17-31.

Audet, D., Davis, D.S., Miron, G., Moriyasu, M., Benhalima, K., and Campbell, R. 2003. Geographical expansion of a nonindigenous crab, *Carcinus maenas* (L.), along the Nova Scotian shore into the southeastern Gulf of St. Lawrence, Canada. *Journal of Shellfish Research* **22.1**, 255-262.

Auer, N.A. 1996. Importance of habitat and migration to sturgeons with emphasis on lake sturgeon. *Canadian Journal of Fisheries and Aquatic Sciences* **53.S1**, 152-160.

Auer, N.A. and Baker, E.A. 2002. Duration and drift of larval lake sturgeon in the Sturgeon River, Michigan. *Journal of Applied Ichthyology* **18.4-6**, 557-564. doi: 10.1046/j.1439-0426.2002.00393.x

Avio, C.G., Gorbi, S., and Regoli, F. 2017. Plastics and microplastics in the oceans: From emerging pollutants to emerged threat. *Marine Environmental Research* **128**, 2-11. doi: 10.1016/j.marenvres.2016.05.012

Bailey, S.A., Duggan, I.C., Jenkins, P.T., and MacIsaac, H.J. 2005. Invertebrate resting stages in residual ballast sediment of transoceanic ships. *Canadian Journal of Fisheries and Aquatic Sciences* **62.5**, 1090-1103. doi: 10.1139/f05-024

Bailey, S.A., Deneau, M.G., Jean, L., Wiley, C.J., Leung, B., and MacIsaac, H.J. 2011. Evaluating efficacy of an environmental policy to prevent biological invasions. *Environmental Science and Technology* **45.7**, 2554-2561. doi: 10.1021/es102655j

Bailey, S.A. 2015. An overview of thirty years of research on ballast water as a vector for aquatic invasive species to freshwater and marine environments. *Aquatic Ecosystem Health & Management* **18.5**, 261-268. doi: 10.1080/14634988.2015.1027129

Bain, M.B., Cornwell, E.R., Hope, K.M., Eckerlin, G.E., Casey, R.N., Groocock, G.H., Getchell, R.G., Bowser, P.R., Winton, J.R., Batts, W.N., Cangelosi, A., and Casey, J.W. 2010. Distribution of an invasive aquatic pathogen (Viral Haemorrhagic Septicemia Virus) in the Great Lakes and its relationship to shipping. *PLoS ONE* **5.4**, e10156. doi: 10.1371/journal.pone.0010156

Becker, B.J., Levin, L.A., Fodrie, F.J., and McMillan, P.A. 2007. Complex larval connectivity patterns among marine invertebrate populations. *Proceedings of the National Academy of Sciences of the United States of America* **104.9**, 3267-3272. doi: 10.1073/pnas.0611651104

Begon, M., Townsend, C.R., and Harper, J.L. 2006. Ecology: From individuals to ecosystems. Blackwell Publishing, Malden, Massachusetts, United States of America, 738 pp.

Benaroya, A.R. 2012. Laboratory tests and field trial of a new method for sediment tracing. Bachelor of Science Honours Thesis, Dalhousie University, Halifax, Nova Scotia, Canada, 36 pp.

Bennion, D.H. and Manny, B.A. 2014. A model to locate potential areas for lake sturgeon spawning habitat construction in the St. Clair–Detroit River System. *Journal of Great Lakes Research* **40.S2**, 43-51. doi: 10.1016/j.jglr.2014.02.002

Benoît, H.P. and Swain, D.P. 2008. Impacts of environmental change and direct and indirect harvesting effects on the dynamics of a marine fish community. *Canadian Journal of Fisheries and Aquatic Sciences* **65.10**, 2088-2104. doi: 10.1139/F08-112

Boase, J.C., Manny, B.A., Donald, K.A.L., Kennedy, G.W., Diana, J.S., Thomas, M.V., and Chiotti, J.A. 2014. Habitat used by juvenile lake sturgeon (*Acipenser fulvescens*) in the North Channel of the St. Clair River (Michigan, USA). *Journal of Great Lakes Research* **40.S2**, 81-88. doi: 10.1016/j.jglr.2013.11.002

Bolsenga, S.J. and Herdendorf, C.E. 1993. Lake Erie and Lake St. Clair Handbook. Wayne State University Press, Detroit, Michigan, United States of America, 475 pp.

Bossenbroek, J.M., Kraft, C.E., and Nekola, J.C. 2001. Prediction of long-distance dispersal using gravity models: Zebra mussel invasion of inland lakes. *Ecological Applications* **11.6**, 1778-1788. doi: 10.1890/1051-0761(2001)011[1778:POLDDU]2.0.CO;2

Botsford, L.W., White, J.W., Coffroth-M.-A., Paris, C.B., Planes, S., Shearer, T.L., Thorrold, S.R., and Jones, G.P. 2009. Connectivity and resilience of coral reef metapopulations in marine protected areas: Matching empirical efforts to predictive needs. *Coral Reefs* **28.2**, 327-337. doi: 10.1007/s00338-009-0466-z

Bouckaert, E.K., Auer, N.A., Roseman, E.F., and Boase, J. 2014. Verifying success of artificial spawning reefs in the St. Clair–Detroit River System for lake sturgeon (*Acipenser fulvescens* Rafinesque, 1817). *Journal of Applied Ichthyology* **30.6**, 1393-1401. doi: 10.1111/jai.12603

Bowler, D.E. and Benton, T.G. 2005. Causes and consequences of animal dispersal strategies: Relating individual behavior to spatial dynamics. *Biological Reviews* **80.2**, 205-225. doi: 10.1017/S1464793104006645

Bradbury, I.R. and Snelgrove, P.V.R. 2001. Contrasting larval transport in demersal fish and benthic invertebrates: The roles of behavior and advective processes in determining spatial pattern. *Canadian Journal of Fisheries and Aquatic Sciences* **58.4**, 811-823. doi: 10.1139/f01-031

Briski, E., Ghabooli, S., Bailey, S.A., and MacIsaac, H.J. 2012. Invasion risk posed by macroinvertebrates transported in ships' ballast tanks. *Biological Invasions* **14.9**, 1843-1850. doi: 10.1007/s10530-012-0194-0

Buck, E.H., Upton, H.F., Stern, C.V., and Nicols, J.E. 2010. Asian carp and the Great Lakes region. Congressional Research Service Reports 12, Congressional Research Service, 23 pp.

Bullock, J.M. and Clarke, R.T. 2000. Long-distance seed dispersal by wind: Measuring and modeling the tail of the curve. *Oecologia* **124.4**, 506-521. doi: 10.1007/PL00008876

Bundy, A., Heymans, J.J., Morissette, L., and Savenkoff, C. 2009. Seals, cod and forage fish: A comparative exploration of variations in the theme of stock collapse and ecosystem change in four Northwest Atlantic ecosystems. *Progress in Oceanography* **81.1-4**, 188-206. doi: 10.1016/j.pocean.2009.04.010

Byers, J.E. and Pringle, J.M. 2006. Going against the flow: Retention, range limits and invasions in advective environments. *Marine Ecology Progress Series* **313**, 27-41. doi: 10.3354/meps313027

Cain, M.L., Milligan, B.G., and Strand, A.E. 2000. Long-distance seed dispersal in plant populations. *American Journal of Botany* **87.9**, 1217-1227. doi: 10.2307/2656714

Carver, C.E., Chisholm, A., and Mallet, A.L. 2003. Strategies to mitigate the impact of *Ciona intestinalis* (L.) biofouling on shellfish production. *Journal of Shellfish Research* **22.3**, 621-631.

Chassé, J. and Miller, R.J. 2010. Lobster larval transport in the southern Gulf of St. Lawrence. *Fisheries Oceanography* **19.5**, 319-338. doi: 10.1111/j.1365-2419.2010.00548.x

Clark, J.S., Fastie, C., Hurtt, G., Jackson, S.T., Johnson, C., King, G.A., Lewis, M., Lynch, J., Pacala, S., Prentice, C., Schupp, E.W., Webb, T., III, and Wyckoff, P. 1998. Reid's paradox of rapid plant migration: Dispersal theory and interpretation of paleoecological records. *BioScience* **48**, 13-24.

Clobert, J., Wolff, J.O., Nichols, J.D., Danchin, E., and Dhondt, A.A. 2001. Introduction. *In*: Clobert, J., Danchin, E., Dhondt, A.A., and Nichols, J.D. (eds.), Dispersal. Oxford University Press, New York, New York, United States of America, pp. xvii-xxi.

Cohen, A.N., Carlton, J.T., and Fountain, M.C. 1995. Introduction, dispersal and potential impacts of the green crab *Carcinus maenas* in San Francisco Bay, California. *Marine Biology* **122.2**, 225-237. doi: 10.1007/BF00348935

Colautti, R.I., Niimi, A.J., van Overdijk, C.D.A., Mills, E.L., Holeck, K., and MacIsaac, H.J. 2003. Spatial and temporal analysis of transoceanic shipping vectors to the Great Lakes. *In:* Invasive species: Ruiz, G.M. and Carlton, J.T. (eds.), Vectors and management strategies. Island Press, Washington, District of Columbia, United States of America, pp. 227-248.

Colautti, R.I., Grigorovich, I.A., and MacIsaac, H.J. 2006. Propagule pressure: A null model for biological invasions. *Biological Invasions* **8.5**, 1023-1037. doi: 10.1007/s10530-005-3735-y

Cole, M., Lindeque, P., Halsband, C., and Galloway, T.S. 2011. Microplastics as contaminants in the marine environment: A review. *Marine Pollution Bulletin* **62.12**, 2588-2597. doi: 10.1016/j.marpolbul.2011.09.025

Collin, S.B., Edwards, P.K., Leung, B., and Johnson, L.E. 2013. Optimizing early detection of non-indigenous species: Estimating the scale of dispersal of a nascent population of the invasive tunicate *Ciona intestinalis* (L.). *Marine Pollution Bulletin* **73.1**, 64-69. doi: 10.1016/j.marpolbul.2013.05.040

Comeau, M. and Hanson, J.M. 2018. American lobster: Persistence in the face of high, size-selective fishing mortality – a perspective from the southern Gulf of St. Lawrence. *Canadian Journal of Fisheries and Aquatic Sciences* **in press**. doi: 10.1139/cjfas-2017-0374

Compton, T.J., Leathwick, J.R., and Inglis, G.J. 2010. Thermogeography predicts the potential global range of the invasive European green crab (*Carcinus maenas*). *Diversity and Distributions* **16.2**, 243-255. doi: 10.1111/j.1472-4642.2010.00644.x

Cooke, S.L. and Hill, W.R. 2010. Can filter-feeding Asian carp invade the Laurentian Great Lakes? A bioenergetic modeling exercise. *Freshwater Biology* **55.10**, 2138-2152. doi: 10.1111/j.1365-2427.2010.02474.x

Cosham, J., Beazley, K.F., and McCarthy, C. 2016. Environmental factors influencing local distributions of European green crab (*Carcinus maenas*) for modeling and management applications. *Environmental Reviews* **24.3**, 244-252. doi: 10.1139/er-2015-0053

Costello, C., Drake, J.M., and Lodge, D.M. 2007. Evaluating an invasive species policy: Ballast water exchange in the Great Lakes. *Ecological Applications* **17.3**, 655-662. doi: 10.1890/06-0190

Costello, C., Rassweiler, A., Siegel, D., De Leo, G., Micheli, F., and Rosenberg, A. 2010. The value of spatial information in MPA network design. *Proceedings of the National Academy of Sciences of the United States of America* **107.43**, 18294-18299. doi: 10.1073/pnas.0908057107

Cowen, R.K., Lwiza, K.M.M., Sponaugle, S., Paris, C.B., and Olson, D.B. 2000. Connectivity of marine populations: Open or closed? *Science* **287.5454**, 857-859. doi: 10.1126/science.287.5454.857

Cowen, R.K., Paris, C.B., and Srinivasan, A. 2006. Scaling of connectivity in marine populations. *Science* **311.5760**, 522-527. doi: 10.1126/science.1122039

Cowen, R.K., Gawarkiewicz, G., Pineda, J., Thorrold, S.R., and Werner, F.E. 2007. Population connectivity in marine systems: An overview. *Oceanography* **20.3**, 14-21.

Cowen, R.K. and Sponaugle, S. 2009. Larval dispersal and marine population connectivity. *Annual Review of Marine Science* **1**, 443-466. doi: 10.1146/annurev.marine.010908.163757

Csanady, G.T. 1982. Circulation in the coastal ocean. D. Reidel Publishing Company, Dordrecht, Holland, 279 pp.

Cuddington, K., Currie, W.J.S., and Koops, M.A. 2014. Could an Asian carp population establish in the Great Lakes from a small introduction? *Biological Invasions* **16.4**, 903-917. doi: 10.1007/s10530-013-0547-3

Daigle, R.M. and Herbinger, C.M. 2009. Ecological interactions between the vase tunicate (*Ciona intestinalis*) and the farmed blue mussel (*Mytilus edulis*) in Nova Scotia, Canada. *Aquatic Invasions* **4.1**, 177-187. doi: 10.3391/ai.2009.4.1.18

Daigle, R.M., Chassé, J., and Metaxas, A. 2016. The relative effect of behavior in larval dispersal in a low energy embayment. *Progress in Oceanography* **144**, 93-117. doi: 10.1016/j.pocean.2016.04.001

D’Aloia, C.C., Bogdanowicz, S.M., Francis, R.K., Majoris, J.E., Harrison, R.G., and Buston, P.M. 2015. Patterns, causes, and consequences of marine larval dispersal. *Proceedings of the National Academy of Sciences of the United States of America* **112.45**, 13940-13945. doi: 10.1073/pnas.1513754112

Davis, R.E. 1985. Drifter observations of coastal surface currents during CODE: The method and descriptive overview. *Journal of Geophysical Research* **90.C3**, 4741-4755.

Dean, B.Y., Corcoran, P.L., and Helm, P.A. 2018. Factors influencing microplastic abundances in nearshore, tributary and beach sediments along the Ontario shoreline of Lake Erie. *Journal of Great Lakes Research* **in press**. doi: 10.1016/j.jglr.2018.07.014

Derraik, J.G.B. 2002. The pollution of the marine environment by plastic debris: A review. *Marine Pollution Bulletin* **44.9**, 842-852. doi: 10.1016/S0025-326X(02)00220-5

DeVanna Fussell, K.M., Smith, R.E.H., Fraker, M.E., Boegman, L., Frank, K.T., Miller, T.J., Tyson, J.T., Arend, K.K., Boisclair, D., Guildford, S.J., Hecky, R.E., Höök, T.O., Jensen, O.P., Llopiz, J.K., May, C.J., Najjar, R.G., Rudstam, L.G., Taggart, C.T., Rao, Y.R., and Ludsin, S.A. 2016. A perspective on needed research, modeling, and management approaches that can enhance Great Lakes fisheries management under changing ecosystem conditions. *Journal of Great Lakes Research* **42.4**, 743-752. doi: 10.1016/j.jglr.2016.04.007

Dextrase, A.J. and Mandrak, N.E. 2006. Impacts of alien invasive species on freshwater fauna at risk in Canada. *Biological Invasions* **8**, 13-24. doi: 10.1007/s10530-005-0232-2

DiBacco, C., Humphrey, D.B., Nasmith, L.E., and Levings, C.D. 2012. Ballast water transport of non-indigenous zooplankton to Canadian ports. *ICES Journal of Marine Science* **69.3**, 483-491. doi: 10.1093/icesjms.fsr133

Döös, K., Rupolo, V., and Brodeau, L. 2011. Dispersion of surface drifters and model-simulated trajectories. *Ocean Modeling* **39.3-4**, 301-310. doi: 10.1016/j.ocemod.2011.05.005

Dopazo, S.N., Corkum, L.D., and Mandrak, N.E. 2008. Fish assemblages and environmental variables associated with Gobiids in nearshore areas of the lower Great Lakes. *Journal of Great Lakes Research* **34.3**, 450-460. doi: 10.3394/0380-1330(2008)34[450:FAAEVA]2.0.CO;2

Drake, J.M. and Lodge, D.M. 2004. Global hot spots of biological invasions: Evaluating options for ballast-water management. *Proceedings of the Royal Society of London B* **271.1539**, 575-580. doi: 10.1098/rspb.2003.2629

Driedger, A.G.J., Dürr, H.H., Mitchell, K., and Van Cappellen, P. 2015. Plastic debris in the Laurentian Great Lakes: A review. *Journal of Great Lakes Research* **41.1**, 9-19. doi: 10.1016/j.jglr.2014.12.020

Drinkwater, K.F. 1989. The response of an open embayment to near-hurricane force winds. *Continental Shelf Research* **9.9**, 823-839. doi: 10.1016/0278-4343(89)90015-0

Dris, R., Imhof, H., Sanchez, W., Gasperi, J., Galgani, F., Tassin, B., and Laforsch, C. 2015. Beyond the ocean: Contamination of freshwater ecosystems with (micro-) plastic particles. *Environmental Chemistry* **12.5**, 539-550. doi: 10.1071/EN14172

Duggan, I.C., van Overdijk, C.D.A., Bailey, S.A., Jenkins, P.T., Limén, H., and MacIsaac, H.J. 2005. Invertebrates associated with residual ballast water and sediments of cargo-carrying ships entering the Great Lakes. *Canadian Journal of Fisheries and Aquatic Sciences* **62.11**, 2463-2474. doi: 10.1139/f05-160

Dyer, R.J. 2007. Powers of discerning: Challenges to understanding dispersal processes in natural populations. *Molecular Ecology* **16.23**, 4881-4882. doi: 10.1111/j.1365-294X.2007.03581.x

Edwards, K.P., Hare, J.A., Werner, F.E., and Seim, H. 2007. Using 2-dimensional dispersal kernels to identify the dominant influences on larval dispersal on continental shelves. *Marine Ecology Progress Series* **352**, 77-87. doi: 10.3354/meps07169

Eerkes-Medrano, D., Thompson, R.C., and Aldridge, D.C. 2015. Microplastics in freshwater systems: A review of the emerging threats, identification gaps and prioritization of research needs. *Water Research* **75**, 63-82. doi: 10.1016/jwatres.2015.02.012

Embke, H.S., Kocovsky, P.M., Richter, C.A., Pritt, J.J., Mayer, C.M., and Qian, S.S. 2016. First direct confirmation of grass carp spawning in a Great Lakes tributary. *Journal of Great Lakes Research* **42.4**, 899-903. doi: 10.1016/j.jglr.2016.05.002

Eriksen, M., Mason, S., Wilson, S., Box, C., Zellers, A., Edwards, W., Farley, H., and Amato, S. 2013. Microplastic pollution in the surface waters of the Laurentian Great Lakes. *Marine Pollution Bulletin* **77.1-2**, 177-182. doi: 10.1016/j.marpolbul.2013.10.007

Escobar, L.E., Kurath, G., Escobar-Dodero, J., Craft, M.E., and Phelps, N.B.D. 2017. Potential distribution of the viral haemorrhagic septicaemia virus in the Great Lakes region. *Journal of Fish Diseases* **40.1**, 11-28. doi: 10.1111/jfd.12490

Faisal, M. and Winters, A.D. 2011. Detection of Viral Haemorrhagic Septicemia Virus (VHSV) from *Diporeia* spp. (Pontoporeiidae, Amphipoda) in the Laurentian Great Lakes, USA. *Parasites and Vectors* **4.2**. doi: 10.1186/1756-3305-4-2

Faisal, M., Shavalier, M., Kim, R.K., Millard, E.V., Gunn, M.R., Winters, A.D., Schulz, C.A., Eissa, A., Thomas, M.V., Wolgamood, M., Whelan, G.E., and Winton, J. 2012. Spread of the emerging Viral Haemorrhagic Septicemia Virus strain, Genotype IVb, in Michigan, USA. *Viruses* **4.5**, 734-760. doi: 10.3390/v4050734

Fiksen, Ø., Jørgensen, C., Kristiansen, T., Vikebø, F., and Huse, G. 2007. Linking behavioral ecology and oceanography: Larval behavior determines growth, mortality and dispersal. *Marine Ecology Progress Series* **347**, 195-205. doi: 10.3354/meps06978

Fischer, H.B., List, E.J., Koh, R.C.Y., Imberger, J., and Brooks, N.H. 1979. Mixing in Inland and Coastal Waters. Academic Press, London, United Kingdom, 483 pp.

Fitridge, I., Dempster, T., Guenther, J., and de Nys, R. 2012. The impact and control of biofouling in marine aquaculture: A review. *Biofouling* **28.7**, 649-669. doi: 10.1080/08927014.2012.700478

Fogarty, M.J. and Botsford, L.W. 2007. Population connectivity and spatial management of marine fisheries. *Oceanography* **20.3**, 112-123.

Francis, J.T., Chiotti, J.A., Boase, J.C., Thomas, M.V., Manny, B.A., and Roseman, E.F. 2014. A description of the nearshore fish communities in the Huron–Erie Corridor using multiple gear types. *Journal of Great Lakes Research* **40.S2**, 52-61. doi: 10.1016/j.jglr.2014.01.007

Franks, P.J.S. 1992. Sink or swim: Accumulation of biomass at fronts. *Marine Ecology Progress Series* **82**, 1-12.

Gaines, S.D., White, C., Carr, M.H., and Palumbi, S.R. 2010. Designing marine reserve networks for both conservation and fisheries management. *Proceedings of the National Academy of Sciences of the United States of America* **107.43**, 18286-18293. doi: 10.1073/pnas.0906473107

García, C. and Borda-de-Água, L. 2017. Extended dispersal kernels in a changing world: Insights from statistics of extremes. *Journal of Ecology* **105.1**, 63-74. doi: 10.1111/1365-2745.12685

Garrett, C. 1983. On the initial streakness of a dispersing tracer in two- and three-dimensional turbulence. *Dynamics of Atmospheres and Oceans* **7.4**, 265-277. doi: 10.1016/0377-0265(83)90008-8

Gawarkiewicz, G., Monismith, S., and Largier, J. 2007. Observing larval transport processes affecting population connectivity: Progress and challenges. *Oceanography* **20.3**, 40-53.

Gerrodette, T. 1981. Dispersal of the solitary coral *Balanophyllia elegans* by demersal planular larvae. *Ecology* **62.3**, 611-619. doi: 10.2307/1937728

Gillespie, R.G., Baldwin, B.G., Waters, J.M., Fraser, C.I., Nikula, R., and Roderick, G.K. 2012. Long-distance dispersal: A framework for hypothesis testing. *Trends in Ecology & Evolution* **27.1**, 47-56. doi: 10.1016/j.tree.2011.08.009

Goldwasser, L., Cook, J., and Silverman, E.D. 1994. The effects of variability on metapopulation dynamics and rates of invasion. *Ecology* **75.1**, 40-47. doi: 10.2307/1939380

Gray, D.K., Johengen, T.H., Reid, D.F., and MacIsaac, H.J. 2007. Efficacy of open-ocean ballast water exchange as a means of preventing invertebrate invasions between freshwater ports. *Limnology and Oceanography* **52.6**, 2386-2397. doi: 10.4319/lo.2007.52.6.2386

Green, A.L., Maypa, A.P., Almany, G.R., Rhodes, K.L., Weeks, R., Abesamis, R.A., Gleason, M.G., Mumby, P.J., and White, A.T. 2015. Larval dispersal and movement patterns of coral reef fishes, and implications for marine reserve network design. *Biological Reviews* **90.4**, 1215-1247. doi: 10.1111/brv.12155

Griffiths, R.W., Thornley, S., and Edsall, T.A. 1991. Limnological aspects of the St. Clair River. *Hydrobiologia* **219**, 97-123.

Grigorovich, I.A., Colautii, R.I., Mills, E.L., Holeck, K.T., Ballert, A.G., and MacIsaac, H.J. 2003. Ballast-mediated animal introductions in the Laurentian Great Lakes: Retrospective and prospective analyses. *Canadian Journal of Fisheries and Aquatic Sciences* **60.6**, 740-756. doi: 10.1139/f03-053

Groocock, G.H., Getchell, R.G., Wooster, G.A., Britt, K.L., Batts, W.N., Winton, J.R., Casey, R.N., Casey, J.W., and Bowser, P.R. 2007. Detection of viral haemorrhagic septicemia in round gobies in New York State (USA) waters of Lake Ontario and the St. Lawrence River. *Diseases of Aquatic Organisms* **76.3**, 187-192. doi: 10.3354/dao076187

Grosholz, E.D. and Ruiz, G.M. 1996. Predicting the impact of introduced marine species: Lessons from the multiple invasions of the European green crab *Carcinus maenas*. *Biological Conservation* **78**, 59-66.

Guizien, K., Brochier, T., Duchêne, J.-C., Koh, B.-S., and Marsaleix, P. 2006. Dispersal of *Owenia fusiformis* larvae by wind-driven currents: Turbulence, swimming behavior and mortality in a three-dimensional stochastic model. *Marine Ecology Progress Series* **311**, 47-66. doi: 10.3354/meps311047

Haarr, M.L. and Rochette, R. 2012. The effect of geographic origin on interactions between adult invasive green crabs *Carcinus maenas* and juvenile American lobsters *Homarus americanus* in Atlantic Canada. *Journal of Experimental Marine Biology and Ecology* **422-423**, 88-100. doi: 10.1016/j.jembe.2012.04.016

Hannah, C.G., Drozdowski, A., Loder, J., Muschenheim, K., and Milligan, T. 2006. An assessment model for the fate and environmental effects of offshore drilling mud discharges. *Estuarine, Coastal and Shelf Science* **70.4**, 577-588. doi: 10.1016/j.ecss.2006.06.008

Hanson, J.M., Comeau, M., and Rondeau, A. 2014. Atlantic rock crab, unlike American lobster, is important to ecosystem functioning in Northumberland Strait. *Transactions of the American Fisheries Society* **143.5**, 1266-1279. doi: 10.1080/00028487.2014.931300

Harding, G.C., Vass, W.P., and Drinkwater, K.F. 1982. Aspects of larval American lobster (*Homarus americanus*) ecology in St. Georges Bay, Nova Scotia. *Canadian Journal of Fisheries and Aquatic Sciences* **39.8**, 1117-1129. doi: 10.1139/f82-149

Henning, B.F., Kapuscinski, K.L., and Farrell, J.M. 2014. Nearshore fish assemblage structure and habitat relationships in protected and open habitats in the upper St. Lawrence River. *Journal of Great Lakes Research* **40.S2**, 154-163. doi: 10.1016/j.jglr.2013.11.003

Herborg, L.-M., Mandrak, N.E., Cudmore, B.C., and MacIsaac, H.J. 2007. Comparative distribution and invasion risk of snakehead (Channidae) and Asian carp (Cyprinidae) species in North America. *Canadian Journal of Fisheries and Aquatic Sciences* **64.12**, 1723-1735. doi: 10.1139/f07-130

Herdendorf, C.E., Raphael, C.N., and Jaworski, E. 1986. The ecology of Lake St. Clair wetlands: A community profile. US Fish and Wildlife Service Biological Report 85(7.7), National Wetlands Research Center, Fish and Wildlife Service, US Department of the Interior, 187 pp.

Hidalgo, F.J., Barón, P.J., and Orensanz, J.M. 2005. A prediction come true: The green crab invades the Patagonian coast. *Biological Invasions* **7.3**, 547-552. doi: 10.1007/s10530-004-5452-3

Higgins, S.I. and Richardson, D.M. 1999. Predicting plant migration rates in a changing world: The role of long-distance dispersal. *The American Naturalist*, **153.5**, 464-475. doi: 10.1086/303193

Hill, A.E. 1990. Pelagic dispersal of Norway lobster Nephrops norvegicus larvae examined using an advection-diffusion-mortality model. *Marine Ecology Progress Series* **64**, 217-226.

Hinterthuer, A. 2012. The explosive spread of Asian carp: Can the Great Lakes be protected? Does it matter? *BioScience* **62.3**, 220-224. doi: 10.1525/bio.2012.62.3.3

Hitchcock, G.L. and Cowen, R.K. 2007. Plankton: Lagrangian inhabitants of the sea. *In*: Griffa, A., Kirwan, Jr., A.D., Mariano, A.J., Özgökmen, T., and Rossby, T. (eds.), Lagrangian Analysis and Prediction of Coastal and Ocean Dynamics. Cambridge University Press, New York, New York, United States of America, pp. 349-400.

Hjort, J. 1914. Fluctuations in the great fisheries of northern Europe viewed in the light of biological research. Rapports et Procès-Vebaux des Réunions du Conceil Permanent International pour l'Exploration de la Mer **XX**, 228 pp.

Hoffman, M.J. and Hittinger, E. 2017. Inventory and transport of plastic debris in the Laurentian Great Lakes. *Marine Pollution Bulletin* **115.1-2**, 273-281. doi: 10.1016/j.marpolbul.2016.11.061

Holeck, K.T., Mills, E.L., MacIsaac, H.J., Dochoda, M.R., Colautti, R.I., and Ricciardi, A. 2004. Bridging troubled waters: Biological invasions, transoceanic shipping, and the Laurentian Great Lakes. *Bioscience* **54.10**, 919-929. doi: 10.1641/0006-3568(2004)054[0919:BTWBIT]2.0.CO;2

Holtgren, J.M. and Auer, N.A. 2004. Movement and habitat of juvenile lake sturgeon (*Acipenser fulvescens*) in the Sturgeon River/Portage Lake system, Michigan. *Journal of Freshwater Ecology* **19.3**, 419-432. doi: 10.1080/02705060.2004.9664915

Holtschlag, D.J., and Koschik, J.A. 2002. A two-dimensional hydrodynamic model of the St. Clair–Detroit River Waterway in the Great Lakes Basin. Water–Resources Investigations Report 01-4236, US Department of the Interior, US Geological Survey, 63 pp.

Hondorp, D.W., Roseman, E.F., and Manny, B.A. 2014. An ecological basis for future fish habitat restoration efforts in the Huron–Erie Corridor. *Journal of Great Lakes Research* **40.S2**, 23-30. doi: 10.1016/j.jglr.2013.12.007

Horton, A.A., Walton, A., Spurgeon, D.J., Lahive, E., and Svendsen, C. 2017. Microplastics in freshwater and terrestrial environments: Evaluating the current understanding to identify the knowledge gaps and future research priorities. *Science of the Total Environment* **586**, 127-141. doi: 10.1016/j.scitotenv.2017.01.190

Hoyer, A.B., Schladow, S.G., and Rueda, F.J. 2015. Local dispersion of nonmotile invasive bivalve species by wind-driven lake currents. *Limnology and Oceanography* **60.2**, 446-462. doi: 10.1002/lno.10046

Hrycik, J.M., Chassé, J., Ruddick, B.R., and Taggart, C.T. 2013. Dispersal kernel estimation: A comparison of empirical and modeled particle dispersion in a coastal marine system. *Estuarine, Coastal and Shelf Science* **133**, 11-22. doi: 10.1016/j.ecss.2013.06.023

Hudon, C. and Fradette, P. 1993. Wind-induced advection of larval decapods into Baie de Plaisance (Îles de la Madeleine, Québec). *Canadian Journal of Fisheries and Aquatic Sciences* **50.7**, 1422-1434. doi: 10.1139/f93-163

Incze, L., Xue, H., Wolff, N., Xu, D., Wilson, C., Steneck, R., Wahle, R., Lawton, P., Pettigrew, N., and Chen, Y. 2010. Connectivity of lobster (*Homarus americanus*) populations in the coastal Gulf of Maine: Part II. Coupled biophysical dynamics. *Fisheries Oceanography* **19.1**, 1-20. doi: 10.1111/j.1365-2419.2009.00522.x

James, M.K., Armsworth, P.R., Mason, L.B., and Bode, L. 2002. The structure of reef fish metapopulations: Modeling larval dispersal and retention patterns. *Proceedings of the Royal Society of London B* **269.1505**, 2079-2086. doi: 10.1098/rspb.2002.2128

Jamieson, G.S., Grosholz, E.D., Armstrong, D.A., and Elner, R.W. 1998. Potential ecological implications from the introduction of the European green crab, *Carcinus maena* (Linneaus), to British Columbia, Canada, and Washington, USA. *Journal of Natural History* **32.10-11**, 1587-1598. doi: 10.1080/00222939800771121

Jones, G.P., Srinivasan, M., and Almany, G.R. 2007. Population connectivity and conservation of marine biodiversity. *Oceanography* **20.3**, 100-111.

Jordano, P. 2017. What is long-distance dispersal? And a taxonomy of dispersal events. *Journal of Ecology* **105.1**, 75-84. doi: 10.1111/1365-2745.12690

Kanary, L., Locke, A., Watmough, J., Chassé, J., Bourque, D., and Nadeau, A. 2011. Predicting larval dispersal of the vase tunicate *Ciona intestinalis* in a Prince Edward Island estuary using a matrix population model. *Aquatic Invasions* **6.4**, 491-506. doi: 10.3391/ai.2011.6.4.14

Kaplan, D.M. 2006. Alongshore advection and marine reserves: Consequences for modeling and management. *Marine Ecology Progress Series* **309**, 11-24. doi: 10.3354/meps309011

Kelly, D.W. 2007. Vectors and pathways for nonindigenous aquatic species in the Great Lakes. Committee on the St. Lawrence Seaway, Transportation Research Board Special Report 291, 27 pp.

Kinlan, B.P., and Gaines, S.D. 2003. Propagule dispersal in marine and terrestrial environments: A community perspective. *Ecology* **84**, 2007-2020. doi: 10.1890/01-0622

Kinlan, B.P., Gaines, S.D., and Lester, S.E. 2005. Propagule dispersal and the scales of marine community process. *Diversity and Distributions* **11.2**, 139-148. doi: 10.1111/j.1366-9516.2005.00158.x

Klassen, G. and Locke, A. 2007. A biological synopsis of the European green crab, *Carcinus maenas*. Canadian Manuscript Report of Fisheries and Aquatic Sciences 2818, 75 pp.

Klein, E.K., Lavigne, C., and Gouyon, P.-H. 2006. Mixing of propagules from discrete sources at long distance: Comparing a dispersal tail to an exponential. *BMC Ecology*, **6.3**. doi: 10.1186/1472-6785-6-3

Kool, J.T., Moilanen, A., and Treml, E.A. 2013. Population connectivity: Recent advances and new perspectives. *Landscape Ecology* **28.2**, 165-185. doi: 10.1007/s10980-012-9819-z

Kot, M., Lewis, M.A., and van den Driessche, P. 1996. Dispersal data and the spread of invading organisms. *Ecology* **77.7**, 2027-2042. doi: 10.2307/2265698

Krieger, J.R. 2017. Habitat utilization and early life history characteristics of larval, young-of-year, and juvenile lake sturgeon (*Acipenser fulvescens*) in the Great Lakes connecting channels. Doctor of Philosophy Thesis, University of Michigan, Ann Arbor, Michigan, United States of America, 112 pp.

Krueck, N.C., Ahmadia, G.N., Green, A., Jones, G.P., Possingham, H.P., Riginos, C., Treml, E.A., and Mumby, P.J. 2017. Incorporating larval dispersal into MPA design for both conservation and fisheries. *Ecological Applications* **27.3**, 925-941. doi: 10.1002/eap.1495

Lang, G.A. and Fontaine, T.D. 1990. Modeling the fate and transport of organic contaminants in Lake St. Clair. *Journal of Great Lakes Research* **16.2**, 216-232.

Largier, J.L. 2003. Considerations in estimating larval dispersal distances from oceanographic data. *Ecological Applications* **13.SP1**, 71-89. doi: 10.1890/1051-0761(2003)013[0071:CIELDD]2.0.CO;2

Lauzier, L.M. 1965. Drift bottle observations in Northumberland Strait, Gulf of St. Lawrence. *Journal of the Fisheries Research Board of Canada* **22.2**, 353-368. doi: 10.1139/f65-035

Ledwell, J.R., Watson, A.J., and Law, C.S. 1998. Mixing of a tracer in the pycnocline. *Journal of Geophysical Research* **103.C10**, 21499-21529. doi: 10.1029/98JC01738

Lee, L. 2010. Toxicity evaluation of magnetic beads using rainbow trout gill, liver, and monocyte/macrophage-like cell lines. Unpublished report, Wilfrid Laurier University, Waterloo, Ontario, Canada, 5 pp.

Lesperance, M., DeYoung, B., and Foley, J. 2011a. Analysis of physical oceanographic data from St. George's Bay, NS: July–August 2009. Physics and Physical Oceanography Data Report 2011-1, Memorial University, St. John's, Newfoundland, Canada, 23 pp.

Lesperance, M., DeYoung, B., and Foley, J. 2011b. Analysis of physical oceanographic data from St. George's Bay, NS: July–August 2010. Physics and Physical Oceanography Data Report 2011-2, Memorial University, St. John's, Newfoundland, Canada, 16 pp.

Levin, L.A. 2006. Recent progress in understanding larval dispersal: New directions and digressions. *Integrative and Comparative Biology* **46.3**, 282-297. doi: 10.1093/icb/icj024

Locke, A., Hanson, J.M., Ellis, K.M., Thompson, J., and Rochette, R. 2007. Invasion of the southern Gulf of St. Lawrence by the clubbed tunicate (*Styela clava* Herdman): Potential mechanisms for invasions of Prince Edward Island estuaries. *Journal of Experimental Marine Biology and Ecology* **342**, 69-77. doi: 10.1016/j.jembe.2006.10.016

Lockwood, J.L., Cassey, P., and Blackburn, T. The role of propagule pressure in explaining species invasions. *Trends in Ecology and Evolution* **20.5**, 223-228. doi: 10.1016/j.tree.2005.02.004

Lu, Y., Thompson, K.R., and Wright, D.G. 2001. Tidal currents and mixing in the Gulf of St. Lawrence: An application of the incremental approach to data assimilation. *Canadian Journal of Fisheries and Aquatic Sciences* **58.4**, 723-735. doi: 10.1139/cjfas-58-4-723

Lumpkin, R. and Pazos, M. 2007. Measuring surface currents with Surface Velocity Program drifters: The instrument, its data, and some recent results. *In*: Griffa, A., Kirwan, Jr., A.D., Mariano, A.J., Özgökmen, T., and Rossby, T. (eds.), Lagrangian Analysis and Prediction of Coastal and Ocean Dynamics (LAPCOD). Cambridge University Press, New York, New York, United States of America, pp. 39-67.

Lutz-Collins, V., Ramsay, A., Quijón, P.A., and Davidson, J. 2009. Invasive tunicates fouling mussel lines: Evidence of their impact on native tunicates and other epifaunal invertebrates. *Aquatic Invasions* **4.1**, 213-220. doi: 10.3391.ai.2009.4.1.22

Lynch, D.R., Gentleman, W.C., McGillicuddy, D.J., Jr., and Davis, C.S. 1998. Biological/physical simulations of *Calanus finmarchicus* population dynamics in the Gulf of Maine. *Marine Ecology Progress Series* **169**, 189-210. doi: 10.3354/meps169189

MacIsaac, H.J., Robbins, T.C., and Lewis, M.A. 2002. Modeling ships' ballast water as invasion threats to the Great Lakes. *Canadian Journal of Fisheries and Aquatic Sciences* **59.7**, 1245-1256. doi: 10.1139/f02-090

MacIsaac, H.J., Borbely, J.V.M., Muirhead, J.R., and Graniero, P.A. 2004. Backcasting and forecasting biological invasions of inland lakes. *Ecological Applications* **14.3**, 773-783. doi: 10.1890/02-5377

MacIsaac, H.J., Beric, B., Bailey, S.A., Mandrak, N.E., and Ricciardi, A. 2015. Are the Great Lakes at risk of new fish invasions from trans-Atlantic shipping? *Journal of Great Lakes Research* **41.4**, 1172-1175. doi: 10.1016/j.jglr.2015.07.004

Mandrak, N.E. and Cudmore, B. 2010. The fall of native fishes and the rise of non-native fishes in the Great Lakes basin. *Aquatic Ecosystem Health and Management* **13.3**, 255-268. doi: 10.1080/14634988.2010.507150

Manny, B.A. and Kennedy, G.W. 2002. Known lake sturgeon (*Acipenser fulvescens*) spawning habitat in the channel between lakes Huron and Erie in the Laurentian Great Lakes. *Journal of Applied Ichthyology* **18.4-6**, 486-490. doi: 10.1046/j.1439-0426.2002.00390.x

Martin, A.P. 2003. Phytoplankton patchiness: The role of lateral stirring and mixing. *Progress in Oceanography* **57.2**, 125-174. doi: 10.1016/S0079-6611(03)00085-5

Matthysen, E. 2012. Multicausality of dispersal: A review. *In*: Clobert, J., Baguette, M., Benton, T.G., and Bullock, J.M. (eds.), Dispersal ecology and evolution. Oxford University Press, Oxford, United Kingdom, pp. 3-18.

Metaxas, A. 2001. Behavior in flow: Perspectives on the distribution and dispersion of meroplanktonic larvae in the water column. *Canadian Journal of Fisheries and Aquatic Sciences* **58.1**, 86-98. doi: 10.1139/f00-159

Metaxas, A. and Saunders, M. 2009. Quantifying the "bio-" components in biophysical models of larval transport in marine benthic invertebrates: Advances and pitfalls. *The Biological Bulletin* **216.3**, 257-272. doi: 10.1086/BBLv216n3p257

McDonald, E.A., McNaught, A.S., and Roseman, E.F. 2014. Use of main channel and two backwater habitats by larval fishes in the Detroit River. *Journal of Great Lakes Research* **40.S2**, 69-80. doi: 10.1016/j.jglr.2013.10.001

Murphy, E.A. and Jackson, P.R. 2013. Hydraulic and water-quality data collection for the investigation of Great Lakes tributaries for Asian carp spawning and egg-transport suitability. Scientific Investigations Report 2013-5106, US Department of the Interior, US Geological Survey, 30 pp.

Nathan, R., Perry, G., Cronin, J.T., Strand, A.E., and Cain, M.L. 2003. Methods for estimating long-distance dispersal. *OIKOS* **103.2**, 263-273. doi: 10.1034/j.1600-0706.2003.12146.x

Nathan, R. 2005. Long-distance dispersal research: Building a network of yellow brick roads. *Diversity and Distributions* **11.2**, 125-130. doi: 10.1111/j.1366-9516.2005.00159.x

Nathan, R. 2006. Long-distance dispersal of plants. *Science* **313.5788**, 786-788. doi: 10.1126/science.1124975

Nathan, R., Schurr, F.M., Spiegel, O., Steinitz, O., Trakhtenbrot, A., and Tsoar, A. 2008. Mechanisms of long-distance seed dispersal. *Trends in Ecology and Evolution* **23.11**, 638-647. doi: 10.1016/j.tree.2008.08.003

Nathan, R., Klein, E., Robledo-Arnuncio, J.J., and Revilla, E. 2012. Dispersal kernels: Review. *In*: Clobert, J., Baguette, M., Benton, T.G., and Bullock, J.M. (eds.), Dispersal ecology and evolution. Oxford University Press, Oxford, United Kingdom, pp. 187-202.

Natunewicz, C.C., Epifanio, C.E., and Garvine, R.W. 2001. Transport of crab larval patches in the coastal ocean. *Marine Ecology Progress Series* **222**, 143-154. doi: 10.3354/meps222143

Neubert, M.G. and Caswell, H. 2000. Demography and dispersal: Calculation and sensitivity analysis of invasion speed for structured populations. *Ecology* **81.6**, 1613-1628. doi: 10.1890/0012-9658(2000)081[1613:DADCAS]2.0.CO;2

Nichols, S.J., Kennedy, G., Crawford, E., Allen, J., French, J., III, Black, G., Blouin, M., Hickey, J., Chernyák, S., Haas, R., and Thomas, M. 2003. Assessment of lake sturgeon (*Acipenser fulvescens*) spawning efforts in the lower St. Clair River, Michigan. *Journal of Great Lakes Research* **29.3**, 383-391. doi: 10.1016/S0380-1330(03)70445-6

Nickols, K.J., Gaylord, B., and Largier, J.L. 2012. The coastal boundary layer: Predictable current structure decreases alongshore transport and alters scales of dispersal. *Marine Ecology Progress Series* **464**, 17-35. doi: 10.3354/meps09875

Nickols, K.J., White, J.W., Largier, J.L., and Gaylord, B. 2015. Marine population connectivity: Reconciling large-scale dispersal and high self-retention. *The American Naturalist* **185.2**, 196-211. doi: 10.1086/679503

North, E.W., Schlag, Z., Hood, R.R., Li, M., Zhong, L., Gross, T., and Kennedy, V.S. 2008. Vertical swimming behavior influences the dispersal of simulated oyster larvae in a coupled particle-tracking and hydrodynamic model of Chesapeake Bay. *Marine Ecology Progress Series* **359**, 99-115. doi: 10.3354/meps07317

Okubo, A. and Levin, S.A. 2010. Diffusion and ecological problems: Modern perspectives. Springer-Verlag, New York, New York, United States of America, 467 pp.

Olson, D.B. 2007. Lagrangian biophysical dynamics. *In*: Griffa, A., Kirwan, Jr., A.D., Mariano, A.J., Özgökmen, T., and Rossby, T. (eds.), Lagrangian Analysis and Prediction of Coastal and Ocean Dynamics (LAPCOD). Cambridge University Press, New York, New York, United States of America, pp. 275-348.

Ottino, J.M. 1989. The kinematics of mixing: Stretching, chaos, and transport. Cambridge University Press, Cambridge, United Kingdom, 365 pp.

Palmer, A.R. and Strathmann, R.R. 1981. Scale of dispersal in varying environments and its implications for life histories of marine invertebrates. *Oecologia* **48.3**, 308-318. doi: 10.1007/BF00346487

Palumbi, S.R. 2003. Population genetics, demographic connectivity, and the design of marine reserves. *Ecological Applications* **13.1**, S146-S158. doi: 10.1890/1051-0761(2003)013[0146:PGDCAT]2.0.CO;2

Peterson, D.L., Vecsei, P., and Jennings, C.A. 2007. Ecology and biology of the lake sturgeon: A synthesis of current knowledge of a threatened North American *Acipenseridae*. *Reviews in Fish Biology and Fisheries* **17.1**, 59-76. doi: 10.1007/s11160-006-9018-6

Petrie, B. and Drinkwater, K.F. 1978. Circulation in an open bay. *Journal of the Fisheries Research Board of Canada* **35.8**, 1116-1123. doi: 10.1139/f78-176

Petrone, C., Jancaitis, L.B., Jones, M.B., Natunewicz, C.C., Tilburg, C.E., and Epifanio, C.E. Dynamics of larval patches: Spatial distribution of fiddler crab larvae in Delaware Bay and adjacent waters. *Marine Ecology Progress Series* **293**, 177-190. doi: 10.3354/meps293177

Pham, P.H. 2009. A new angle on plastic debris in the aquatic environment: Investigating interactions between viral haemorrhagic septicaemia virus (VHSV) and inanimate surfaces. Master of Science Thesis, University of Waterloo, Waterloo, Ontario, Canada, 97 pp.

Pham, P.H., Jung, J., Lumsden, J.S., Dixon, B., and Bols, N.C. 2012. The potential of waste items in aquatic environments to act as a fomites for viral haemorrhagic septicaemia virus. *Journal of Fish Diseases* **35.1**, 73-77. doi: 10.1111/j.1365-2761.2011.01323.x

Pineda, J., Hare, J.A., and Sponaugle, S. 2007. Larval transport and dispersal in the coastal ocean and consequences for population connectivity. *Oceanography* **20.3**, 22-39.

Pineda, J. and Reyns, N. 2018. Larval transport in the coastal zone: Biological and physical processes. *In*: Carrier, T.J., Reitzel, A.M., and Heyland, A. (eds.), Evolutionary ecology of marine invertebrate larvae. Oxford University Press, Oxford, United Kingdom, pp. 145-163.

Planes, S., Jones, G.P., and Thorrold, S.R. 2009. Larval dispersal connects fish populations in a network of marine protected areas. *Proceedings of the National Academy of Sciences of the United States of America* **106.14**, 5693-5697. doi: 10.1073/pnas.0808007106

Putman, N.F. and He, R. 2013. Tracking the long-distance dispersal of marine organisms: Sensitivity to ocean model resolution. *Journal of the Royal Society Interface* **10.81**, 20120979. doi: 10.1098/rsif.2012.0979

Quinn, F.H. 1992. Hydraulic residence times for the Laurentian Great Lakes. *Journal of Great Lakes Research* **18.1**, 22-28.

Ramsay, A., Davidson, J., Landry, T., and Arsenault, G. 2008. Process of invasiveness among exotic tunicates in Prince Edward Island, Canada. *Biological Invasions* **10.8**, 1311-1316. doi: 10.1007/s10530-007-9205-y

Ramsay, A. ,Davidson, J., Bourque, D., and Stryhn, H. 2009. Recruitment patterns and population development of the invasive ascidian *Ciona intestinalis* in Prince Edward Island, Canada. *Aquatic Invasions* **4.1**, 169-176. doi: 10.3391/ai.2009.4.1.17

Rao, Y.R. and Schwab, D.J. 2007. Transport and mixing between the coastal and offshore waters in the Great Lakes: A review. *Journal of Great Lakes Research* **33.1**, 202-218. doi: 10.3394/0380-1330(2007)33[202:TAMBTC]2.0.CO;2

Rasmussen, L.L., Cornuelle, B.D., Levin, L.A., Largier, J.L., and Di Lorenzo, E. 2009. Effects of small-scale features and local wind forcing on tracer dispersion and estimates of population connectivity in a regional scale circulation model. *Journal of Geophysical Research* **114.C1**, C01012. doi: 10.1029/2008JC004777

Ricciardi, A. and Rasmussen, J.B. 1998. Predicting the identity and impact of future biological invaders: A priority for aquatic resource management. *Canadian Journal of Fisheries and Aquatic Sciences* **55.7**, 1759-1765. doi: 10.1139/f98-066

Ricciardi, A. and MacIsaac, H.J. 2000. Recent mass invasion of the North American Great Lakes by Ponto-Caspian species. *Trends in Ecology and Evolution* **15.2**, 62-65. doi: 10.1016/S0169-5347(99)01745-0

Ricciardi, A. 2006. Patterns of invasion in the Laurentian Great Lakes in relation to changes in vector activity. *Diversity and Distributions* **12.4**, 425-433. doi: 10.1111/j.1366-9516.2006.00262.x

Ridderinkhof, H. and Zimmerman, J.T.F. 1992. Chaotic stirring in a tidal system. *Science* **258.5085**, 1107-1111. doi: 10.1126/science.258.5085.1107

Rocha-Santos, T. and Duarte, A.C. 2015. A critical overview of the analytical approaches to the occurrence, the fate and the behavior of micdroplastics in the environment. *TrAC Trends in Analytical Chemistry* **65**, 47-53. doi: 10.1016/j.trac.2014.10.011

Roman, J. 2006. Diluting the founder effect: Cryptic invasions expand a marine invader's range. *Proceedings of the Royal Society B* **273**, 2453-2459. doi: 10.1098/rspb.2006.3597

Roseman, E.F., Thompson, P.A., Farrell, J.M., Mandrak, N.E., and Stepien, C.A. 2014. Conservation and management of fisheries and aquatic communities in Great Lakes connecting channels. *Journal of Great Lakes Research* **40.S2**, 1-6. doi: 10.1016/j.jglr.2014.03.003

Rossby, T. 2007. Evolution of Lagrangian methods in oceanography. *In*: Griffa, A., Kirwan, Jr., A.D., Mariano, A.J., Özgökmen, T., and Rossby, T. (eds.), Lagrangian Analysis and Prediction of Coastal and Ocean Dynamics (LAPCOD). Cambridge University Press, New York, New York, United States of America, pp. 1-38.

Ruddick, B.R. and Taggart, C.T. 2006. Apparatus, System and Method for Evaluating Fluid Systems. United States of America Patent Application No. 11/458,287, filed 18 July 2006, Pending.

Ruddick, B.R. and Taggart, C.T. 2011. A new approach to tracing particulates from produced water. *In*: Lee, K. and Neff, J. (eds.), Produced Water. Springer Science-Business Media, New York, New York, United States of America, pp. 249-257.

Rup, M.P., Bailey, S.A., Wiley, C.J., Minton, M.S., Miller, A.W., Ruiz, G.M., and MacIsaac, H.J. 2010. Domestic ballast operations on the Great Lakes: Potential importantce of Lakers as a vector for introduction and spread of nonindigenous species. *Canadian Journal of Fisheries and Aquatic Sciences* **67.2**, 256-268. doi: 10.1139/F09-180

Sale, P.F., Cowen, R.K., Danilowicz, B.S., Jones, G.P., Kritzer, J.P., Lindeman, K.C., Planes, S., Polunin, N.V.C., Russ, G.R., Sadovy, Y.J., and Steneck, R.S. 2005. Critical science gaps impede use of no-take fishery reserves. *Trends in Ecology and Evolution* **20.2**, 74-80. doi: 10.1016/j.tree.2004.11.007

Saucier, F.J. and Chassé, J. 2000. Tidal circulation and buoyancy effects in the St. Lawrence Estuary. *Atmosphere-Ocean* **38.4**, 505-556. doi: 10.1080/07055900.2000.9649658

Saucier, F.J., Roy, F., Gilbert, D, Pellerin, P., and Ritchie, H. 2003. Modeling the formation and circulation processes of water masses and sea ice in the Gulf of St. Lawrence, Canada. *Journal of Geophysical Research* **108.C8**, 3269. doi: 10.1029/2000JC000686

Savenkoff, C., Swain, D.P., Hanson, J.M., Castonguay, M., Hammill, M.O., Bourdages, H., Morissette, L., and Chabot, D. 2007. Effects of fishing and predation in a heavily exploited ecosystem: Comparing periods before and after the collapse of groundfish in the southern Gulf of St. Lawrence (Canada). *Ecological Modeling* **204.1-2**, 115.128. doi: 10.1016/j.ecolmodel.2006.12.029

Savina, M., Lacroix, G., and Ruddick, K. 2010. Modeling the transport of common sole larvae in the southern North Sea: Influence of hydrodynamics and larval vertical movements. *Journal of Marine Systems* **81.1-2**, 86-98. doi: 10.1016/j.jmarsys.2009.12.008

Scheltema, R.S. 1986. On dispersal and planktonic larvae of benthic invertebrates: An eclectic overview and summary of problems. *Bulletin of Marine Science* **39.2**, 290-322.

Schnute, J.T. and Richards, L.J. 2001. Use and abuse of fishery models. *Canadian Journal of Fisheries and Aquatic Sciences* **58.1**, 10-17. doi: 10.1139/f00-150

Schwab, D.J., Clites, A.H., Murthy, C.R., Sandall, J.E., Meadows, L.A., and Meadows, G.A. 1989. The effect of wind on transport and circulation in Lake St. Clair. *Journal of Geophysical Research* **94.C4**, 4947-4958. doi: 10.1029/JC094iC04p04947

Shanks, A.L., Grantham, B.A., and Carr, M.H. 2003. Propagule dispersal distance and the size and spacing of marine reserves. *Ecological Applications* **13.1**, S159-S169. doi: 10.1890/1051-0761(2003)013[0159:PDDATS]2.0.CO;2

Shields, W.M. 1987. Dispersal and mating systems: Investigating their causal connections. *In*: Chepko-Sade, B.D. and Halpin, Z.T. (eds.), Mammalian dispersal patterns: the effects of social structure on population genetics. The University of Chicago Press, Chicago, Illinois, United States of America, pp. 3-24.

Shigesada, N. and Kawasaki, K. 2002. Invasion and the range expansion of species: Effects of long-distance dispersal. *In:* Bullock, J.M., Kenward, R.E., and Hails, R.S. (eds.), Dispersal ecology. Blackwell Publishing, Malden, Massachusetts, United States of America, pp. 350-373.

Siegel, D.A., Kinlan, B.P., Gaylord, B., and Gaines, S.D. 2003. Lagrangian descriptions of marine larval dispersion. *Marine Ecology Progress Series* **260**, 83-96. doi: 10.3354/meps260083

Sieracki, J.L., Bossenbroek, J.M., and Chadderton, W.L. 2014a. A spatial modeling approach to predicting the secondary spread of invasive species due to ballast water discharge. *PLoS ONE* **9.12**, e114217. doi: 10.1371/journal.pone.0114217

Sieracki, J.L., Bossenbroek, J.M., and Faisal, M. 2014b. Modeling the secondary spread of viral haemorrhagic septicaemia virus (VHSV) by commercial shipping in the Laurentian Great Lakes. *Biological Invasions* **16.5**, 1043-1053. doi: 10.1007/s10530-013-0056-2

Simberloff, D. 2009. The role of propagule pressure in biological invasions. Annual *Review of Ecology, Evolution, and Systematics* **40**, 81-102. doi: 10.1146/annurev.ecolsys.110308.120304

Simpson, S.D., Harrison, H.B., Claereboudt, M.R., and Planes, S. 2014. Long-distance dispersal via ocean currents connects *Omani* clownfish populations throughout entire species range. *PLoS ONE* **9.9**, e107610. doi: 10.1371/journal.pone.0107610

Skarpaas, O. and Shea, K. 2007. Dispersal patterns, dispersal mechanisms, and invasion wave speeds for invasive thistles. *The American Naturalist* **170.3**, 421-430. doi: 10.1086/519854

Smagorinsky, J. 1963. General circulation experiments with the primitive equations: I. The basic experiment. *Monthly Weather Review* **91.3**, 99-164. doi: 10.1175/1520-0493(1963)091<0099:GCEWTP>2.3.CO;2

Smith, S.D.P., McIntyre, P.B., Halpern, B.S., Cooke, R.M., Marino, A.L., Boyer, G.L., Buchsbaum, A., Burton, G.A., Jr., Campbell, L.M., Ciborowski, J.J.H., Doran, P.J., Infante, D.M., Johnson, L.B., Read, J.G., Rose, J.B., Rutherford, E.S., Steinman, A.D., and Allan, J.D. 2015. Rating impacts in a multi-stressor world: A quantitative assessment of 50 stressors affecting the Great Lakes. *Ecological Applications* **25.3**, 717-728. doi: 10.1890/14-0366.1

Southwood, T.R.E. 1978. Ecological methods. Chapman & Hall, London, United Kingdom, 524 pp.

Sponaugle, S., Paris, C., Walter, K.D., Kourafalou, V., and D'Alessandro, E. 2012. Observed and modeled larval settlement of a reef fish to the Florida Keys. *Marine Ecology Progress Series* **453**, 201-212. doi: 10.3354/meps09641

Stenseth, N.C. and Lidicker, W.Z., Jr. 1992. The study of dispersal: A conceptual guide. *In:* Stenseth, N.C. and Lidicker, W.Z., Jr. (eds.), Animal Dispersal: small mammals as a model. Chapman & Hall, London, United Kingdom, pp. 5-20.

Stockstad, E. 2010. Biologists rush to protect Great Lakes from onslaught of carp. *Science* **327.5968**, 932. doi: 10.1126/science.327.5968.932

Sullivan, T.J. and Stepien, C.A. 2014. Genetic diversity and divergence of yellow perch spawning populations across the Huron–Erie Corridor, from Lake Huron through western Lake Erie. *Journal of Great Lakes Research* **40.S2**, 101-109. doi: 10.1016/j.jglr.2012.12.004

Sun, Y., Wells, M.G., Bailey, S.A., and Anderson, E.J. 2013. Physical dispersion and dilution of ballast water discharge in the St. Clair River: Implications for biological invasions. *Water Resources Research* **49.5**, 2395-2407. doi: 10.1002/wrcr.20201

Taggart, C.T. and Leggett, W.C. 1987. Wind-forced hydrodynamics and their interactions with larval fish and plankton abundance: A time-series analysis of physical-biological data. *Canadian Journal of Fisheries and Aquatic Sciences* **44.2**, 438-451. doi: 10.1139/f87-052

Thackeray, S.J., George, D.G., Jones, R.I., and Winfield, I.J. 2004. Quantitative analysis of the importance of wind-induced circulation for the spatial structuring of planktonic populations. *Freshwater Biology* **49.9**, 1091-1102. doi: 10.1111/j.1365-2427.2004.01252.x

Therriault, T.W., Herborg, L.M., Locke, A., and McKindsey, C.W. 2008. Risk assessment for European green crab (*Carcinus maenas*) in Canadian waters. Department of Fisheries and Oceans Canadian Stock Assessment Secretariat Research Document 2008/042, 40 pp.

Thorrold, S.R., Jones, G.P., Hellberg, M.E., Burton, R.S., Swearer, S.E., Neigel, J.E., Morgan, S.G, and Warner, R.R. 2002. Quantifying larval retention and connectivity in marine populations with artificial and natural markers. *Bulletin of Marine Science* **70.1**, 291-308.

Tilburg, C.E., Houser, L.T., Steppe, C.N., Garvine, R.W., and Epifano, C.E. 2006. Effects of coastal transport on larval patches: Models and observations. *Estuarine, Coastal and Shelf Science* **67.1-2**, 145-160. doi: 10.1016/j.ecss.2005.11.019

Trakhtenbrot, A., Nathan, R., Perry, G., and Richardson, D.M. 2005. The importance of long-distance dispersal in biodiversity conservation. *Diversity and Distributions* **11.2**, 173-181. doi: 10.1111/j.1366-9516.2005.00156.x

Treml, E.A., Halpin, P.N., Urban, D.L., and Pratson, L.F. 2008. Modeling population connectivity by ocean currents, a graph-theoretic approach for marine conservation. *Landscape Ecology* **23.S1**, 19-36. doi: 10.1007/s10980-007-9138-y

Twiss, M.R. 2016. Standardized methods are required to assess and manage microplastic contamination of the Great Lakes system. *Journal of Great Lakes Research* **42.5**, 921-925. doi: 10.1016/j.jglr.2016.07.032

Vanderploeg, H.A., Nalepa, T.F., Jude, D.J., Mills, E.L., Holeck, K.T., Liebig, J.R., Grigorovich, I.A., and Ojaveer, H. 2002. Dispersal and emerging ecological impacts of Ponto-Caspian species in the Laurentian Great Lakes. *Canadian Journal of Fisheries and Aquatic Sciences* **59.7**, 1209-1228. doi: 10.1139/F02-087

VHSV Expert Panel and Working Group. 2010. Viral haemorrhagic septicaemia virus (VHSV IVb) risk factors and association measures derived by expert panel. *Preventive Veterinary Medicine* **94.1-2**, 128-139. doi: 10.1016/j.prevetmed.2009.11.020

Wagner, M., Scherer, C., Alvarez-Muñoz, D., Brennholt, N., Bourrain, X., Buchinger, S., Fries, E., Grosbois, C., Klasmeier, J., Marti, T., Rodriguez-Mozaz, S., Urbatzka, R., Vethaak, A.D., Winther-Nielson, M., and Reifferscheid, G. 2014. Microplastics in freshwater ecosystems: What we know and what we need to know. *Environmental Sciences Europe* **26**, 12. doi: 10.1186/s12302-014-0012-7

Waples, J.T., Eadie, B., Val Klump, J., Squires, M., Cotner, J., and McKinley, G. 2008. The Laurentian Great Lakes. Report of the North American Continental Margins Working Group for the US Carbon Cycle Scientific Steering Group and Interagency Working Group, US Carbon Cycle Science Program, pp. 73-80.

Weins, J.A. 2001. The landscape context of dispersal. *In*: Clobert, J., Danchin, E., Dhondt, A.A., and Nichols, J.D. (eds.), Dispersal. Oxford University Press, New York, New York, United States of America, pp. xvii-xxi.

Wells, M.G., Bailey, S.A., and Ruddick, B.R. 2011. The dilution and dispersion of ballast water discharged into Goderich Harbor. *Marine Pollution Bulletin* **62.6**, 1288-1296. doi: 10.1016/j.marpolbul.2011.03.005

Welsh, A., Mohr, L., and Boase, J. 2017. Identifying conservation hotspots in non-breeding areas: A case study of lake sturgeon (*Acipenser fulvescens*) in the Great Lakes. *Biodiversity and Conservation* **26.4**, 931-941. doi: 10.1007/s10531-016-1280-x

Werner, F.E., Quinlan, J.A., Blanton, B.O., and Luettich, R.A., Jr. 1997. The role of hydrodynamics in explaining variability in fish populations. *Journal of Sea Research* **37.3-4**, 195-212. doi: 10.1016/S1385-1101(97)00024-5

Werner, F.E., Cowen, R.K., and Paris, C.B. 2007. Coupled biological and physical models: Present capabilities and necessary developments for future studies of population connectivity. *Oceanography* **20.3**, 54-69.

Wittmann, M.E., Jerde, C.L., Howeth, J.G., Maher, S.P., Deines, A.M., Jenkins, J.A., Whitledge, G.W., Burbank, S.R., Chadderton, W.L., Mahon, A.R., Tyson, J.T., Gantz, C.A., Keller, R.P., Drake, J.M., and Lodge, D.M. 2014. Grass carp in the Great Lakes region: Establishment potential, expert perceptions, and re-evaluation of experimental evidence of ecological impact. *Canadian Journal of Fisheries and Aquatic Sciences* **71.7**, 992-999. doi: 10.1139/cjfas-2013-0537

Wolanski, E. and Kingsford, M.J. 2014. Oceanographic and behavioral assumptions in models of the fate of coral and coral reef fish larvae. *Journal of the Royal Society Interface* **11.98**, 20140209. doi: 10.1098/rsif.2014.0209

Wolfenbarger, D.O. 1975. Factors affecting dispersal distances of small organisms. Exposition Press, Hicksville, New York, United States of America, 230 pp.

Xue, H., Incze, L., Xu, D., Wolff, N., and Pettigrew, N. 2008. Connectivity of lobster populations in the coastal Gulf of Maine: Part I. Circulation and larval transport potential. *Ecological Modeling* **210.1-2**, 193-211. doi: 10.1016/j.ecolmodel.2007.07.024

Yamazaki, H. 1993. Lagrangian study of planktonic organisms: Perspectives. *Bulletin of Marine Science* **53.1**, 265-278.

Zbyszewski, M. and Corcoran, P.L. 2011. Distribution and degradation of fresh water plastic particles along the beaches of Lake Huron, Canada. *Water, Air, & Soil Pollution* **220.1-4**, 365-372. doi: 10.1007/s11270-011-0760-6

Zbyszewski, M., Corcoran, P.L., and Hockin, A. 2014. Comparison of the distribution and degradation of plastic debris along shorelines of the Great Lakes, North America. *Journal of Great Lakes Research* **40**, 288-299. doi: 10.1016/j.jglr.2014.02.012

Zimmerman, J.T.F. 1986. The tidal whirlpool: A review of horizontal dispersion by tidal and residual currents. *Netherlands Journal of Sea Research* **20.2-3**, 133-154. doi: 10.1016/0077-7579(86)90037-2

Appendix A

Supplementary Figures and Tables: Chapter 3

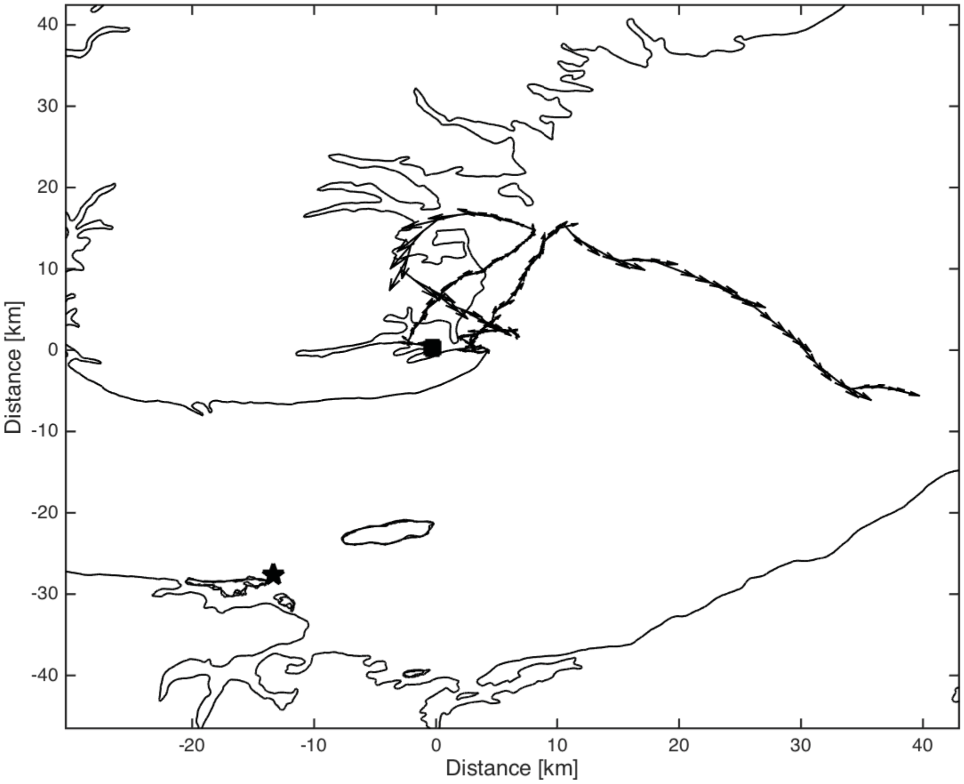

Figure A.1 Coastline chart of the eastern Northumberland Strait illustrating the progressive vector plot of surface-layer wind-drift over the 7-day study, where the size of the arrows are proportional to speed. Although the winds were recorded at weather station Caribou Point (star), the origin of the progressive vector is placed at Murray Harbour (square), starting at 08:00 on 21 August 2009, coincident with the timing of MAP release, and ending at 09:00 on 28 August 2009, the time of retrieval of the last magnetic-collector.

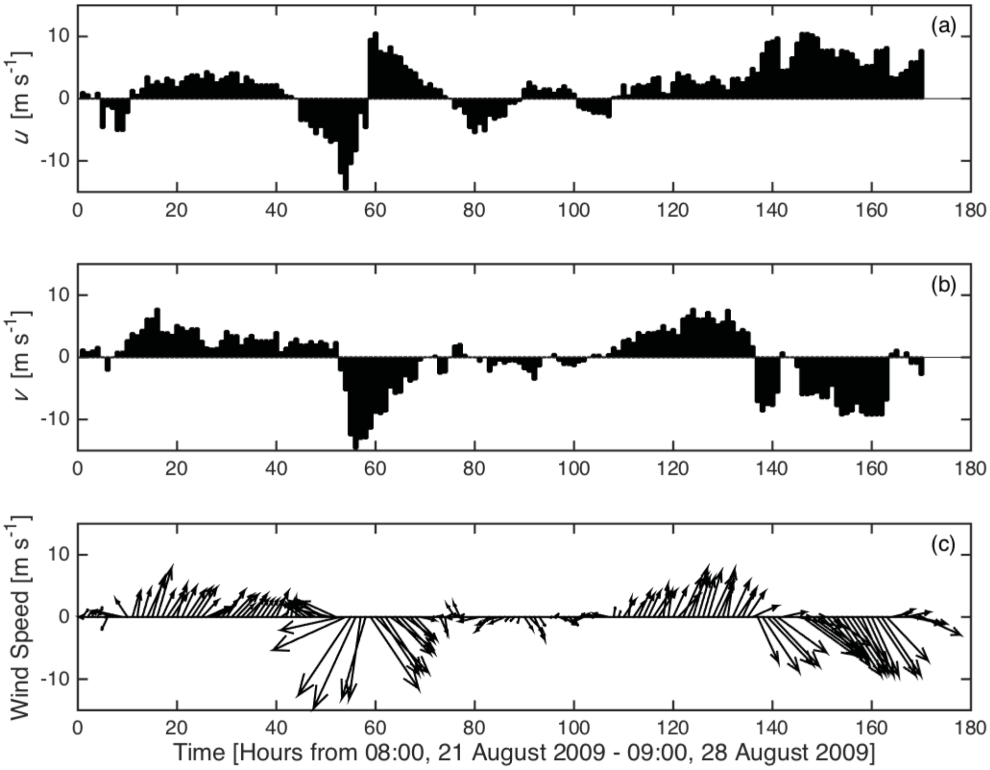

Figure A.2 (a) East-west (*u*) and (b) north-south (*v*) wind components at weather station Caribou Point in the Northumberland Strait during the particle tracing study in Murray Harbour (MH) in August 2009. (c) Wind speed during the particle tracing study, also recorded at Caribou Point, where the lengths of the arrows are proportional to speed. Both histograms and arrows are depicted at a 1.00-h resolution.

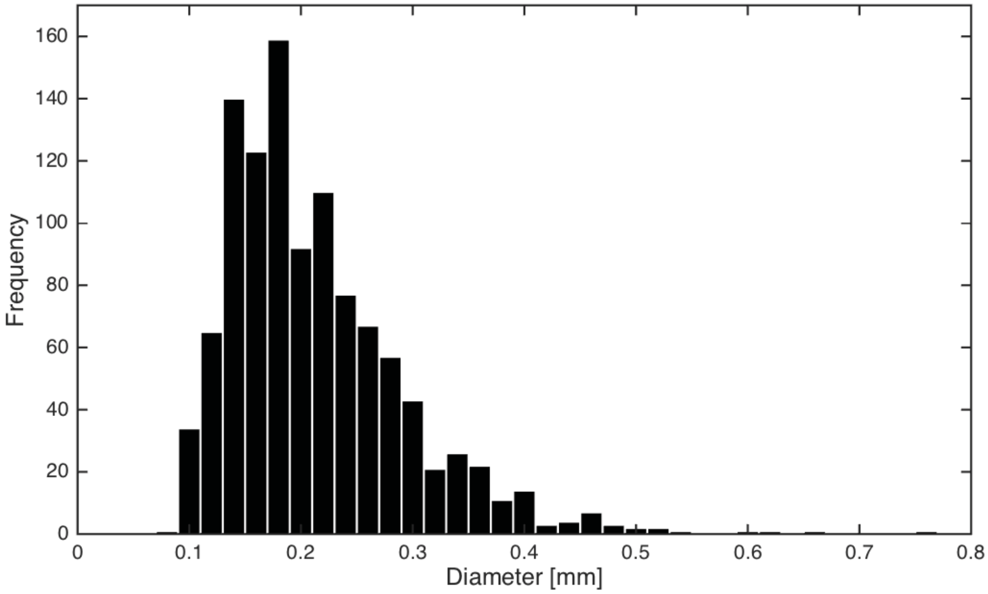

Figure A.3 Size frequency histogram distribution of a haphazardly selected subsample (n = 1090) of magnetically attractive particles (MAPs) released within Murray Harbour during the August 2009 particle tracing study, with a median esd of 195 μm and a geometric mean esd of 200 μm.

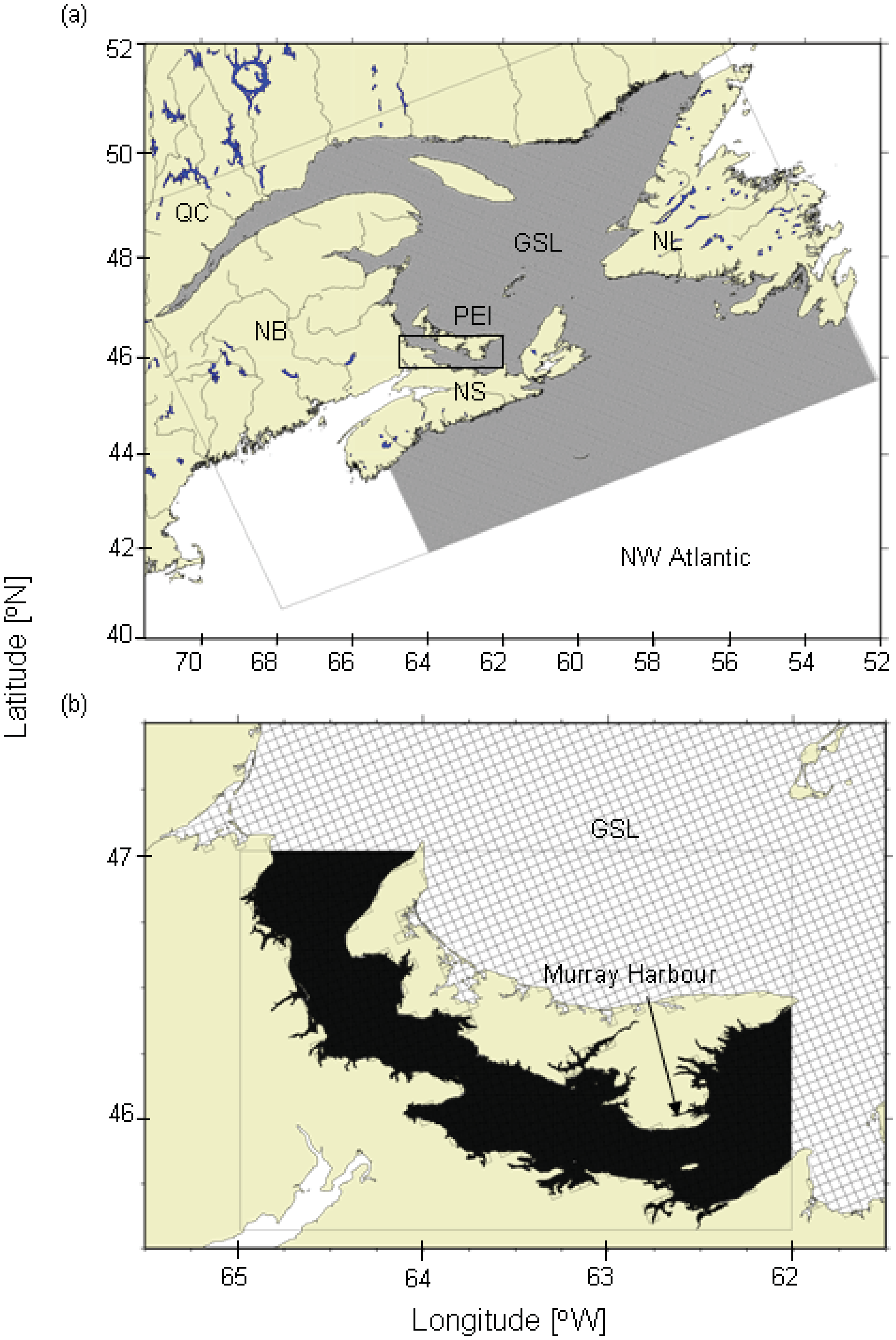

Figure A.4 Coastline charts of the Gulf of St. Lawrence (GSL) region including Prince Edward Island (PE) and bounded by Nova Scotia (NS), New Brunswick (NB), Québec (QC), and Newfoundland (NL), illustrating the model domain (gray) that incorporates (a) the 4 km model mesh (cross-hatch), and (b) the Northumberland Strait 200 m model domain (black) nested within the 4 km model. Murray Harbour is located on the north side of the Murray Head peninsula.

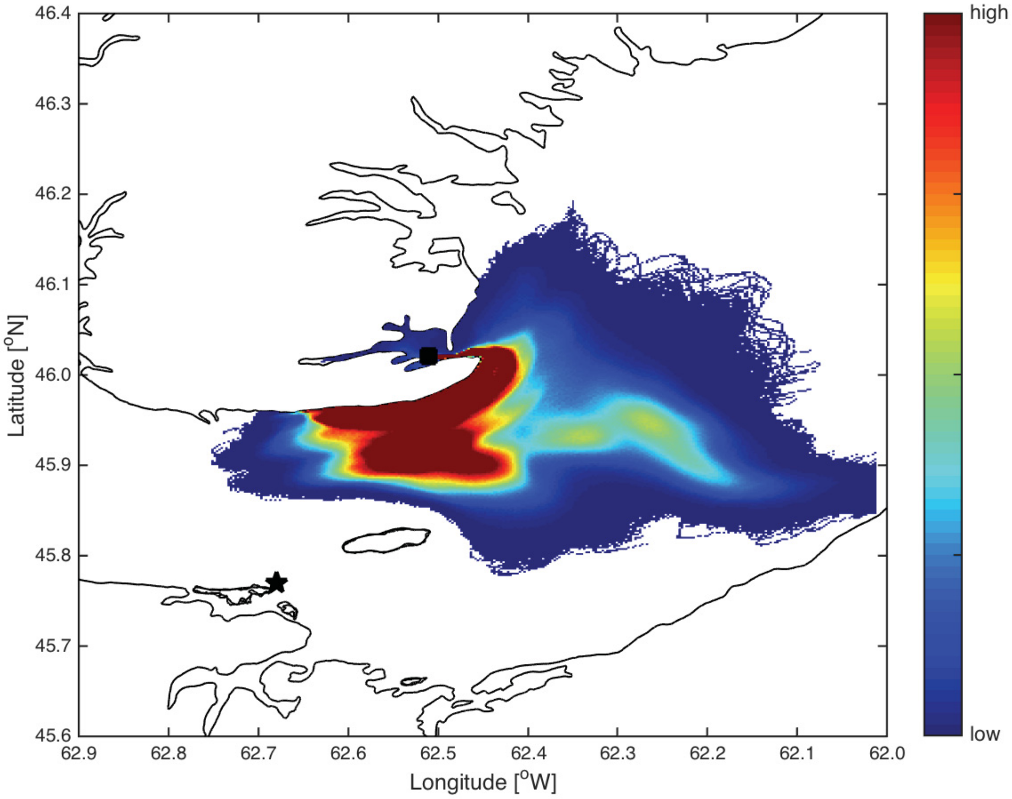

Figure A.5 Coastline chart of the eastern Northumberland Strait and scale bar illustrating the exposition number (E_{ij}; low to high) of VPs (released in Murray Harbour; black square) at each grid cell across the model domain as of 09:00 h on 28 August 2009 and based on a small-scale diffusion constant of 2 $m^2 s^{-1}$. VPs cannot move beyond the right-hand boundary of the model domain that parallels 62°W longitude. The location of weather station Caribou Point, where wind speed and direction were recorded, is indicated with a star.

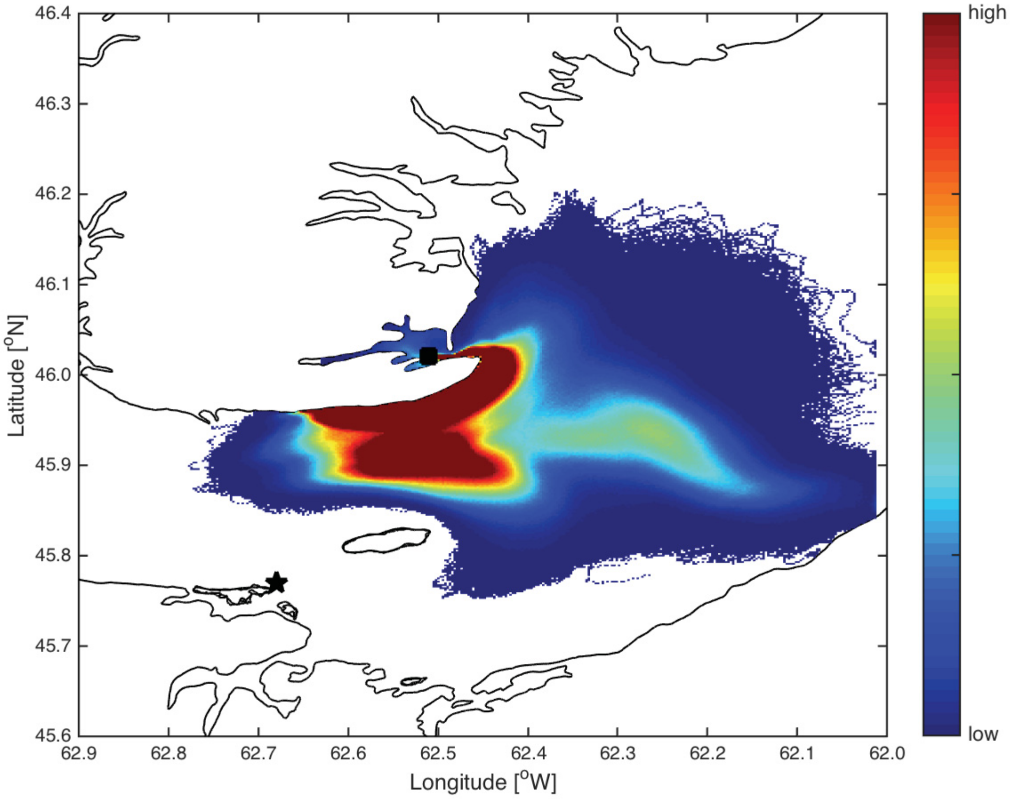

Figure A.6 Coastline chart of the eastern Northumberland Strait and scale bar illustrating the exposition number (E_{ij}; low to high) of VPs (released in Murray Harbour; black square) at each grid cell across the model domain as of 09:00 h on 28 August 2009 and based on a small-scale diffusion constant of 5 $m^2 s^{-1}$. VPs cannot move beyond the right-hand boundary of the model domain that parallels 62°W longitude. The location of weather station Caribou Point, where wind speed and direction were recorded, is indicated with a star.

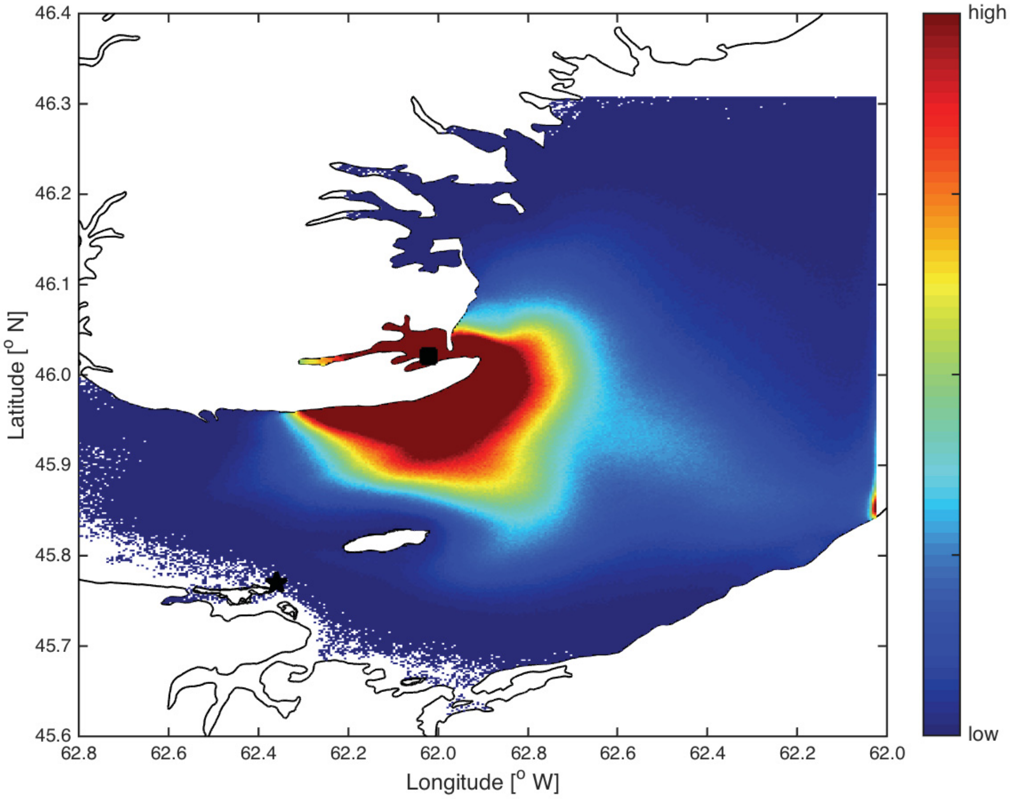

Figure A.7 Coastline chart of the eastern Northumberland Strait and scale bar illustrating the exposition number (E_{ij}; low to high) of VPs (released in Murray Harbour; black square) at each grid cell across the model domain as of 09:00 h on 28 August 2009 and based on a small-scale diffusion minimum of 50 $m^2 s^{-1}$. VPs cannot move beyond the right-hand boundary of the model domain that parallels 62°W longitude. The location of weather station Caribou Point, where wind speed and direction were recorded, is indicated with a star.

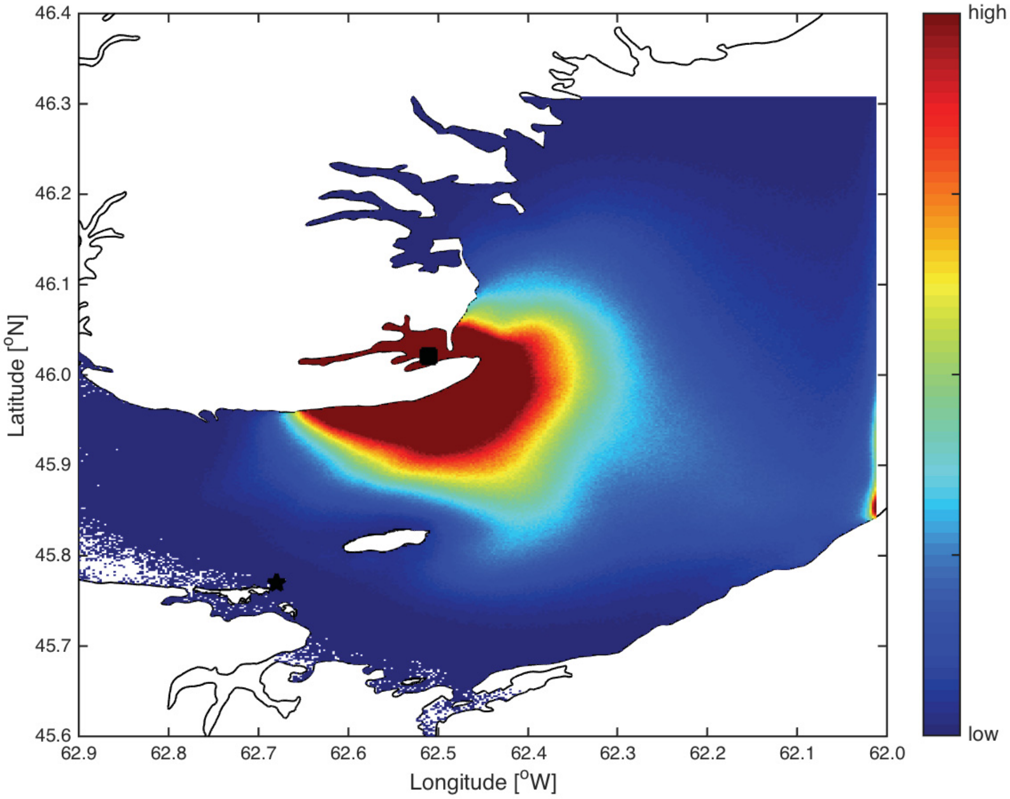

Figure A.8 Coastline chart of the eastern Northumberland Strait and scale bar illustrating the exposition number (E_{ij}; low to high) of VPs (released in Murray Harbour; black square) at each grid cell across the model domain as of 09:00 h on 28 August 2009 and based on a small-scale diffusion minimum of 80 $m^2 s^{-1}$. VPs cannot move beyond the right-hand boundary of the model domain that parallels 62°W longitude. The location of weather station Caribou Point, where wind speed and direction were recorded, is indicated with a star.

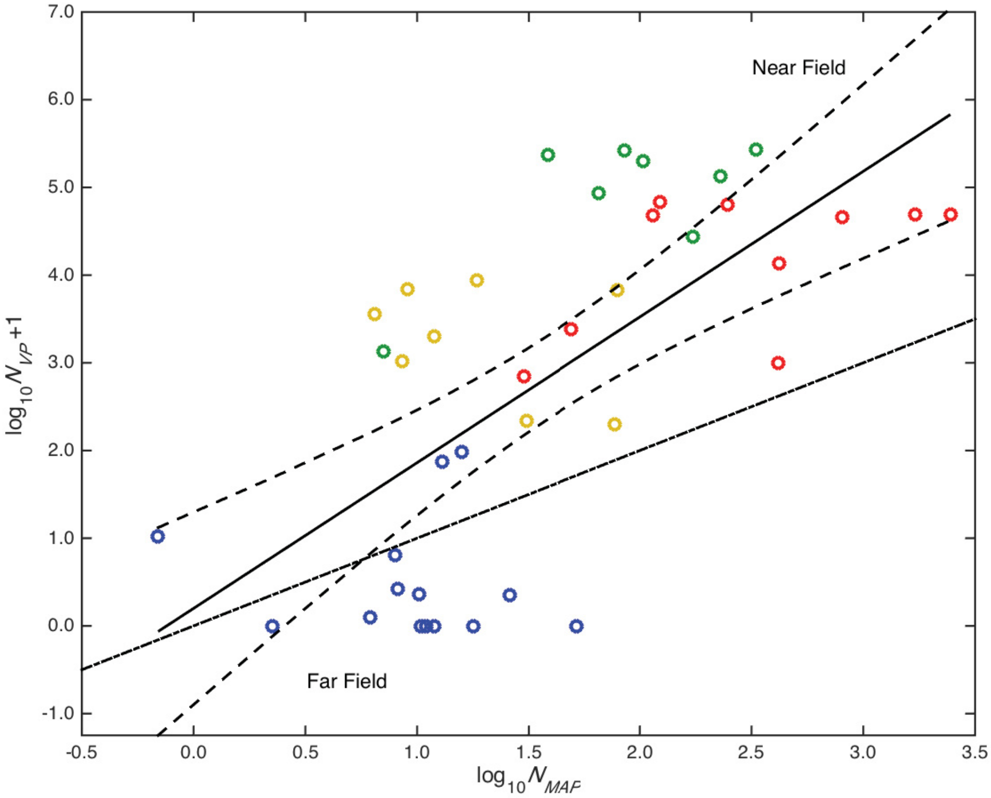

Figure A.9 Log-log relation of N_{VP} as a function of N_{MAP} where N_{VP} modeling used a constant K_p of 2 m^2 s^{-1}. The fitted regression model [$\log_{10}N_{VP} = 0.20 + 1.66 \log_{10}N_{MAP}$; $r^2 = 0.44$; $p < 0.001$] is illustrated by a solid line with the 95% confidence interval around the model (dashed lines) fitted to the estimates nominally classified as near- to far-field distances from the source inside Murray Harbour (red), along the coast of the peninsula (green), in nearshore open waters (yellow), and offshore open waters (blue). The 1:1 relation is illustrated as a dashed-dotted line.

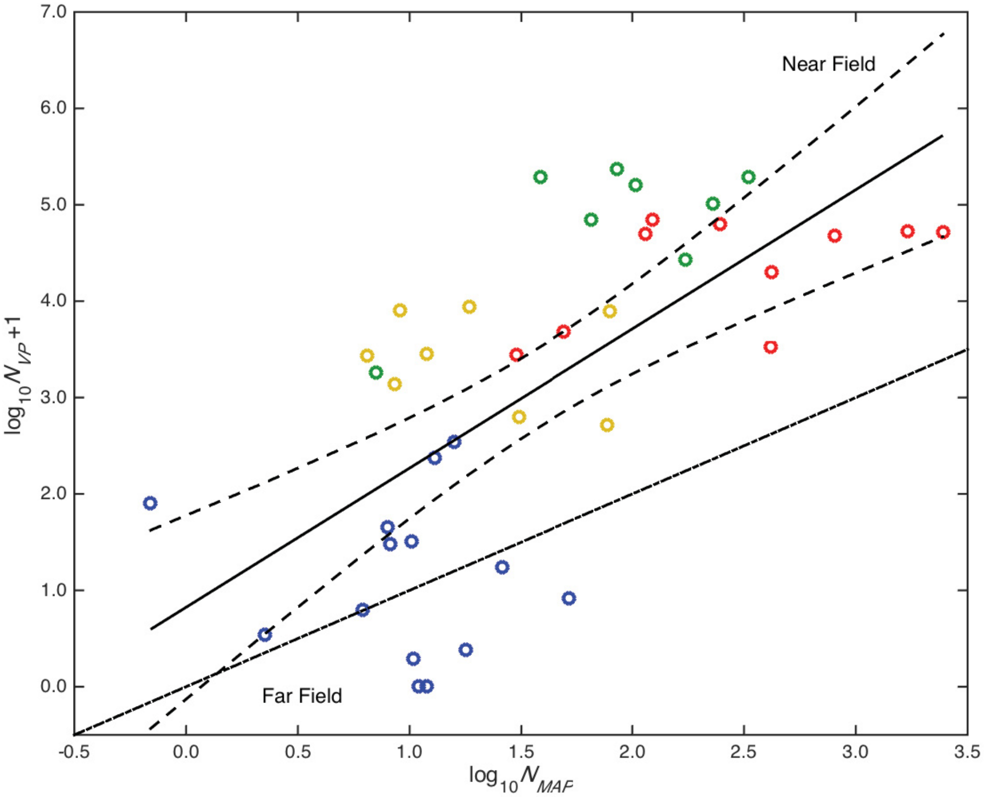

Figure A.10 Log-log relation of N_{VP} as a function of N_{MAP} where N_{VP} modeling used a constant K_p of 5 $m^2 s^{-1}$. The fitted regression model [$\log_{10}N_{VP} = 0.82 + 1.44 \log_{10}N_{MAP}$; $r^2 = 0.44$; $p < 0.001$] is illustrated by a solid line with the 95% confidence interval around the model (dashed lines) fitted to the estimates nominally classified as near- to far-field distances from the source inside Murray Harbour (red), along the coast of the peninsula (green), in nearshore open waters (yellow), and offshore open waters (blue). The 1:1 relation is illustrated as a dashed-dotted line.

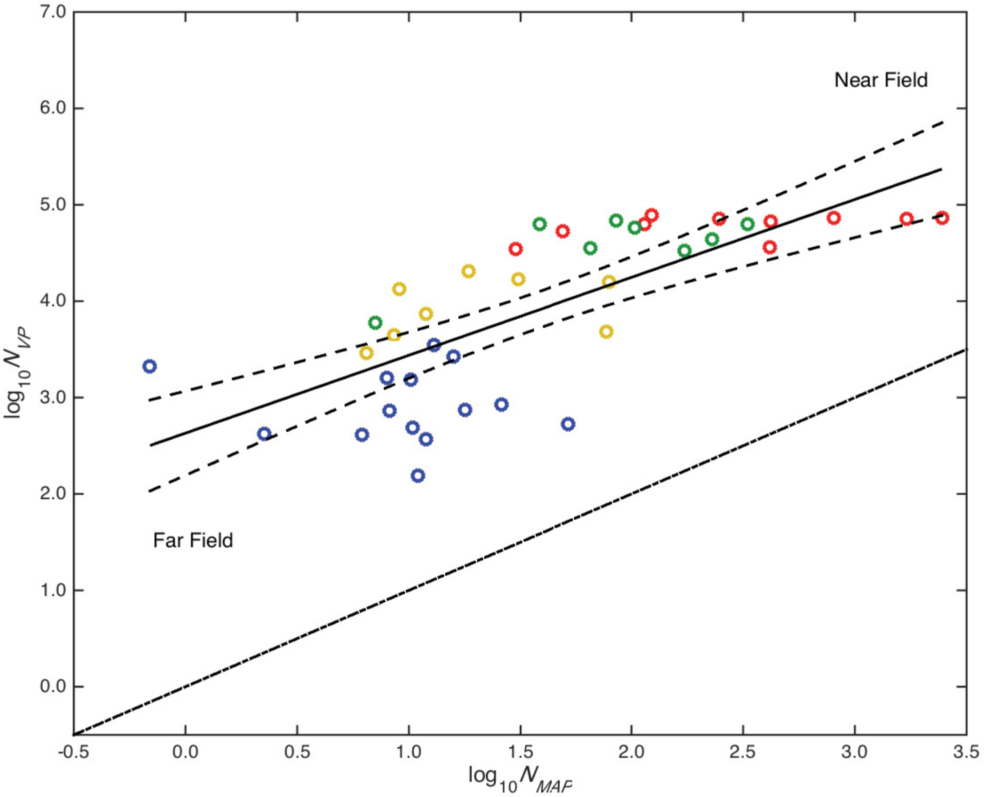

Figure A.11 Log-log relation of N_{VP} as a function of N_{MAP} where N_{VP} modeling used a minimum K_p of 50 $m^2\,s^{-1}$. The regression model [$\log_{10}N_{VP} = 2.63 + 0.81 \log_{10}N_{MAP}$; $r^2 = 0.54$; $p < 0.001$] is illustrated by a solid line with the 95% confidence interval around the model (dashed lines) fitted to the estimates nominally classified as near- to far-field distances from the source inside Murray Harbour (red), along the coast of the peninsula (green), in nearshore open waters (yellow), and offshore open waters (blue). The 1:1 relation is illustrated as a dashed-dotted line.

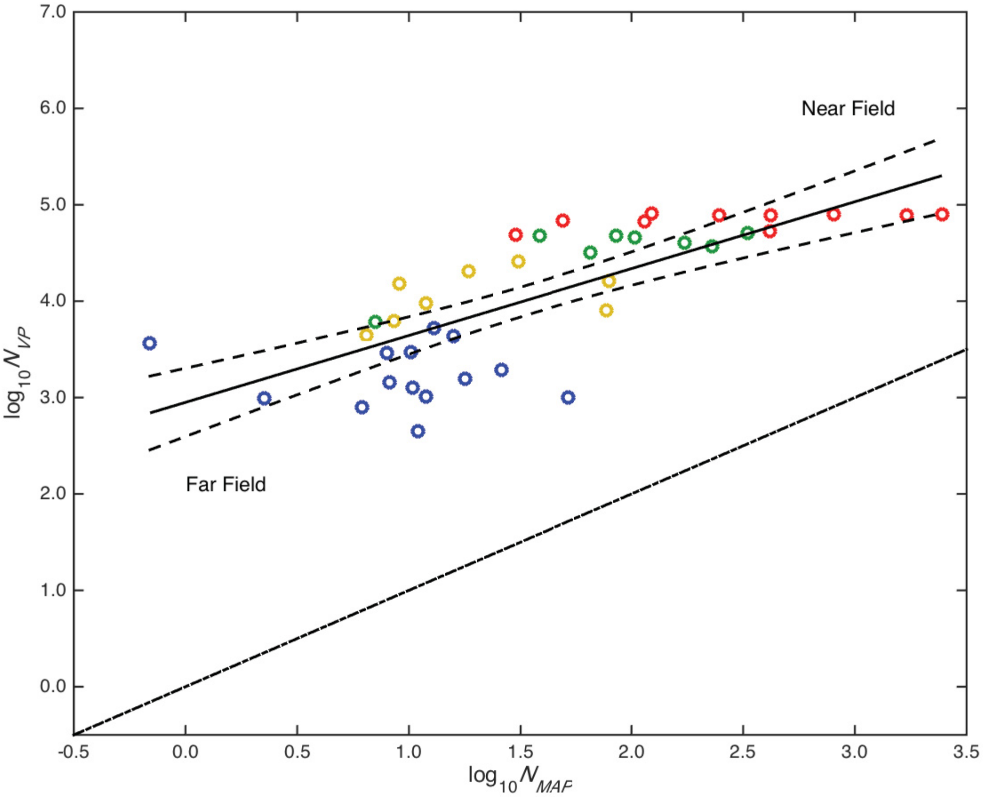

Figure A.12 Log-log relation of N_{VP} as a function of N_{MAP} where N_{VP} modeling used a minimum K_p of 80 $m^2 s^{-1}$. The fitted regression model [$\log_{10}N_{VP} = 2.95 + 0.69 \log_{10}N_{MAP}$; $r^2 = 0.57$; $p < 0.001$] is illustrated by a solid line with the 95% confidence interval around the model (dashed lines) fitted to the estimates nominally classified as near- to far-field distances from the source inside Murray Harbour (red), along the coast of the peninsula (green), in nearshore open waters (yellow), and offshore open waters (blue). The 1:1 relation is illustrated as a dashed-dotted line.

Table A.1 Summary of the log-log regressions and associated Figures as a function of constant (2, 5, and 25 $m^2 s^{-1}$) and minimum (50 and 80 $m^2 s^{-1}$) K_p values used in N_{VP} modeling, indicating slopes and their associated 95% confidence intervals, intercepts and their associated 95% confidence intervals, r^2 values, and *p*-values.

Small-scale diffusivity, K_p ($m^2 s^{-1}$)	Slope	95% CI	Intercept	95% CI	r^2	*p*-value	**Figure**
2	1.66	± 0.62	0.20	± 1.10	0.44	< 0.001	**A.9**
5	1.44	± 0.53	0.82	± 0.95	0.44	< 0.001	**A.10**
25	1.00	± 0.33	2.08	± 0.59	0.49	< 0.001	**3.9**
50	0.81	± 0.25	2.63	± 0.44	0.54	< 0.001	**A.11**
80	0.69	± 0.20	2.95	± 0.35	0.57	< 0.001	**A.12**

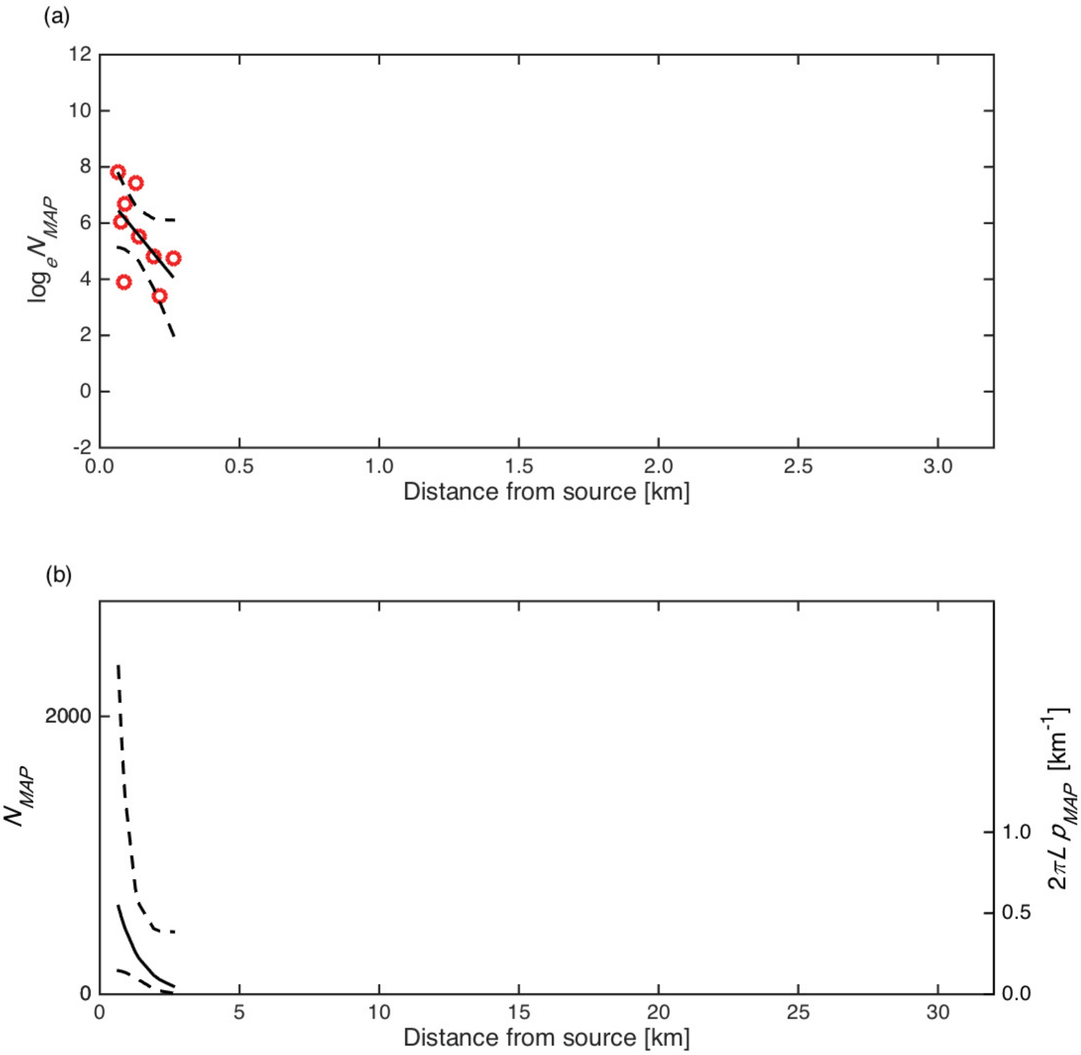

Figure A.13 Log-linear (a) and exponential decay (b) of N_{MAP} as a function of distance L (km) from the source location, using only magnetic-collectors located within Murray Harbour. The regression model [$\log_e N_{MAP} = 7.25 - 1.21\ L$; $r^2 = 0.33$; $p = 0.08$] in (a) is illustrated by a solid line with the upper and lower 95% confidence limits around the model (dashed lines) fitted to the N_{MAP} estimates. The exponential decay [$N_{MAP} = 1.41 \times 10^3\ e^{-1.21\ L}$] in (b) is illustrated by a solid line with the upper and lower 95% confidence limits (dashed lines). The exponential decay (solid line) can be interpreted as $2\pi L\ p_{MAP}$ (right ordinate) with an *e*-folding scale of 0.82 km that has upper and lower 95% confidence limits of 5.13 and 0.38 km.

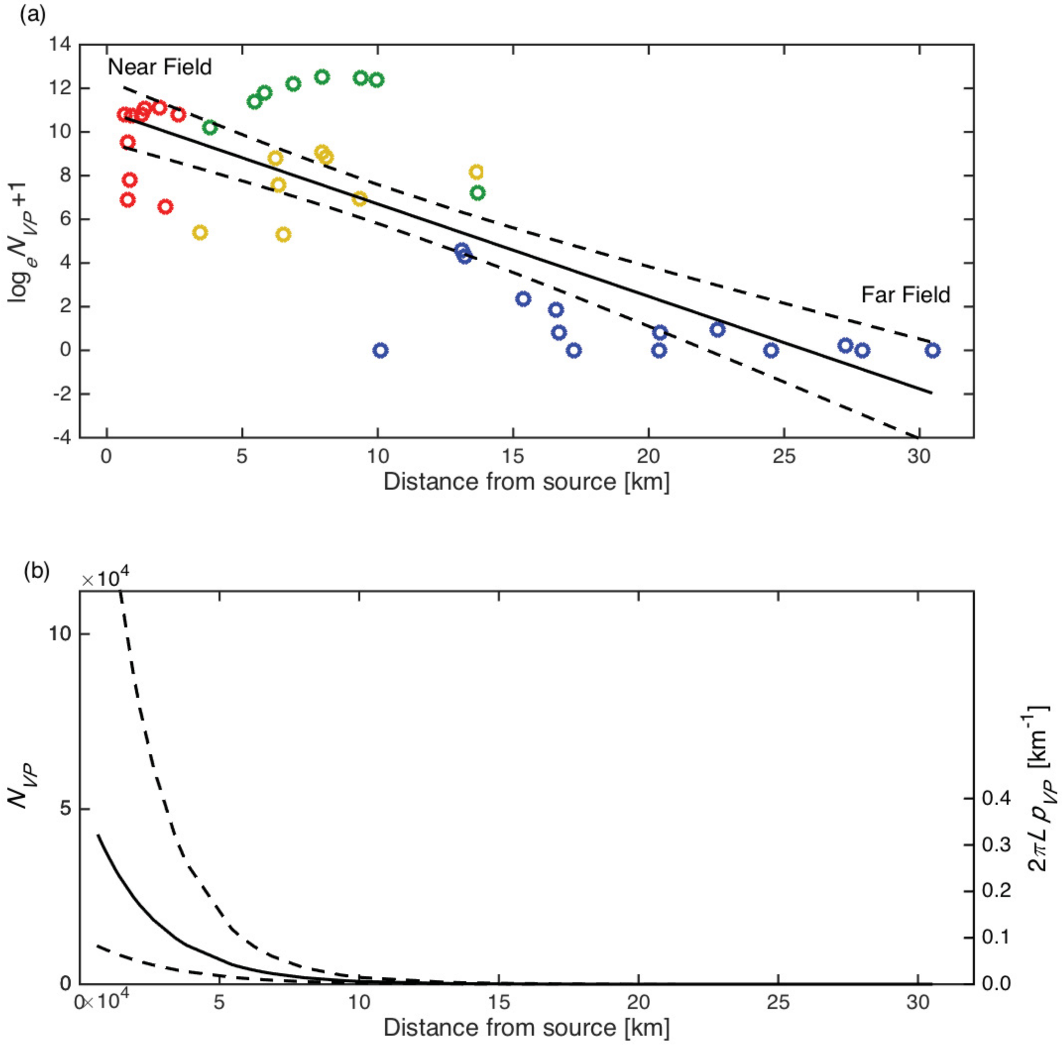

Figure A.14 Log-linear (a) and exponential decay (b) of N_{VP} as a function of distance L (km) from the source location and based on a constant K_p of 2 $m^2\,s^{-1}$. The regression model [$\log_e N_{VP} = 10.94 - 0.42\,L$; $r^2 = 0.63$; $p < 0.001$] in (a) is illustrated by a solid line with the upper and lower 95% confidence limits around the model (dashed lines) fitted to the N_{VP} estimates nominally classified as near- to far-field distances from the source inside Murray Harbour (red), along the coast of the peninsula (green), in nearshore open waters (yellow), and in offshore open waters (blue). The exponential decay [$N_{VP} = 5.61 \times 10^4\, e^{-0.42\,L}$] in (b) is illustrated by a solid line with the upper and lower 95% confidence limits (dashed lines). The exponential decay (solid line) can be interpreted as $2\pi L\, p_{VP}$ (right ordinate) with an e-folding scale of 2.36 km that has upper and lower 95% confidence limits of 3.16 and 1.89 km.

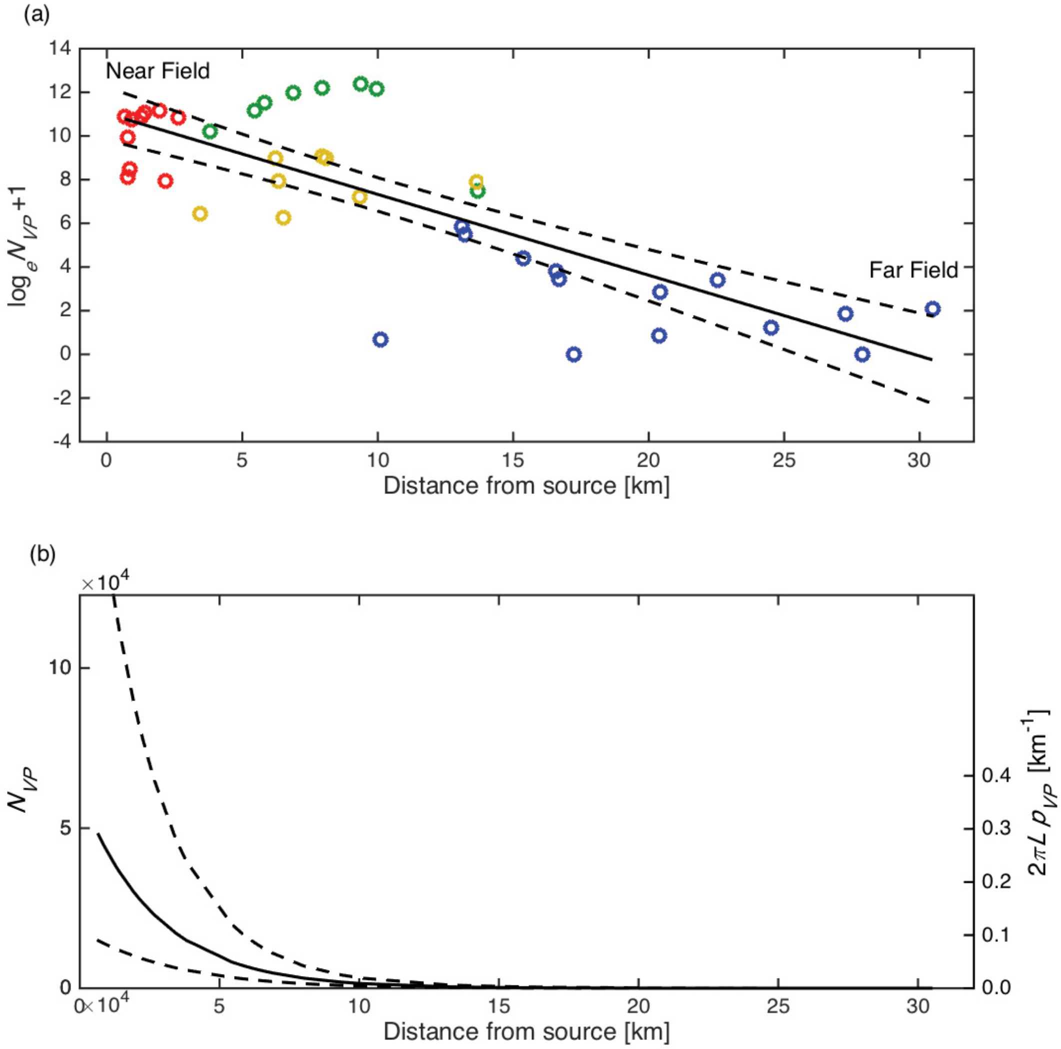

Figure A.15 Log-linear (a) and exponential decay (b) of N_{VP} as a function of distance L (km) from the source location and based on a constant K_p of 5 m^2 s^{-1}. The regression model [$\log_e N_{VP} = 11.02 - 0.37\, L$; $r^2 = 0.64$; $p < 0.001$] in (a) is illustrated by a solid line with the upper and lower 95% confidence limits around the model (dashed lines) fitted to the N_{VP} estimates nominally classified as near- to far-field distances from the source inside Murray Harbour (red), along the coast of the peninsula (green), in nearshore open waters (yellow), and in offshore open waters (blue). The exponential decay [$N_{VP} = 6.14 \times 10^4\ e^{-0.37\, L}$] in (b) is illustrated by a solid line with the upper and lower 95% confidence limits (dashed lines). The exponential decay (solid line) can be interpreted as $2\pi L\ p_{VP}$ (right ordinate) with an e-folding scale of 2.70 km that has upper and lower 95% confidence limits of 3.60 and 2.16 km.

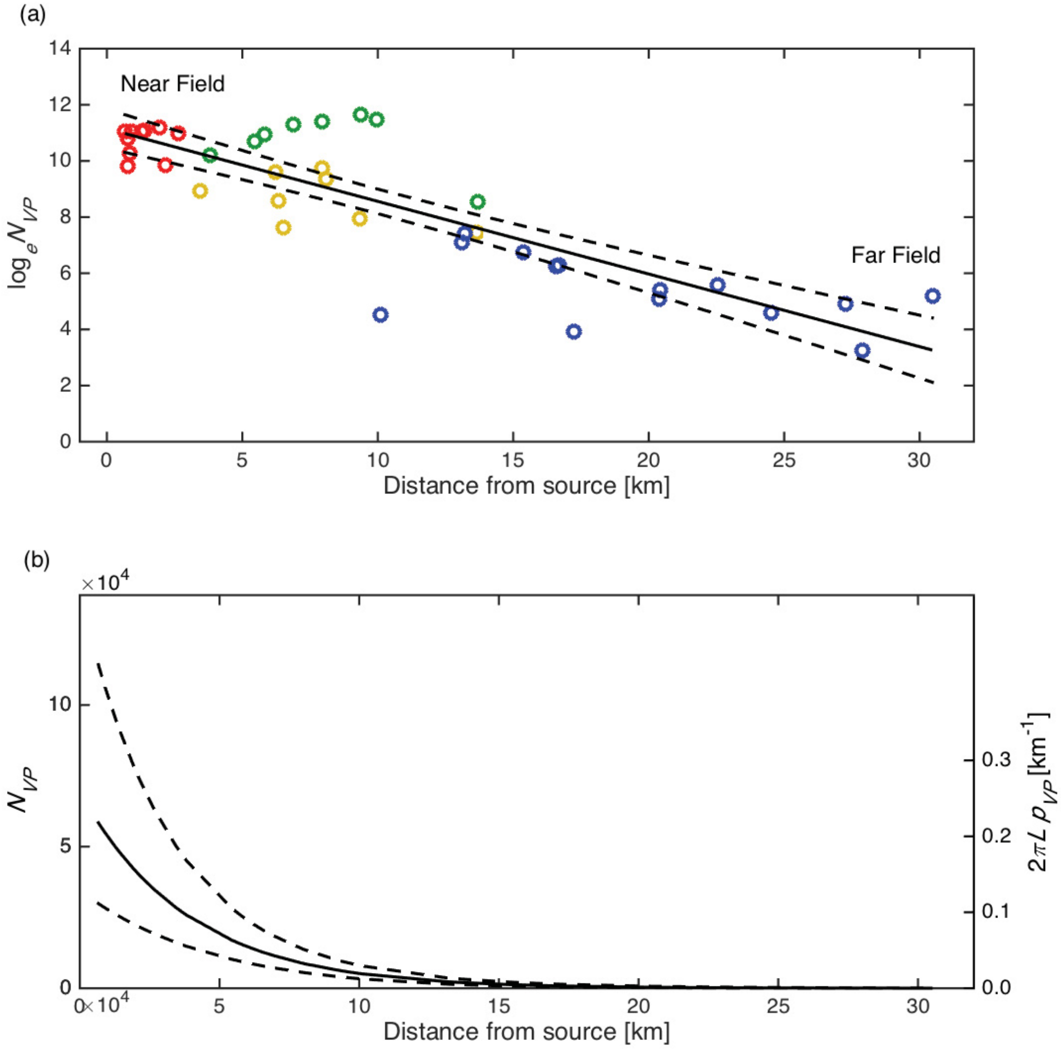

Figure A.16 Log-linear (a) and exponential decay (b) of N_{VP} as a function of distance L (km) from the source location and based on a constant K_p of 25 $m^2\ s^{-1}$. The regression model [$\log_e N_{VP} = 11.15 - 0.26\ L$; $r^2 = 0.72$; $p < 0.001$] in (a) is illustrated by a solid line with the upper and lower 95% confidence limits around the model (dashed lines) fitted to the N_{VP} estimates nominally classified as near- to far-field distances from the source inside Murray Harbour (red), along the coast of the peninsula (green), in nearshore open waters (yellow), and in offshore open waters (blue). The exponential decay [$N_{VP} = 9.64 \times 10^4\ e^{-0.26\ L}$] in (b) is illustrated by a solid line with the upper and lower 95% confidence limits (dashed lines). The exponential decay (solid line) can be interpreted as $2\pi L\ p_{VP}$ (right ordinate) with an e-folding scale of 3.86 km that has upper and lower 95% confidence limits of 4.85 and 3.21 km.

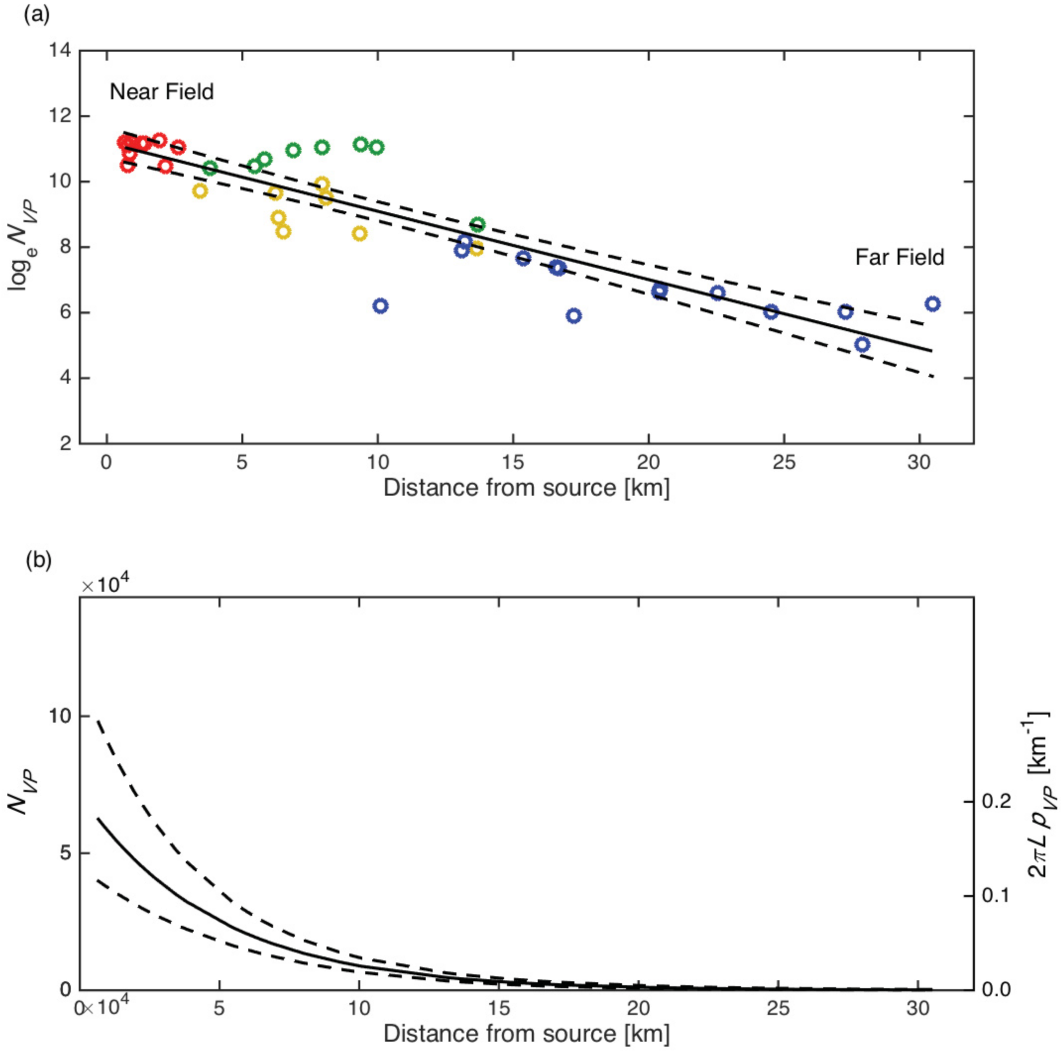

Figure A.17 Log-linear (a) and exponential decay (b) of N_{VP} as a function of distance L (km) from the source location and based on a minimum K_p of 50 m^2 s^{-1}. The regression model [$\log_e N_{VP} = 11.18 - 0.21\ L$; $r^2 = 0.79$; $p < 0.001$] in (a) is illustrated by a solid line with the upper and lower 95% confidence limits around the model (dashed lines) fitted to the N_{VP} estimates nominally classified as near- to far-field distances from the source inside Murray Harbour (red), along the coast of the peninsula (green), in nearshore open waters (yellow), and in offshore open waters (blue). The exponential decay [$N_{VP} = 7.17 \times 10^4\ e^{-0.21\ L}$] in (b) is illustrated by a solid line with the upper and lower 95% confidence limits (dashed lines). The exponential decay (solid line) can be interpreted as $2\pi L\ p_{VP}$ (right ordinate) with an e-folding scale of 4.79 km that has upper and lower 95% confidence limits of 5.77 and 4.10 km.

Table A.2 Summary of the log-linear relations and associated Figures of N_{VP} as a function of in-water distance L from the source location based on constant (2, 5, and 25 $m^2 s^{-1}$) and minimum (50 and 80 $m^2 s^{-1}$) K_p values used in N_{VP} modeling, indicating slopes and their associated 95% confidence intervals, r^2 values, and p-values.

Small-scale diffusivity, K_p ($m^2 s^{-1}$)	Slope	95% CI	r^2	p-value	**Figure**
2	-0.42	± 0.11	0.63	< 0.001	**A.14a**
5	-0.37	± 0.09	0.64	< 0.001	**A.15a**
25	-0.26	± 0.05	0.72	< 0.001	**A.16a**
50	-0.21	± 0.04	0.79	< 0.001	**A.17a**
80	-0.18	± 0.03	0.84	< 0.001	**3.8a**

Appendix B

Supplementary Figures and Tables: Chapter 4

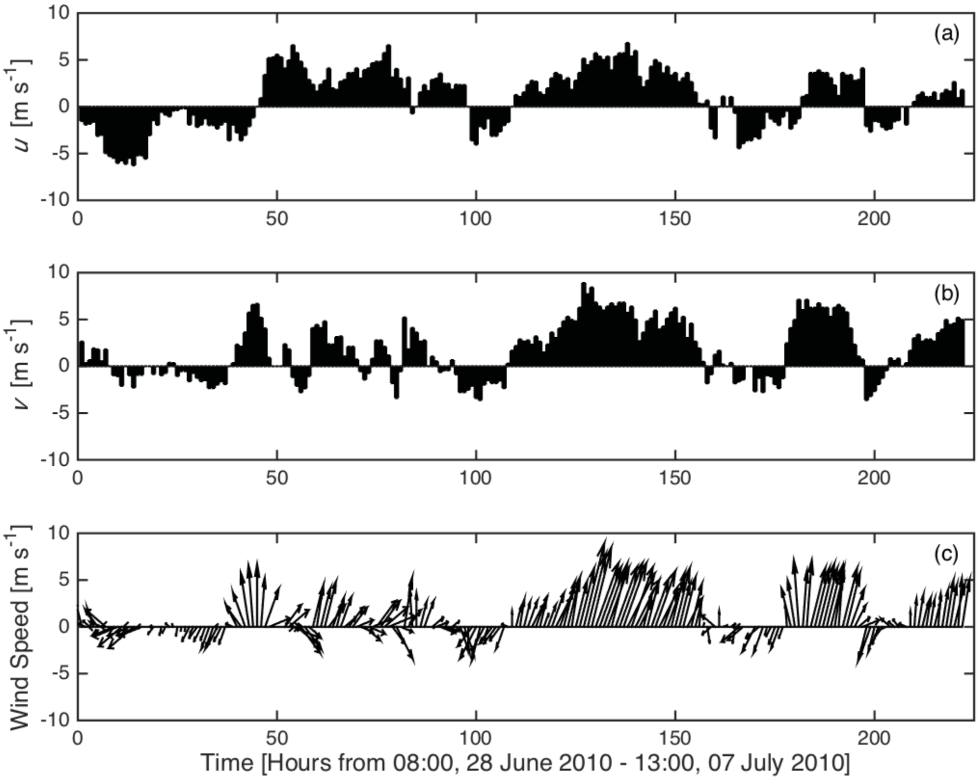

Figure B.1 (a) East-west (*u*) and (b) north-south (*v*) wind components at weather station Summerside in the Northumberland Strait during the Shediac (SH) particle tracing study in June and July 2010. (c) Wind speed during the particle tracing study, also recorded at Summerside, where the lengths of the arrows are proportional to speed. Both histograms and arrows are depicted at a 1.00-h resolution.

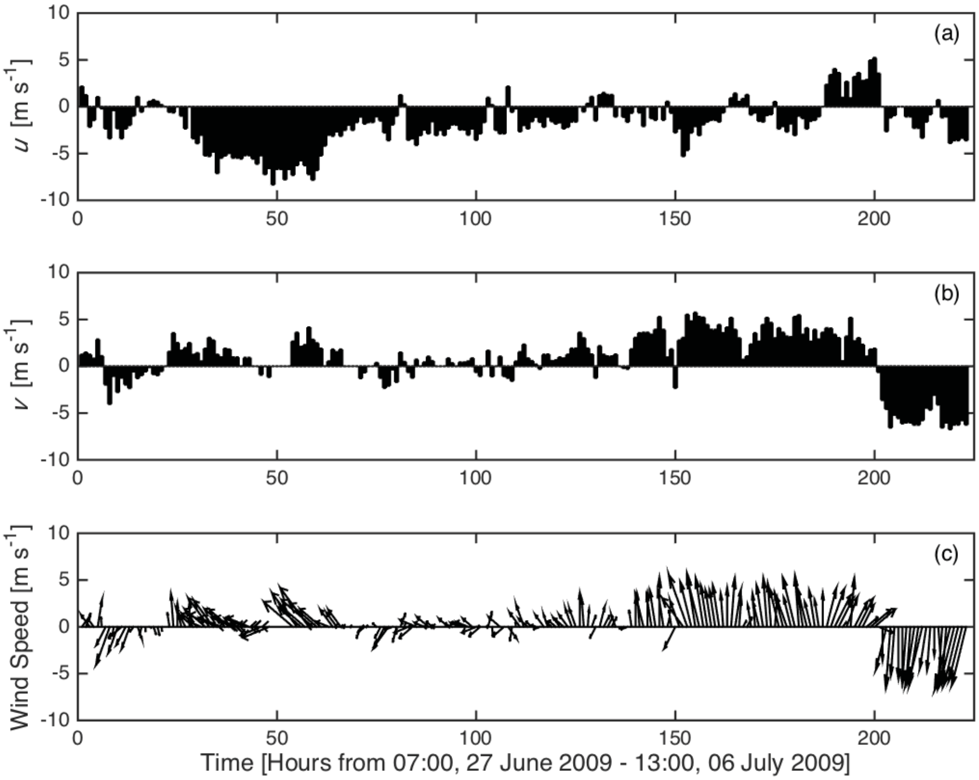

Figure B.2 (a) East-west (*u*) and (b) north-south (*v*) wind components at weather station Summerside in the Northumberland Strait during the Cape Tormentine (CT) particle tracing study in June and July 2009. (c) Wind speed during the particle tracing study, also recorded at Summerside, where the lengths of the arrows are proportional to speed. Both histograms and arrows are depicted at a 1.00-h resolution.

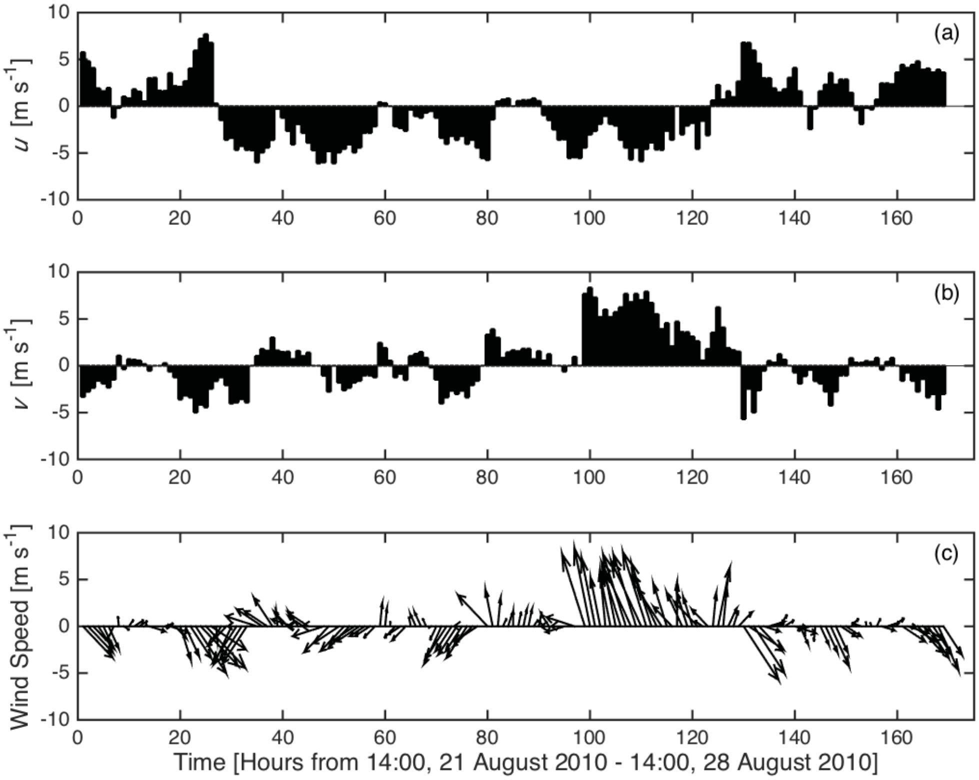

Figure B.3 (a) East-west (u) and (b) north-south (v) wind components at weather station Caribou Point in the Northumberland Strait during the particle tracing study west of Cape George (CG) in August 2010. (c) Wind speed during the particle tracing study, also recorded at Caribou Point, where the lengths of the arrows are proportional to speed. Both histograms and arrows are depicted at a 1.00-h resolution.

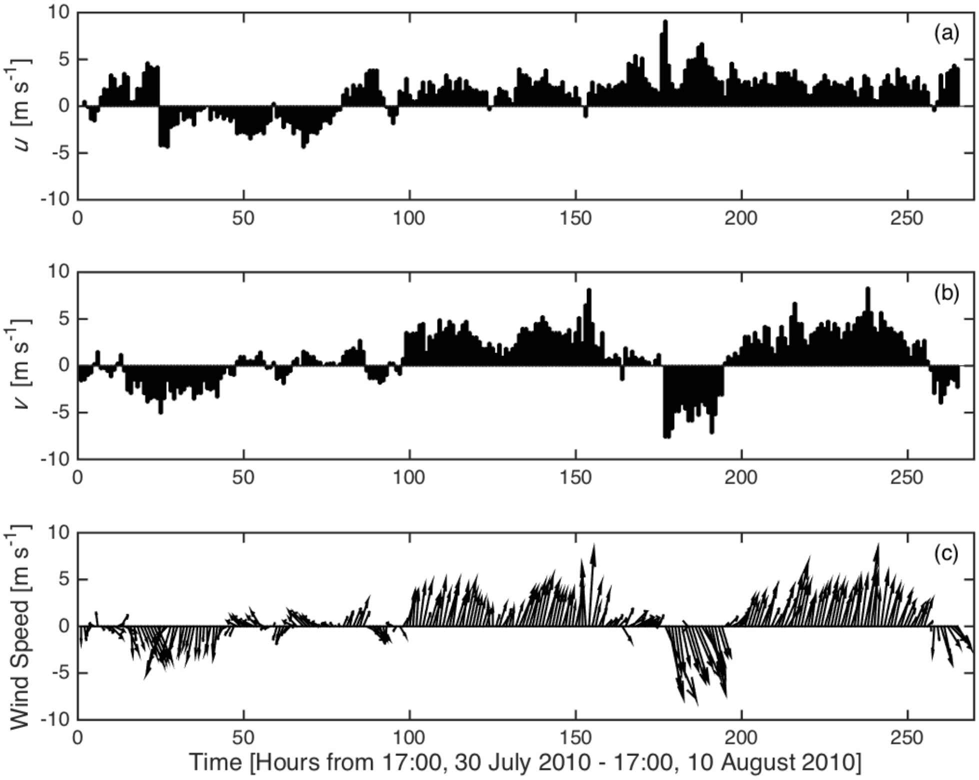

Figure B.4 (a) East-west (*u*) and (b) north-south (*v*) wind components at weather station Caribou Point in the Northumberland Strait during the particle tracing study in St. George's Bay (GB) in July and August 2010. (c) Wind speed during the particle tracing study, also recorded at Caribou Point, where the lengths of the arrows are proportional to speed. Both histograms and arrows are depicted at a 1.00-h resolution.

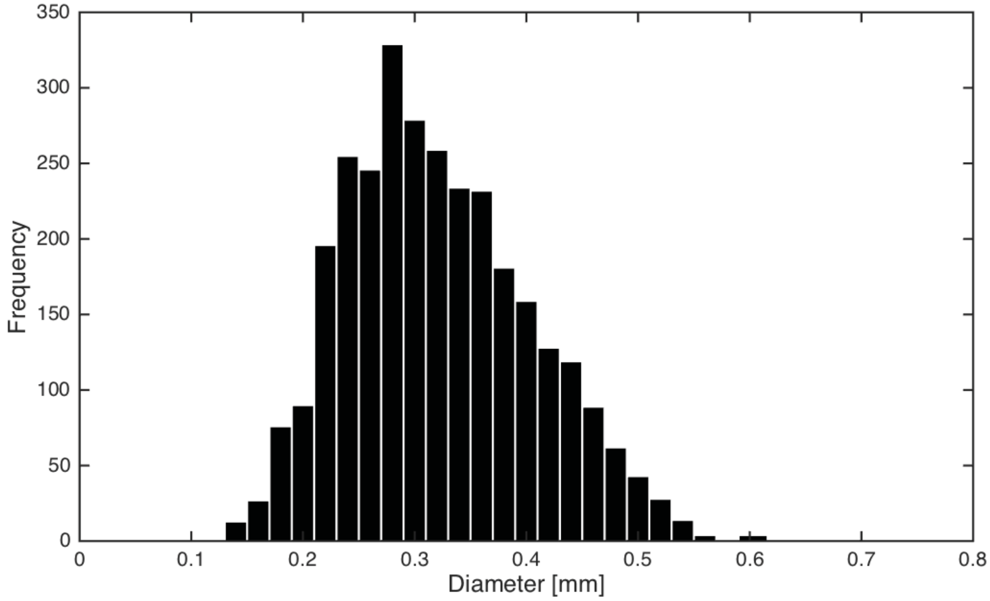

Figure B.5 Size frequency histogram distribution of a haphazardly selected subsample (*n* = 3069) of magnetically attractive particles (MAPs) released off the coast of Shediac during the June 2010 particle tracing study, with a median esd of 312 μm and a geometric mean esd of 311 μm.

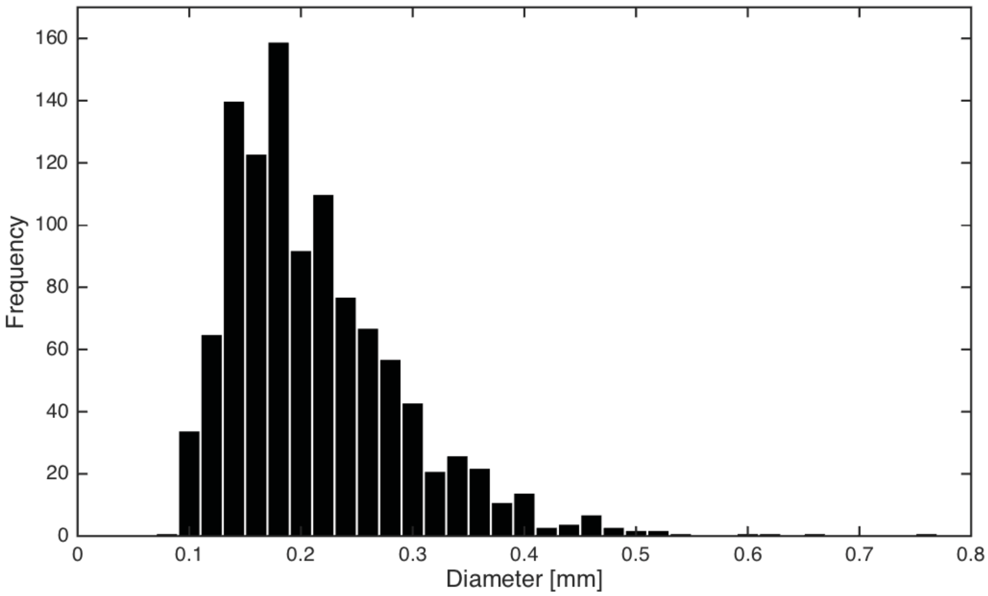

Figure B.6 Size frequency histogram distribution of a haphazardly selected subsample (*n* = 1090) of magnetically attractive particles (MAPs) released both off the coast of Cape Tormentine and within Murray Harbour during the 2009 particle tracing studies, with a median esd of 195 µm and a geometric mean esd of 200 µm.

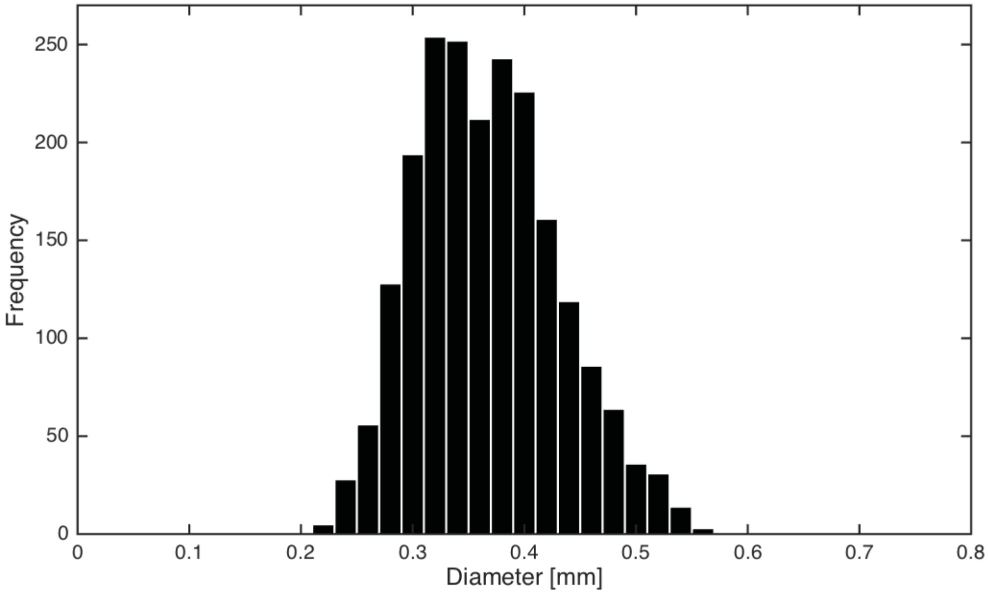

Figure B.7 Size frequency histogram distribution of a haphazardly selected subsample (*n* = 2115) of magnetically attractive particles (MAPs) released off the coast west of Cape George during the August 2010 particle tracing study, with a median esd of 361 μm and a geometric mean esd of 362 μm.

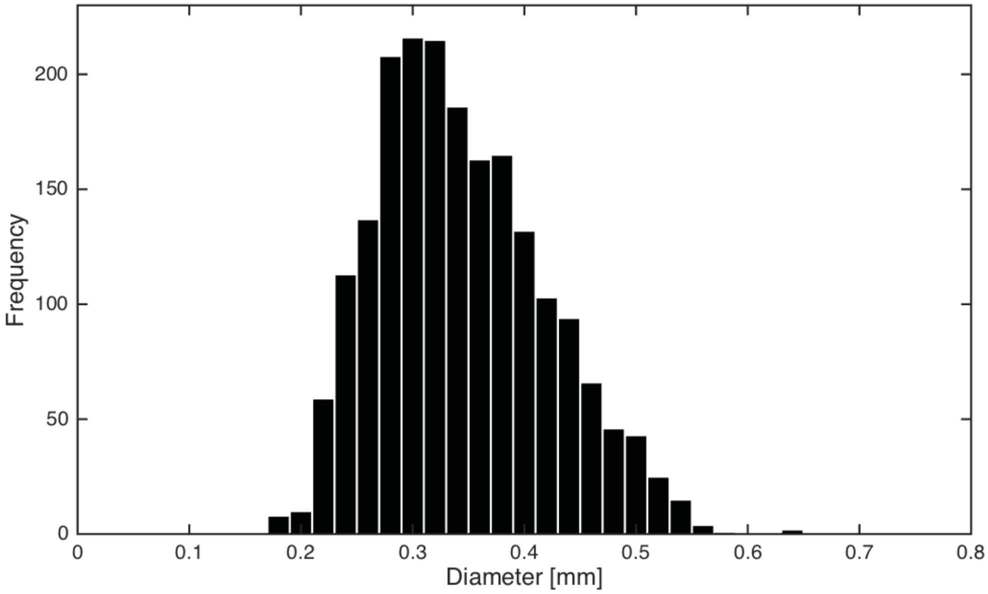

Figure B.8 Size frequency histogram distribution of a haphazardly selected subsample (n = 2011) of magnetically attractive particles (MAPs) released within St. George's Bay during the July 2010 particle tracing study, with a median esd of 336 μm and a geometric mean esd of 336 μm.

Appendix C

Supplementary Figures and Tables: Chapter 5

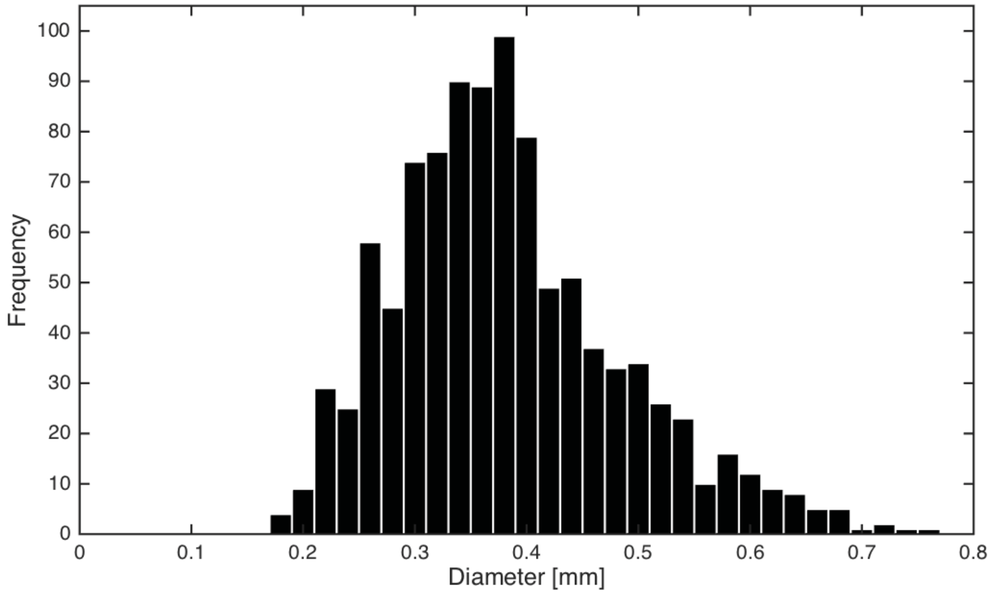

Figure C.1 Size frequency histogram distribution of a haphazardly selected subsample (*n* = 1000) of A+B magnetically attractive particles (MAPs) released within Lake St. Clair during the July 2009 particle tracing study, with a median esd of 371 μm and a geometric mean esd of 370 μm.

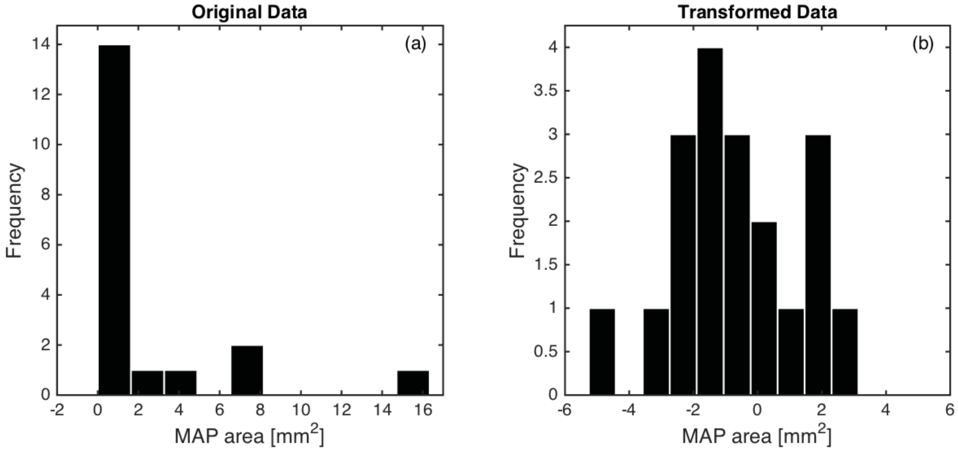

Figure C.2 Frequency histogram distributions of (a) the non-normal original A+B MAP area (mm^2) data and (b) the approximately normal Box-Cox transformed A+B MAP area (mm^2) data used in the optimal interpolation.

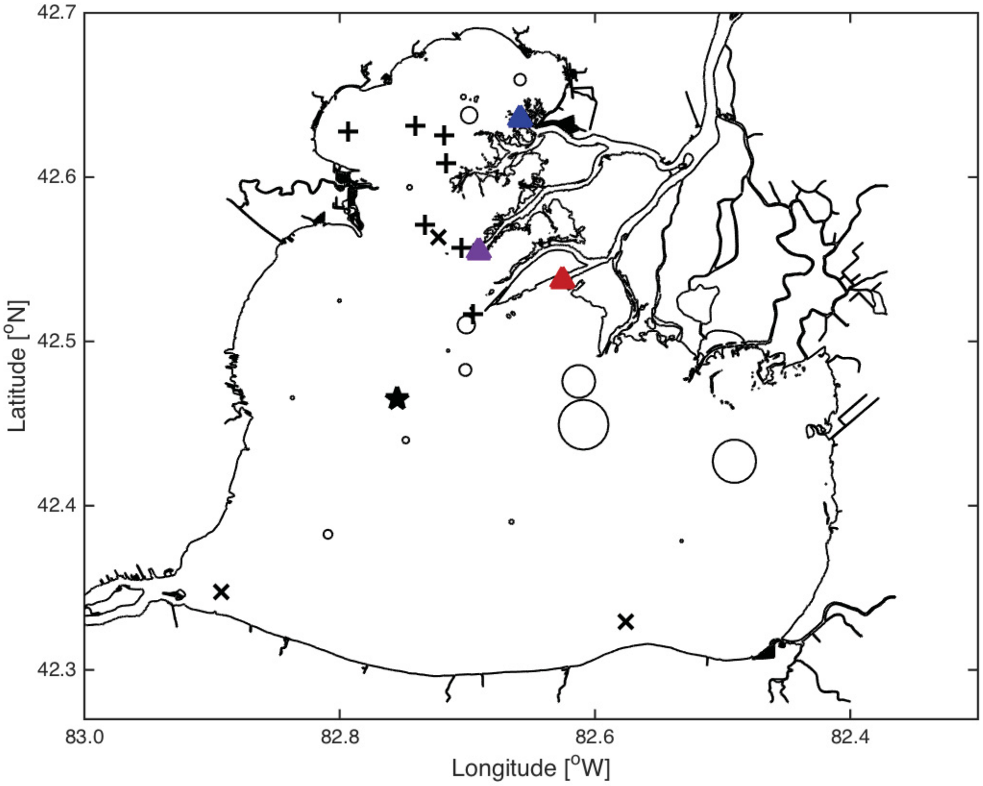

Figure C.3 Coastline chart of Lake St. Clair illustrating the location-specific relative number (linearly expanding-area circles) of A-MAPs captured among the recovered collectors. MAP source locations are denoted by triangles, where the northern triangle (blue) represents the B-source, the southern triangle (red) represents the A-source, and the intermediate triangle (purple) represents the hypothetical averaged A+B source. An "x" denotes the locations of empty recovered collectors (i.e., zero returns) while crosses denote the locations of collectors not recovered. Note that there were also unrecovered collectors at all three MAP source locations. The location of Station LSCM4, where wind speed and direction were recorded, is indicated with a star.

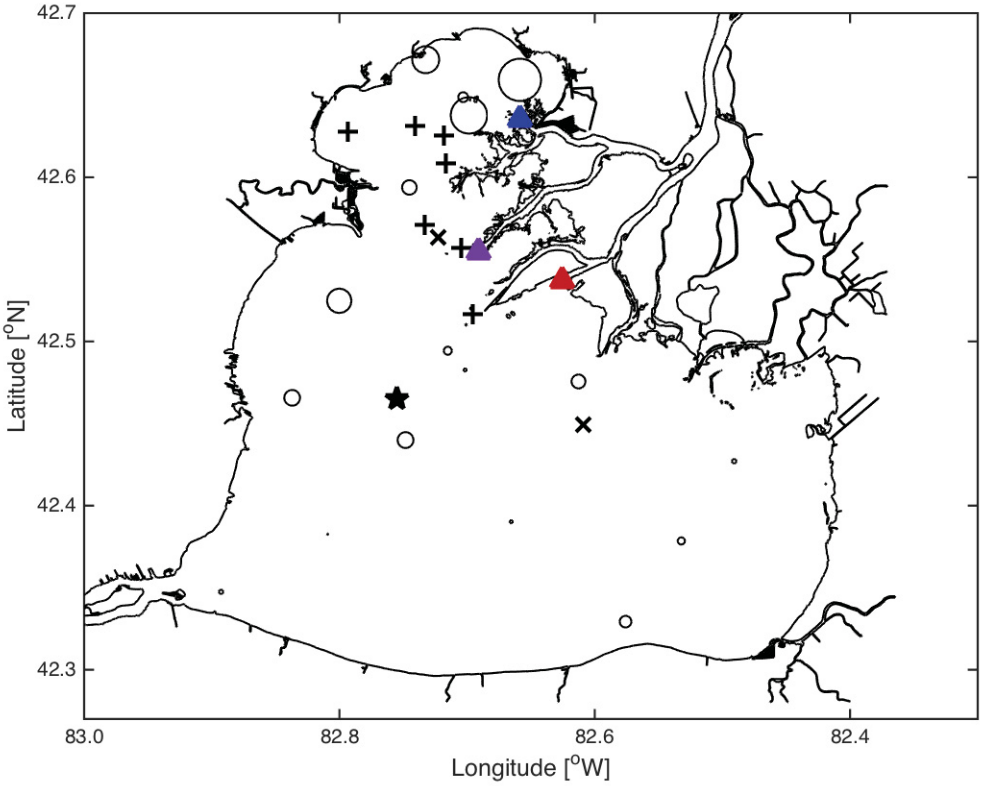

Figure C.4 Coastline chart of Lake St. Clair illustrating the location-specific relative number (linearly expanding-area circles) of B-MAPs captured among the recovered collectors. MAP source locations are denoted by triangles, where the northern triangle (blue) represents the B-source, the southern triangle (red) represents the A-source, and the intermediate triangle (purple) represents the hypothetical averaged A+B source. An "x" denotes the locations of empty recovered collectors (i.e., zero returns) while crosses denote the locations of collectors not recovered. Note that there were also unrecovered collectors at all three MAP source locations. The location of Station LSCM4, where wind speed and direction were recorded, is indicated with a star.

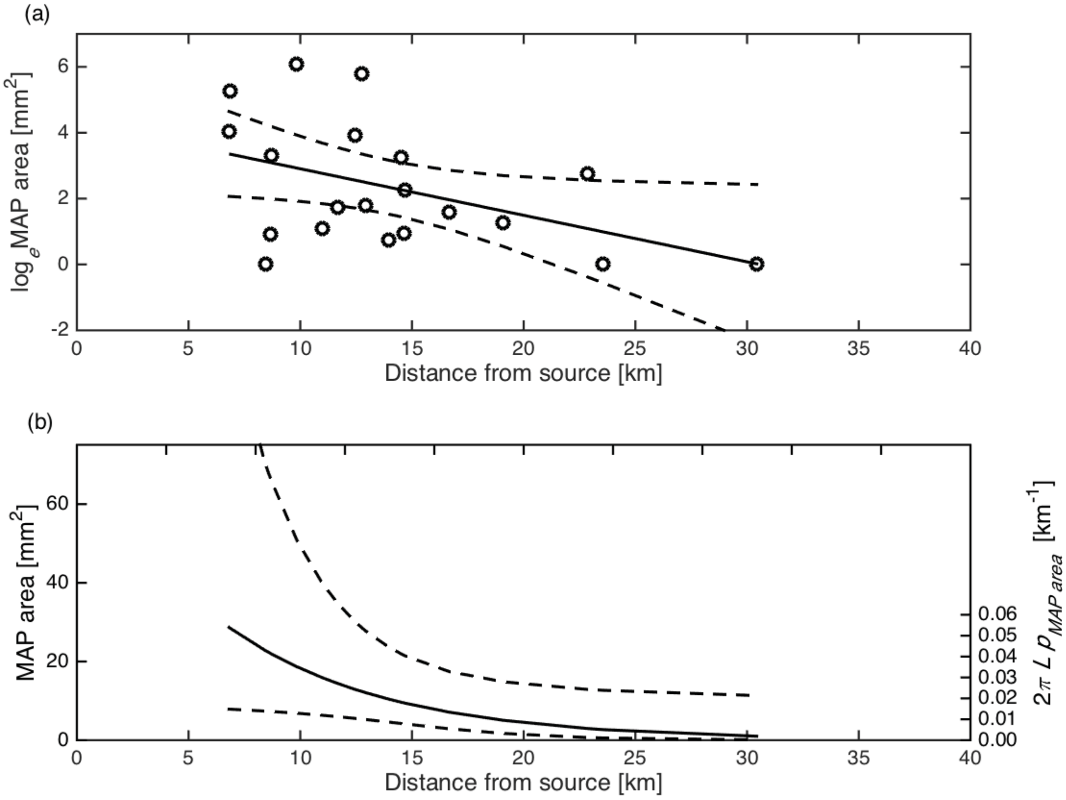

Figure C.5 Log-linear (a) and exponential decay (b) of A-MAP area (mm^2) as a function of distance *L* (km) from the A-source location. The regression model [$\log_e$MAP area = 4.32 – 0.14 L; $r^2 = 0.20$; $p = 0.05$] in (a) is illustrated by a solid line with the upper and lower 95% confidence limits around the model (dashed lines) fitted to the MAP area estimates. The exponential decay [MAP area = $7.52 \times 10^1 e^{-0.14L}$] in (b) is illustrated by a solid line with the upper and lower 95% confidence limits (dashed lines). The exponential decay (solid line) can be interpreted as $2\pi L\ p_{MAP}$ (right ordinate) with an *e*-folding scale of 7.08 km that has upper and lower 95% confidence limits of 322.58 and 3.58 km.

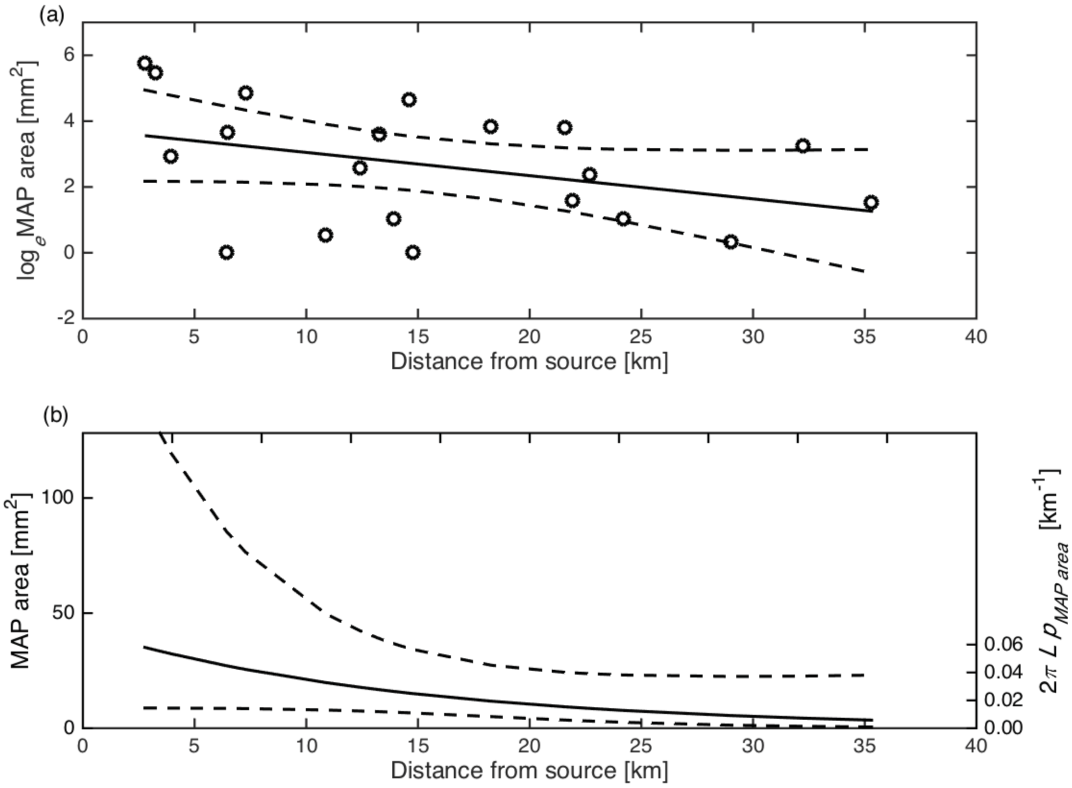

Figure C.6 Log-linear (a) and exponential decay (b) of B-MAP area (mm^2) as a function of distance L (km) from the B-source location. The regression model [$\log_e$MAP area = 3.76 – 0.07 L; $r^2 = 0.14$; $p = 0.10$] in (a) is illustrated by a solid line with the upper and lower 95% confidence limits around the model (dashed lines) fitted to the MAP area estimates. The exponential decay [MAP area = $4.29 \times 10^1 e^{-0.07L}$] in (b) is illustrated by a solid line with the upper and lower 95% confidence limits (dashed lines). The exponential decay (solid line) can be interpreted as $2\pi L\ p_{MAP}$ (right ordinate) with an e-folding scale of 14.16 km that has upper and lower 95% confidence limits of 63.29 and 6.37 km.

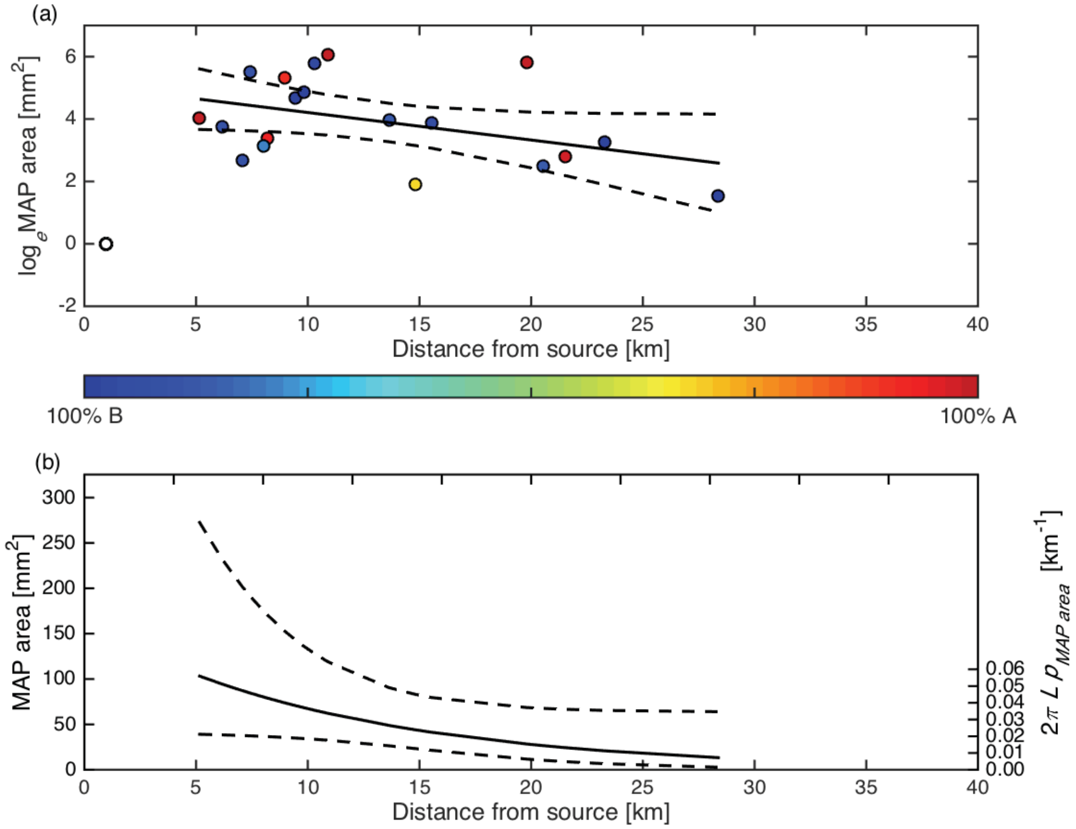

Figure C.7 Log-linear (a) and exponential decay (b) of A+B MAP area (mm^2) as a function of distance L (km) from the hypothetical averaged A+B source location. The regression model [$\log_e$MAP area = $5.09 - 0.09L$; $r^2 = 0.19$; $p = 0.07$] in (a) is illustrated by a solid line with the upper and lower 95% confidence limits around the model (dashed lines) fitted to the MAP area estimates, classified by the proportion of A- and B-MAPs according to the color scale bar. The empty recovered collector (i.e., zero return) is shown with no color and is not included in the regression model. The exponential decay [MAP area = $1.63 \times 10^2 e^{-0.09L}$] in (b) is illustrated by a solid line with the upper and lower 95% confidence limits (dashed lines). The exponential decay (solid line) can be interpreted as $2\pi L\ p_{MAP}$ (right ordinate) with an e-folding scale of 11.34 km that has upper and lower 95% confidence limits of 156.25 and 5.47 km.

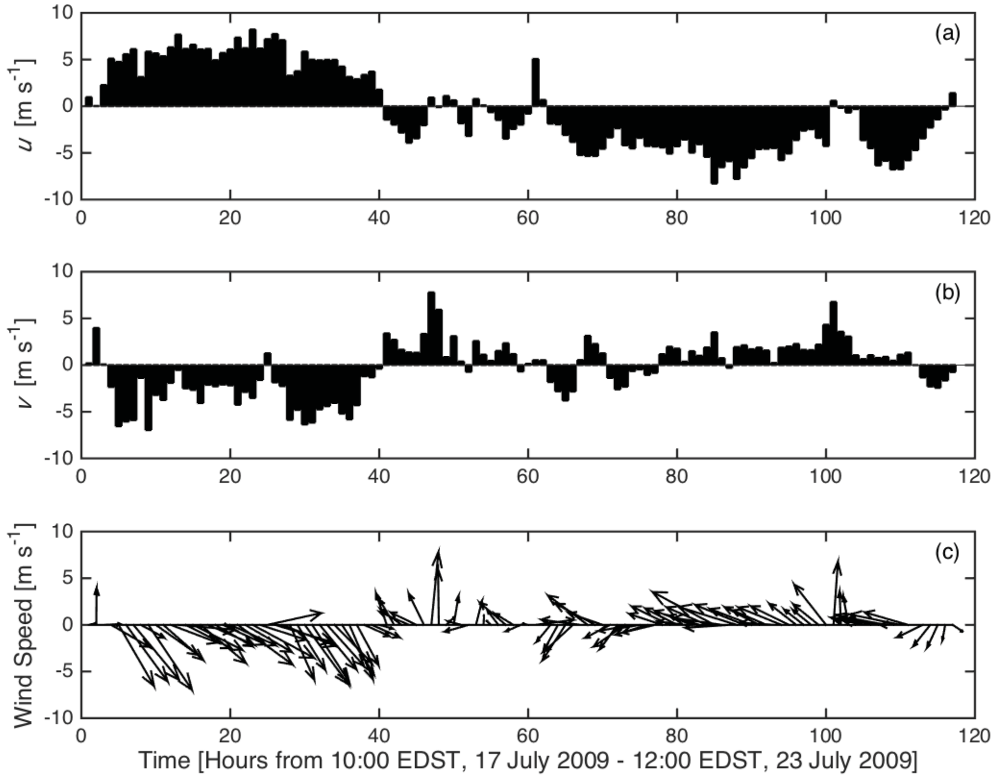

Figure C.8 (a) East-west (*u*) and (b) north-south (*v*) wind components at Station LSCM4 in Lake St. Clair during the particle tracing study in July 2009. (c) Wind speed during the particle tracing study, also recorded at LSCM4, where the lengths of the arrows are proportional to speed. Both histograms and arrows are depicted at a 1.25-h resolution.

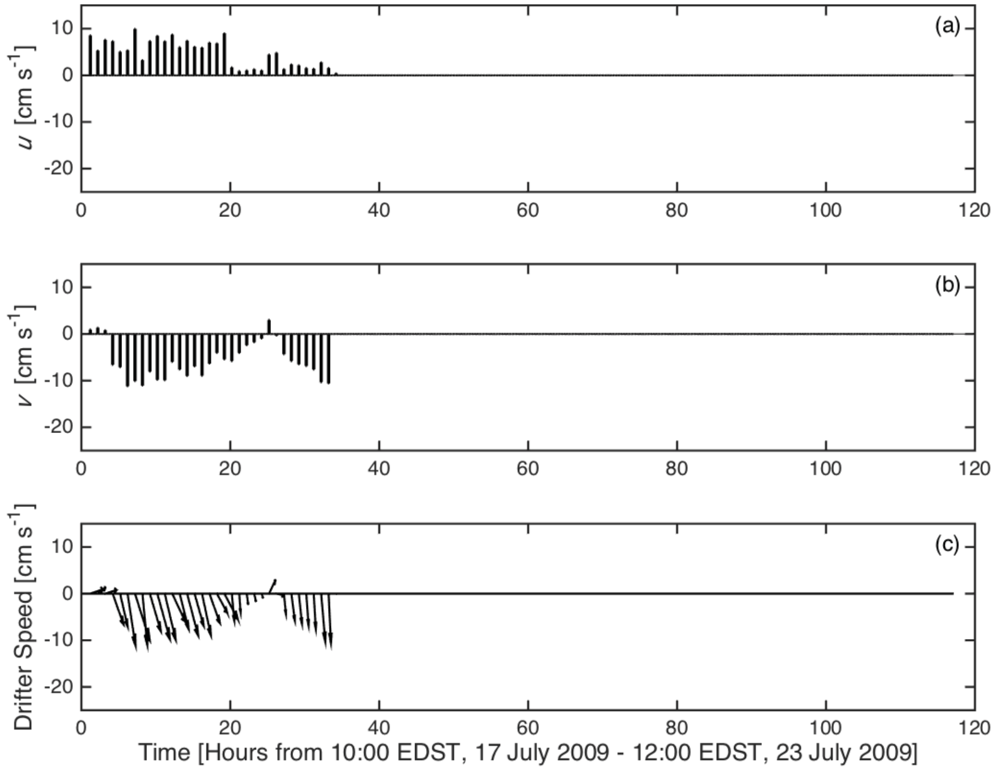

Figure C.9 (a) East-west (*u*) and (b) north-south (*v*) components of D1 during the particle tracing study in July 2009. (c) D1 speed during the particle tracing study, where the lengths of the arrows are proportional to speed. Both histograms and arrows are depicted at a 1.25-h resolution.

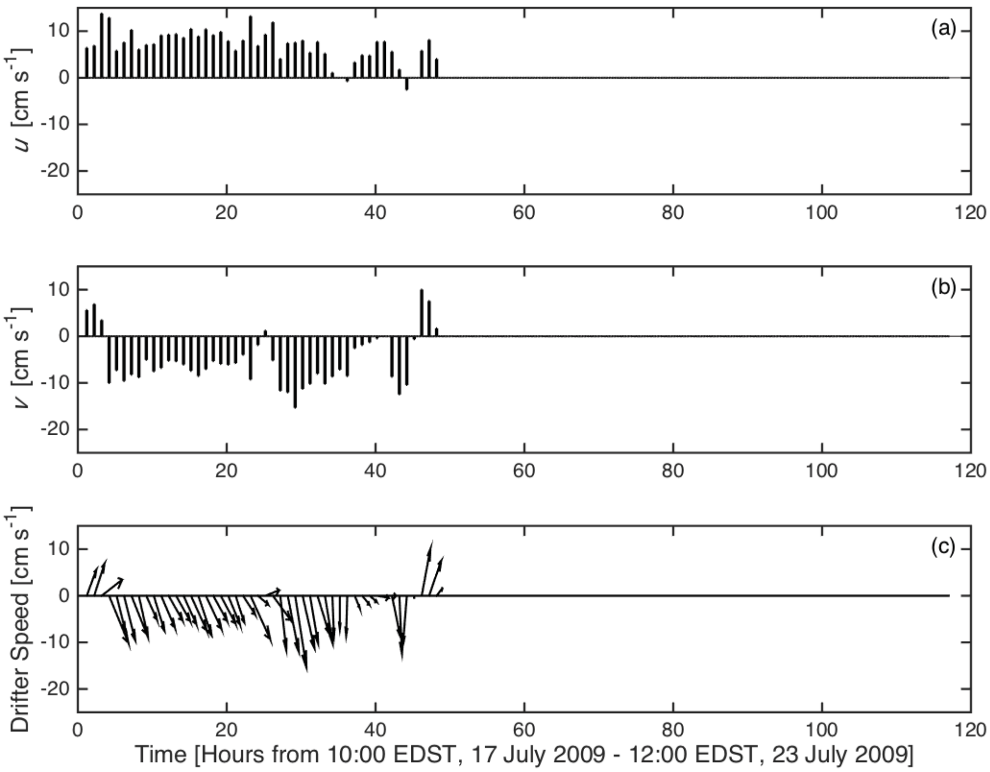

Figure C.10 (a) East-west (*u*) and (b) north-south (*v*) components of D2 during the particle tracing study in July 2009. (c) D2 speed during the particle tracing study, where the lengths of the arrows are proportional to speed. Both histograms and arrows are depicted at a 1.25-h resolution.

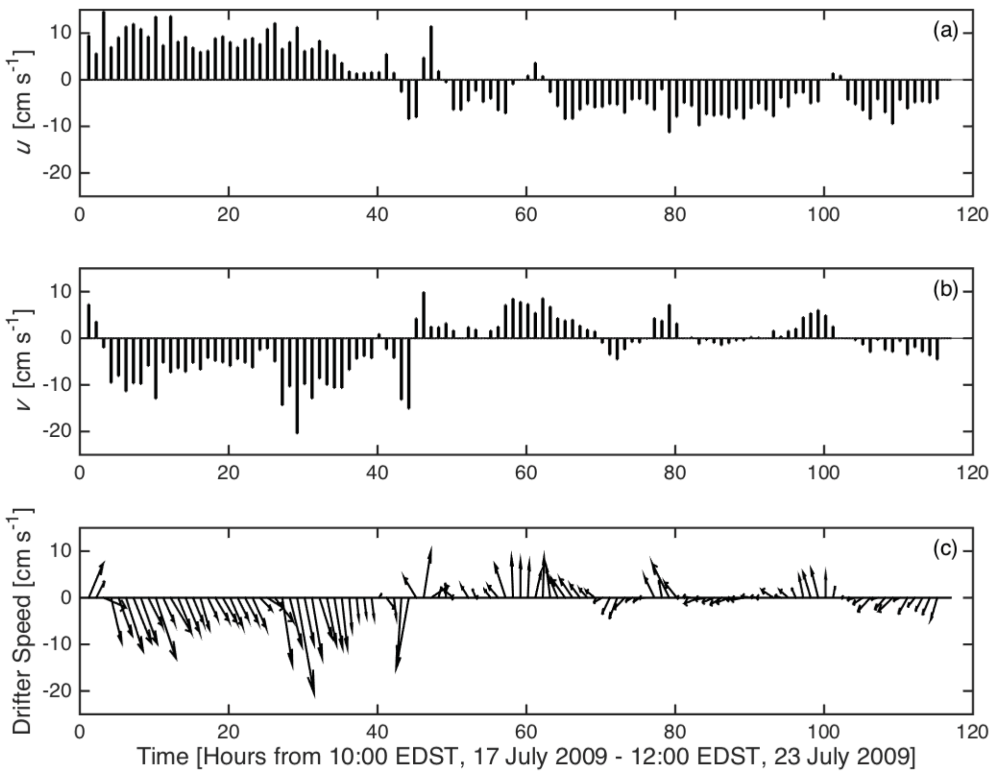

Figure C.11 (a) East-west (u) and (b) north-south (v) components of D3 during the particle tracing study in July 2009. (c) D3 speed during the particle tracing study, where the lengths of the arrows are proportional to speed. Both histograms and arrows are depicted at a 1.25-h resolution.

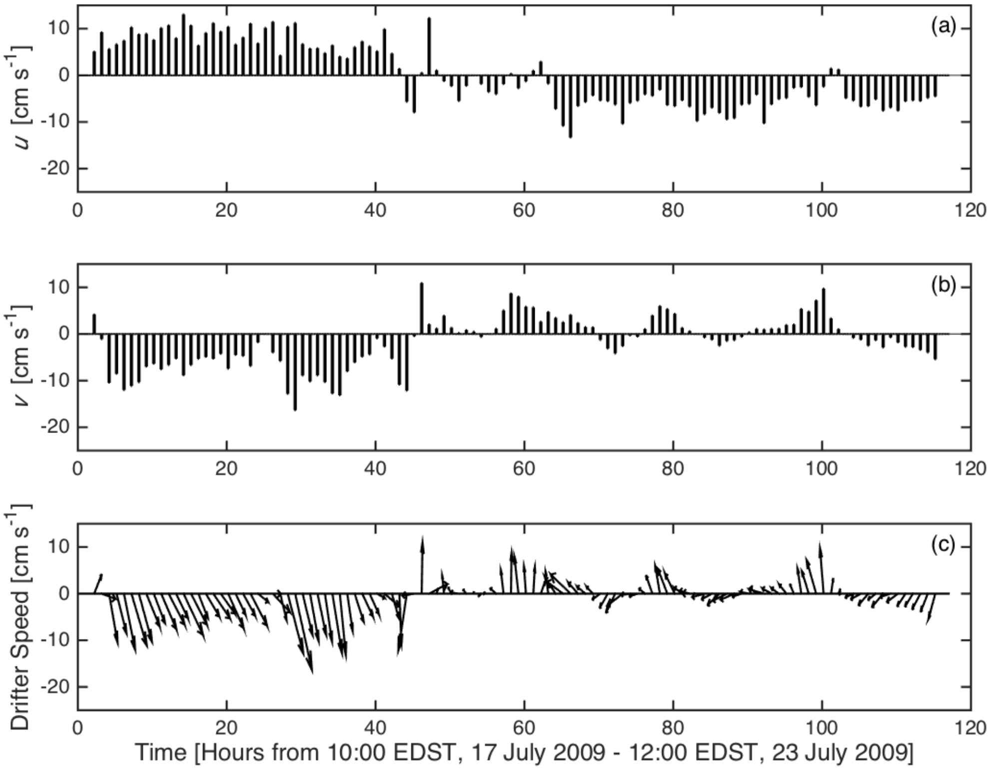

Figure C.12 (a) East-west (*u*) and (b) north-south (*v*) components of D4 during the particle tracing study in July 2009. (c) D4 speed during the particle tracing study, where the lengths of the arrows are proportional to speed. Both histograms and arrows are depicted at a 1.25-h resolution.

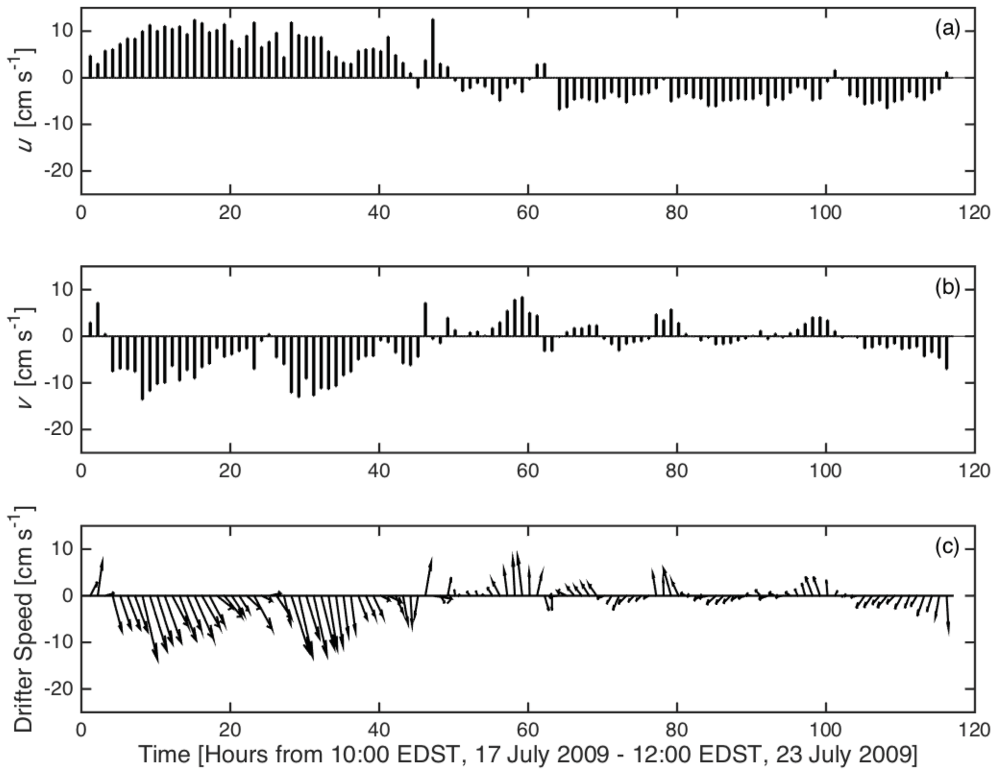

Figure C.13 (a) East-west (*u*) and (b) north-south (*v*) components of D5 during the particle tracing study in July 2009. (c) D5 speed during the particle tracing study, where the lengths of the arrows are proportional to speed. Both histograms and arrows are depicted at a 1.25-h resolution.

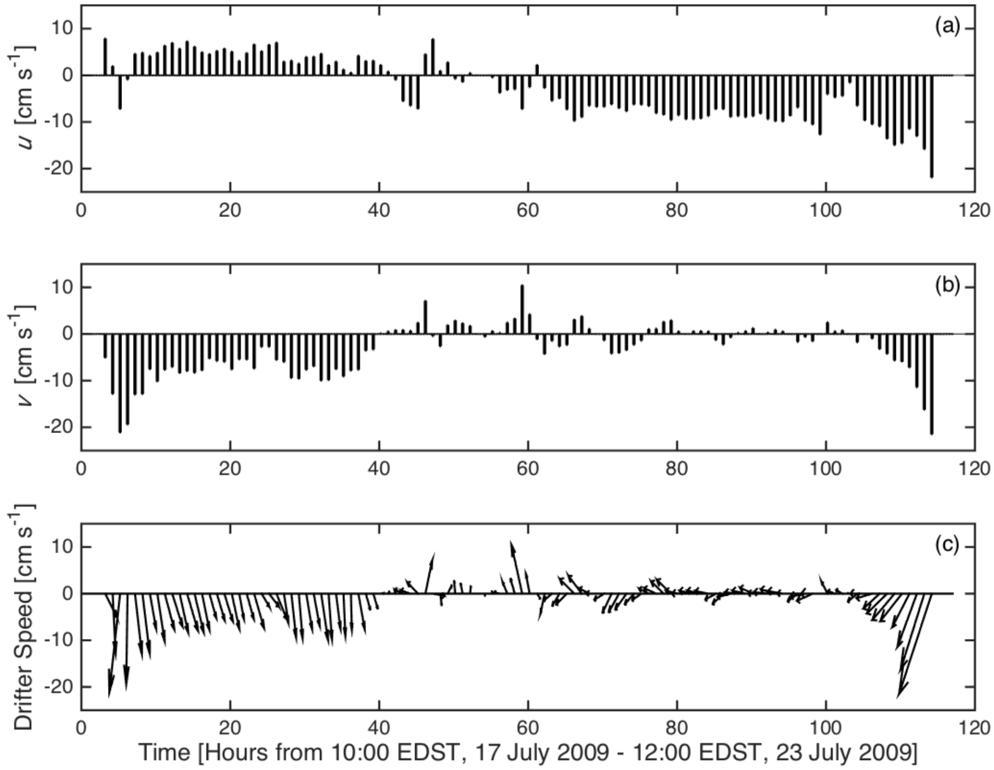

Figure C.14 (a) East-west (*u*) and (b) north-south (*v*) components of D7 during the particle tracing study in July 2009. (c) D7 speed during the particle tracing study, where the lengths of the arrows are proportional to speed. Both histograms and arrows are depicted at a 1.25-h resolution.

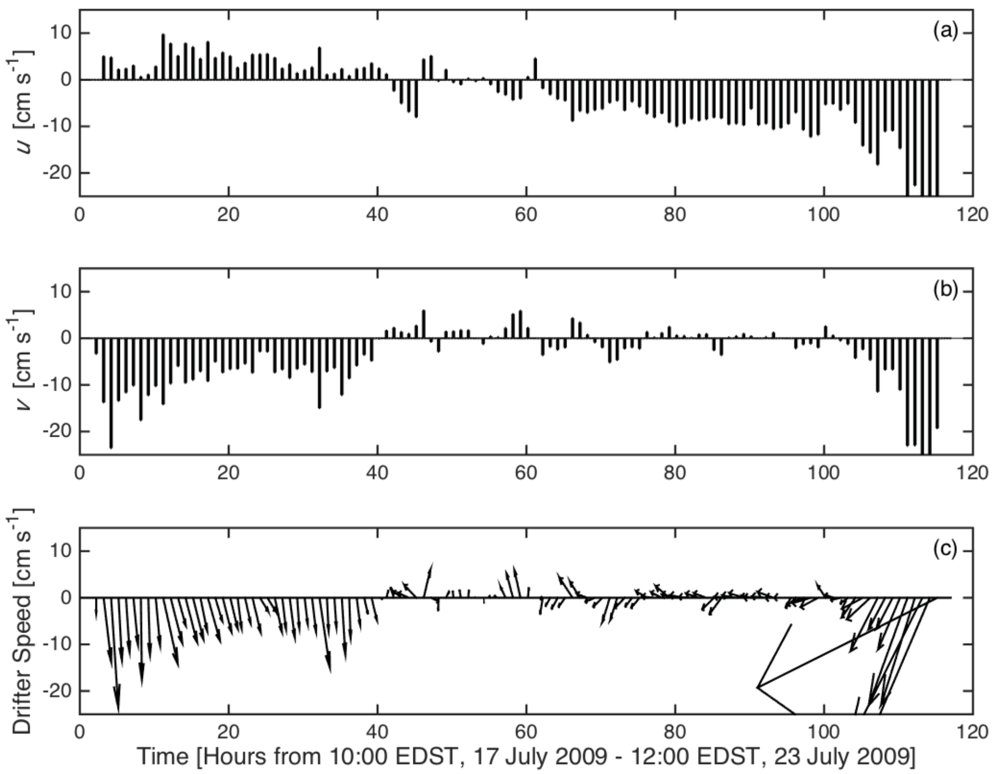

Figure C.15 (a) East-west (*u*) and (b) north-south (*v*) components of D8 during the particle tracing study in July 2009. (c) D8 speed during the particle tracing study, where the lengths of the arrows are proportional to speed. Both histograms and arrows are depicted at a 1.25-h resolution.

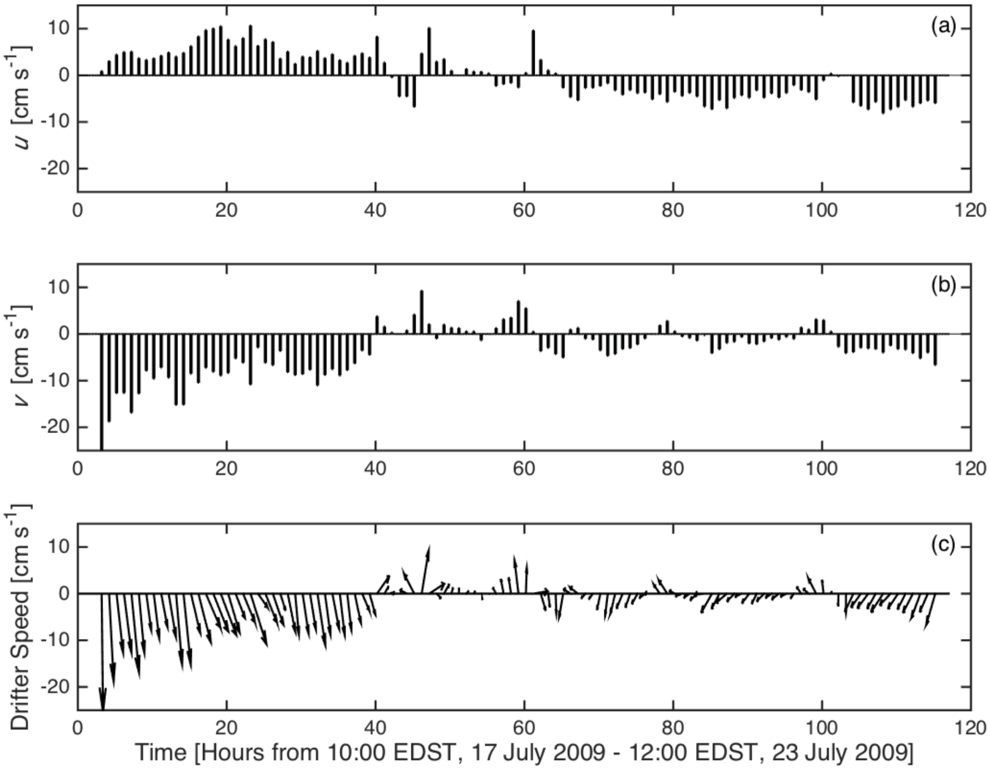

Figure C.16 (a) East-west (*u*) and (b) north-south (*v*) components of D9 during the particle tracing study in July 2009. (c) D9 speed during the particle tracing study, where the lengths of the arrows are proportional to speed. Both histograms and arrows are depicted at a 1.25-h resolution.

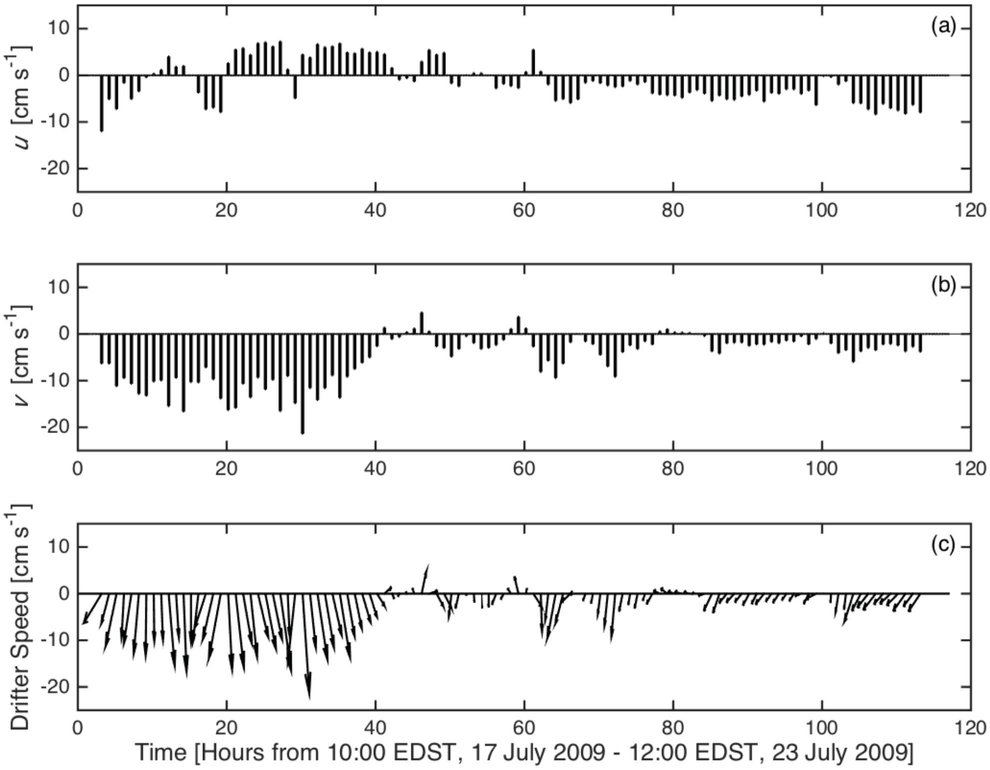

Figure C.17 (a) East-west (*u*) and (b) north-south (*v*) components of D10 during the particle tracing study in July 2009. (c) D10 speed during the particle tracing study, where the lengths of the arrows are proportional to speed. Both histograms and arrows are depicted at a 1.25-h resolution.

Table C.1 Summary of the coefficients of determination (r^2) for the complex regressions between wind (W; cm s^{-1}) and each drifter (D1-D10; cm s^{-1}) $u + iv$ estimate and all possible pairs of drifter $u + iv$ estimates. The drifters with anomalous behaviors (explained in the text) are labeled with asterisks.

	W	**D1***	**D2***	**D3**	**D4**	**D5**	**D7**	**D8***	**D9**	**D10**
W	1.00	0.10	0.42	0.68	0.68	0.68	0.67	0.31	0.66	0.56
D1*	0.10	1.00	0.16	0.03	0.03	0.06	0.02	0.00	0.01	0.01
D2*	0.42	0.16	1.00	0.19	0.18	0.15	0.09	0.03	0.08	0.05
D3	0.68	0.03	0.19	1.00	0.88	0.82	0.59	0.30	0.62	0.42
D4	0.68	0.03	0.18	0.88	1.00	0.87	0.63	0.32	0.63	0.45
D5	0.68	0.06	0.15	0.82	0.87	1.00	0.64	0.33	0.63	0.44
D7	0.67	0.02	0.09	0.59	0.63	0.64	1.00	0.62	0.69	0.53
D8*	0.31	0.00	0.03	0.30	0.32	0.33	0.62	1.00	0.42	0.29
D9	0.66	0.01	0.08	0.62	0.63	0.63	0.69	0.42	1.00	0.59
D10	0.56	0.01	0.05	0.42	0.45	0.44	0.53	0.29	0.59	1.00

Table C.2 Summary of the regression parameters for drifter speed (D1$_{sp}$-D10$_{sp}$; cm s^{-1}) as a function of wind speed (W$_{sp}$; cm s^{-1}), indicating the slopes, intercepts, coefficients of determination (r^2), and p-values associated with the first row of **Figure 5.10**. The average slope and its associated 95% confidence interval is 1.11 x 10^{-2} cm s^{-1} ± 1.41 x 10^{-3} cm s^{-1}, where D1, D2, and D8 (*) are excluded due to their anomalous behaviors explained in the text.

	D1*	**D2***	**D3**	**D4**	**D5**	**D7**	**D8***	**D9**	**D10**
Slope ($\times 10^{-2} \pm \times 10^{-3}$)	0.19 ± 4.08	0.80 ± 1.77	1.04 ± 1.21	1.05 ± 1.15	1.07 ± 1.27	0.92 ± 1.80	0.18 ± 4.51	1.13 ± 1.45	1.44 ± 1.59
Intercept (cm s^{-1})	9.84 ± 2.84	5.28 ± 1.13	2.82 ± 0.66	2.67 ± 0.64	1.57 ± 0.69	3.68 ± 0.99	9.26 ± 2.48	1.28 ± 0.80	0.23 ± 0.88
r^2	0.01	0.25	0.33	0.35	0.32	0.15	0.00	0.29	0.36
p-value	0.354	< 0.001	< 0.001	< 0.001	< 0.001	< 0.001	0.441	< 0.001	< 0.001

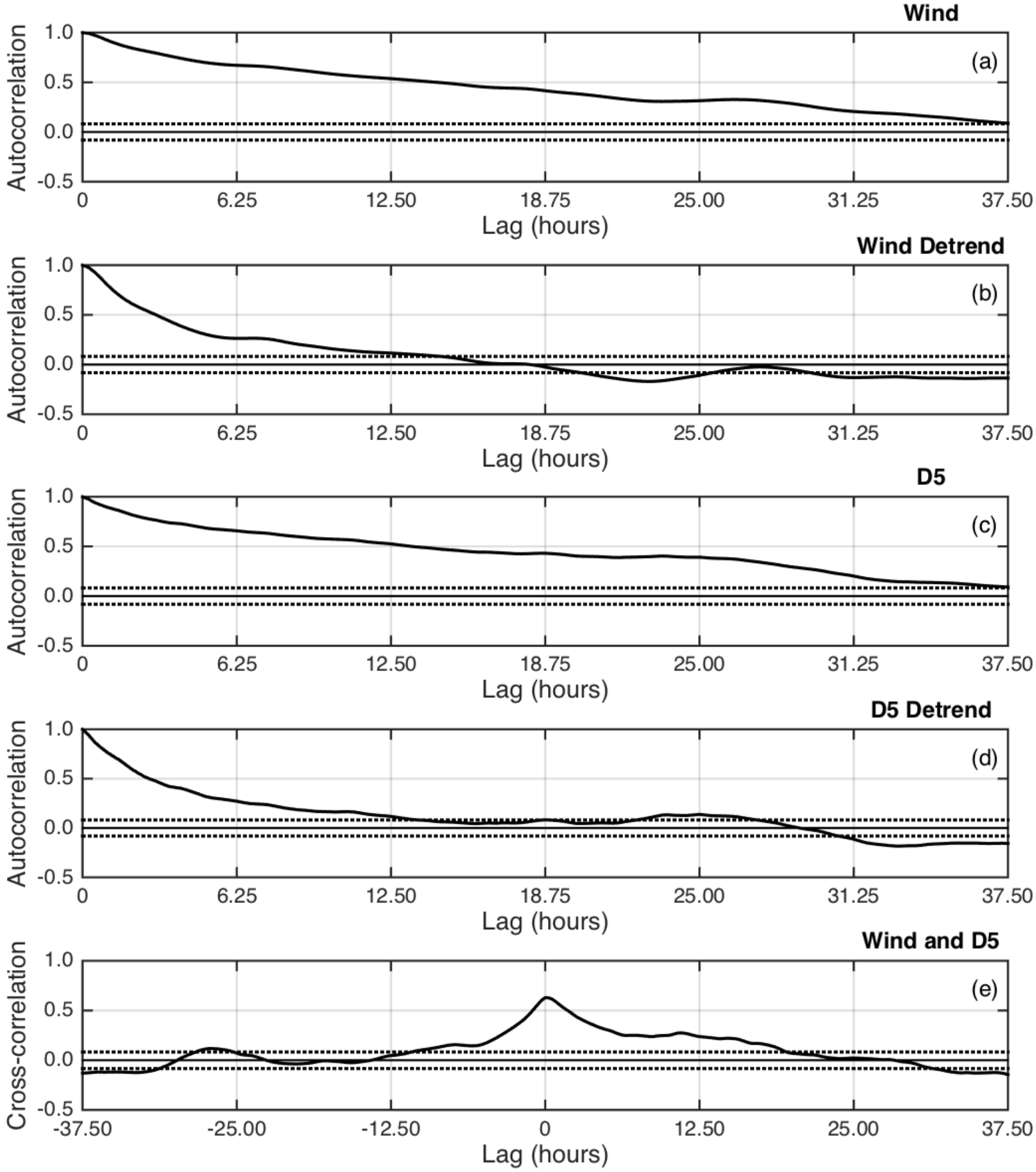

Figure C.18 Auto-correlograms (n = 575) of the complex regressions $u + iv$ for (a) wind, (b) wind with the trend removed, (c) D5, and (d) D5 with the trend removed. Dotted lines approximate upper and lower 95% confidence limits of ± 2 SD away from zero (solid lines). (e) Cross-correlogram of the complex regressions $u + iv$ for de-trended wind and de-trended D5, with dotted lines approximating upper and lower 95% confidence limits of ± 2 SD away from zero (solid lines). All data has been interpolated to a 15-m resolution.

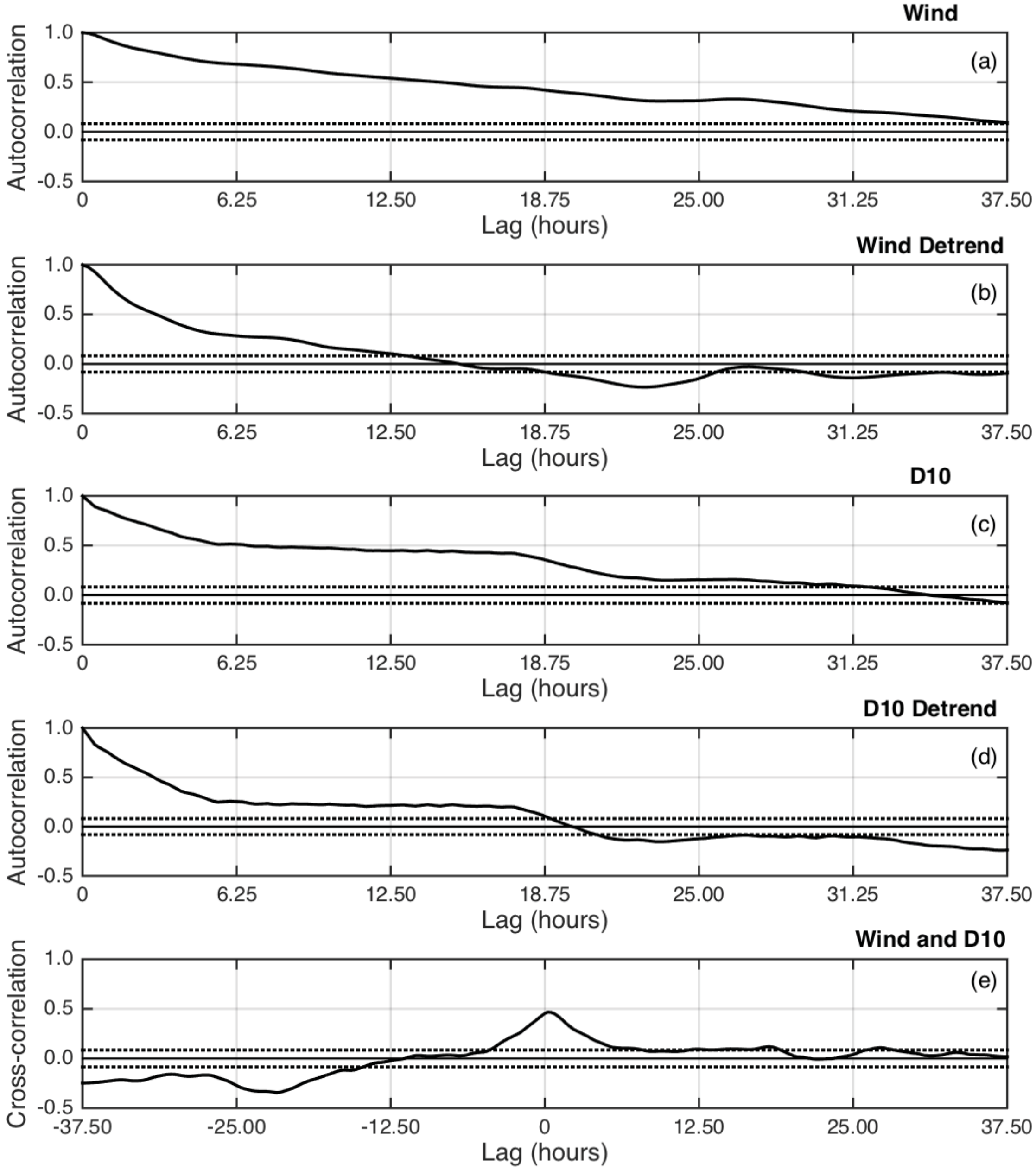

Figure C.19 Auto-correlograms ($n = 575$) of the complex regressions $u + iv$ for (a) wind, (b) wind with the trend removed, (c) D10, and (d) D10 with the trend removed. Dotted lines approximate upper and lower 95% confidence limits of ± 2 SD away from zero (solid lines). (e) Cross-correlogram of the complex regressions $u + iv$ for de-trended wind and de-trended D10, with dotted lines approximating upper and lower 95% confidence limits of ± 2 SD away from zero (solid lines). All data has been interpolated to a 15-m resolution.

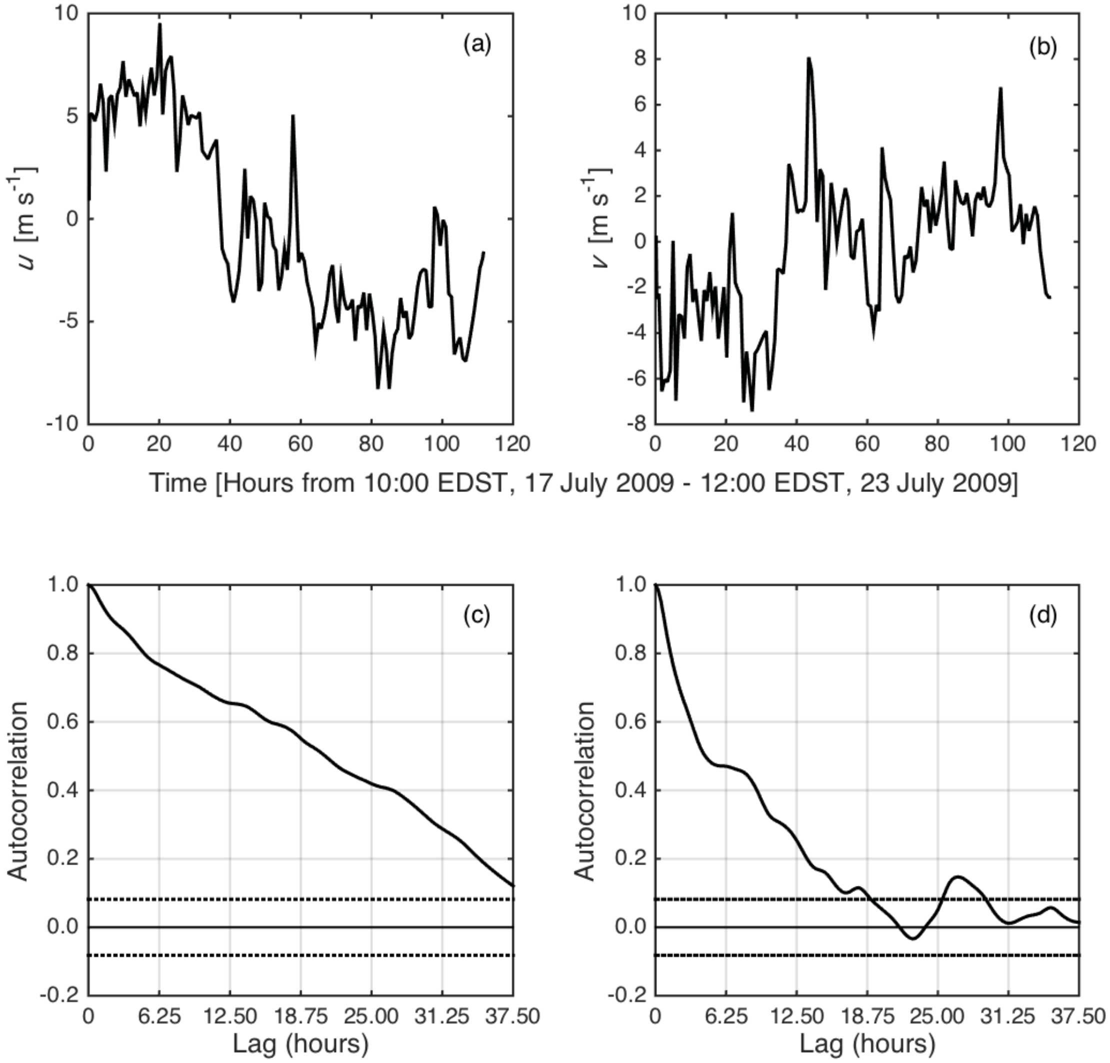

Figure C.20 (a) East-west (*u*) and (b) north-south (*v*) wind components at Station LSCM4 in Lake St. Clair during the particle tracing study in July 2009. Auto-correlograms of the (c) *u* and (d) *v* wind components, with dotted lines approximating upper and lower 95% confidence limits of ± 2 SD away from zero (solid lines). All data has been interpolated to a 15-m resolution.

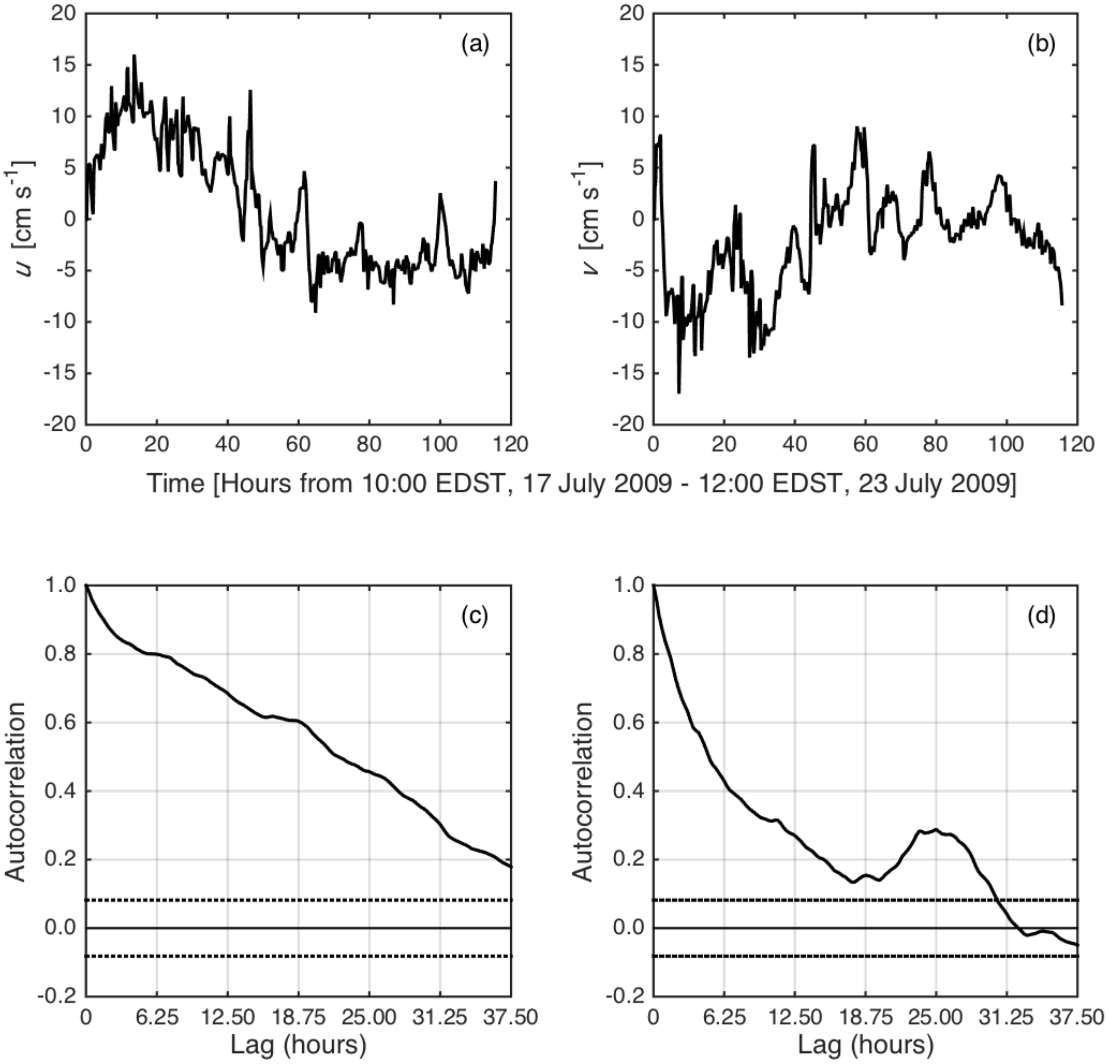

Figure C.21 (a) East-west (*u*) and (b) north-south (*v*) components of D5 during the particle tracing study in July 2009. Auto-correlograms of the (c) *u* and (d) *v* components of D5, with dotted lines approximating upper and lower 95% confidence limits of ± 2 SD away from zero (solid lines). All data has been interpolated to a 15-m resolution.

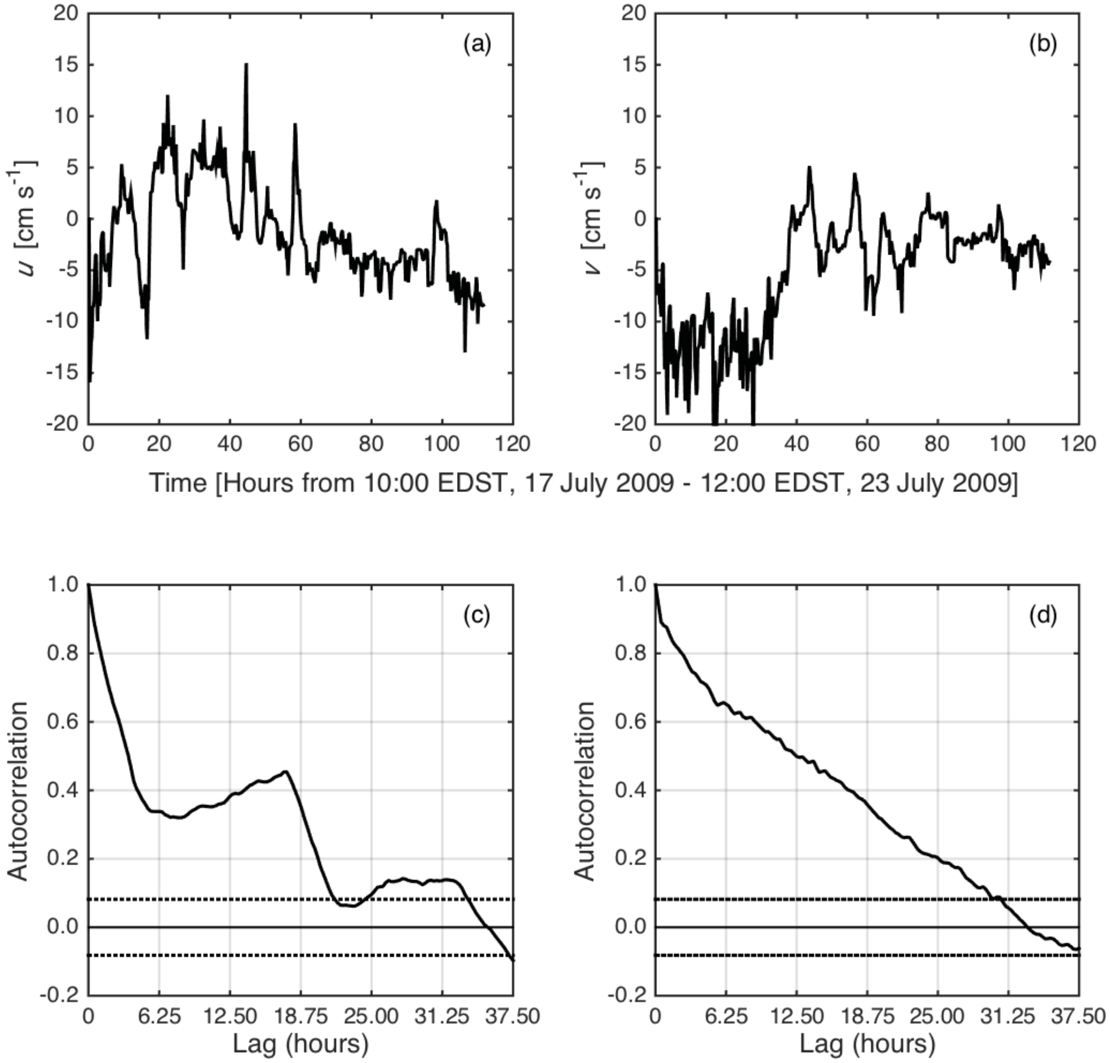

Figure C.22 (a) East-west (*u*) and (b) north-south (*v*) components of D10 during the particle tracing study in July 2009. Auto-correlograms of the (c) *u* and (d) *v* components of D10, with dotted lines approximating upper and lower 95% confidence limits of ± 2 SD away from zero (solid lines). All data has been interpolated to a 15-m resolution.

Table C.3 Summary of the complex regression parameters for drifter $u + \mathrm{i}v$ (D1–D10; cm s^{-1}) as a function of wind $u + \mathrm{i}v$ (W; cm s^{-1}), indicating the residual speed (cm s^{-1}) and angle (degrees), the optimal wind scale and rotation (degrees), and the coefficients of determination (r^2). The drifters with anomalous behaviors (explained in the text) are labeled with asterisks.

	D1*	**D2***	**D3**	**D4**	**D5**	**D7**	**D8***	**D9**	**D10**
Residual speed (cm s^{-1})	4.54	4.52	1.28	1.46	2.21	3.57	5.36	3.31	5.25
Residual direction (degrees)	-31.02	-39.41	-67.42	-69.10	-47.21	-131.69	-134.76	-81.41	-98.32
Optimal wind scale (x 10^{-2})	0.59	0.91	1.34	1.30	1.17	1.29	1.39	1.11	0.98
Optimal wind rotation (degrees)	-40.83	-6.95	-4.26	-4.01	-5.68	-8.50	-6.65	-15.14	-36.21
r^2	0.10	0.42	0.68	0.68	0.68	0.67	0.31	0.66	0.56

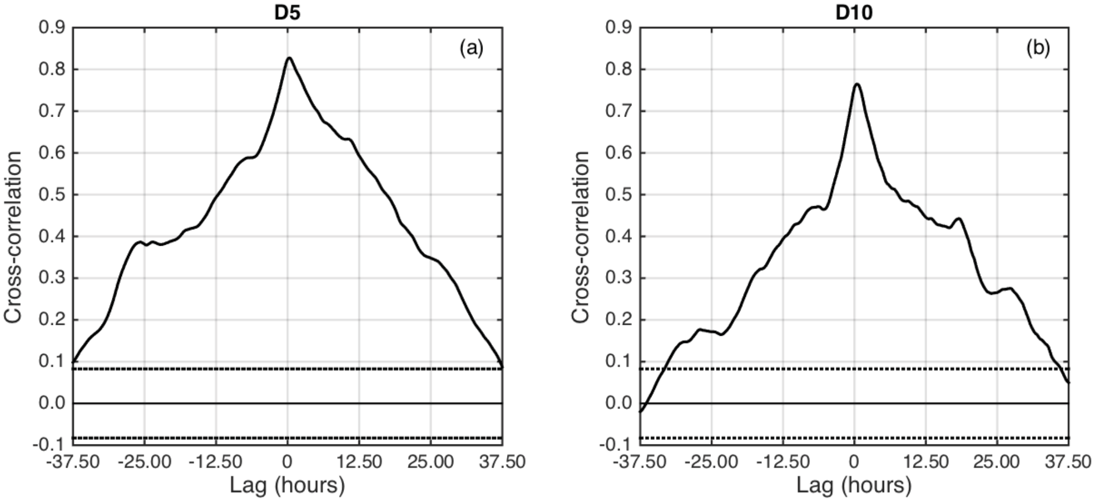

Figure C.23 Cross-correlograms of the complex regressions u + iv for observed and predicted drifter movement in (a) D5 and (b) D10. Dotted lines approximate upper and lower 95% confidence limits of ± 2 SD away from zero (solid lines). All data has been interpolated to a 15-m resolution.

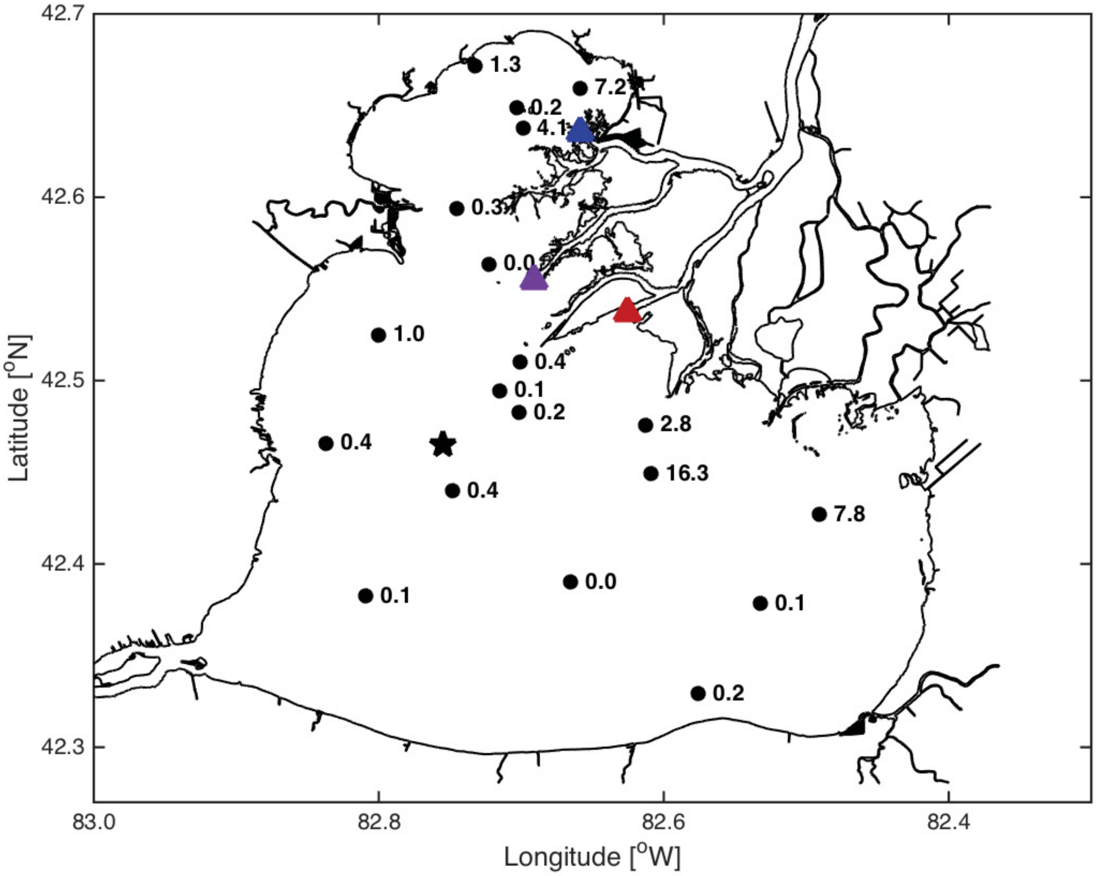

Figure C.24 Coastline chart of Lake St. Clair illustrating the location-specific A+B MAP area (mm^2) captured among the recovered collectors (black filled circles). MAP source locations are denoted by triangles, where the northern triangle (blue) represents the B-source, the southern triangle (red) represents the A-source, and the intermediate triangle (purple) represents the hypothetical averaged A+B source. The location of Station LSCM4, where wind speed and direction were recorded, is indicated with a star.

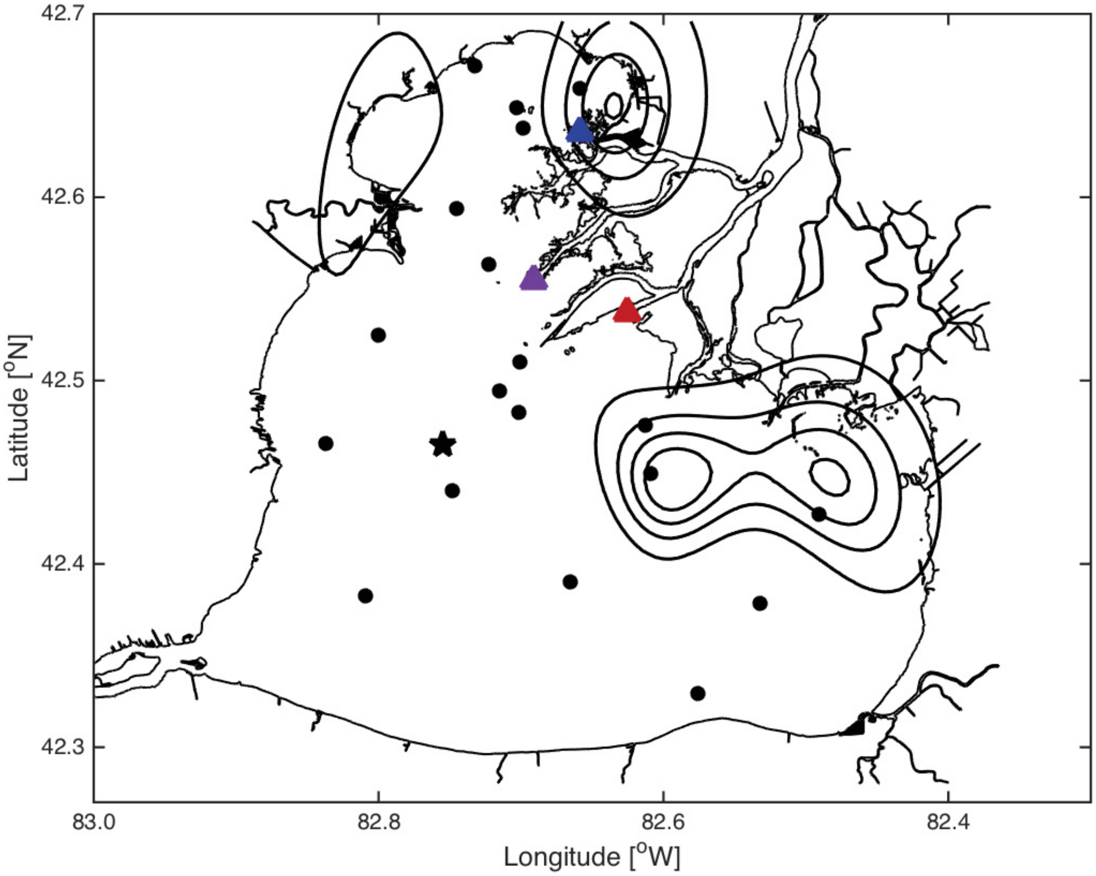

Figure C.25 Coastline chart of Lake St. Clair illustrating the relative concentration isopleths (2, 4, 6, 8) of A+B captured MAPs, with recovered collector locations denoted by black filled circles. MAP source locations are denoted by triangles, where the northern triangle (blue) represents the B-source, the southern triangle (red) represents the A-source, and the intermediate triangle (purple) represents the hypothetical averaged A+B source. The location of Station LSCM4, where wind speed and direction were recorded, is indicated with a star.

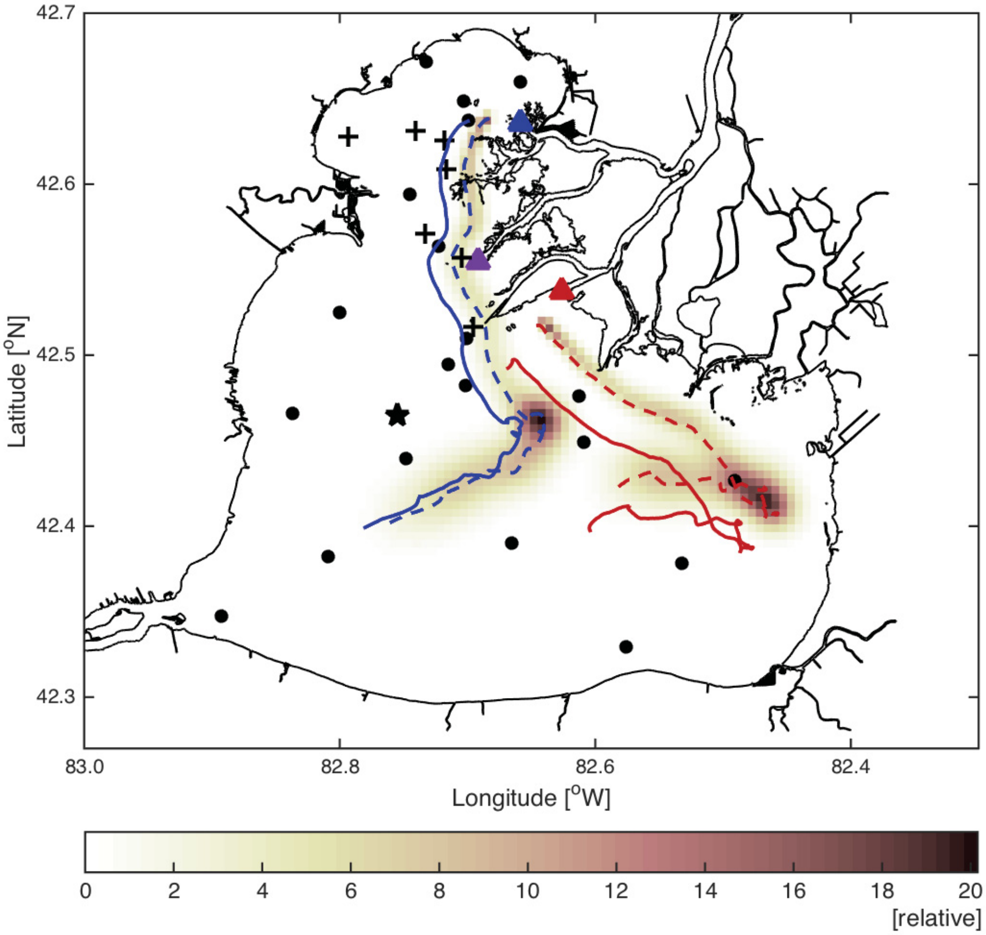

Figure C.26 Coastline chart of Lake St. Clair and scale bar illustrating the relative number of VPs at each grid cell across the model domain as of 09:00 h EDST on 23 July 2009, and based on a small-scale diffusivity (K_p) constant of 2 $m^2\ s^{-1}$. The observed drifter trajectories are shown with solid lines (D5 red; D10 blue) and the modeled drifter trajectories are shown with dashed lines (D5 red; D10 blue). Black filled circles denote recovered collector locations. MAP source locations are denoted by triangles, where the northern triangle (blue) represents the B-source, the southern triangle (red) represents the A-source, and the intermediate triangle (purple) represents the hypothetical averaged A+B source. The location of Station LSCM4, where wind speed and direction were recorded, is indicated with a star. VPs cannot move beyond the coastline.

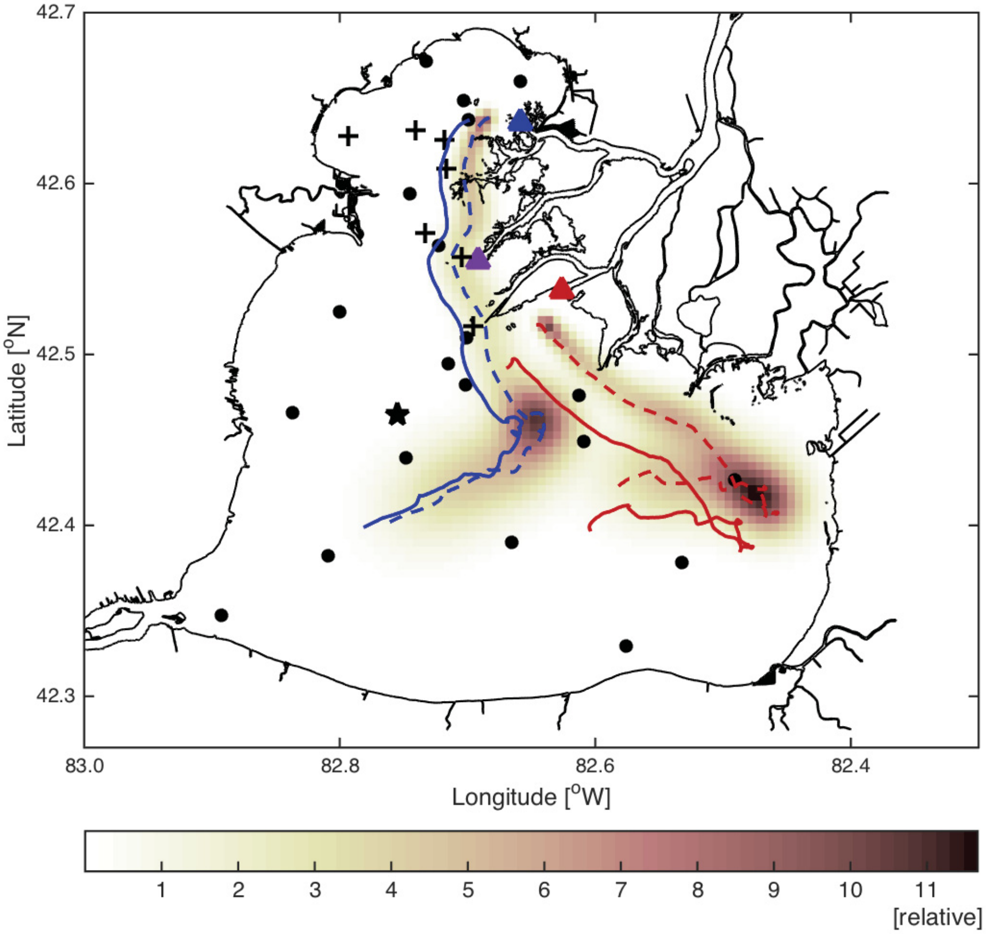

Figure C.27 Coastline chart of Lake St. Clair and scale bar illustrating the relative number of VPs at each grid cell across the model domain as of 09:00 h EDST on 23 July 2009, and based on a small-scale diffusivity (K_p) constant of 5 m^2 s^{-1}. The observed drifter trajectories are shown with solid lines (D5 red; D10 blue) and the modeled drifter trajectories are shown with dashed lines (D5 red; D10 blue). Black filled circles denote recovered collector locations. MAP source locations are denoted by triangles, where the northern triangle (blue) represents the B-source, the southern triangle (red) represents the A-source, and the intermediate triangle (purple) represents the hypothetical averaged A+B source. The location of Station LSCM4, where wind speed and direction were recorded, is indicated with a star. VPs cannot move beyond the coastline.

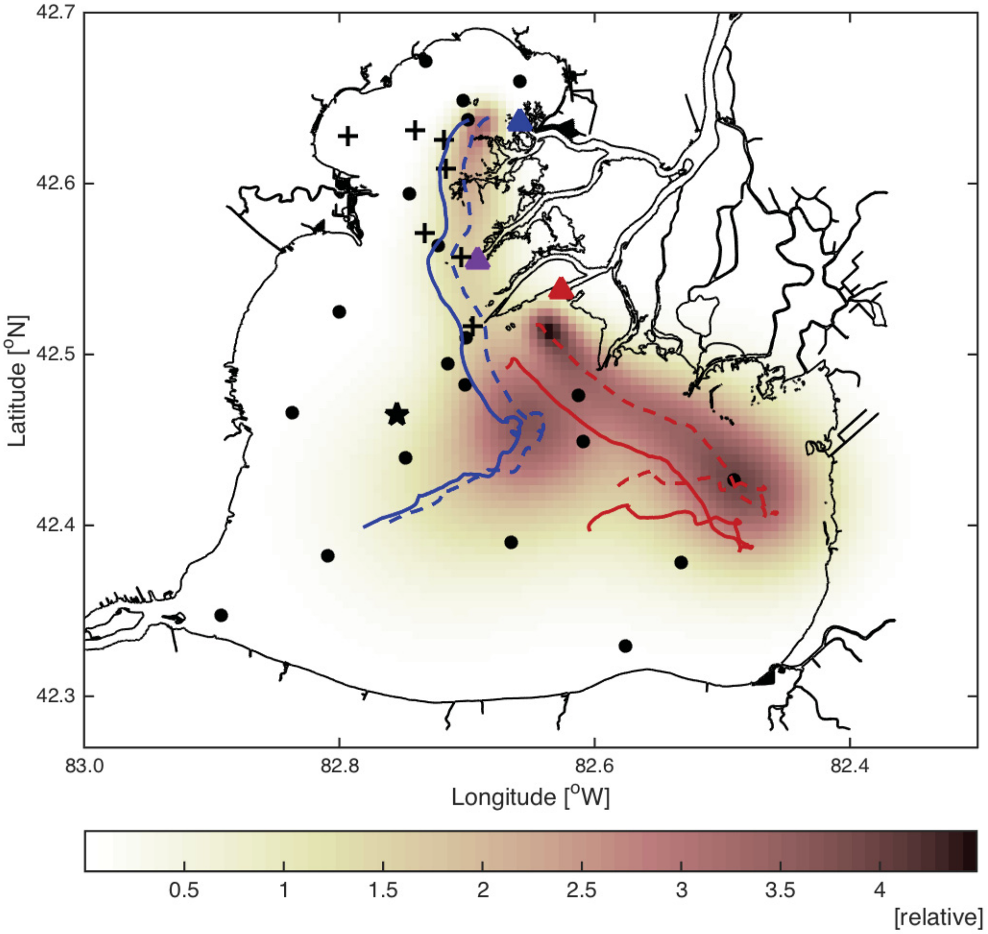

Figure C.28 Coastline chart of Lake St. Clair and scale bar illustrating the relative number of VPs at each grid cell across the model domain as of 09:00 h EDST on 23 July 2009, and based on a small-scale diffusivity (K_p) constant of 25 m^2 s^{-1}. The observed drifter trajectories are shown with solid lines (D5 red; D10 blue) and the modeled drifter trajectories are shown with dashed lines (D5 red; D10 blue). Black filled circles denote recovered collector locations. MAP source locations are denoted by triangles, where the northern triangle (blue) represents the B-source, the southern triangle (red) represents the A-source, and the intermediate triangle (purple) represents the hypothetical averaged A+B source. The location of Station LSCM4, where wind speed and direction were recorded, is indicated with a star. VPs cannot move beyond the coastline.

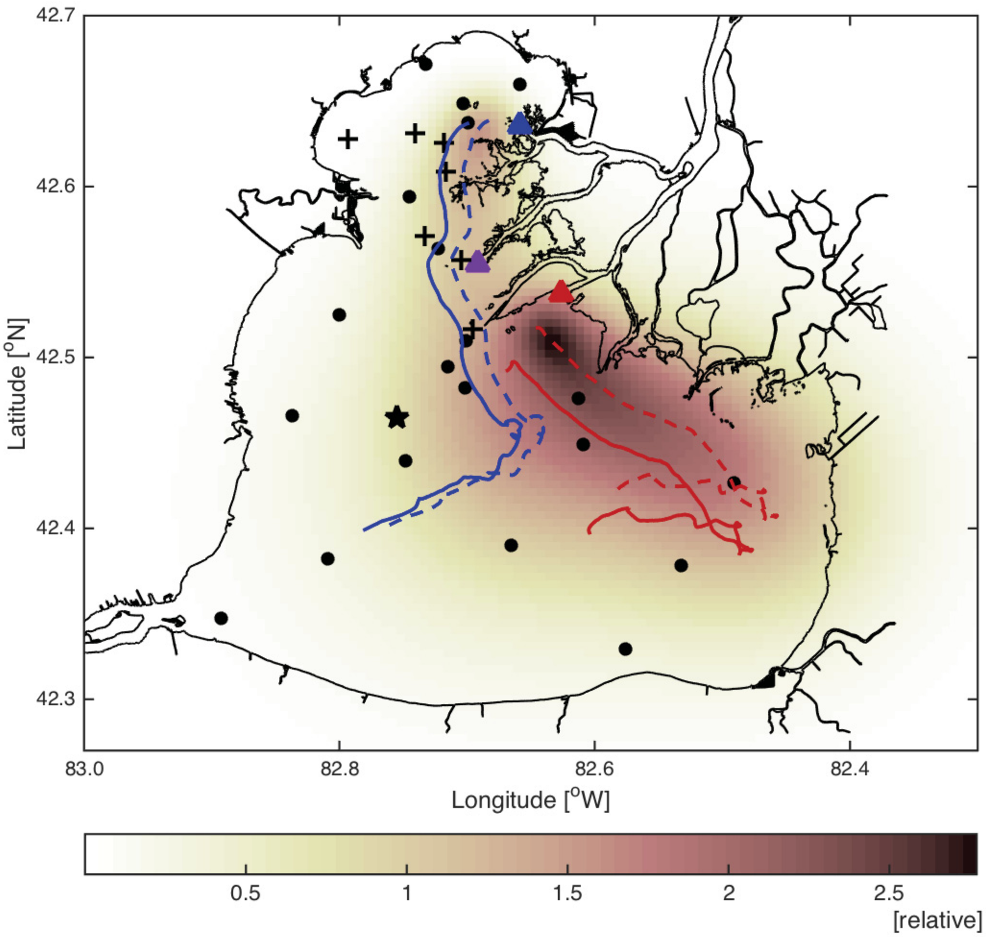

Figure C.29 Coastline chart of Lake St. Clair and scale bar illustrating the relative number of VPs at each grid cell across the model domain as of 09:00 h EDST on 23 July 2009, and based on a small-scale diffusivity (K_p) constant of 80 $m^2 s^{-1}$. The observed drifter trajectories are shown with solid lines (D5 red; D10 blue) and the modeled drifter trajectories are shown with dashed lines (D5 red; D10 blue). Black filled circles denote recovered collector locations. MAP source locations are denoted by triangles, where the northern triangle (blue) represents the B-source, the southern triangle (red) represents the A-source, and the intermediate triangle (purple) represents the hypothetical averaged A+B source. The location of Station LSCM4, where wind speed and direction were recorded, is indicated with a star. VPs cannot move beyond the coastline.